



The Evolution of Rotation and Magnetism in Small Stars Near the Sun

Citation

Newton, Elisabeth R. 2016. The Evolution of Rotation and Magnetism in Small Stars Near the Sun. Doctoral dissertation, Harvard University, Graduate School of Arts & Sciences.

Permanent link

<http://nrs.harvard.edu/urn-3:HUL.InstRepos:33493355>

Terms of Use

This article was downloaded from Harvard University's DASH repository, and is made available under the terms and conditions applicable to Other Posted Material, as set forth at <http://nrs.harvard.edu/urn-3:HUL.InstRepos:dash.current.terms-of-use#LAA>

Share Your Story

The Harvard community has made this article openly available.
Please share how this access benefits you. [Submit a story](#).

[Accessibility](#)

© 2016 — Elisabeth R. Newton

All rights reserved.

The Evolution of Rotation and Magnetism in Small Stars Near the Sun

Abstract

Despite the prevalence of M dwarfs, the smallest and most common type of main sequence star, their sizes, compositions, and ages are not well-constrained. Empirical determination of these properties is important for gaining insight into their stellar structure, magnetic field generation, and angular momentum evolution. I obtained low-resolution ($R = 2000$) near-infrared spectra of 447 nearby mid-to-late M dwarfs. I measured their absolute radial velocities with an accuracy of 4.4 km/s by exploiting telluric lines to establish an absolute wavelength calibration. I estimated their metallicities from the equivalent width of the sodium absorption feature at $2.2\ \mu\text{m}$ to a precision of 0.12 dex, and from 2MASS colors to a precision of 0.15 dex. Using stars with radii measured from interferometry, I showed that the equivalent widths of aluminum and magnesium absorption features can be used to infer K and M dwarf temperatures to a precision of 69 K, and radii to $0.027\ R_{\odot}$. I applied these relations to planet-hosting stars from Kepler, showing that the typical planet is 15% larger than inferred when adopting stellar parameters from other recent catalogs. Using photometry from the MEarth-North Observatory, I measured rotation periods from 0.1 to 140 days for 387 M dwarfs. I found a prevalence of stable spot patterns, and no correlation between period and amplitude for fully-convective stars. Using galactic kinematics as a proxy for age, I found that rapid rotators ($P < 10$ days) are < 2 Gyr,

and that the slowest are on average 5 ± 3 Gyr old. I then showed that for early M dwarfs the typical stellar rotation period at 5 Gyr coincides with the orbital period at which habitable planets are found, and I suggest that mid-to-late M dwarfs are optimal targets around which to search for habitable-zone planets. I obtained optical spectra of 247 nearby M dwarfs, and measured the strength of the chromospheric $H\alpha$ emission line. I identified a well-defined boundary in the mass–period plane that separates active and inactive M dwarfs. $H\alpha$ activity is therefore a simple, accessible diagnostic for stellar rotation period, and I present a mass–period relation for inactive M dwarfs. I found a significant (p value $< 10^{-4}$) positive correlation between $H\alpha$ emission strength and photometric variability amplitude, which implies that stars with stronger magnetic fields have both higher levels of chromospheric activity and larger or more abundant spots. I suggest that fully convective stars maintain rapid rotation rates and saturated magnetic activity for about 2 Gyr. They then undergo rapid angular momentum evolution upon reaching some critical threshold. Only upon reaching long rotation periods (around 70 days for a $0.2 M_{\odot}$ star) do their magnetic activity levels drop below what is required for $H\alpha$ to be seen in emission. The stars I have observed in pursuit of this work are the nearest low-mass stars. As such they are the best targets around which to search for habitable, rocky worlds, and my work provides the means to constrain the sizes, temperatures, and ages of those planets.

Contents

Abstract	iii
Acknowledgments	x
1 Introduction	1
1.1 Observations of M Dwarf Stars	2
1.2 The Structure of Cool Stars	5
1.3 The Physics of Cool Stars	10
1.4 M Dwarfs as Exoplanet Hosts	18
1.5 New Observations of Mid-to-late M Dwarfs in the Solar Neighborhood	21
1.5.1 Chapter 2 — Fundamental Stellar Parameters: A Spectroscopic Survey in the NIR	21
1.5.2 Chapter 3 — The Properties of Exoplanet Hosts: Determining the Sizes of Cool Stars	24
1.5.3 Chapter 4 — Angular Momentum Evolution: Stellar Rotation at the Bottom of the Main Sequence	27
1.5.4 Chapter 5 — The Hunt for Habitable Planets: The Impact of Stellar Rotation on Radial Velocity Surveys	29
1.5.5 Chapter 6 — The Origin of Magnetism: Magnetic Activity in Nearby M Dwarfs	30
1.6 Looking Back, Looking Forward: Insight into the Structure and Physics of M Dwarf Stars	32

CONTENTS

2	Near-infrared Metallicities, Radial Velocities and Spectral Types for 447 Nearby M Dwarfs	37
2.1	Introduction	37
2.2	Sample	44
2.2.1	MEarth M dwarfs	49
2.2.2	Spectroscopy targets	49
2.3	Observations	51
2.4	Estimation of uncertainty	54
2.5	NIR spectral types	56
2.5.1	Spectral typing routine	59
2.5.2	IRTF spectral standards	65
2.5.3	Comparing measures of spectral type	66
2.5.4	Spectroscopic distances	67
2.6	Metallicity calibration	69
2.6.1	Metallicities of the primary stars	71
2.6.2	Identification of calibrators	73
2.6.3	Empirical metallicity calibration	76
2.6.4	Influence of effective temperature and surface gravity on the metallicity calibration	89
2.6.5	Tests of our metallicity relation	97
2.6.6	Inclusion of previous metallicity estimates	99
2.7	Photometric metallicity calibrations	100
2.8	Radial velocities from NIR spectroscopy	104
2.8.1	Radial velocity method	107
2.8.2	Using precise RVs to investigate errors and systematics	110
2.8.3	Validating the use of SpeX for radial velocities	114
2.9	Conclusions	116

CONTENTS

3	An Empirical Calibration to Estimate Cool Dwarf Fundamental Parameters from <i>H</i>-band Spectra	119
3.1	Introduction	119
3.2	Observations and measurements	124
3.2.1	Stars with interferometric measurements	125
3.2.2	MEarth M dwarfs	129
3.2.3	Cool KOIs	130
3.3	Inferring stellar parameters	131
3.3.1	Behavior of <i>H</i> -band spectral features as a function of effective temperature	133
3.3.2	Empirical calibrations for stellar parameters using spectral features	135
3.3.3	Systematic uncertainties in the calibrations	141
3.4	Application to M dwarfs from MEarth	142
3.4.1	Using luminosities to revisit the metallicities of the MEarth sample	147
3.4.2	Comparison to the Mann et al. temperature and radius calibrations	152
3.4.3	Trends between absolute M_K and inferred stellar parameters . .	154
3.4.4	Identifying over-luminous objects	156
3.5	Applications to <i>Kepler</i> Objects of Interest	158
3.5.1	Comparison to previous work	163
3.5.2	Updated stellar and planetary parameters	165
3.5.3	Comments on individual systems	169
3.6	Summary	172
4	The Rotation and Galactic Kinematics of Mid M dwarfs in the Solar Neighborhood	178
4.1	Introduction	178
4.2	Photometry from MEarth	183

CONTENTS

4.3	Determining rotation periods	188
4.3.1	Period detection	188
4.3.2	Identifying multiples	193
4.3.3	Defining a statistical sample	197
4.4	Comparison to previous period measurements	198
4.4.1	Comparison to ground-based photometry	201
4.4.2	Comparison to <i>Kepler</i>	202
4.4.3	Comparison with <i>vsini</i> measurements	205
4.5	Spot characteristics	215
4.5.1	Amplitude of variability	217
4.5.2	Spot patterns and stability	220
4.5.3	Recovery fractions	221
4.6	Kinematics and metallicities of the rotators	224
4.6.1	De-biasing the kinematics	225
4.6.2	General kinematic properties of the sample	226
4.6.3	Disk membership	228
4.6.4	Metallicities of the rotators	229
4.7	The age-rotation relation	231
4.8	The mass-period relation	240
4.9	Summary	244
4.10	Conclusions	247
5	The Impact of Stellar Rotation on the Detectability of Habitable Planets Around M Dwarfs	251
5.1	Introduction	251
5.2	Stellar rotation periods and masses across the main sequence	254
5.3	Stellar rotation and the habitable zone	257

CONTENTS

5.4	M dwarfs with photometric monitoring as targets for radial velocity surveys	263
5.5	Discussion	265
6	Hα Emission in Nearby M dwarfs and its Relation to Stellar Rotation	270
6.1	Introduction	270
6.2	Data	273
6.2.1	Our nearby M dwarf sample	273
6.2.2	Literature compilation	277
6.2.3	New optical spectra from FAST	282
6.3	Analysis	283
6.3.1	Radial velocities	283
6.3.2	H α EWs	285
6.3.3	H α luminosity and χ	287
6.4	Results	289
6.4.1	Activity versus rotation period	289
6.4.2	The active/inactive boundary	294
6.4.3	Stars with unusual activity levels	298
6.4.4	Activity versus photometric amplitude	299
6.5	Discussion	302
	References	307

Acknowledgments

Though not quite comparable to the challenge of finishing my Ph.D., I found it very difficult to write these acknowledgements. The road here has been a long one, and on the way I am fortunate to have had more supportive and caring individuals in my life than I could possibly thank. My parents, Carol Lashof and William Newton, have supported me every step of the way (they even follow me on Twitter now). My sister Erica Newton and my entire family have been a lifelong source of encouragement and inspiration. I think you all know that I wouldn't be here without you. Bill Sowerwine, thank you for sticking by me through everything the last ten years have brought, and for always pushing me in the right direction. My friends, from Berkeley to Boston, you know who you are. Thank you for the hikes, the drinks, the dinners, and the quiet nights in. It means so much to me that I have gotten to be a part of your lives; and I am thankful for your patience all these years.

I owe substantial thanks to my friends and colleagues at the Center for Astrophysics. I am especially grateful to Peg Herlihy, Robb Scholten, and Geri Barney, without whom the CfA wouldn't run nearly so smoothly. You see so many of us pass through and yet you treat each of us with such kindness. I am indebted to the members of my research group, both past and present, and to the CfA graduate community. Thank you for your support, for your advice, and for your enthusiasm. I am especially appreciative of the members of my thesis advisory committee and dissertation examiners: Edo Berger, Dave Latham, John Johnson, Charlie Conroy, and Eric Mamajek. Thank you for your guidance over the past few years.

When I started my research career at UC Santa Barbara, I had the fortune to

have Tommaso Treu and Phil Marshall as supervisors. I learned so much from you about how to be an astronomer, and your tireless support helped me find my way here. I would also like to thank my mentors David Cannell and Ruth Murray-Clay, and the people who have been both friends and mentors: Sarah Rugheimer, Ragnhild Lunnan, Wen-Fai Fong, Zach Berta-Thompson, and especially Sarah Ballard. You all set the example of the kind of scientist I want to be at the next step of the journey.

Finally, I am indebted to my research mentor Jonathan Irwin, and to my thesis advisor Dave Charbonneau, without whom this thesis wouldn't have happened. Jonathan, I would not be half the scientist I am today without your careful and constant guidance. Dave, you have been tirelessly looking out for me since day one. Thank you for always supporting me and my goals, not just as a scientist but as a whole person.

Chapter 1

Small Stars Near the Sun

We understand the possibility of determining their shapes, their distances, their sizes and their movements; whereas we would never know how to study by any means their chemical composition, or their mineralogical structure, and, even more so, the nature of any organized beings that might live on their surface.

Comte, 1835

1.1 Observations of M Dwarf Stars

Most nearby stars are unlike our Sun: three-quarters of the stars in our galaxy are M dwarfs, with masses from 0.08 to 0.6 that of the Sun. If one were to spend one day exploring each of our nearest stellar neighbors, it would take just about a year to visit each stellar system out to a distance of 10 pc ¹. During this time, one would spend less than month visiting the 20 G-type stars, while nine out of twelve months would be devoted to M dwarf stars.

Though M dwarf stars have been called "the least spectacular" and "a shade passé" (Reid et al. 2002; Reid & Hawley 2005), understanding the nature of the lowest-mass stars has implications across astrophysics. M dwarfs are a laboratory in which to explore stellar structure and high-energy phenomena, providing important tests of theoretical stellar models in a regime very different from the Sun. They offer the opportunity to advance our knowledge of convection, magnetic dynamos, starspots, and the impact of stellar activity across the Hertsprung-Russell diagram (e.g. Reiners 2012; Feiden 2015; Testa et al. 2015). Since they comprise 75% of all the stars in the Galaxy and have main sequence lifetimes much longer than a Hubble time (10 trillion years for the lowest-mass stars; Laughlin et al. 1997), M dwarfs act as a probe of galactic evolution (e.g. Reid et al. 1995; West et al. 2008). The majority also host planetary systems (Dressing & Charbonneau 2015); thus research on these low-mass stars has the potential to elucidate the nature of both our nearest stellar and our nearest planetary neighbors.

¹A total of 365 systems, including white dwarfs but not substellar objects, by the best accounting as of 1/1/2015 (Henry et al. 2015)

CHAPTER 1. INTRODUCTION

In 1864, Angelo Secchi was the first to group M type stars together on the basis of their strong titanium oxide bands, which remain the defining characteristic of this spectral type². The "M" spectral type itself was defined by Williamina Fleming in her classification system for the Henry Draper Memorial Catalog of 1890. However, none of these M type stars were on the main sequence. According to Gray (2009), the first spectrum of an M-type dwarf star was acquired by Adams (1913)³. Shortly thereafter, in a study of ten of the least luminous stars known at the time, Adams & Pease (1914) reported M spectral types for eight of them⁴. Presumably, this was the first indication of the abundance of M dwarf stars.

The fact that a spectrum of an M dwarf was not obtained until the most intrinsically faint stars were specifically targeted is indicative of the technical challenge M dwarfs presented until recently. In their position at the bottom of the main sequence, M dwarfs are the least luminous type of star: it would take a mid-sized M dwarf three years to output as much energy as the Sun emits in a single day. Moreover, as a result of their cool surface temperatures, they emit most of this light at infrared wavelengths, and infrared detector technology is still catching up to that of optical CCDs. For example, the number of pixels per sensor lags by about a decade (Rogalski 2012), and detectors are relatively costly (Karim & Andersson 2013). Consequently, M dwarfs have not been available for the same in-depth study as solar-type stars until the last several decades.

²This history is described in Reid & Hawley (2005).

³The spectrum was of Groombridge 34, more commonly known as Gl 15A

⁴One of the non-M dwarfs, a faint companion to a brighter star, was classified as A0, which is presumably in error. The second was a K6.

CHAPTER 1. INTRODUCTION

Equally as important, the interior structure of an M dwarf differs significantly from that of the Sun. Our understanding of stellar physics is informed greatly by in-depth studies of the Sun, which unfortunately has no M dwarf companion for us to observe in as much detail. The nearest M dwarf is Proxima Centauri at a distance of 1.3 pc⁵, and we cannot expect to make *in situ* measurements of Proxima for some time. As a result, there are outstanding challenges in understanding the physics of these common stars despite their prevalence. What are properties of the nearest stars: their motions through the galaxy, their sizes and their ages? What governs the evolution of their angular momentum? What drives the magnetic dynamo in fully-convective stars? How do these stellar properties influence the discovery and characterization of exoplanets?

In the remainder of this introduction, I offer an outline of the pertinent physics and discuss the key uncertainties in our understanding M dwarf stars, using the Sun as a guide. I focus on two aspects: our ability to determine the basic parameters of cool stars and our understanding of stellar rotation and magnetism. I will also briefly consider M dwarfs in their role as exoplanet host stars. I then summarize the contributions I have made through observations of the nearby population.

⁵Proxima also happens to be the nearest star of any type (Lurie et al. 2014).

1.2 The Structure of Cool Stars

Without spectroscopy, Comte's assertion that we would never learn about the interiors of stars would likely remain true⁶. Advances in physics lead to two key breakthroughs in the study of stellar spectra in the 1920s: The eponymous ionization balance equation of Saha (1921) determined the stellar temperature scale (with further refinement by Fowler & Milne 1923). Payne (1925) used this equation to measure the relative abundances of elements in a sample of stars, showing that stars are made predominantly of hydrogen and proving Comte wrong.

Today, spectral synthesis is the standard technique to determine the properties of an F, G or K-type star⁷. The method requires matching the observed stellar spectrum, or parameters derived from it, to model spectra. The key parameters derived are (T_{eff}), surface gravity ($\log g$), and metallicity ($[M/H]$) or iron abundance ($[Fe/H]$). The abundances of individual elements are also determined in some cases. Valenti & Fischer (2005, the SPOCS catalog) determined T_{eff} to a typical precision of 44 K and derived radii and luminosities with median errors of 4% and 6%, respectively. A high-resolution spectrum is required, but these data are readily available for many solar-type stars of interest (Petigura 2014; Fleming et al. 2015, e.g.). Systematic uncertainties in modeling still dominate the error budget, but greater precision can be achieved by considering only stars with parameters similar to the Sun (solar twins), and determining the properties of the solar twins based on differences between their spectra and the solar spectrum (Meléndez et al. 2009). With considerable care,

⁶See Hearnshaw (2010) for a discussion and historical overview.

⁷G, K and M type stars comprise the group of stars known as "cool stars."

CHAPTER 1. INTRODUCTION

relative errors in abundances of 0.01 dex can be reached (Bedell et al. 2014).

The cool photospheric temperatures of M dwarfs have frustrated attempts to apply spectral synthesis methods. The optical spectra of M dwarfs are blanketed by molecular features, and there is no longer a well-defined continuum with isolated atomic features, such as the Fe lines typically used for spectral synthesis in solar-type dwarfs. Line lists are incomplete for some molecules and there are missing sources of opacity in even the most recent model atmospheres (Baraffe et al. 2015). Furthermore, the faintness of M dwarfs makes gathering high-quality, high-resolution spectra observationally intensive. As a result, spectral synthesis in the optical has proven challenging (Woolf & Wallerstein 2005; Bean et al. 2006a), though more success has been found in the near-infrared (NIR) where there are fewer molecular features (Önehag et al. 2012).

Of additional concern is the disagreement between the observed and theoretical stellar properties, the latter are the basis on which masses, radii and ages are determined from spectral synthesis. An M dwarf is characterized by lower temperatures and higher densities than Sun-like stars, where non-ideal gas effects are important for the equation of state and nuclear reaction rates (see Chabrier & Baraffe 1997, for a review). Of key importance are the boundary conditions for the stellar model, which rely on opacities in the outer layers of the star. For $T_{\text{eff}} < 5000$ K, molecular features become the dominant sources of opacity and it is important that boundary conditions be derived from model atmospheres (Saumon et al. 1994; Chabrier & Baraffe 1997). The use of model atmospheres and improvements in molecular line lists (particularly TiO) have greatly improved the agreement between models and the observed colors of M dwarfs (Baraffe et al. 2015).

CHAPTER 1. INTRODUCTION

Though significant theoretical progress has been made, current models under predict the radii of M dwarfs at a given mass, T_{eff} , or luminosity. This is seen in the mass and radius measurements from double-lined eclipsing binaries (see Torres et al. 2009; Feiden 2015, for reviews), as well as in the interferometric radii measurements and temperature estimates for single stars (Berger et al. 2006; Boyajian et al. 2012). Feiden & Chaboyer (2012) find that the most recent models from the Dartmouth Stellar Evolution Program under predict radii by a mean absolute deviation of 2.3%, with all but two stars within about 4%. Similar offsets are found when comparing to other state-of-the-art models (Spada et al. 2013; Choi et al. 2016). Feiden & Chaboyer (2012) suggest that most of the discrepancy can be explain by unaccounted-for systematic errors in the observations. Errors of these size could be due to large spots (e.g. Morales et al. 2010; Windmiller et al. 2010); Feiden & Chaboyer (2014) contains a discussion of these results. I also note that Feiden & Chaboyer (2012) have fit each system to a grid of isochrones, which will naturally minimize the offset between the models and observations.

Magnetic fields are generally invoked to explain the observed radius inflation. The fields themselves are challenging to probe observationally (Reiners 2012), so emission that is thought to result from heating of the stellar atmosphere by magnetic effects, are used as tracers. Ribas (2006), Torres et al. (2006), and Lopez-Morales (2007) demonstrated that activity correlates with the observed radius inflation using double-lined eclipsing binaries, for which both the masses and radii can be measured directly. However, Feiden & Chaboyer (2012) point out that the correlation is strongly driven by two highly inflated, strongly X-ray active stars. Using the temperatures and luminosities of single M dwarfs to infer radii, Mullan & MacDonald (2001) and

CHAPTER 1. INTRODUCTION

Morales et al. (2008) showed that active M dwarfs are larger than inactive M dwarfs at a single T_{eff} .

Models also support the idea that magnetism can inflate the radii of low-mass stars. Strong magnetic fields can effectively decrease the efficiency of convective heat transport, resulting in larger stars. Feiden & Chaboyer (2014, §4.1) contains a useful explanation of why this occurs. Cox et al. (1981) showed that models where the mixing length parameter has been decreased from the value typically adopted for the Sun provide a better match to observations⁸. Various authors have returned to this idea or variants thereof over the past 15 years (D’Antona et al. 2000; Mullan & MacDonald 2001; Chabrier et al. 2007; Feiden & Chaboyer 2013). With sufficiently large internal magnetic fields, Mullan & MacDonald (2001) and Chabrier et al. (2007) also find that radiative cores can remain in stars that otherwise would be fully convective. Whether the magnetic field strengths required to bring models and observations into agreement are realistic is a matter of debate (Chabrier et al. 2007; Morales et al. 2010; Feiden & Chaboyer 2012; MacDonald & Mullan 2012; Feiden & Chaboyer 2014). I will return to the origins of these magnetic fields in the following section.

In face of these challenges, observers often turn to empirical relations between basic stellar parameters, calibrating these relations against the small sample of stars with reliably determined parameters. For stars with trigonometric parallaxes, masses can be estimated using the mass to absolute K-band magnitude (M_K) relation (Delfosse et al. 2000), and radii can then be calculated using a mass–radius

⁸Mullan & MacDonald (2001) also credit Gabriel (1969), but I was unable to locate the text of this reference.

CHAPTER 1. INTRODUCTION

relation (e.g. Bayless & Orosz 2006; Boyajian et al. 2012). The former is derived from astrometric binaries, and the latter using spectroscopic eclipsing binaries (Bayless & Orosz 2006) or radii measured from interferometry and the mass–magnitude relation (Boyajian et al. 2012). Both have precisions of about 10%. Relations to estimate metallicities and iron abundances have also been derived. In this case, the calibration sample is M dwarfs in wide binaries with a solar-type companion, for which the metallicity can be measured using standard spectral synthesis techniques (Gizis & Reid 1997; Gizis 1997; Bonfils et al. 2005a). The first calibrations used scatter in the color– M_K diagram as a tracer of metallicities (Bonfils et al. 2005a; Johnson & Apps 2009; Schlafman & Laughlin 2010), while Rojas-Ayala et al. (2010, 2012) pioneered the use of NIR EWs.

Depending on the available information, these empirical relations are not always applicable. In particular, determining stellar mass and radius requires a parallax, which are not widely available for M dwarfs. Several authors have therefore developed techniques that are based on stellar models (but which are distinct from spectral synthesis). The infrared flux method (Blackwell & Shallis 1977; Blackwell et al. 1979, 1980) uses the ratio of infrared to bolometric flux and a grid of stellar models to determine T_{eff} . This method was extended to M dwarfs and to include estimation of $[M/H]$ by Casagrande et al. (2008). Rojas-Ayala et al. (2012) calibrated the curvature of the K -band as an indicator of T_{eff} by measuring the parameter in model spectra. Muirhead et al. (2012b) used T_{eff} and $[Fe/H]$ from the Rojas-Ayala et al. (2012) calibrations to match stars to model isochrones, thereby inferring their temperatures and radii.

The approach taken by Muirhead et al. (2012b) is interesting for its similarities

to the way relative abundances are determined in studies of solar twins (e.g. Meléndez et al. 2009). Muirhead et al. (2012b) noted that KOI-961 has very similar properties to Barnard’s star, which is a quiet, slowly rotating mid M dwarf with an interferometrically measured radius. They infer the T_{eff} , $[\text{Fe}/\text{H}]$, and $[\text{M}/\text{H}]$ of these two stars from the spectroscopic calibrations from Rojas-Ayala et al. (2012), and use stellar models to determine a correction for KOI-961. They thus are able to infer KOI-961’s mass, radius, and luminosity.

Though these techniques represent a great improvement in our ability to determine M dwarf temperatures and radii, they are still based on stellar models.

1.3 The Physics of Cool Stars

Naked-eye observations of dark blemishes on the face of the Sun date back at least several thousand years, with the earliest well-documented observations coming from the Han dynasty more than 2000 years ago (Ancient Sunspot Records Research Group at Yunnan Observatory 1977; Wittmann & Xu 1987; Yau & Stephenson 1988; Vaquero & Vázquez 2009). These sunspots, which are cooler than the photosphere, are products of a strong magnetic fields emerging from the stellar interior. In the canonical picture of a sunspot, a magnetic flux loop emerges at the stellar photosphere. The magnetic field inside the flux tubes obstructs convection, thereby inhibiting the transport of heat upwards and making sunspot appear dark (see Rempel & Schlichenmaier 2011, for a review).

The first evidence for solar rotation came from telescopic observations of the

CHAPTER 1. INTRODUCTION

motion of sunspots across the disk of the Sun in the early 1600s, though who deserves the credit for this is a matter that may be lost to history⁹. More than two centuries later, spectroscopy enabled measurements of the Doppler shifts at different locations on the Sun. The approaching and receding limbs have different velocities and the rotation period of the Sun was confirmed (see Hearnshaw 2014, for an accounting). Both of these techniques remain important methods in modern stellar astronomy. Although in except in rare cases starspots on surfaces of distant stars cannot be resolved, we can observe changes in their brightness as dark sunspots rotate in and out of view. In the integrated light from the stellar disk, the Doppler shifts from stellar rotation cause measurable broadening in spectral lines.

The proximity of the Sun enables not only detailed measurement of its exterior, but also of its interior: helioseismology has offered an unprecedented probe of the Solar interior, contributing significantly to our understanding of solar physics. Helioseismology revealed that the Sun's inner radiative zone rotates as a solid body, and that there is strong rotational shear in the convective envelope, which was contrary to the prevailing views at the time (see Thompson et al. 2003, for a review). This has important implications for the origin of the large-scale magnetic field and 11-year solar cycle, in which the magnetic field structure oscillates from poloidal to toroidal and back again. As the Sun is composed of ionized gas in motion, it is

⁹Galileo usually receives the credit (e.g. Livingston 1969), but according to Mitchell (1915) the first publication (at least in Europe) was by Johann Fabricius, and there were unpublished observations from around the same time by Thomas Harriot. Christopher Scheiner made the discovery around the same time as Galileo. Tassoul & Tassoul (2014) also provides an overview of this history. This measurement has also been made by generations of astronomy students, including those in Astronomy 16 at Harvard, for which I was a Teaching Fellow.

CHAPTER 1. INTRODUCTION

able to produce small-scale magnetic fields. The question is: how is this small-scale field organized into the observed dipole? This is an area of active research, with the primary focus being the $\alpha\Omega$ dynamo (for a review, see Charbonneau 2010). In the Ω effect, differential rotation causes the poloidal (meridional) field to be wound up. A definitive mechanism for the α effect has not been established, but is ultimately responsible for twisting the now-toroidal field. On emerging at the stellar photosphere, these magnetic flux loops result in sunspots (Charbonneau 2010). Meridional flows complete the transition back to a poloidal field. In the canonical dynamo model, the α and Ω effects occur at the interface between the radiative and convective zones, called the tachocline. The tachocline is of key importance: here, there is strong rotational shear, and magnetic flux loops have time to experience both the Ω and the α effects. In contrast, flux loops in the convective zone drift to the stellar photosphere within months (Schrijver & Zwaan 2000).

The interplay between the magnetic dynamo and stellar rotation gives rise to a relationship between magnetic activity, rotation and age. As I have discussed, rotation is key to the generation of the Sun's magnetic field. The solar wind, which is coupled to the magnetic field out to a distance of several solar radii, removes angular momentum (Weber & Davis 1967). Therefore, the Sun and stars like it spin down with age; and as their rotation rates decrease, their magnetic fields and the associated activity diminish. Though the early rotational evolution includes a complex dependence on initial conditions, spin-up due to angular momentum conservation, and interactions with the stellar disk (e.g. Bouvier et al. 1997a), the late-time angular momentum evolution of Sun-like stars appears to only depend on color (or mass) and age. This was first demonstrated in Ca H&K emission and rotational velocities

CHAPTER 1. INTRODUCTION

by Wilson (1963), Wilson & Skumanich (1964) and Kraft (1967). Using the Pleiades and Hyades stars and the Sun as anchors, Skumanich (1972) showed that both the equatorial rotation velocities (or equivalently, angular velocities) and Ca H&K emission decrease together as the square-root of age. Angular momentum evolution of this style is now generally referred to as Skumanich-style spin-down. This idea has been revisited from an observational perspective in greater detail in the decades since, and the necessary color- (or mass-)dependence added, particularly by Soderblom (1983), Soderblom et al. (1991), and Mamajek & Hillenbrand (2008). The well-defined rotation-age relation and the lack of dependence on initial conditions gives rise to the method of gyrochronology (Barnes 2003; Mamajek & Hillenbrand 2008; Meibom et al. 2011, 2015, e.g.).

The interior structure of M dwarfs differs in important ways from that of solar-type stars, which has implications for the picture of rotation and magnetism outlined above. Progressing towards later M spectral types, the radiative-convective boundary is found at greater depths into the star. Around a stellar mass of $0.35 M_{\odot}$, the tachocline disappears entirely: the lowest mass M dwarfs are fully convective (Chabrier & Baraffe 1997). This means that the interface $\alpha\Omega$ dynamo cannot be responsible for the global magnetic fields of lower-mass M dwarfs. Durney et al. (1993) therefore predicted that M dwarfs would not have large-scale magnetic fields, and instead hypothesized that they would have disorganized, kiloGauss-strength fields driven by turbulence.

Donati et al. (2006) and Morin et al. (2008b) used Zeeman Doppler Imaging (ZDI) to demonstrate, contrary to expectations, fully convective stars can support large-scale, axisymmetric magnetic fields. Subsequent studies from this group have

CHAPTER 1. INTRODUCTION

focused on early (Donati et al. 2008), mid (Morin et al. 2008a) and late (Morin et al. 2010) M dwarfs¹⁰. These authors found that early M dwarfs tend to have toroidal and non-axisymmetric poloidal fields, and show evidence of differential rotation and evolution. Mid M dwarfs have stable, strong, axisymmetric and mostly dipolar (poloidal) fields. Some late M dwarfs have fields similar to earlier M dwarfs, while others have weaker, more asymmetric fields. Reiners & Basri (2009b) showed that 85% of the magnetic flux is in small-scale magnetic fields invisible to ZDI, and the fully convective M dwarfs stored more energy in large-scale structure than partially convective stars. However, their sample included only two of the former and four of the latter.

Theorists are faced with the challenge of matching both the large- and small-scale magnetic fields in these stars. Most efforts have focused on the strengthening of the magnetic field that results from the twisting field lines due to turbulence. This α^2 dynamo can operate in absence of rotational shear, but generally still depends on rotation (Chabrier & Küker 2006). In the presence of rapid rotation, large-scale fields can be generated. Simulations have resulted both in large-scale dipolar fields (Dobler et al. 2006; Browning 2008) and non-axisymmetric fields (Küker & Rüdiger 1999; Chabrier & Küker 2006). Some simulations have explored a range of parameter space, finding that either geometry can arise depending on the regime (e.g. Christensen & Aubert 2006; Gastine et al. 2012; Schrunner et al. 2012). Schrunner et al. (2012) and Gastine et al. (2012) show that rotation rate may not uniquely determine the magnetic field geometry. Yadav et al. (2015b) were able to self-consistently produce large,

¹⁰An overview of ZDI measurements for stars with a range of masses and ages can be found in Vidotto et al. (2014).

CHAPTER 1. INTRODUCTION

persistent polar spots on fully convective stars, which are the result of large-scale magnetic fields suppressing convection. However, they note that rapid rotation is required to produce polar spots. In Yadav et al. (2015a), they showed that their models were able to match the field strengths and geometries of the ZDI maps. The results from Yadav et al. (2015b) highlight that starspots on M dwarfs may be fundamentally different than sunspots, which are produced by magnetic flux tubes (e.g. Schrijver 2002; Solanki 2002).

The activity of solar-type stars shows a tight relationship when compared to R_o (Noyes et al. 1984; Soderblom et al. 1993). The Rossby number (R_o) compares the convective overturn timescale, which depends on stellar mass, to the stellar rotation period. With R_o below a certain threshold (rapid rotation), activity maintains a saturated value, while at higher R_o (slower spins) activity and R_o are correlated (e.g. Pallavicini et al. 1981; Noyes et al. 1984; Pizzolato et al. 2003).

Despite the expected differences in their magnetic dynamo, early and mid M dwarfs show a similar rotation–activity relation as shown by Kiraga & Stepien (2007) when using photometrically determined rotation periods and x-ray emission. This has been studied extensively using rotational broadening in place of photometric periods, at a range of ages and using a variety of tracers of magnetic activity. It is in general seen that rapidly rotating early and mid M dwarfs maintain a saturated activity level similar to what is seen in higher-mass stars. M dwarfs without detectable rotational broadening, which are predominantly slower rotators, are found to have a range of activity levels. This has been interpreted as being the result of a unsaturated rotation–activity relation. This is seen when activity is traced using emission in the x-ray (e.g. Stauffer et al. 1997a; Wright et al. 2011), $H\alpha$

CHAPTER 1. INTRODUCTION

(e.g. Soderblom et al. 1993; Delfosse et al. 1998; Hawley et al. 1999; Reiners et al. 2012), Ca H&K (Browning et al. 2010), and Ca infrared triplet (Jackson & Jeffries 2010). Radio emission, which results from accelerated electrons and more directly traces the magnetic field than does chromospheric or coronal emission, does not show a saturated relation with rotation. Instead, the ratio of radio to bolometric luminosity continues to increase with decreasing R_o (McLean et al. 2012). McLean et al. (2012) and Williams et al. (2014) suggest that magnetic field topology may play an important role in determining the magnetic emission from cool stars.

The rotation–activity relation followed by higher-mass stars breaks down for the ultracool dwarfs, with spectral types later than about M7V. X-ray and H α luminosities diminish relative to the bolometric luminosities (e.g. Gizis et al. 2000; Mohanty & Basri 2003; Mohanty et al. 2002; McLean et al. 2012), while radio emission does not. The persistence of radio emission indicates that strong magnetic fields are still present (e.g. Berger 2002, 2006). The decline of x-ray and H α emission may instead indicate a decrease in the efficiency of magnetic heating of the chromosphere, perhaps as a result of the stellar atmospheres becoming predominantly neutral for stars later than M7V (Mohanty et al. 2002).

Historically, investigation of the rotation–activity relation has been based on measurements of rotational broadening. For M dwarfs, rotational broadening is only detectable for stars rotating with periods faster than a few days. Furthermore, this method measures only the projected rotation velocity, so there is a degeneracy between the inclination angle of the star and true rotation period. Photometric rotation period measurements enable investigations at longer rotation periods, and are not subject to the unknown inclination angle. They provide a means to probe

CHAPTER 1. INTRODUCTION

the unsaturated regime of the rotation–activity relation. Recent work on clusters has been based on increasingly large samples of stars with photometrically determined rotation periods, rather than rotational broadening of spectral lines (e.g. Scholz et al. 2011; Douglas et al. 2014). However, the M dwarfs in clusters are all rapidly rotating, and studies of field stars have typically continued to rely on rotational broadening. The few exceptions (e.g. Kiraga & Stepien 2007; Wright et al. 2011), have by necessity not included large samples of M dwarfs with photometrically determined rotation periods.

The timespan over which M dwarfs retain rapid rotation and are magnetic active increases with decreasing mass (see e.g. the compilation in Irwin et al. 2011a). This is seen both in young clusters and in the field population. In clusters, the threshold color (or mass) at which the rotation rates and activity levels of members drops is shifted to lower masses for the older clusters (e.g. Kafka & Honeycutt 2006; Scholz et al. 2011; Delorme et al. 2011; Núñez et al. 2015). Kinematic analysis of field mid M dwarfs indicates similar trends. Inactive M dwarfs are found to predominantly belong to an older kinematic population (Giampapa & Liebert 1986; Hawley et al. 1996; Gizis et al. 2002). West et al. (2008) used M dwarfs in the Sloan Digital Sky Survey to probe M dwarfs out to 500 pc from the Galactic plane. They found that the lifetime of magnetic activity increases sharply around M4V (from 1 – 2 Gyr to 8 Gyr, but see Chapter 4 for discussion of kinematic–age relations). The decay of rotation periods below what can be detected from rotation broadening takes a substantial fraction of the age of the galactic thin disk (Delfosse et al. 1998; Mohanty & Basri 2003), while Irwin et al. (2011a) showed that long-period rotators are kinematically older than short-period rotators.

Because the spin-down timescale for M dwarfs extends beyond the age of nearby stellar clusters, we must turn to field stars in pursuit of understanding their magnetic dynamos and angular momentum evolution. This gives rise to two distinct challenges: measuring the rotation periods of stars distributed across the sky, and robustly constraining their ages (see Soderblom 2010, for a discussion of the difficulty of estimating ages reliably).

1.4 M Dwarfs as Exoplanet Hosts

Though of interest in their own right, M dwarfs have seen a resurgence in popularity due to their role as exoplanet host stars. These small stars present a unique opportunity for the detection and characterization of habitable Earth-sized planets (e.g. Charbonneau & Deming 2007; Nutzman & Charbonneau 2008). Recent analyses from Kepler demonstrate the prevalence of planetary systems around M dwarfs: there are at least 2.5 planets per M dwarf star (Dressing & Charbonneau 2015). Their stellar size is favorable for the detection of orbiting planets via the transit or radial velocity technique, since the former depends on the ratio of the planetary and stellar cross-sectional area and the latter on the planet-to-star mass ratio and M dwarfs are both smaller and less massive than other stars. Due to the low stellar luminosities, the orbital period at which a planet receives Earth-like insolation is shorter, making transits more likely and more frequent: for a $0.2 M_{\odot}$ star (approximately M4.5V) the period of a habitable planet is two weeks, compared with one year for a solar-type star. The small radius of an M dwarf is also favorable for precise observations of an orbiting planet's atmosphere with transmission or occultation techniques.

CHAPTER 1. INTRODUCTION

Furthermore, simulations indicate that the atmospheres of planets orbiting the most nearby mid M dwarfs may be within reach of the Extremely Large Telescopes (Snellen et al. 2013; Rodler & López-Morales 2014).

M dwarf planetary systems offer laboratories in which to test theories of planet formation. Creating a planetary system around a small star is one of the simplest ways to test the effect of initial conditions: the disk out of which planets form is less massive around an M dwarf than around a more massive star (Andrews et al. 2013). Occurrence rates derived from planets found as part of the *Kepler* survey indicate that giant planets are less common around M dwarfs than around solar-type stars, but that Earth- to Neptune-sized planets are more common (e.g. Howard et al. 2012; Fressin et al. 2013; Mulders et al. 2015). Radial velocity surveys reveal similar trends in planetary mass (e.g. Johnson et al. 2007; Cumming et al. 2008; Bonfils et al. 2013; Montet et al. 2014). There is also evidence for a bimodal distribution of multiples (the "Kepler dichotomy"), seen in the excess of stars with a single transiting planet (Lissauer et al. 2011). The dichotomy is seen in both solar-type stars (Hansen & Murray 2013; Swift et al. 2013) and M dwarfs (Ballard & Johnson 2016), and may be the result of dynamical interactions or of the planet formation process (see e.g. Dawson et al. 2015; Ballard & Johnson 2016).

The MEarth Project, of which I have been a member throughout my time at Harvard, is a survey looking for transiting planets around M dwarfs in the solar neighborhood (Nutzman & Charbonneau 2008; Berta et al. 2012; Irwin et al. 2015). The two planets we have discovered to date offer illustrative examples of the points above. Charbonneau et al. (2009) presented the discovery of GJ 1214b, a $2.6 R_{\oplus}$ planet orbiting a mid M dwarf. Berta-Thompson et al. (2015) reported the discovery of GJ

CHAPTER 1. INTRODUCTION

1132b, which was an effort in which I participated. The host star GJ 1132 is similar in size to GJ 1214, but its planet is smaller ($1.2 R_{\oplus}$). Berta et al. (2013) showed that planets like GJ 1214b are relatively rare, but results from *Kepler* indicate that smaller planets like GJ 1132b are abundant (e.g. Dressing & Charbonneau 2015; Muirhead et al. 2015). Unlike the exoplanets discovered around *Kepler* M dwarfs, the proximity of GJ 1214 and GJ 1132 enable precise study of their atmospheres. Transmission spectroscopy of GJ 1214b has demonstrated the presence of clouds (e.g. Berta et al. 2012; Kreidberg et al. 2014), while observations of GJ 1132b have only just begun.

The uncertainties in M dwarf properties pose a fundamental problem for learning about their planets: errors in stellar parameters translate directly to errors in the properties of orbiting planets. Planetary radii, for example, are measured only relative to the stars' radii, so one may mistake a rocky, Earth-like planet for a larger one if its star's radius is not well-determined. Magnetic activity and rotation can mimic, or hide, the signals of orbiting planet. Stellar winds and magnetic fields can strip the planetary atmosphere, potentially rendering the planet uninhabitable (Cohen et al. 2015). Once reaching the main sequence, M dwarfs do not evolve much over a Hubble time so inferring their ages is challenging (see Soderblom 2010, for a review of methods to estimate stellar ages). Gyrochronology relations offer a potential way to determine their ages, but have yet to be calibrated for M dwarfs. Thus, improved knowledge of M dwarf stellar physics will contribute to the advancement of exoplanet research.

1.5 New Observations of Mid-to-late M Dwarfs in the Solar Neighborhood

My motivation for carrying out this thesis work was two-fold: (1) to gain insight into the structure and physics of the most abundant stars in our galaxy, and (2) to establish reliable methods to determine the fundamental properties of planet-hosting stars. In Chapter 2, I present my NIR spectroscopic survey and discuss the development of our methods to determine spectral types, metallicities, and radial velocities. I then present a new technique to determine the radii, effective temperatures, and luminosities of late K and early M dwarfs from NIR spectra in Chapter 3. In Chapter 4, I use photometry from MEarth to determine the rotation periods of nearby M dwarfs. Utilizing radial velocities from Chapter 2, I use galactic kinematics as a proxy for age and estimate the M dwarf spin-down timescale. I show how the rotation periods of typical M dwarfs will impact radial velocity searches for habitable planets in Chapter 5. In Chapter 6, I measure $H\alpha$ emission for M dwarfs for which I have determined rotation periods and investigate the rotation–activity relation. I summarize my conclusions and discuss future prospects at the close of this Chapter.

1.5.1 Chapter 2 — Fundamental Stellar Parameters: A Spectroscopic Survey in the NIR

Interest in M dwarfs is in part fueled by prospects for testing theories of planet formation; and the metallicity of the disk out of which planets form is expected to be an important parameter (e.g. Dawson et al. 2015). The high metallicity of solar-type

CHAPTER 1. INTRODUCTION

stars that host close-in giant planets (e.g. Gonzalez 1997; Fischer & Valenti 2005) is in agreement with predictions from core accretion. Efforts have been made to extend these relations to the lowest stellar masses (e.g. Johnson & Apps 2009; Schlaufman & Laughlin 2010, 2011; Rojas-Ayala et al. 2012; Mann et al. 2013a), but have been limited by the small number of planets currently known around nearby M dwarfs and by the challenge of constraining M dwarf metallicities. Metallicity may also play a role in explaining the *Kepler* dichotomy (Dawson et al. 2015, Moriarty, Ballard & Fischer, private communication 2015).

Rojas-Ayala et al. (2010) showed that low-resolution NIR spectra can be used to estimate the metallicities and temperatures of M dwarfs. Rojas-Ayala et al. (2012) used 18 M dwarfs in wide binaries with a solar-type primary, where the primary had a measured metallicity, to calibrate an empirical metallicity relationship (e.g. Bonfils et al. 2005a). Their method is particularly useful: unlike the color- M_K relation first calibrated by Bonfils et al. (2005a), it requires neither parallaxes nor accurate magnitudes, which are not widely available for M dwarfs. Rojas-Ayala et al. (2012) demonstrated that their metallicities produced reasonable results for solar neighborhood M dwarfs, with the more metal-poor stars generally being kinematically older and less magnetically active. This result highlights the broader context in which constraints on the physical properties of M dwarfs are applicable. For example, metallicity is an important means of testing galactic evolution and star formation models (e.g. Bochanski et al. 2007a, 2010; Woolf & West 2012).

I obtained NIR spectra of 447 nearby M dwarfs using the SpeX instrument on NASA’s Infrared Telescope Facility (IRTF). I found that correlated noise dominated the error budget in our high signal-to-noise spectra. We therefore include the effect

CHAPTER 1. INTRODUCTION

correlated noise when performing Monte Carlo simulations to estimate our errors; our method is effectively the same as a Gaussian Process using a Gaussian kernel. I determined NIR spectral types for each star by eye, tying our spectral types to the KHM spectral standards (Kirkpatrick et al. 1991, 1995, 1999), and creating new solar-metallicity spectral templates for IRTF in the Y , J , H and K -bands.

I developed a method to wavelength calibrate SpeX M dwarf spectra using telluric features present in the data to provide the absolute wavelength calibration, and measured absolute radial velocities for the stars in my sample to an accuracy of 4.4 km/s. I expect this technique to be applicable to any M dwarf with an extant moderate resolution NIR spectrum.

I used an expanded sample of 36 FGK-M common proper motion pairs to derive a new metallicity calibration, extending the Rojas-Ayala et al. (2012) calibration to lower masses and lower metallicities. We validated the physical association of these pairs using proper motions, radial velocities and spectroscopic distance estimates, finding that Gl 806.1B, CE 226, HD 46375B, LP 731-76 had distances or radial velocities that were in strong disagreement with their potential primary star. This suggests that the pairs are not physically associated and should not be used as calibrators, though they had been included in previous calibrations. My metallicity calibration used the sodium doublet at $2.2\mu\text{m}$ as the sole indicator for metallicity. It has a precision of 0.12 dex and is valid for NIR spectral types from M1V to M5V and for $-1.0 < [\text{Fe}/\text{H}] < +0.35$ dex. I also presented a new color-color metallicity relation using $J - H$ and $J - K$ colors that directly relates two observables: the distance from the M dwarf main sequence and equivalent width of the sodium line at $2.2\mu\text{m}$.

CHAPTER 1. INTRODUCTION

NIR metallicity calibrations have also been investigated by Terrien et al. (2012), Mann et al. (2013a), and Mann et al. (2014). Mann et al. (2013a) expanded the sample of calibrators significantly and identified over 100 metal-sensitive features in the NIR and optical. Their calibration sample included 112 FGK-M CPM pairs selected on the basis of common proper motion and galactic models. They constructed metallicity relations in the optical and in each of the NIR bands out of metallicity sensitive features and a single parameter to account for temperature dependencies. Their $[\text{Fe}/\text{H}]$ calibrations had residual mean square errors between 0.08 dex and 0.13 dex. In Newton et al. (2015, see Chapter 3), I revisited my metallicity calibration. I showed that our metallicity calibration had temperature biases resulting, and determined that, though not ideal, a combination of the Mann et al. (2013a) and Mann et al. (2014) calibrations provided the best available metallicity estimates.

1.5.2 Chapter 3 — The Properties of Exoplanet Hosts: Determining the Sizes of Cool Stars

It is commonly said in the exoplanet community that "you only know your planet as well as you know its host star." Stellar characterization is not yet as reliable for cooler dwarfs as it is for F, G and K dwarfs, for which fundamental stellar parameters can be determined with reasonable precision and accuracy (e.g. Valenti & Fischer 2005). The interpretation of M dwarf spectra and colors is challenging due to their strong molecular absorption bands, missing sources of opacity in the model atmospheres, and discrepancies between their observed and predicted properties (e.g. Torres et al. 2009; Feiden 2015; Baraffe et al. 2015). These uncertainties directly impact our

CHAPTER 1. INTRODUCTION

knowledge of orbiting exoplanets.

For field M dwarfs, empirical calibrations are an important tool for determining their masses, radii, temperatures, and luminosities. The most widely used of these calibrations are based on parallaxes. Delfosse et al. (2000) presented a relationship between absolute K -band magnitude and stellar mass. Once a stellar mass has been estimated, the radius can be inferred using a mass–radius relation (e.g., Bayless & Orosz 2006; Boyajian et al. 2012). Both the mass-magnitude and mass-radius relations have precisions of about 10%.

The confirmed and candidate planets found around M dwarfs in the *Kepler* field have spurred the development of new methods that do not require parallaxes, for example Dressing & Charbonneau (2013) matched observed colors to stellar isochrones. Building on the method used by Muirhead et al. (2012b), Ballard et al. (2013) used four stars with interferometric radii as proxies to infer the stellar properties of Kepler-61. As discussed by Ballard et al. (2013), the use of proxies fills a particularly crucial niche: while the temperature-sensitive index used by Muirhead et al. (2012a,b, 2014) saturates $T_{\text{eff}} > 3800$ K, the *Kepler* sample is rich in planets orbiting early M and late K dwarfs.

I used stars with interferometrically measured radii, bolometric luminosities, and effective temperatures to develop empirical calibrations for these stellar properties based on low-resolution, near-infrared spectra. I derived functions that relate effective temperature, radius and log luminosity to the EWs of H -band Mg and Al spectral features. The standard deviations in the residuals of our best fits are 73 K, $0.027 R_{\odot}$, and 0.049 dex (an 11% error on luminosity). My calibrations are valid from

CHAPTER 1. INTRODUCTION

mid-K to mid-M dwarf stars, roughly corresponding to temperatures between 3100 and 4800 K.

I applied my *H*-band calibrations to M dwarfs for which I had previously obtained NIR spectra (Chapter 2). I identified stars with absolute magnitudes too bright for the spectroscopically estimated luminosity. Many of these outliers are known binaries, and I present the remaining overluminous objects as candidate multiples.

I applied my calibrations to the cool *Kepler* Objects of Interest (KOIs) using spectra from Muirhead et al. (2014). The temperatures I inferred for the KOIs agree remarkably well with those from the literature; however, my stellar radii are systematically larger than those presented in previous works that derive radii from model isochrones. This results from a sensitive metallicity dependence to model radii that are not present in the observed sample. My new stellar parameters show that the typical planet is 15% larger than one would have inferred if using the stellar properties from works that relied on stellar models. However, my results confirmed the derived parameters from previous in-depth studies of KOIs 961 (Kepler-42), 254 (Kepler-45), and 571 (Kepler-186), the latter of which hosts a rocky planet orbiting in its star's habitable zone.

1.5.3 Chapter 4 — Angular Momentum Evolution: Stellar Rotation at the Bottom of the Main Sequence

The rotation of cool stars is both age- and mass-dependent. After reaching the main sequence, angular momentum loss is dominated by magnetized stellar winds, the strength of which may depend on mass. For solar-type stars, more rapidly-rotating stars spin down more quickly (e.g. Kawaler 1988; Bouvier et al. 1997b; Reiners & Mohanty 2012). The result is that by the age of the Hyades, the rotation periods of solar-type dwarfs have converged to a narrow sequence. They subsequently spin down following the prescription from Skumanich (1972). The well-behaved relationship between rotation, age, and color for solar-type stars with ages older than roughly 650 Myr can be used to infer ages of isolated field stars through gyrochronology, by measuring their rotation period and color (e.g. Barnes 2003; Mamajek & Hillenbrand 2008; Meibom et al. 2015).

At the age of the Hyades (650 Myr, from isochrone fitting; Perryman et al. 1998), the lowest mass stars have not yet begun to spin down. Observations of field M dwarfs are therefore particularly important for constraining their rotational evolution. Kinematic analysis of field mid M dwarfs shows that the time for them to spin down to rates below what can be detected from the rotation broadening of spectral lines takes a substantial fraction of the age of the galactic thin disk (Delfosse et al. 1998; Mohanty & Basri 2003). Studies based on photometric rotation periods for field stars indicate that while M dwarfs maintain rapid rotation rates for longer, they eventually spin down to slower rotation periods (Irwin et al. 2011a; McQuillan et al. 2013). Irwin et al. (2011a) contributed rotation periods for 41 mid-to-late M dwarfs

CHAPTER 1. INTRODUCTION

from the MEarth Survey, which comprised the majority of measurements available for fully convective stars. By assigning stars to the thin/young and thick/old disk based on their space velocities, Irwin et al. (2011a) showed that the rapidly-rotating M dwarfs were on average younger than the slowly-rotating stars.

We extended the analysis of Irwin et al. (2011a) to the full northern sample of M dwarfs observed by MEarth. We performed an automatic period search, then examined each object by eye. I reported the secure detection of rotation in 387 M dwarfs with periods ranging from 0.1 to 140 days. Our periods are in excellent agreement with rotation periods in the literature that are derived from photometry, but I find discrepancies in estimates of rotation period based on the rotational broadening of spectral features.

The typical rotator has stable, sinusoidal photometric modulations at a semi-amplitude of 0.5 to 1%. Consistent with Hartman et al. (2011) and McQuillan et al. (2014), I found an anti-correlation between period and amplitude for higher-mass M dwarfs. However, I found no period-amplitude relation for stars below $0.25 M_{\odot}$. Considering the subset of stars with the highest-quality light curves, I recovered rotation periods in $47 \pm 5\%$ of stars. Considering the limits of other surveys, our recovery rate is consistent with that of Hartman et al. (2011), but is lower than is expected based on surveys using rotational broadening (e.g. Delfosse et al. 1998; Mohanty & Basri 2003; Browning et al. 2010).

The Galactic kinematics of our sample is consistent with the local population of G and K dwarfs (Nordstrom et al. 2004; Holmberg et al. 2009), and rotators have metallicities characteristic of the solar neighborhood. I used the W space velocities

and established age–velocity relations to estimate that stars with $P < 10$ days have ages of on average < 2 Gyrs, and that those with $P > 70$ days have ages of 5^{+4}_{-2} Gyr. We find a gap in the rotation period distribution at intermediate periods, which grows larger at lower masses, which we interpret as an era of rapid rotational evolution.

1.5.4 Chapter 5 — The Hunt for Habitable Planets: The Impact of Stellar Rotation on Radial Velocity Surveys

In our pursuit of follow-up observations of K2-3, an early M dwarf with three confirmed transiting super-Earths (Crossfield et al. 2015), we noted that the stellar rotation period of around 40 days is very close to the 44 day orbital period of K2-3d, a planet near the inner edge of the habitable zone. Though the signatures of planetary and stellar activity are distinct in transits, both produce similar sinusoidal signals in the RV amplitude; we expected that the proximity of the stellar rotation period to this planet’s orbital period would make characterization of its mass from RVs challenging. Indeed, Almenara et al. (2015) find that stellar activity impedes their ability to precisely constrain the masses of K2-3c and d. For planets that do not transit, stellar activity can call into question the planetary nature of a signal. This has been seen, for example, for planetary signals around Gl 581 (e.g. Baluev 2012; Robertson et al. 2014).

We systematically investigated the stellar masses at which stellar rotation periods are likely to frustrate the detection of habitable planets. We compiled rotation periods for field M dwarfs, drawing on the rotation periods we presented in Chapter 4 for the

mid-to-late sample. We showed that for stars with masses between 0.25 and $0.5 M_{\odot}$ (M4V–M1V), the stellar rotation period typical of field stars coincides with the orbital periods of planets in the habitable zone. This will pose a fundamental challenge to the discovery and characterization of potentially habitable planets around early M dwarfs. Due to the longer rotation periods reached by mid M dwarfs and the shorter orbital period at which the planetary habitable zone is found, stars with masses between 0.1 and $0.25 M_{\odot}$ (M6V–M4V) offer better opportunities for the detection of habitable planets via radial velocities.

1.5.5 Chapter 6 — The Origin of Magnetism: Magnetic Activity in Nearby M Dwarfs

Magnetic activity amongst M dwarfs is prevalent, with emission from the x-ray to the radio (e.g. Berger et al. 2010; Stelzer et al. 2013). There exists a correlation between R_o and the ratio of chromospheric or coronal activity to bolometric luminosity: up to a saturation threshold, more rapidly rotating stars are also more magnetically active (e.g. Delfosse et al. 1998; Mohanty & Basri 2003; Kiraga & Stepien 2007; Reiners & Basri 2009a; Browning et al. 2010; Reiners et al. 2012; Douglas et al. 2014)¹¹.

Much of the work on the rotation–activity relation done to date, particularly in field stars, is based on rotational broadening measurements. This results a strong

¹¹However, these activity levels drop for ultracool dwarfs (e.g. Gizis et al. 2000; Mohanty & Basri 2003; Mohanty et al. 2002; McLean et al. 2012). On the other hand, radio persists in these stars at a constant luminosity, perhaps indicating the importance of magnetic field topology (McLean et al. 2012; Williams et al. 2014)

CHAPTER 1. INTRODUCTION

observational bias: at best, rotational broadening is measured from spectra with resolution of around 3 km/s, which for a $0.2 R_{\odot}$ star corresponds to a rotation period of only 3.3 days. Additionally, only the projected rotational velocity is measured, so inferring the true rotation requires knowing the inclination angle. Photometric rotation period measurements, which can probe longer periods, are therefore key to studying the late stages of rotational evolution of low mass stars and the unsaturated rotation–activity relation.

In West et al. (2015), members of the MEarth team measured $H\alpha$ emission for 164 M dwarfs with preliminary rotation periods from the MEarth Observatory. They found that both the fraction of stars that are active and the strength of magnetic activity declines with increasing rotation period for early M dwarfs. Late M dwarfs were found to remain magnetically active out to longer rotation periods, beyond which the active fraction and activity level diminished abruptly. We leveraged the full rotation period sample from Chapter 4 and gathered 247 new optical spectra. Incorporating a compilation of $H\alpha$ and rotation period measurements from the literature, I undertook an in-depth study of magnetic activity in nearby M dwarfs.

I observed a threshold in the mass–period plane that separates active ($H\alpha$ EW $< -1 \text{ \AA}$) and inactive ($H\alpha$ EW $> -1 \text{ \AA}$) M dwarfs. The threshold coincides with the lower edge of the slowly rotating population, at approximately the rotation period at which rapid rotational evolution appears to cease. The well-defined active/inactive boundary indicates that $H\alpha$ activity is a useful diagnostic for stellar rotation period, e.g. for target selection for exoplanet surveys, and I present a mass-period relation for inactive M dwarfs.

I see a relationship between $L_{\text{H}\alpha}/L_{\text{bol}}$ and R_o that is similar to solar-type stars: M dwarfs with R_o below around 0.1 show a saturated level of activity, while M dwarfs with R_o greater than 0.1 show a negative correlation between $L_{\text{H}\alpha}/L_{\text{bol}}$ and R_o . I also found a significant ($p\text{-value} < 10^{-4}$), moderate (Spearman rank correlation coefficient 0.4) correlation between $L_{\text{H}\alpha}/L_{\text{bol}}$ and variability amplitude: more magnetically active stars display higher levels of photometric variability.

1.6 Looking Back, Looking Forward: Insight into the Structure and Physics of M Dwarf Stars

The components of this thesis constitute new measurements of stellar properties for the nearby, northern M dwarf sample. In Figure 1.1, I show the measurements now available for M dwarfs within 20 pc. In Chapters 2 and 3, I presented work related to a large NIR spectroscopic survey of 447 mid-to-late M dwarfs in the solar neighborhood. I measured absolute kinematic RVs and determined NIR spectral types, and provided estimates of stellar metallicity, radius, temperature, and luminosity. In Chapter 4, I presented rotation period measurements for 387 mid M dwarfs. In Chapter 6, we obtained new optical spectra and compiled both photometric rotation periods and $\text{H}\alpha$ EWs from the literature. This dissertation is accompanied online catalogs containing the measurements we have made and those we have compiled from the literature.

In Chapters 2 and 3, I developed tools to stellar metallicity, radius, and temperature in the absence of a parallax. To further enable the use of these tools by

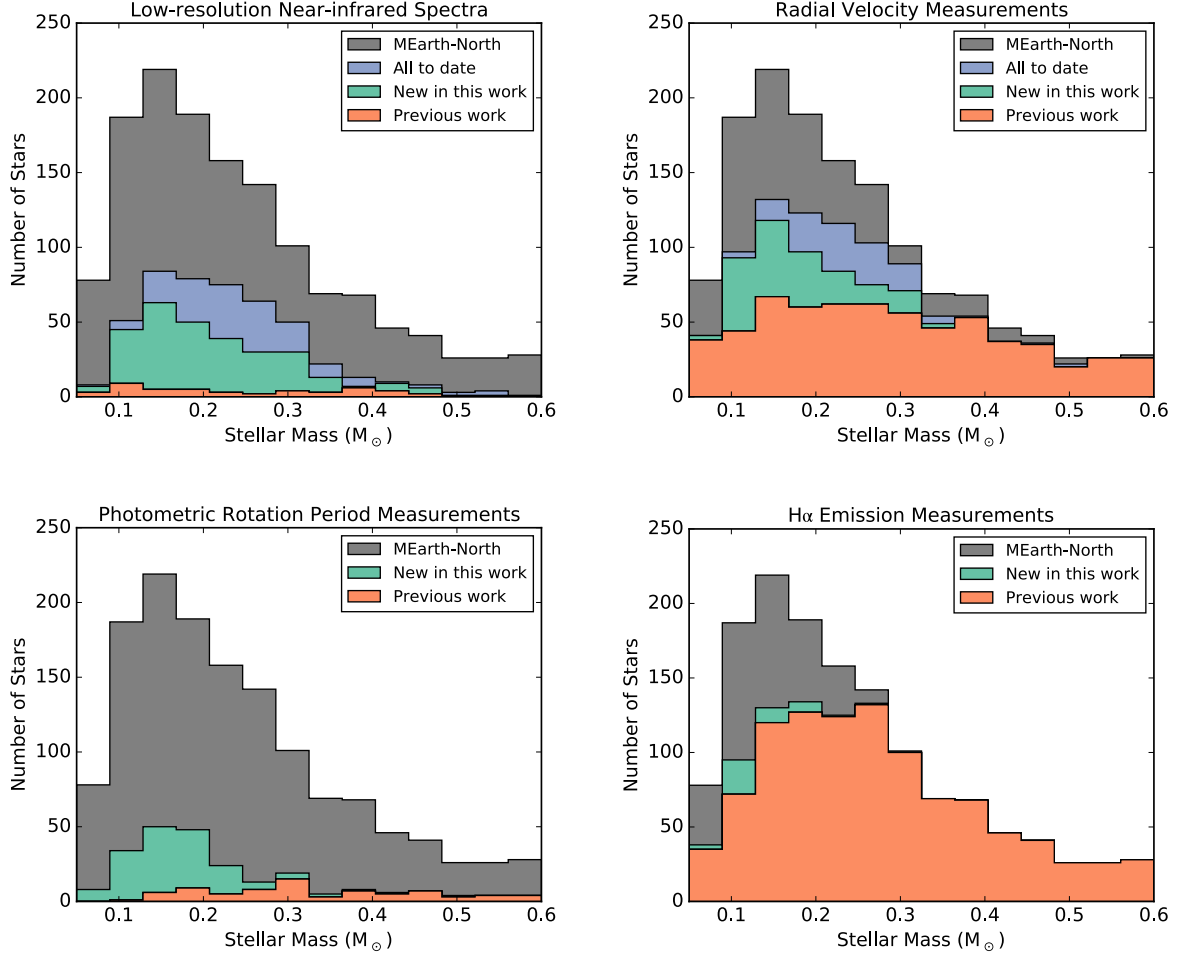


Figure 1.1.— An overview of measurements available for M dwarfs within 20 pc. Distributions are shown as a function of stellar mass, and the full set of stars that comprise this sample is shown (gray histogram). I show measurements available prior to the work presented in this thesis (orange histogram) and the new observations made in this work (green histogram). Adding new data from after the publication of our relevant work gives full sample of stars with measurements presently available (purple histogram).

CHAPTER 1. INTRODUCTION

the community, I have made my code for measuring EWs and RVs, NIREW (Newton 2015a) and TELLRV (Newton 2015b), publicly available on github. These routines use the methods described in Chapter 2. Newton (2015a) additionally includes routines to apply the empirical calibrations presented in Chapter 3 to estimate stellar parameters. As part of my contribution to Berta-Thompson et al. (2015), I used these tools to infer the properties of GJ 1132, using a spectrum I had obtained with the FIRE spectrograph on Magellan prior to the discovery of the planet. I determined $L = 0.0044 \pm 0.0001 L_{\odot}$ and $T_{\text{eff}} = 3130 \pm 120$ K, which are consistent with the luminosity ($L = 0.00438 \pm 0.00034 L_{\odot}$) and T_{eff} (3270 ± 140 K) we infer from the parallax and photometric color. Using the rotation period we measured, my estimate of the spin-down time from Chapter 4, and the ages and rotation periods of Proxima and Barnard’s star, we estimated that the planet has an age of > 5 Gyr.

My investigation of stellar rotation, kinematics, and activity suggests a scenario in which mid-to-late M dwarfs maintain rapid rotation rates and high levels of magnetic activity for several Gyr. The low velocity dispersion I saw for the most rapidly rotating field M dwarfs ($P < 10$ days) indicates that they are likely not much older than the Hyades and Praesepe. Stars with $M < 0.3 M_{\odot}$ in these clusters are not on the narrow mass–period sequence to which higher-mass stars have converged. Instead, they display a range of rotation rates, from approximately 0.2 days to 5 day (Scholz et al. 2011; Agüeros et al. 2011; Douglas et al. 2016). This period range includes the majority of our $P < 10$ day sample. During this time, they display strong levels of magnetic activity, independent of their (rapid) rotation rate. For mid M dwarfs, I do not see a correlation between the amplitude of variability and the rotation period. However, I did find evidence that the amplitude depends on the

CHAPTER 1. INTRODUCTION

strength of the magnetic activity, suggesting that increasing the total strength of the magnetic field produces both higher levels of chromospheric activity and a larger contrast between the spotted and unspotted photosphere.

We suggest that upon reaching some mass-dependent threshold, mid-to-late M dwarfs then undergo rapid angular momentum. My kinematic analysis suggested that this occurs around 2 Gyr and is complete by 5 Gyr, the average age of our slowly-rotating population. The total space velocities suggests that for $P > 10$ days the mean age increases monotonically with rotation period, but the W velocity component I used for our kinematic analysis does not confirm this and additional data are required. $L_{H\alpha}/L_{\text{bol}}$ indicates a smooth decline in $H\alpha$ emission as rotation periods approach the convective overturn timescale, between Rossby numbers of about 0.1 and 1. Thus only at the end of their phase of rapid rotational evolution do the magnetic activity levels of mid-to-late M dwarfs drop below what is required to heat the chromosphere enough for $H\alpha$ to be seen in emission.

At the close of this thesis, I am left with more questions than answers. What is nature of the magnetic dynamo in fully-convective stars? What is the relation between M dwarf interior properties and the magnetic activity signatures we observe? How are stellar magnetism, rotation, and mass loss connected? I see three paths forward for the immediate future:

- We must test predictions for the rotation–activity relation for M dwarfs, including its scaling with stellar parameters and the existence of supersaturation. Archival data, observations underway, and proposed programs, provide a rich dataset in which to explore emission from the x-ray to the radio and its

CHAPTER 1. INTRODUCTION

connection to stellar rotation.

- We must investigate the evolution of M dwarf magnetic fields using Zeeman broadening, and explore the connection between magnetic field strength, activity indicators, and stellar rotation. Past studies of magnetic field strengths using Zeeman broadening indicate strong fields on rapid rotators, but few measurements exist for stars with rotation periods longer than 20 days. Furthermore, time-resolved measurements have the potential to illuminate the structure of starspots and the magnetic field.
- We must study the angular momentum evolution of low-mass stars through photometric observations from space-based observatories. Data from *Kepler* and from the upcoming *TESS* mission offer new opportunities. Overcoming the systematics due to *Kepler*'s quarterly data downlinks would permit investigation into long-period rotators as well as magnetic cycles. Meanwhile, *Kepler*'s sensitivity enables statistical studies of the spin-down timescale.

The nearby M dwarfs that formed the basis for this thesis (shown in Figure 1.1), and which I will continue to study, provide accessible laboratories in which to study the physics of the most common type of star in our galaxy. These same stars are also our best prospects around which to find habitable, rocky worlds. It is the planets orbiting these stars whose atmospheres we will be able to study with the next generation of telescopes, and on which we will first have the capability to detect signs of life. By understanding the properties of these stars and the physical mechanisms that govern them, I hope to accelerate us towards a future where we can ask—and answer—new scientific questions about the Earth-like planets that orbit other stars.

Chapter 2

Near-infrared Metallicities, Radial Velocities and Spectral Types for 447 Nearby M Dwarfs

E. R. Newton, D. Charbonneau, J. Irwin, Z.K. Berta-Thompson, B. Rojas-Ayala,
K. Covey, *and* J.P. Lloyd

The Astronomical Journal, Volume 147, Issue 1, Article 20, 2014

2.1 Introduction

MEarth is a transiting planet survey looking for super Earths around nearby mid to late M dwarfs. As part of our efforts to characterize the local M dwarf population, the MEarth team and collaborators are gathering a diverse data set on these low

mass stars. These unique data have already begun to bear fruit. Charbonneau et al. (2009) reported the discovery of a super Earth transiting the mid M dwarf GJ 1214. Irwin et al. (2011a) took advantage of our long-baseline photometry to measure rotation periods as long as 120 days for 41 M dwarfs and investigated their angular momentum evolution, finding that strong winds may be needed to explain the population of slowly rotating field M dwarfs. Irwin et al. (2011b) presented a long period M dwarf-M dwarf eclipsing binary and measured the masses of the two components and the sum of their radii. They find the radii to be inflated by 4% relative to theoretical predictions, reflecting a well-known problem with stellar models at the bottom of the main sequence (e.g. Lopez-Morales 2007; Boyajian et al. 2012).

Interest in M dwarfs is fueled by prospects for testing theories of planet formation. Creating a planetary system around a small star is one of the simplest ways to test the effect of initial conditions: the disk out of which planets form is less massive around an M dwarf than around a more massive star. Core accretion and gravitational instability models predict different rates of occurrence of planets around low-mass stars, with the formation of giant planets through core accretion being hampered by the low disk surface density and long orbital time scale in M dwarf protoplanetary disks (Laughlin et al. 2004). Recent results from *Kepler* showed that giant planets are less likely to be found around K and early M stars than around F and G stars, lending support to the core accretion model (Borucki et al. 2011; Fressin et al. 2013). A similar finding was reported for M dwarfs targeted by radial velocity surveys (Johnson et al. 2007; Cumming et al. 2008). The high metallicity of solar-type stars that host close-in giant planets was confirmed over a decade

(e.g. Fischer & Valenti 2005), but smaller planets have been found around stars of a range of metallicities (Buchhave et al. 2012). Efforts have been made to extend these relations to the lowest stellar masses (e.g. Johnson & Apps 2009; Schlaufman & Laughlin 2010; Rojas-Ayala et al. 2012), but have been limited by the small number of planets currently known around M dwarfs.

M dwarfs present a unique opportunity for the detection and characterization of habitable Earth-sized planets. Mid to late M dwarfs are favorable targets for transiting planet searches (Nutzman & Charbonneau 2008). Their low luminosity puts the habitable zone at smaller orbital radii, making transits more likely and more frequent: for an M4 dwarf, the period of a habitable planet is two weeks, compared to one year for a solar-type star. Because the transit depth is set by the planet-to-star radius ratio, smaller planets are more readily detectable around these stars. The small radius of an M dwarf is also favorable for follow-up studies of an orbiting planet's atmosphere with transmission or occultation techniques and nearby mid M dwarfs are bright enough in the NIR for precise spectroscopic studies (e.g. Bean et al. 2011; Crossfield et al. 2011; Berta et al. 2012).

In contrast to solar type stars, the physical parameters of M dwarfs are not in general well understood and present a major hurdle for studying transiting planets orbiting M dwarfs. Few M dwarfs are bright enough for direct measurement of their radii (e.g. Berger et al. 2006; Boyajian et al. 2012), and discrepancies between the observed radii and theoretical predictions persist (see Torres 2013, for a review). Empirical calibrations provide an inroad. For example, Muirhead et al. (2012a) and Muirhead et al. (2012b) exploited the *K*-band metallicity and temperature relations of Rojas-Ayala et al. (2012, hereafter R12) to estimate new planet properties for the

Kepler Objects of Interest (KOIs) orbiting the coolest *Kepler* stars and discovered the planetary system with the smallest planets currently known, the *Kepler*-42 system (née KOI-961). Johnson et al. (2012) combined existing photometric relations to estimate the stellar properties of KOI-254, one of the few M dwarfs known to host a hot Jupiter. Ballard et al. (2013) used M dwarfs with interferometric radii as a proxy to constrain the radius and effective temperature of *Kepler*-61b.

Several studies have used M dwarf model atmospheres matched to high resolution spectra to determine stellar parameters. Woolf & Wallerstein (2005) estimated M dwarf temperatures and surface gravities from photometry, then, fixing these parameters, inferred the metallicity from the equivalent widths (EWs) of metal lines. Updating and modifying the spectral synthesis method of Valenti et al. (1998), Bean et al. (2006a) used TiO and atomic lines in combination with NextGen PHOENIX model atmospheres (Hauschildt et al. 1999) to measure the physical properties of M dwarfs. Most recently, Önehag et al. (2012) matched model spectra from MARCS (Gustafsson et al. 2008) to observations of FeH molecular features in the infrared and found metallicities higher than those inferred by Bean et al. (2006b). The MARCS model atmospheres do not include dust formation and are not applicable to M dwarfs later than M6V. However, uncertain sources of opacity in the model atmospheres complicate direct interpretation of observed spectra throughout the M spectral class.

An effective technique for quantitatively studying the metallicities of M dwarfs makes use of cool stars in common proper motion (CPM) pairs with an F, G or K-type star, where the primary has a measured metallicity. Assuming the two are coeval, one can infer the metallicity of the low-mass companion and subsequently use a sample

of CPM pairs to confirm or empirically calibrate tracers of M dwarf metallicity. Gizis & Reid (1997) applied this idea to the M subdwarf population, using observations of late-type companions to F and G subdwarfs of known metallicity to confirm the metallicity relation of Gizis (1997), which used optical spectral indices to infer the metallicity of M subdwarfs.

Bonfils et al. (2005a) pioneered the empirical calibration of M dwarf metallicities using CPM pairs. The authors found that a metal-rich M dwarf has a redder $V - K$ color at a given absolute K magnitude, due to increased line blanketing by molecular species, particularly TiO and VO. The calibration is valid for $4 < M_K < 7.5$, $2.5 < V - K < 6$ and $-1.5 < [\text{Fe}/\text{H}] < +0.2$ dex. Bonfils et al. (2005a) reported a standard deviation of 0.2 dex. Johnson & Apps (2009), finding the calibration of Bonfils et al. (2005a) to systematically underestimate the metallicities of metal-rich stars, updated the relation by considering the offset from the mean main sequence (MS), assuming the mean MS defined an isometallicity contour with $[\text{Fe}/\text{H}] = -0.05$ dex. Their calibration sample used six metal-rich calibrators. Schlafman & Laughlin (2010) found that the previous works had systematic errors at low and high metallicities and further updated the photometric relation. They used a larger calibration sample comprised only of M dwarfs with precise V magnitudes in CPM pairs with an F, G or K-star, where the primary's metallicity had been determined from high resolution spectroscopy. They also updated the determination of the mean MS, finding that it corresponded to an isometallicity contour with $[\text{Fe}/\text{H}] = -0.14$ dex. However, external information was still required to determine the mean MS. The standard deviation of their fit was 0.15 dex.

Neves et al. (2012) tested the photometric calibrations of Bonfils et al. (2005a),

Johnson & Apps (2009), and Schlafman & Laughlin (2010) on a new sample of FGK-M CPM pairs that had precise V -band photometry. With their sample of 23 M dwarfs, they found the Schlafman & Laughlin (2010) calibration had the lowest residual mean square error ($\sigma_{[\text{Fe}/\text{H}]} = 0.19 \pm 0.03$ dex) and highest correlation coefficient ($R_{ap}^2 = 0.41 \pm 0.29$), performing marginally better than the Bonfils et al. (2005a) calibration. They updated the Schlafman & Laughlin (2010) calibration, though the diagnostic values did not improve by more than the associated errors. Neves et al. (2013) used the photometric metallicities inferred from the Neves et al. (2012) calibration to fit a relation based on the EWs of features in HARPS spectra, reporting a dispersion of 0.08 dex between their new calibration and the photometric calibration.

Rojas-Ayala et al. (2010, hereafter R10) took a different approach and used moderate resolution K -band spectra ($R \approx \Delta\lambda/\lambda \approx 2700$) to measure metallicity. They used the EWs of the Na I doublet and Ca I triplet to measure metallicity and the $\text{H}_2\text{O-K2}$ index to account for the effects of temperature. The calibration was updated in R12, who demonstrated that their empirical metallicities gave reasonable results for solar neighborhood M dwarfs. With 18 calibrators, this method yielded $\text{RMSE} = 0.14$ dex and $R_{ap}^2 = 0.67$ for their $[\text{Fe}/\text{H}]$ calibration. The lines used in this calibration are isolated across the entire M dwarf spectral sequence and are located near the peak of the M dwarf spectral energy distribution (SED). Parallaxes and accurate magnitudes, which are scarce for M dwarfs, are not required, placing metallicities within reach for many M dwarfs.

Terrien et al. (2012) applied the methods of R10 to spectra obtained with the SpeX instrument on the NASA Infrared Telescope Facility (IRTF), using 22 CPM pairs as

calibrators. They updated the K -band R10 calibration ($\text{RMSE} = 0.14 \text{ dex}$, $R_{ap}^2 = 0.74$) and presented an H -band calibration ($\text{RMSE} = 0.14 \text{ dex}$, $R_{ap}^2 = 0.73$). Mann et al. (2013a) expanded the sample of calibrators and identified over 100 metal-sensitive features in the NIR and optical. Their calibration sample included 112 FGK-M CPM pairs, selected on the basis of common proper motion and galactic models. They constructed metallicity relations in the optical and in each of the NIR bands out of metallicity sensitive features and a single parameter to account for temperature dependencies. Their $[\text{Fe}/\text{H}]$ calibrations had RMSEs between 0.08 dex and 0.13 dex and R_{ap}^2 values ranging from 0.68 to 0.86. They also updated the color-color relation of Johnson et al. (2012) and the K - and H -band spectroscopic relations of Terrien et al. (2012) and R12.

We also note the larger context in which constraints on the physical properties of M dwarfs are applicable. For example, Bochanski et al. (2007a) used SDSS M dwarfs to test the Besançon galactic model (Robin et al. 2003), comparing observed kinematics to the model and comparing the observed metallicities and active fractions of the thin and thick disk. In this study and others using SDSS, optical molecular indices were used as a proxy for metallicity (e.g. Gizis & Reid 1997; Woolf & Wallerstein 2006). The ζ -index, which uses CaH and TiO molecular band heads, is commonly used to identify subdwarfs and extreme subdwarfs (Lepine et al. 2007; Dhital et al. 2012). Theories of star formation must also match the observed luminosity and mass functions of M dwarfs, which are in turn important input into galactic models. Bochanski et al. (2010), again exploiting SDSS, measured the M dwarf luminosity and mass functions. Photometric distance estimates were used in this work, and one of the primary factors complicating these estimates was

uncertainty in how metallicity affects absolute magnitude.

In this work, we present our observation and analysis of near infrared (NIR) moderate resolution ($R \approx 2000$) spectra of 447 MEarth M dwarfs. Our sample is presented in §2.2 and in §2.3 we discuss our observations and data reduction. We account for correlated noise when estimating the error on our measurements, as we discuss in §2.4. In §2.5, we present by-eye NIR spectral types for each star and a new spectroscopic distance calibration. Our metallicity measurements, described in §4.6.4, are based on the method developed by R12: we use EWs of spectral features in the NIR as empirical tracers of metallicity, using M dwarfs in CPM pairs to calibrate our relationship. We present a color-color metallicity calibration in §2.7. In §2.8, we discuss our method for measuring radial velocities, which uses telluric features to provide the wavelength calibration, and demonstrate 4 km/s accuracy. Our data are presented in Table 2.1 and we include updated parameters for those stars observed by R12 in Table 2.2. We include radial velocities, spectral types and parallaxes compiled from the literature. Table 2.1 and 2.2 are published in their entirety in a machine readable format. Descriptions for table columns are included here for guidance regarding their form and content.

2.2 Sample

Our sample consists of 447 M dwarfs targeted by the MEarth transiting planet survey and 46 M dwarfs in CPM pairs with an F, G or K star of known metallicity, a subset of which we used to calibrate our empirical metallicity relation.

Table 2.1. Data for stars from our rotation and nearby samples (table format)

Column	Format	Units	Description
1	A23	...	Name in LSPM Catalog; for binaries which were not resolved in the LSPM catalogs but which we resolve, we use the appropriate LSPM name in the first column and identify the components in the second column
2	A2	...	Binary component; where not resolved in PMSU
3	I2	h	Hour of RA from LS05 and LSPM-South (J2000)
4	I2	min	Minute of RA from LS05 and LSPM-South (J2000)
5	F5.2	s	Second of RA from LS05 and LSPM-South (J2000)
6	A1	...	Sign of the Dec. from LS05 and LSPM-South (J2000)
7	I2	deg	Degree of Dec. from LS05 and LSPM-South (J2000)
8	I2	arcmin	Arcminute of Dec. from LS05 and LSPM-South (J2000)
9	F4.1	arcsec	Arcsecond of Dec. from LS05 and LSPM-South (J2000)
10	F6.3	arcsec/yr	Proper motion along RA from LS05 and LSPM-South
11	F6.3	arcsec/yr	Proper motion along Dec. from LS05 and LSPM-South
12	F6.3	mag	Apparent K_S magnitude from S06
13	I1	...	Flag for poor quality 2MASS magnitudes; 1 if the 2MASS qual_flag is something other than AAA, the highest quality
14	I1	...	Flag for joint values for binaries; 1 if the astrometry and magnitudes are for the joint system
15	A5		NIR spectral type assigned by eye in this work
16	A5		Optical spectral type from PMSU
17	F4.2	0.1nm	EW of Na line at 2.21 microns
18	F4.2	0.1nm	Error in Na EW
19	F4.2	0.1nm	Equivalent width of Ca line at 2.26 microns
20	F4.2	0.1nm	Error in Ca EW
21	F5.3	...	Value of the H ₂ O-K2 index
22	F5.3	...	Error in H ₂ O-K2
23	F5.2	dex	Iron abundance with respect to solar
24	F4.2	dex	Error in iron abundance
25	I4	km/s	RV measured from NIR spectrum

Table 2.1—Continued

Column	Format	Units	Description
26	I2	km/s	Error in RV
27	F6.1	km/s	Radial velocity from PMSU
28	I1	...	Flag for joint PMSU spectral type and RV; 1 if the PMSU values are for the joint system
29	I2	pc	Distance estimate using H ₂ O-K2 index with an error of 22%; for binaries where individual magnitudes are not available, we assume the two components have equal luminosities when computing the spectroscopic distances
30	I1	...	Flag for distance estimate quality; 1 if quality is uncertain (see columns 13 and 14)
31	F5.1	mas	Parallax
32	F4.1	mas	Error in parallax
33	I1	...	Flag for parallax; 1 if assumed to be that of the common proper motion primary
34	A4	...	Reference for parallax
35	F9.1	...	Julian date of start of observation
36	A9	...	Observational sample

Note. — This table is available online in its entirety in a machine-readable format. References in this table: M92 = Monet et al. (1992); H93 = Harrington et al. (1993); vA95 = van Altena et al. (2001); R97 = Reid et al. (1997), see Reid et al. (1995) and Hawley et al. (1996); D98 = Ducourant et al. (1998); B00 = Benedict et al. (2000); H06 = Henry et al. (2006); S07 = Smart et al. (2007); vL07 = van Leeuwen (2007); G08 = Gatewood (2008); G09 = Gatewood & Coban (2009); L09 = Lépine et al. (2009); S10 = Smart et al. (2010); R10 = Riedel et al. (2010); K10 = Khrutskaya et al. (2010); S12 = Shkolnik et al. (2012); A13 = Anglada-Escudé et al. (2013a)

Table 2.2. Data for stars observed by R12 (table format)

Column	Format	Units	Description
1	A17	...	Name in LSPM Catalog
2	A23	...	Name in R12 Catalog
3	I2	h	Hour of RA (J2000)
4	I2	min	Minute of RA (J2000)
5	F5.2	s	Second of RA (J2000)
6	A1	...	Sign of the Dec. (J2000)
7	I2	deg	Degree of Dec. (J2000)
8	I2	arcmin	Arcminute of Dec. (J2000)
9	F4.1	arcsec	Arcsecond of Dec. (J2000)
10	F6.3	arcsec/yr	Proper motion along RA
11	F6.3	arcsec/yr	Proper motion along Dec.
12	A4	...	Reference for Astrometry
13	F6.3	mag	Apparent K_S magnitude from S06
14	A3	...	NIR spectral type
15	A5	...	Optical spectral type from PMSU
16	F4.2	0.1nm	EW of Na line at 2.21 μm from R12 converted to equivalent IRTF value as described in the text
17	F4.2	0.1nm	Error in Na EW
18	F4.2	0.1nm	EW of Ca line at 2.26 μm from R12 converted to equivalent IRTF value as described in the text
19	F4.2	0.1nm	Error in Ca EW
20	F5.3	...	Value of the H ₂ O-K2 index
21	F5.3	...	Error in H ₂ O-K2
22	F5.2	dex	Iron abundance with respect to solar using calibration from this work
23	F4.2	dex	Error in iron abundance
24	F6.1	km/s	Radial velocity from PMSU
25	I2	pc	Distance estimate using H ₂ O-K2 index with an error of 22%

Table 2.2—Continued

Column	Format	Units	Description
26	F4.1	pc	Distance from parallax
27	A4	...	Reference for parallax
28	A12	...	Observational sample listed in R12

Note. — This table is available online in its entirety in a machine-readable format. References in this table: B90 = Bessel (1990); GJ91 = Gliese & Jahreiß (1991); L92 = Leggett (1992); vA95 = van Altena et al. (2001); R97 = Reid et al. (1997), see Reid et al. (1995) and Hawley et al. (1996); GC04 = Gould & Chaname (2004); L05 = Lépine (2005); S06 = Skrutskie et al. (2006); vL07 = van Leeuwen (2007); K10 = Koen et al. (2010); LG11 = Lépine & Gaidos (2011)

2.2.1 MEarth M dwarfs

The MEarth project is photometrically monitoring 2000 of the nearest mid to late M dwarfs in the northern sky with the goal of finding transiting super Earths. Nutzman & Charbonneau (2008) described how the MEarth targets were selected from the Lépine-Shara Proper Motion catalog of northern stars (LSPM-North; Lépine & Shara 2005). For completeness, we summarize their method here. From the subset of stars believed to be within 33 pc (Lépine 2005), using spectroscopic or photometric distance estimates where parallaxes were unavailable, they selected those with $V - J > 2.3$, $J - K_S > 0.7$, and $J - H > 0.15$, resulting in a sample of probable nearby M dwarfs. The radius for each probable M dwarf was estimated by first using the absolute K_S magnitude-to-mass relation of Delfosse et al. (2000), and inputting this mass into the mass-to-radius relationship from Bayless & Orosz (2006). They subsequently selected all objects with estimated radii below $0.33 R_{\odot}$, driven by the desire to maintain sensitivity to planets with radii equal to twice Earth's.

MEarth is a targeted survey, visiting each object with a cadence of 20-30 minutes on each night over one or more observing seasons. A fraction of the sample has sufficient coverage and quality to estimate their rotation periods, with recovered periods ranging from 0.1 to 90 days. These will be discussed in a subsequent paper.

2.2.2 Spectroscopy targets

We targeted a subset of the MEarth M dwarfs for NIR spectroscopy. We re-observed 30 stars in common with R12, who focused their efforts on M dwarfs within 8pc, in

order to evaluate any systematic differences between our instruments and methods. The IRTF declination limit prevented us from observing stars above $+70^\circ$. We divide our targets into four subsamples based on the reason for their selection:

- Rotation sample: 181 M dwarfs with preliminary rotation periods measured from MEarth photometry. These show periodic photometric modulation presumed to be due to star spots rotating in and out of view.
- Nearby sample: 257 M dwarfs drawn from the full MEarth sample, for which no clear periodic photometric modulation was detected at the time of selection. This included 131 M dwarfs selected because they have parallaxes available from the literature, 94 M dwarfs with photometric distance estimates, and 32 "photometrically quiet" M dwarfs. The photometrically quiet M dwarfs are those for which phase coverage and photometric noise were sufficient to achieve good sensitivity to rotationally induced photometric modulations, but for which no such modulations were observed.
- Metallicity calibrators: 46 M dwarfs in CPM pairs with an F, G or K dwarf, where a metallicity measurement is available for the primary. These are discussed in §4.6.4. We used 36 M dwarfs in our final metallicity calibration.
- Potential calibrators: 10 potential calibrators are in CPM pairs with an F, G or K star but do not have a metallicity measurement available for the primary. We did not include these stars in our metallicity calibration.

We present new observations of 447 nearby M dwarfs in Table 2.1 (the rotation and nearby samples and potential calibrators). Data for our 46 M dwarf metallicity

calibrators are presented separately.

2.3 Observations

We conducted our observations with the SpeX instrument on the NASA Infrared Telescope Facility (Rayner et al. 2003, IRTF). We used the short cross dispersed (SXD) mode with the $0.3 \times 15''$ slit. This yielded spectra with $R \approx 2000$ covering $0.8 - 2.4\mu\text{m}$, with gaps between orders where there is strong atmospheric absorption. Our observations spanned 25 partial nights over 4 semesters. Observing conditions are summarized in Table 2.3; in moderate clouds, we observed bright targets.

We typically acquired four observations of each object, with two observations at each of two nod positions (A and B), in the sequence ABBA. We used the default A position and nod distance, with the A and B positions falling $3''.75$ from the edge of the slit (a $7''.5$ separation). Most of our targets were observed within half an hour of meridian crossing. For hour angles greater than one, we aligned the slit with the parallactic angle. We observed A0V stars for use as telluric standards within one hour of each science target, at angular separations no more than 15° , and with airmass differences of no more than 0.1 when possible (see §2.4). We took flat field spectra (using an internal quartz lamp) and wavelength calibrations (using internal Thorium-Argon lamps) throughout the night, at one hour intervals or after large slews. The typical observation time for a $K = 9$ target at each nod was 100 seconds (for a total integration time of 400 seconds). Combining four nods yielded a total signal-to-noise ratio (S/N) of 250 per resolution element.

Table 2.3. Observing conditions

Start date (UT)	Seeing	Weather conditions
2011A Semester		
May 15	0.6 – 1''	Mostly clear, humid
May 16	0.4 – 0''.8	Some cirrus, humid
May 17	0''.5	Heavy clouds, then clear
May 18	0''.5	Clear
2011B Semester		
June 9	0''.7	Some clouds
Aug 11	0''.5	Some clouds
Aug 12	0''.5	Heavy clouds
Aug 13	0''.5	Mostly clear
Aug 14	0''.4	Mostly cloudy
Oct 7	0''.8	Some clouds
Oct 8	0''.8	Heavy intermittent clouds
Oct 9	0''.6	Mostly clear
2012A Semester		
Feb. 14	1''	Clear
Feb 15	0.5 – 1''	Clear
Feb 16	0''.8	Clear
Feb 24	0''.8	Clear
Feb 27	1''	Heavy intermittent clouds
Feb 28	0''.8	Clear
May 1	0.3 – 1''.2	Clear
May 2	0''.6	Clear
2012B Semester		
Aug 14	1 – 2''	Clear
Aug 26	0''.5	Clear
Aug 27	0''.5	Clear
Jan 26	0''.8	Clear
Jan 27	1''.1	Heavy morning clouds

CHAPTER 2. A NIR SPECTROSCOPIC SURVEY OF M DWARFS

We reduced the data with the instrument-specific pipeline Spextool (Cushing et al. 2004), modified to allow greater automation and to use higher S/N flat fields, created by median combining all flat field frames from a given night. Images were first flat-field corrected using the master flat from the given night. After subtracting the A and B images, we used boxcar extraction with an aperture radius equal to the full width at half maximum (FWHM) of the average spatial profile and subtracted the residual sky background. To determine the background sky level in the AB subtracted image, we used a linear fit to the regions beginning $1''.2$ from the edges of the aperture. This step was important near sunrise and sunset and increasingly important in bluer orders, but the *K*-band was largely unaffected. Each spectrum was wavelength calibrated using the set of Thorium-Argon exposure most closely matching in time.

We combined individual spectra for the same object (typically 4 per object) using the Spextool routine `xcombspec`. We scaled the raw spectra to the median flux level within a fixed wavelength region and removed low order variations in the spectral shapes. We used the highest S/N region of the *H*-band for scaling. The modified spectra were combined using the robust weighted mean algorithm, which removed outliers beyond 8σ .

We used `xtellcor` to perform the telluric corrections (Vacca et al. 2003). We used the Paschen δ line near $1\mu\text{m}$ in the A0V telluric standard to create a function to describe the instrumental profile and the rotational broadening observed in spectrum. We used `xtellcor` to convolve this function with a model of Vega and shifted the model to match the star's observed radial velocity. We scaled the line strengths of individual lines to match those observed; for data taken in 2012, we adjusted the

scaling by hand. We found this to be a necessary step because even for sub-1% matches to the Vega model, residual hydrogen lines were apparent. The atmospheric absorption spectrum, as observed by the instrument, was found by dividing the observed A0V spectrum by the modified Vega spectrum. We shifted the atmospheric absorption spectrum to match the absorption features in the object spectrum and divided to remove the atmospheric absorption features present. We performed this step separately in each order, using a region dominated by telluric features to shift the spectra.

We performed flux calibration as part of the telluric correction, but variable weather conditions and slit losses made the absolute flux level unreliable. We do not require absolute flux calibration for our project goals.

2.4 Estimation of uncertainty

Given the high S/N (typically > 200) of our spectra, the uncertainties in quantities measured from our data are dominated by correlated noise, rather than random photon-counting errors. Correlated noise could be introduced by poorly-corrected telluric lines or by unresolved features in the region of the spectra assumed to represent the continuum.

We drew our errors from a multivariate Gaussian with Gaussian weights along the diagonal of the covariance matrix. At each pixel, we simulated Gaussian random noise using the errors returned by the SpeX pipeline, which included photon, residual sky, and read noise and which were propagated through the Spextool pipeline. We

multiplied the error realization by a Gaussian centered on that pixel with unit area and full width at half maximum (FWHM) equal to the width of the autocorrelation function. To determine the appropriate FWHM, we autocorrelated each order of several spectra of different S/N and found that a Gaussian with a FWHM of 1.5 pixels approximated the width of the autocorrelation function; we used this FWHM for all stars. We did this for each pixel, resulting in an array of overlapping Gaussians of unit area, one centered on each pixel. We then added the contributions from the Gaussians at each pixel, and took the sum at each pixel to be the error on that pixel. This effectively spread the error associated with a single pixel over the neighboring pixels according to the autocorrelation function.

We then re-measured spectral indices (described below), EWs (described in §2.6.3) and the radial velocity (as described in §2.8.1). We repeated this process 50 times and calculated the 1σ confidence intervals, which we took to be the errors on our measurements.

To assess the accuracy of our error estimates, we considered stars that we observed on two separate occasions, which have different observing conditions and S/N. By comparing independent measurements of the same object, we determined whether our error estimates accurately model the observed differences in the measurements. We used EWs, which we measure by numerically integrating within a defined region, as indicators of M dwarf metallicity (our method is described in detail in §4.6.4). The line of most interest to us is the Na I line at $2.2\mu\text{m}$. The median error on EW_{Na} is 0.17 \AA , typically 5%, which was achieved with $\text{S/N} = 300$. 92% of our spectra have S/N in the *K*-band greater than 200 and 67% have errors on EW_{Na} less than 0.2 \AA . In Figure 2.1, we compare EW_{Na} for stars that were observed multiple

times, finding that our method accurately captures the observed errors.

We also measure 10 spectral indices (§2.6.3), including the H₂O-K2 index, a temperature-sensitive index that measures the curvature of the *K*-band by considering the flux level in three *K*-band regions (R12). It is defined as:

$$\text{H}_2\text{O-K2} = \frac{\langle 2.070 - 2.090 \rangle / \langle 2.235 - 2.255 \rangle}{\langle 2.235 - 2.255 \rangle / \langle 2.360 - 2.380 \rangle} \quad (2.1)$$

Angle brackets represent the median flux within the wavelength range indicated, where wavelengths are given in microns. In Figure 2.2, we compare measurements of the H₂O-K2 index for objects which were observed multiple times. Our autocorrelation analysis underestimated the true uncertainties. The largest discrepancies arose when airmass differed by more than 0.2 or time of observation differed by more than two hours (these were not typical occurrences amongst our sample). If using the H₂O-K2 index for metallicity or temperature measurements, we suggest taking particular care to observe a telluric standard immediately before or after each science observation, and as closely matching in airmass as possible, as described in Vacca et al. (2003).

2.5 NIR spectral types

We determined NIR spectral types by eye for each star using the *K*, *H*, *J* and *Y*-bands. Our NIR spectral types are based on the spectral typing system defined by Kirkpatrick et al. (1991, 1995, 1999), hereafter the KHM system. We used a custom spectral typing program to match each science spectrum to a library of spectral type standards created from our data (§2.5.1-§2.5.2). We considered the differences

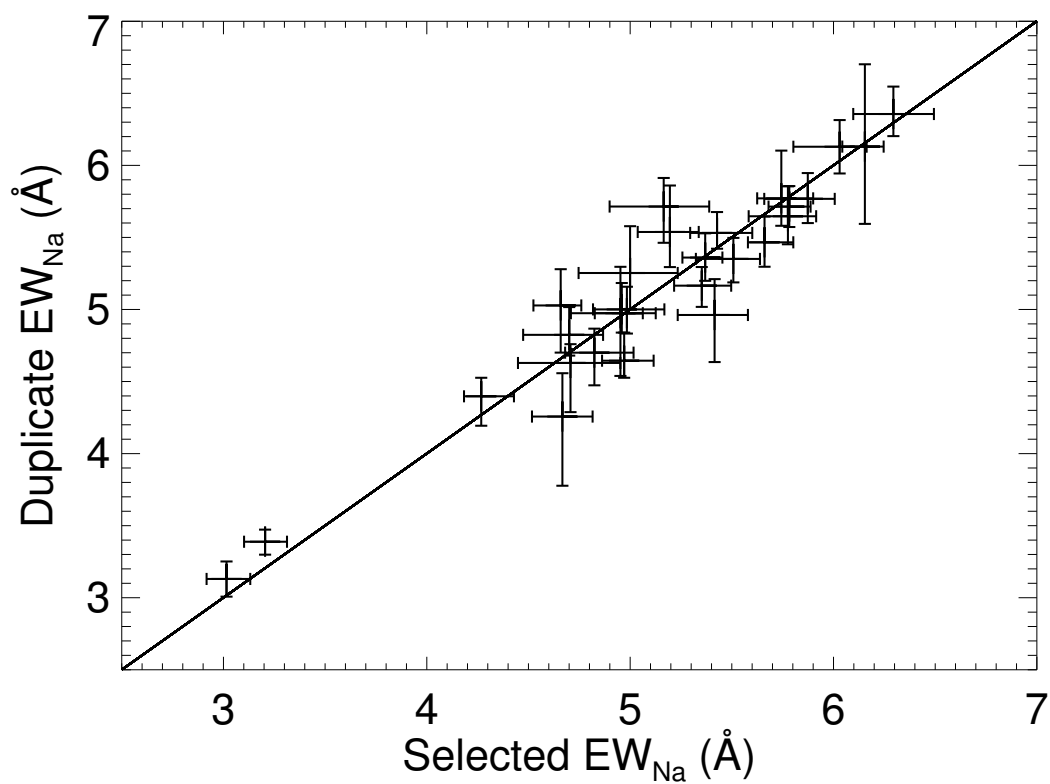


Figure 2.1.— We compare EW_{Na} measurements for stars for which we have more than one observation. The horizontal axis shows the EW_{Na} of the selected observation and the vertical axis shows the EW_{Na} of the alternate observation, both in Å. We also include the 1σ confidence intervals from 50 trials.

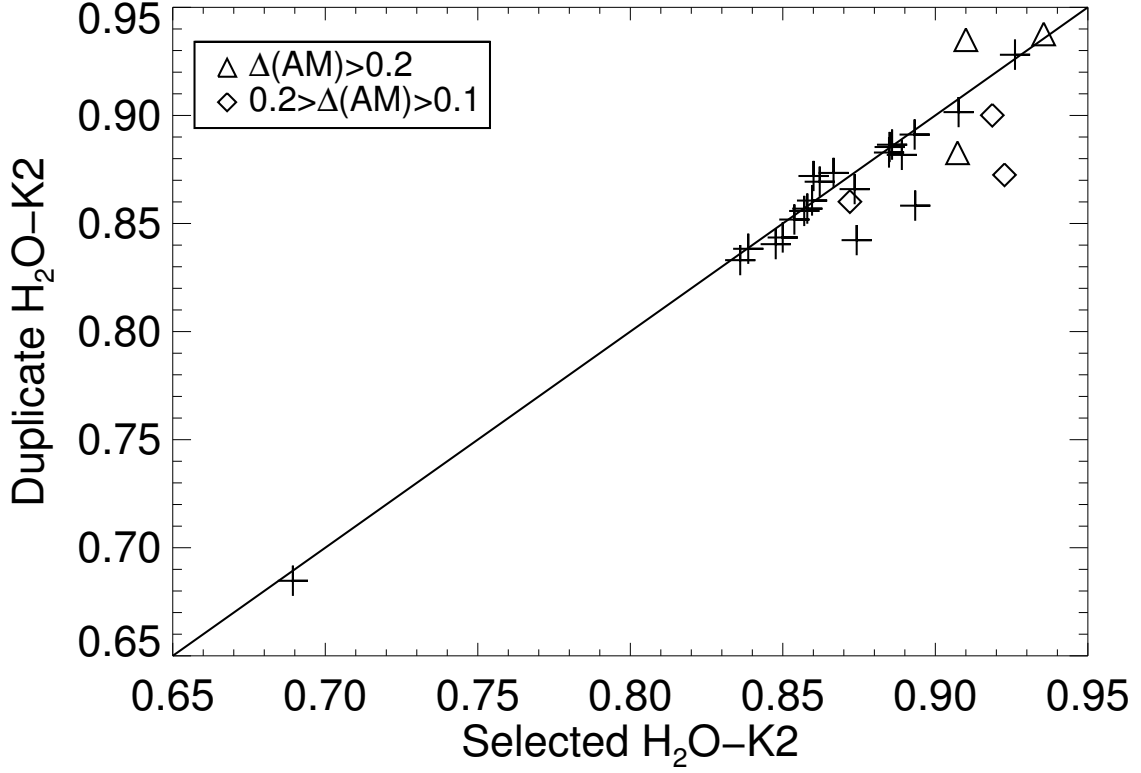


Figure 2.2.— We compare measurements of the H₂O-K2 index for stars which we observed multiple times. On the horizontal axis we show the H₂O-K2 index of the selected observation and on the vertical axis, the H₂O-K2 index of the alternate observation. The errors from 50 trials are smaller than the data points. We indicate the cases of significant airmass discrepancies between the science and telluric spectra as triangles (for $\Delta\text{AM} > 0.2$) and diamonds (for $0.2 > \Delta\text{AM} > 0.1$). The two cases with large discrepancies in the H₂O-K2 index but for which the science and telluric spectra are closely matching in airmass are instances where the science and telluric observations were separated by more than two hours.

between our NIR spectral types and other spectral type indicators (§2.5.3) and calibrated a new spectroscopic distance relation using apparent K_S magnitude and either NIR spectral type or the H_2O -K2 index (§2.5.4).

2.5.1 Spectral typing routine

We first estimated the spectral type for each star using the relationship between H_2O -K2 index and spectral type that was presented in R12. We displayed the object spectrum and two spectral standards: the spectral standard with the estimated spectral type and the spectral standard with the spectral type one subtype later. We indicated the FeH bands identified in Cushing et al. (2005) with dashed lines, though the Wing-Ford FeH band at $0.99\mu\text{m}$ is the only band head apparent across the entire M spectral sequence. FeH is known to be sensitive to spectral type (e.g. Schiavon et al. 1997; Cushing et al. 2005). Using a GUI, we checked earlier and later spectral standards as desired, then selected a spectral type for the object. An example is shown in Figure 2.3.

We did not consider half-spectral types. We found the difference between late K dwarfs and M0V stars, and similarly between M8V and M9V stars, to be marginal in the NIR. We used a combined M8V/M9V spectral standard in our program. While K7V and M0V spectral standards were included separately in our spectral typing code, in our later analysis stars we considered a joint K7/M0V spectral class. We took a holistic approach to spectral typing due to the metallicity-dependence of many spectral features. We placed more weight on the redder orders and less weight on features known to be sensitive to metal content (such as the sodium line at $2.2\mu\text{m}$).

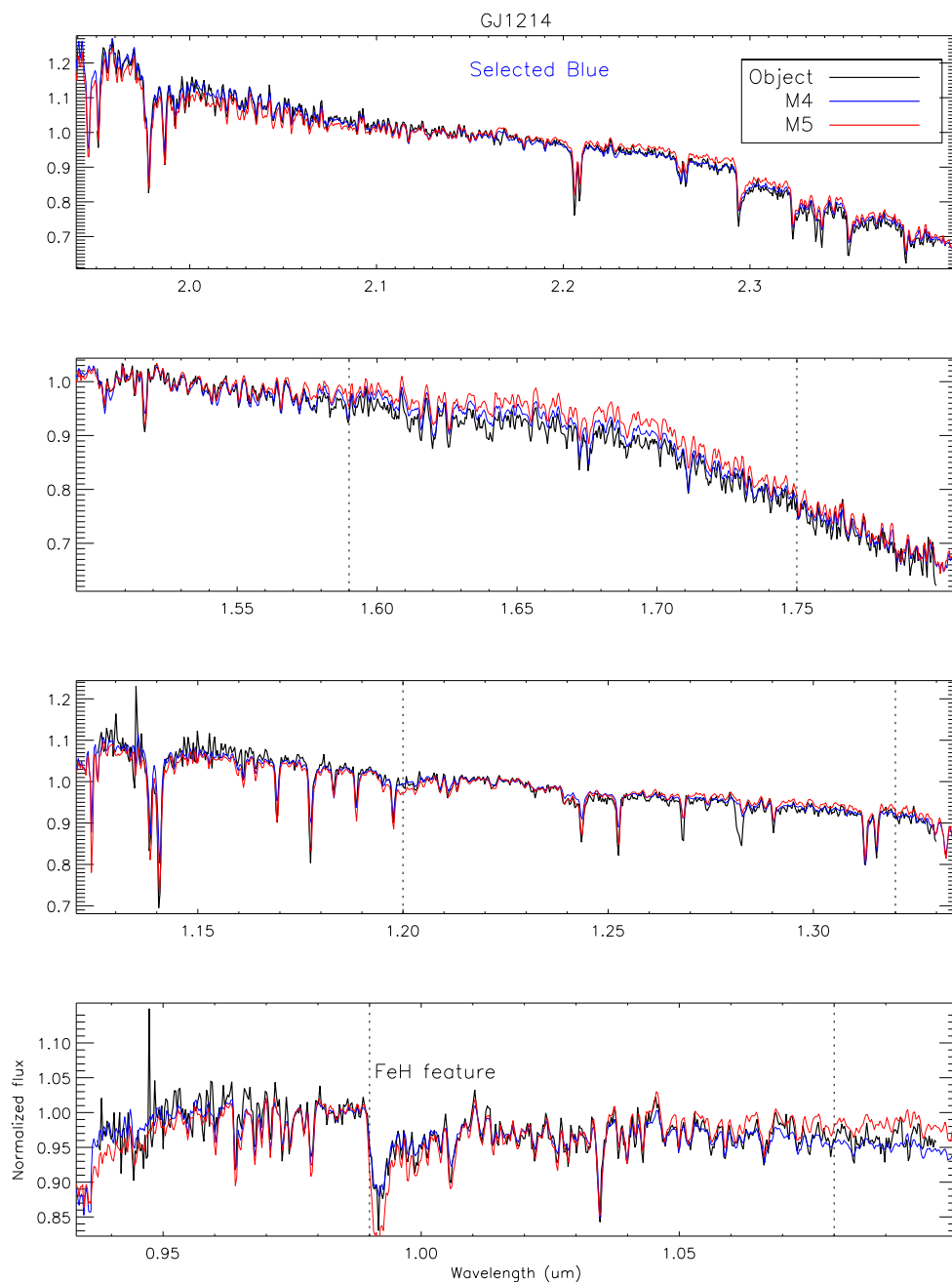


Figure 2.3.— An example of the output from our spectral typing routine. We included the K , H , J and Y -bands in our program. We show the object spectrum, in this case GJ 1214, in black. We overplot two spectral standards in blue and red. Dashes indicate FeH bands; only the Wing-Ford band head at $0.99\mu\text{m}$ is apparent in mid M dwarfs. In this case, we selected the blue spectral standard, M4V, as the best match to the object spectrum. The spectral type from Reid et al. (1995) is M4.5V.

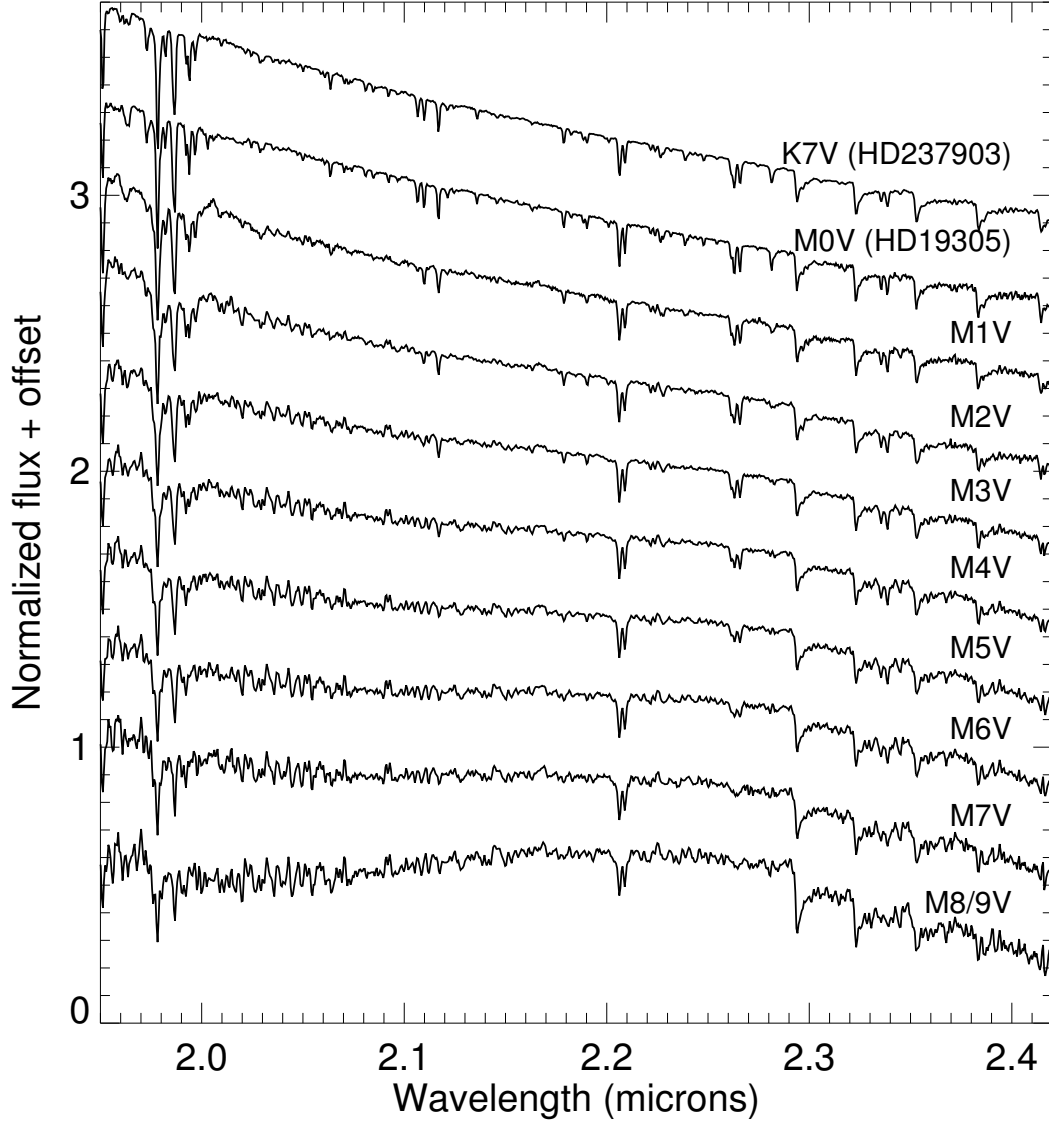


Figure 2.4.— Our IRTF spectral sequence from K7V to M9V for the *K* band. For K7V and M0V, we used the spectral standards from the IRTF library. For the remaining spectral types, we created standards from our observations by median-combining stars of a single spectral type. We were unable to reliably separate M8V and M9V stars and therefore treat them as one spectral category (see §2.5.1). In practice, we also could not distinguish between K7V and M0V and assigned these a K7/M0V spectral type.

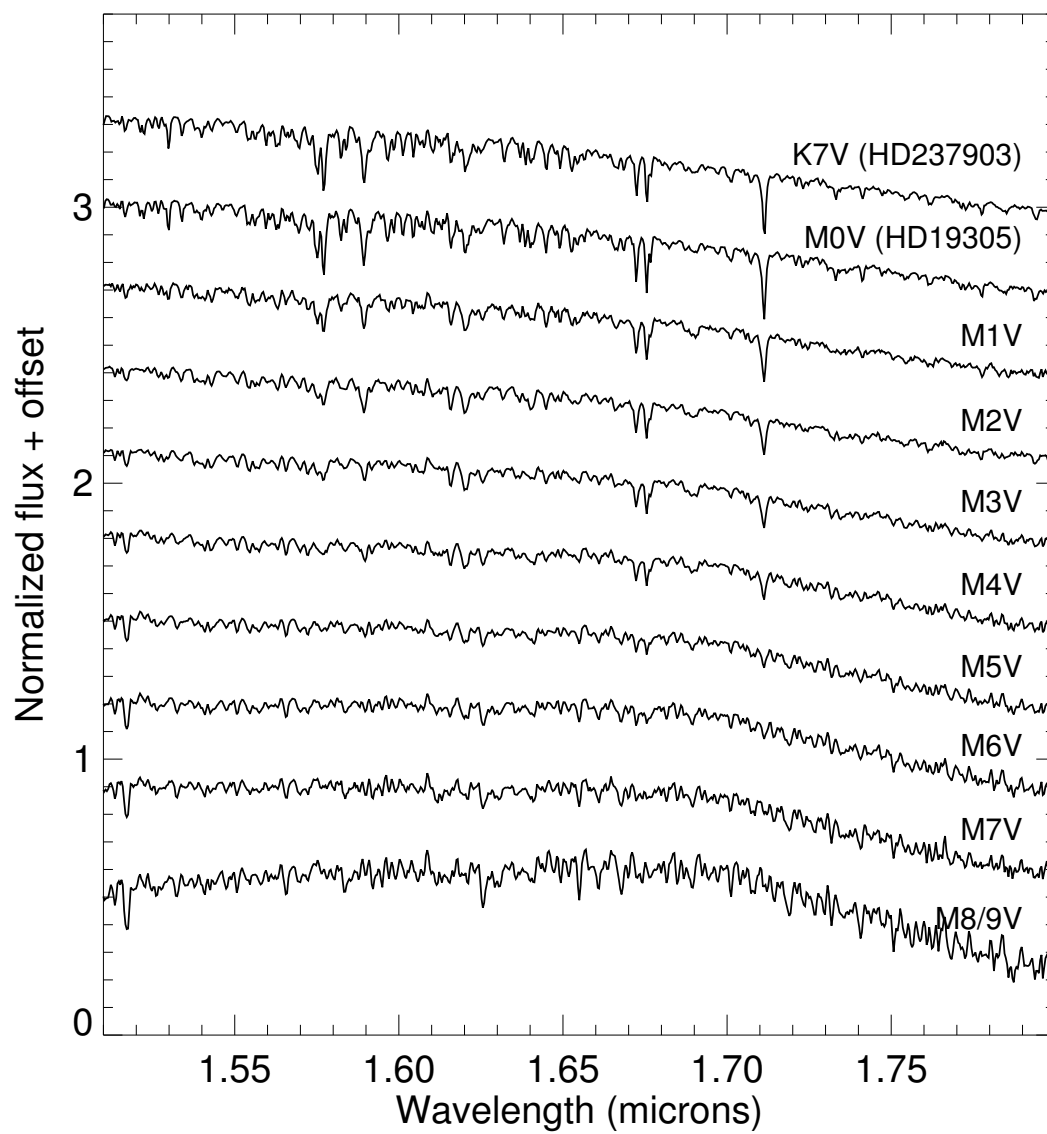


Figure 2.5.— Same as in Figure 2.4 but for the *H* band.

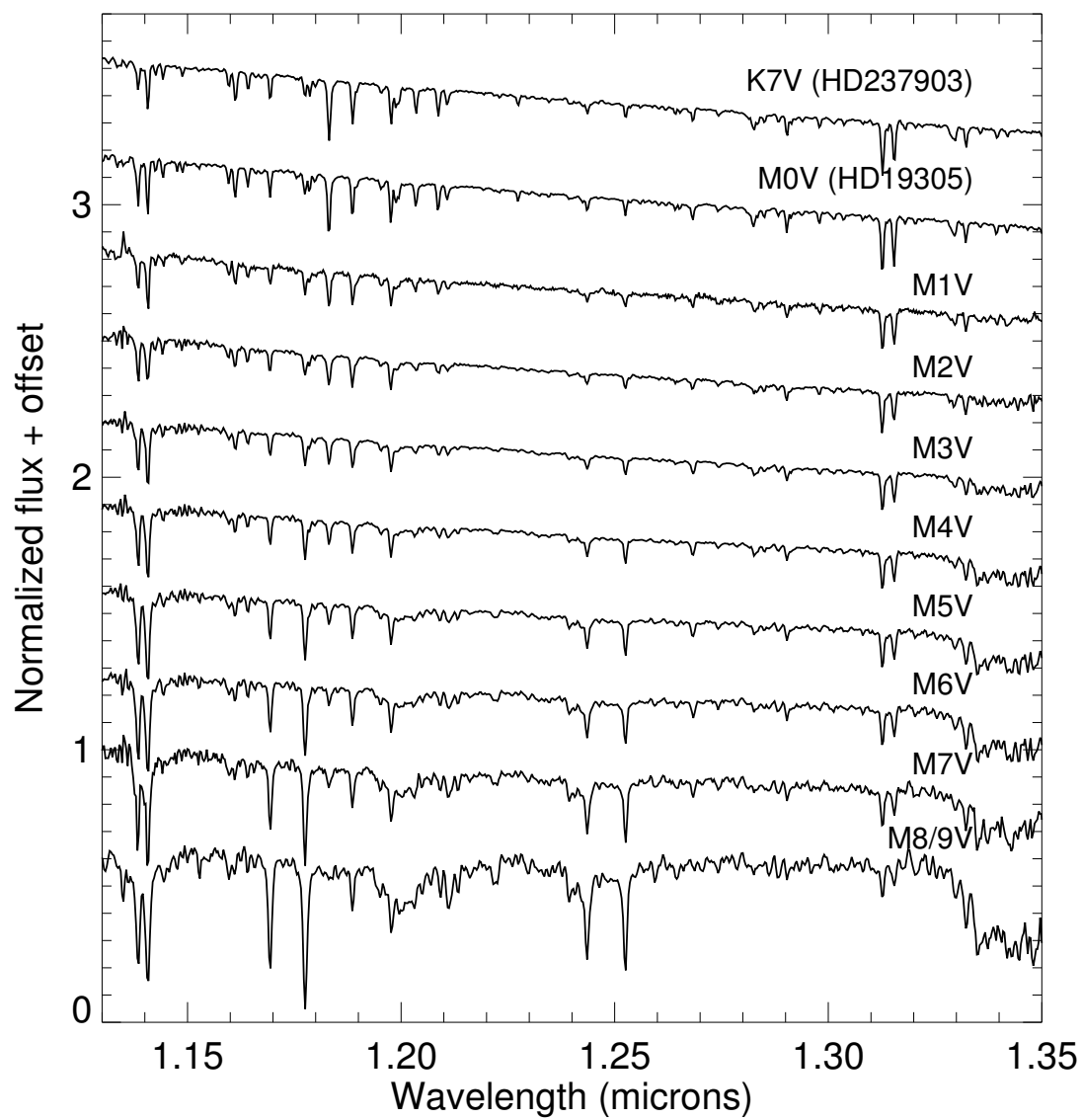


Figure 2.6.— Same as in Figure 2.4 but for the *J* band.

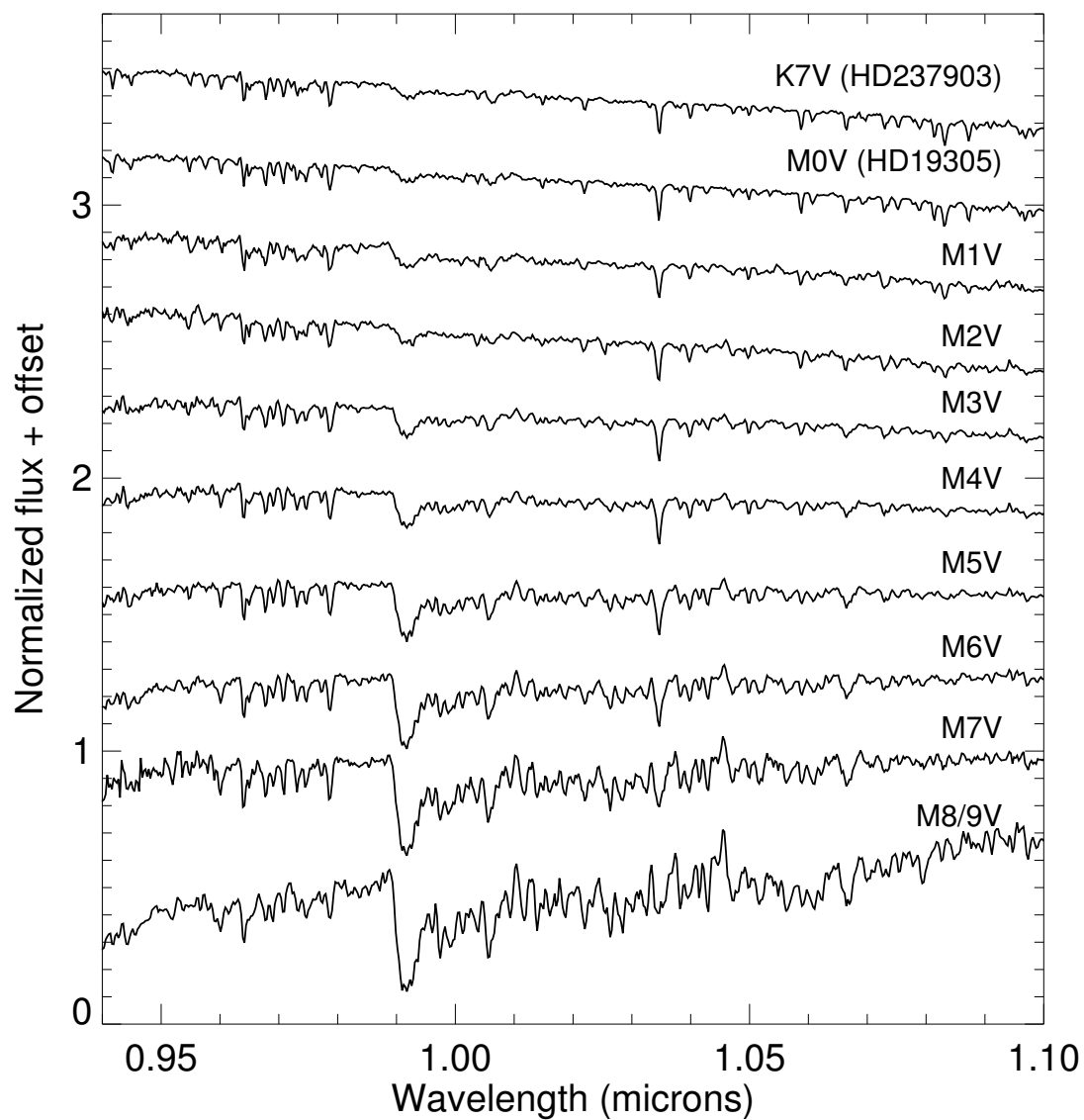


Figure 2.7.— Same as in Figure 2.4 but for the Y band.

Our NIR spectral types are included in Table 2.1.

2.5.2 IRTF spectral standards

We initially used the M dwarfs in the IRTF spectral library (Rayner et al. 2009) as spectral standards, using the KHM spectral standards except for our M0V (HD19305), M3V (AD Leo/G1 388) and M6V (CN Leo/G1 406) spectral standards. However, we noted several differences between the strengths of features in the standard spectra and the typical object spectra. In particular, the M4V spectral standard, G1 213, is metal poor. This is to be expected: Cushing et al. (2005) identify G1 213 as a probable low-metallicity object on the basis of its low Fe, Al, Na, and Ca EWs. By comparison with neighboring spectral standards and using our holistic approach to spectral typing, we were nevertheless able to accurately assess the NIR spectral types of solar metallicity stars.

To address the concern of spectral standards with extreme metallicities or other unique features, we created our own standard spectra. We assessed the spectral type of all stars observed through the 2012A semester by eye once, using the IRTF spectral library stars as standards. We then median-combine stars of a single spectral type that were within 0.2 dex of solar metallicity or, for M5V-M7V stars, within 0.1 dex of solar (see §4.6.4 for a description of how we determine metallicities for our stars). There were two stars comprising the M1V spectral standard (with median $\overline{[\text{Fe}/\text{H}]} = 0.05$), 10 in M2V ($\overline{[\text{Fe}/\text{H}]} = 0.0$), 17 in M3V ($\overline{[\text{Fe}/\text{H}]} = 0.02$), 45 in M4V ($\overline{[\text{Fe}/\text{H}]} = 0.01$), 48 in M5V ($\overline{[\text{Fe}/\text{H}]} = 0.03$), 18 in M6V ($\overline{[\text{Fe}/\text{H}]} = 0.04$) and six in M7V ($\overline{[\text{Fe}/\text{H}]} = 0.04$). We included all five M8/9V stars observed through the 2012A

semester in the M8/M9V spectral standard. We continued to use the IRTF spectral library standards for K dwarfs and M0V stars. We show our spectral sequence in four IRTF bands, from K7V to M8/9V, in Figs. 2.4-2.7. We then re-classified each star by eye using our new standard spectra.

2.5.3 Comparing measures of spectral type

We first compare our by-eye NIR spectral types to those measured with the H₂O-K2 index, using the relation in R12. These measures agree to within one spectral type; however, our by-eye spectral types are on average half a spectral type later than those measured using the H₂O-K2 index. We express M subtype numerically as Sp_{NIR} , where positive values are M subtypes (e.g. $Sp_{\text{NIR}} = 4$ corresponds to M4V) and negative values are K subtypes (e.g. $Sp_{\text{NIR}} = -1$ corresponds to K7V and $Sp_{\text{NIR}} = -2$ corresponds to K5V). We find:

$$Sp_{\text{NIR}} = 25.4 - 24.2 (\text{H}_2\text{O-K2}) \quad (2.2)$$

Over 100 of our objects have optical spectral types from the Palomar/Michigan State University (PMSU) Survey (Reid et al. 1995; Hawley et al. 1996, included for comparison in Table 2.1). The PMSU survey used the depth of the strongest TiO feature in optical M dwarf spectra as the primary indicator of spectral type, and calibrated their relation against nearly 100 spectral classifications on the KHM system. As in R12, we find a systematic difference between the PMSU spectral types and the NIR spectral types as a function of metallicity, shown in Figure 2.8 for stars earlier than M5V. For M5V stars, there appears to be no clear trend with metallicity.

For early and mid M dwarfs, the NIR spectral type is typically half a spectral type later than the PMSU spectral type, with more metal poor stars being prone to the largest differences between the PMSU and NIR spectral types. We see the same trend with metallicity as in R12: stars that are metal poor were assigned PMSU spectral types that are earlier than the NIR spectral type we assigned.

We calibrated a metallicity-sensitive function relating NIR spectral type to PMSU spectral type, to facilitate joint use of our data. We found that a linear combination of NIR spectral type and metallicity is sufficient only between NIR spectral types M1V and M3V, while a non-linear combination qualitatively explains the trends seen in our data. Our best fitting non-linear relation is given by:

$$\begin{aligned} \text{Sp}_{\text{PMSU}} = & 0.47 + 0.82 (\text{Sp}_{\text{NIR}}) + 4.5 ([\text{Fe}/\text{H}]) \\ & - 0.89 (\text{Sp}_{\text{NIR}}) ([\text{Fe}/\text{H}]) \end{aligned} \quad (2.3)$$

where spectral types are expressed numerically, as described above, and $[\text{Fe}/\text{H}]$ is given in dex. It is valid over NIR spectral types from M1V-M4V and has a scatter of half a subtype.

2.5.4 Spectroscopic distances

We used NIR spectral type and the $\text{H}_2\text{O-K2}$ index to calibrate a relation with absolute K_S magnitude, using 187 M dwarfs with parallaxes and K_S magnitudes (Figure 2.9). We calculated errors on absolute K_S magnitude from the parallax errors, imposing a lower limit of 0.01 magnitudes (this limit was applied to three stars). We performed a linear least squares fit, using the average of the positive and negative errors on

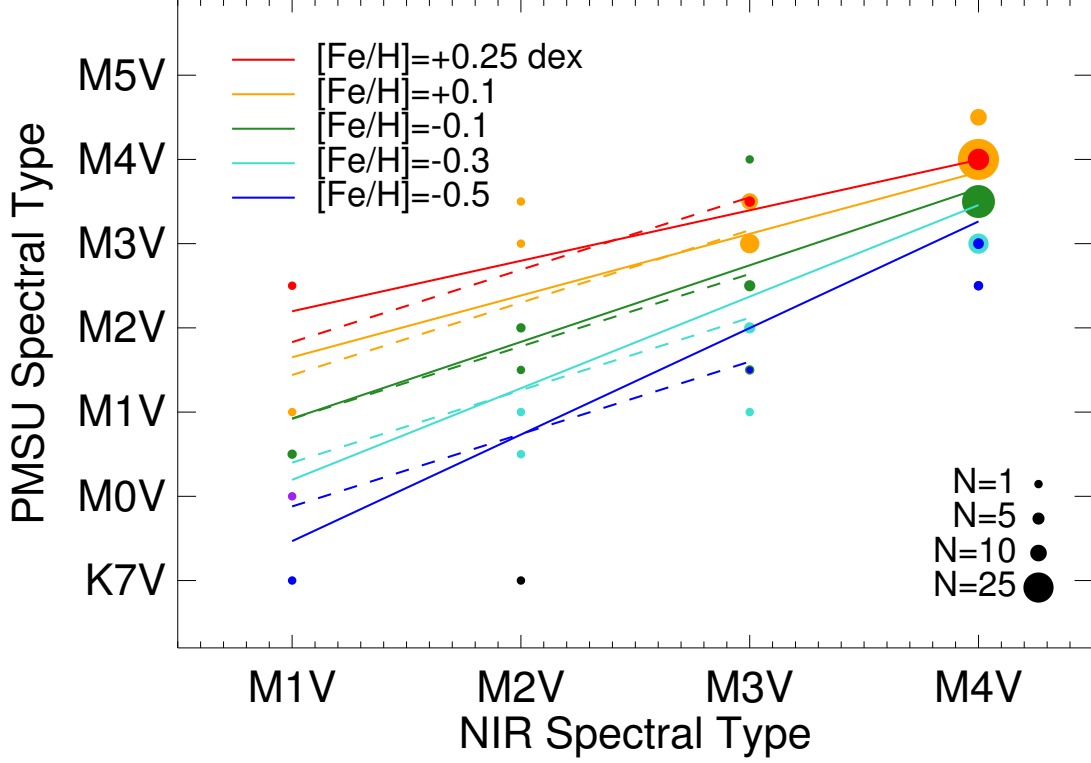


Figure 2.8.— Relation between NIR spectral type, metallicity and PMSU spectral type. The horizontal axis is the NIR spectral type determined by eye in this work. The vertical axis is the spectral type from PMSU (Reid et al. 1995; Hawley et al. 1996), determined from optical spectral features. We represent each bin as a single point, using color to indicate the mean metallicity and size to indicate the number of objects in each bin. In cases where a quarter of the stars fall into a metallicity bin different than the mean, we plot a second data point interior to the first. The area of the interior point relative to the exterior is proportional to the fraction of stars with the second metallicity. Overplotted is our best fitting relation (solid lines). We also include the best fitting linear relation (dashed lines), which extend across the region for which they were calibrated. Contours for our best fits are given by metallicities indicated in the legend and correspond to the colors used for the data points. The metallicity bins used to color data points are: $-1.0 < [\text{Fe}/\text{H}] < -0.6$ dex (purple), $-0.6 < [\text{Fe}/\text{H}] < -0.4$ (blue), $-0.4 < [\text{Fe}/\text{H}] < -0.2$ (cyan), $-0.2 < [\text{Fe}/\text{H}] < 0.0$ (green), $0.0 < [\text{Fe}/\text{H}] < +0.2$ (orange), and $+0.2 < [\text{Fe}/\text{H}] < +0.3$ (red).

the distance to calculate the K_S magnitude measurement error. The fit is valid for NIR spectral types M0V-M8V or $0.7 < \text{H}_2\text{O-K2} < 1.06$. Expressing the M subtype numerically, our best fits are:

$$\begin{aligned} M_K &= 4.72 + 0.64 (\text{Sp}_{\text{NIR}}) \\ &= 20.78 - 15.26 (\text{H}_2\text{O-K2}) \end{aligned} \tag{2.4}$$

To estimate the error on the inferred magnitudes and distances, we remove 5σ outliers and calculate the standard deviation between the measured and inferred absolute magnitudes. Outlier rejection removes four objects for the spectral type relation and three for the $\text{H}_2\text{O-K2}$ relation. The standard deviation is 0.30 magnitudes for the NIR spectral type relation and 0.27 magnitudes for the $\text{H}_2\text{O-K2}$ relation, indicating that most of the scatter is intrinsic, rather than due to binning by spectral type. Using standard Gaussian error propagation, we estimated that the uncertainty in the distances inferred using Equation 2.4 is approximately 22%¹. Spectroscopic distance estimates based on the $\text{H}_2\text{O-K2}$ index are included for stars in our sample in Table 2.1. For binaries where only the total magnitude of two components is available, we assume they contribute equally to the luminosity.

2.6 Metallicity calibration

We calibrated our metallicity relation using M dwarfs in CPM pairs with FGK stars, where the primary has a measured metallicity (§2.6.1). Our method of identifying

¹This has been corrected from the published value of 14%

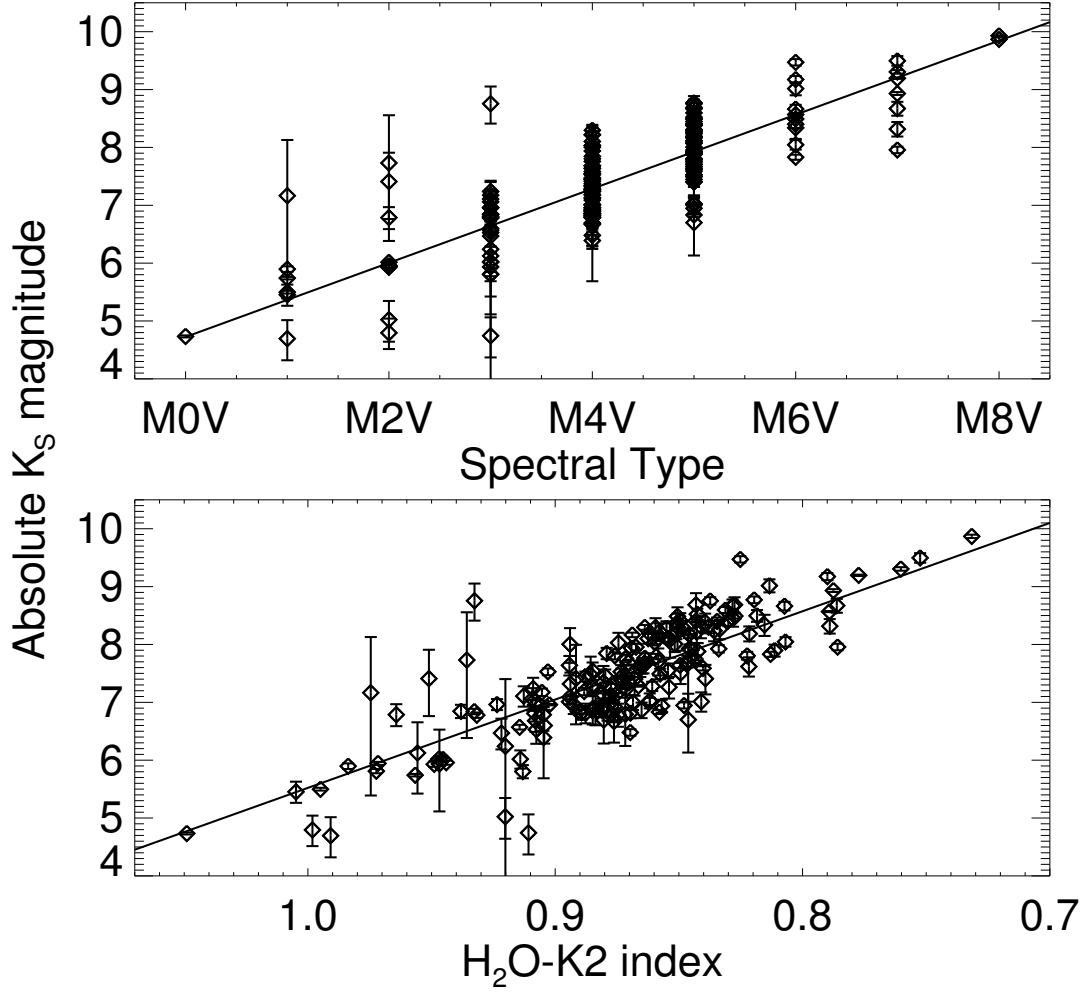


Figure 2.9.— Absolute K_S magnitude versus NIR spectral type (top panel) and H₂O-K2 (bottom panel) for 187 M dwarfs. Overplotted are our best fits. Excluding 5σ outliers, the standard deviation is 0.30 magnitudes for the NIR spectral type relation and 0.27 magnitudes for the H₂O-K2 relation. The error in the distance inferred by this method is 22%.

CPM pairs and additional validation using radial velocities and spectroscopic distance estimates is described in §2.6.2. We searched the NIR for suitable tracers of metallicity (§2.6.3) and looked into potential sources of bias (§2.6.4). We tested our calibration using M dwarf-M dwarf binaries and M dwarfs observed at multiple epochs (§2.6.5) and compared measurements from R12 to those from this work (§2.6.6).

2.6.1 Metallicities of the primary stars

For our potential primary stars, we used FGK stars with metallicities measured by Valenti & Fischer (2005, hereafter VF05), Santos et al. (2004, 2005, 2011, hereafter Santos+), Sousa et al. (2006, 2008, 2011, hereafter Sousa+), and Bonfils et al. (2005a). We use VF05 metallicities where available. We also considered those stars with metallicities measured from Sozzetti et al. (2009). VF05 and Sozzetti et al. (2009) fit an observed spectrum to a grid of model spectra (Kurucz 1992). They reported errors of 0.03 dex on $[\text{Fe}/\text{H}]$ for measurements of a single spectrum. Work by Santos+, Sousa+, and Bonfils et al. (2005a) used the EWs of iron lines in conjunction with model spectra to measure $[\text{Fe}/\text{H}]$.

We verified that $[\text{Fe}/\text{H}]$ measurements for FGK stars from different sources are not subject to systematic differences. In Figure 2.10, we compare the $[\text{Fe}/\text{H}]$ values measured by Sousa+, Santos+, and Sozzetti et al. (2009) to the VF05 measurements for single FGK stars, finding the majority of measurements are within 0.1 dex. The differences between the metallicities from these sources and VF05 are 0.00 ± 0.05 for Sousa+, 0.00 ± 0.06 for Santos+, and -0.05 ± 0.13 for Sozzetti et al. (2009). Our

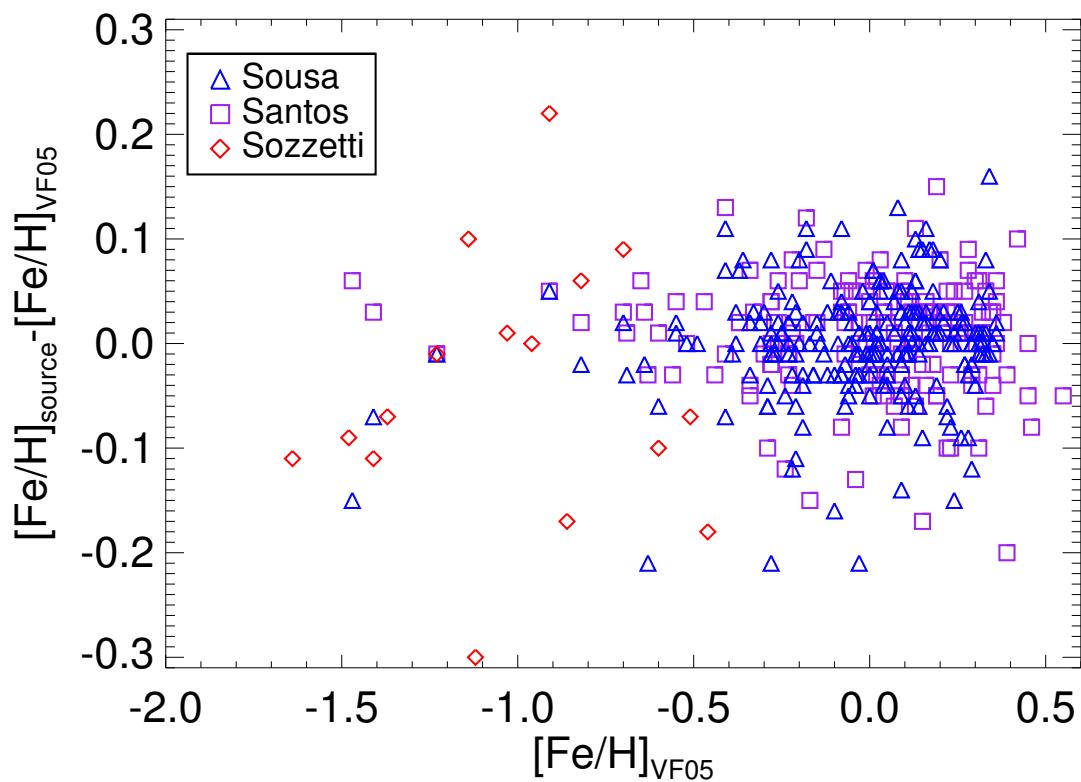


Figure 2.10.— Comparison of $[\text{Fe}/\text{H}]$ measurements for single FGK stars from Sousa+ (blue triangles), Santos+ (purple squares) and Sozzetti et al. (2009, red diamonds) to VF05 $[\text{Fe}/\text{H}]$ measurements. Metallicities are in dex. We did not use measurements from Sozzetti et al. (2009) to calibrate our relation.

findings are consistent with those from Sousa et al. (2011) and Sozzetti et al. (2009). We did not have a large sample with which to compare $[\text{Fe}/\text{H}]$ measurements from Bonfils et al. (2005a) and VF05. However, Bonfils et al. (2005a) followed the methods of Santos et al. (2004) to measure $[\text{Fe}/\text{H}]$ and found that their work is in agreement.

Out of the 46 M dwarfs in FGK-M CPM pairs with metallicity measurements, there are four M dwarfs for which only a metallicity measurement from Sozzetti et al. (2009) was available: LSPM J0315+0103, LSPM J1208+2147N, LSPM J1311+0936 and PM I16277-0104. These M dwarfs are useful in extending the calibration regime to lower metallicities, but the scatter in their measured metallicities was large enough to be of concern, so we did not use these M dwarfs as part of our final calibration sample. However, we did use these four stars to validate the extrapolation of our calibration to $[\text{Fe}/\text{H}] = -1.0$ dex.

We used 0.03 dex divided by the square root of the number of spectra analyzed as the error for VF05 metallicity measurements, as described by the authors (typically 1-2 spectra were analyzed in VF05). Errors for metallicities from Santos+, Sousa+, and Bonfils et al. (2005a) were reported individually in the literature. Since the errors were consistent with the scatter we find between VF05 and these measurements, we did not further inflate the error bars.

2.6.2 Identification of calibrators

We used calibrators from previous works (Bonfils et al. 2005a; Johnson & Apps 2009; Schlafman & Laughlin 2010; Terrien et al. 2012), but also identified new calibrators. To locate new FGK-M CPM pairs, we cross-matched the LSPM-North

and LSPM-South (Lépine, private communication) catalogs with themselves and with those stars with measured metallicities from VF05, Sousa+, Santos+, or Sozzetti et al. (2009). Our search was subject to the following requirements: the secondary must be within $5'$, have colors consistent with an M dwarf ($V - J > 2$, $J - K_S > 0.6$ and $H - K_S > 0.1$), and have proper motions within 6σ of the primary, where the uncertainties were assumed to be those stated in the LSPM catalogs.

We used a χ^2 statistic to identify CPM pairs. The statistic was constructed from the angular separation (a), the difference in proper motions ($\Delta PM = |PM_1 - PM_2|$), and the difference in distance moduli ($\Delta DM = DM_1 - DM_2$). For the distance, we used parallaxes where available, and otherwise used the M_J versus $V - J$ relation (Lépine 2005) using the $V - J$ estimates from Lépine & Shara (2005):

$$\chi^2 = \left(\frac{a}{2'}\right)^2 + \left(\frac{\Delta PM}{\sigma_{\Delta PM}}\right)^2 + \left(\frac{\Delta DM}{\sigma_{\Delta DM}}\right)^2 \quad (2.5)$$

We required $\chi^2 < 15$ for selection of an object as a candidate binary.

We note that the M_J values estimated from Lépine & Shara (2005) $V - J$ measure were often highly uncertain, because many were derived from photographic estimates of the V magnitude. Thus, the constraints from requiring a common distance modulus are weak in these cases. Additionally, the LSPM catalogs gave the same proper motion value for many very close systems where separate values could not be measured; our analysis assumed that the proper motions were independently measured.

After gathering our observations, we checked that the RV of the primary was in agreement with our measurement of the RV of the secondary and that the distance to the primary was in agreement with our spectroscopic distance estimate for the

secondary. We compared the RV and distance measurements for each calibrator and three stars were immediately obvious as outliers. Two have RVs differing by more than 10σ : Gl 806.1B and CE 226. One has a distance differing by 7.5σ : HD 46375B. (This star is noted on SIMBAD as not being a CPM pair, although in MEarth imaging they do appear to move in tandem). LP 731-76, a mid M dwarf, has the same K_S magnitude as its primary, an early K dwarf, clearly indicating that these are not associated. We did not include these four stars in our final sample of calibrators. While some of these systems may be physically associated, unresolved hierarchical triples, we consider the purity of our sample to be more important than its completeness.

Two of the remaining calibrators are concerning, but we do not have sufficient cause to exclude them from our sample. LSPM J0045+0015N has a distance estimate of 22pc (compared to 41pc for the primary) and an RV of 16 km/s (compared to 32 km/s). 2MASS J03480588+4032226 has a distance estimate of 30pc (compared to 50pc for the primary) and an RV of 0 km/s (compared to -10 km/s); the low proper motion of this object means that the evidence for the physical association of the pair from proper motion alone is weakened.

We identified 2MASS J17195815-0553043 as a visual double, and a comparison between the National Geographic Society-Palomar Observatory Sky Survey and 2MASS indicates the pair likely has a common proper motion. The distance estimates and radial velocities of the components also support the pair being physical associated. To estimate the distance to 2MASS J17195815-0553043, we assumed the two components had equal magnitudes such that the sum of their fluxes matched the published value. PM I14574-2124W (Gl 570BC) is a known spectroscopic

binary, comprised of $0.6 M_{\odot}$ and $0.4 M_{\odot}$ components (Forveille et al. 1999). As we demonstrate below, the Na I line we use to measure metallicity appears to be only weakly sensitive to temperature over the spectral type range of our calibration, and therefore the EWs should not be strongly influenced by the presence of a binary companion, and this object was not removed from the calibration sample. To be consistent with our treatment of known and unknown spectroscopic binaries, we use the total magnitude of PM I14574-2124W when estimating its distance.

The M dwarf calibrators and our observations are presented in Tables 2.4 and 2.5. 46 FGK-M CPM pairs appear in these tables. As previously stated, four of these objects were removed from our final calibration sample because they may not be physically associated. An additional four M dwarfs with measurements of the primary star's metallicity from Sozzetti et al. (2009) were not included in the calibration sample, although we used them to validate our calibration to lower metallicities. Two M0V dwarfs were also not included in our final metallicity calibration, as is discussed in subsequent sections. Our final calibration sample therefore consisted of 36 M dwarfs with NIR spectral types from M1V to M5V, with one M7 dwarf, and metallicities between -0.7 and $+0.45$ dex. The typical calibrator is an M4 or M5 dwarf and has a metallicity within 0.2 dex of solar.

2.6.3 Empirical metallicity calibration

We looked for combinations of spectral features that are good tracers of $[\text{Fe}/\text{H}]$. Based on the lines listed in Cushing et al. (2005) and Covey et al. (2010), we identified 27 spectral lines prominent across most of our sample for which relatively

Table 2.4. Observational properties of M dwarf common proper motion pairs

Secondary	RA ^a (hh:mm:ss)	Dec ^a (dd:mm:ss)	PM _{RA} (as/yr)	PM _{Dec} (as/yr)	Astrom. ^b (Ref.)	K _S ^c (mag)	d _{Sp} ^d (pc)	Primary	PM _{RA} ^e (as/yr)	PM _{Dec} ^e (as/yr)	d ^e (pc)
M dwarfs used to calibrate metallicity relation											
LSPM J0045+0015N	00:45:13.58	+00:15:51.0	0.207	-0.041	LS05	9.260	22	HD 4271	0.265	-0.051	41
Gl 53.1B	01:07:38.53	+22:57:20.8	0.102	-0.492	LS05	8.673	20	HD 6660	0.099	-0.492	20
G 272-119	01:54:20.96	-15:43:48.2	0.295	-0.137	Sk06/SG03	9.434	38	HD 11683	0.299	-0.137	36
LSPM J0236+0652	02:36:15.26	+06:52:18.0	1.813	1.447	LS05	6.570	6	HD 16160	1.810	1.449	7
LSPM J0255+2652W	02:55:35.78	+26:52:20.5	0.270	-0.191	LS05	8.660	20	HD 18143	0.274	-0.185	22
GJ 3195B	03:04:43.45	+61:44:09.0	0.717	-0.697	LS05	8.103	19	HD 18757	0.721	-0.693	22
J03480588+4032226	03:48:05.8	+40:32:22.6	0.049	0.022	LG11	8.450	28	HD 23596	0.054	0.021	50
Gl 166C	04:15:21.56	-07:39:21.2	-2.239	-3.419	Sk06/SG03	5.962	3	HD 26965	-2.239	-3.420	5
LSPM J0455+0440W	04:55:54.46	+04:40:16.4	0.136	-0.185	LS05	7.620	21	HD 31412	0.136	-0.185	30
LSPM J0528+1231	05:28:56.50	+12:31:53.6	0.093	-0.211	LS05	8.790	18	HD 35956	0.087	-0.216	28
LSPM J0546+0112	05:46:19.38	+01:12:47.2	-0.066	-0.148	LS05	8.800	39	HD 38529	-0.079	-0.141	42
LSPM J0617+0507	06:17:10.65	+05:07:02.3	-0.198	0.164	LS05	8.270	16	HD 43587	-0.195	0.165	19
PM I06523-0511	06:52:18.05	-05:11:24.2	-0.576	-0.011	LG11	5.723	7	HD 50281	-0.544	-0.003	8
Gl 297.2B	08:10:34.26	-13:48:51.4	-0.250	0.050	Sk06/SG03	7.418	17	HD 68146	-0.251	0.058	22
LSPM J0849+0329W	08:49:02.26	+03:29:47.1	-0.149	0.056	LS05	9.910	29	HD 75302	-0.148	0.060	29
LSPM J0852+2818	08:52:40.86	+28:18:59.0	-0.467	-0.238	LS05	7.670	11	HD 75732	-0.485	-0.234	12
Gl 376B	10:00:50.23	+31:55:45.2	-0.529 ^f	-0.429 ^f	Sk06	9.275	11	HD 86728	-0.529	-0.429	14
LSPM J1248+1204	12:48:53.45	+12:04:32.7	0.225	-0.128	LS05	10.570	36	HD 111398	0.234	-0.141	36
Gl 505B	13:16:51.54	+17:00:59.9	0.632	-0.261	LS05	5.749	10	HD 115404	0.631	-0.261	11
Gl 544B	14:19:35.83	-05:09:08.1	-0.633	-0.122	Sk06/SG03	9.592	23	HD 125455	-0.632	-0.122	20
PM II4574-2124W	14:57:26.51	-21:24:40.6	0.987	-1.667	LG11	3.802	3:	HD 131977	1.034	-1.726	5
LSPM J1535+6005E	15:35:25.69	+60:05:00.6	0.166	-0.160	LS05	8.410	15	HD 139477	0.171	-0.163	19
LSPM J1604+3909W	16:04:50.85	+39:09:36.1	-0.547	0.055	LS05	9.160	18	HD 144579	-0.572	0.052	14
PM II7052-0505	17:05:13.81	-05:05:38.7	-0.921	-1.128	LG11	5.975	8	HD 154363	-0.917	-1.138	10
J17195815-0553043A ^g	17:19:58.15 ^j	-05:53:04.5 ^j	0.049 ^j	-0.182 ^j	LS05	10.385 ^j	55:	HD 156826	0.045	-0.194	53

Table 2.4—Continued

Secondary	RA ^a (hh:mm:ss)	Dec ^a (dd:mm:ss)	PM _{RA} (as/yr)	PM _{Dec} (as/yr)	Astrom. ^b (Ref.)	K _S ^c (mag)	d _{Sp} ^d (pc)	Primary	PM _{RA} ^e (as/yr)	PM _{Dec} ^e (as/yr)	d ^e (pc)
J17195815-0553043B ^g	17:19:58.15J	-05:53:04.5J	0.049J	-0.182J	LS05	10.385J	41:	HD 156826	0.045	-0.194	53
LSPM J1800+2933NS	18:00:45.43	+29:33:56.8	-0.128	0.169	LS05	8.230	24	HD 164595	-0.139	0.173	28
PM II9321-III9	19:32:08.11	-11:19:57.3	0.237	0.026	LG11	8.706	18	HD 183870	0.235	0.018	18
Gl 768.1B	19:51:00.67	+10:24:40.1	0.240	-0.135	2MASS	8.012	15	HD 187691	0.240	-0.135	19
LSPM J2003+2951	20:03:26.58	+29:51:59.4	0.689	-0.515	LS05	8.710	14	HD 190360	0.684	-0.524	17
LSPM J2011+161IE	20:11:13.26	+16:11:08.0	-0.432	0.399	LS05	8.880	16	HD 191785	-0.413	0.398	20
LSPM J2040+1954	20:40:44.52	+19:54:03.2	0.107	0.312	LS05	7.420	12	HD 197076A	0.118	0.310	19
LSPM J2231+4509	22:31:06.51	+45:09:44.0	-0.167	0.027	LS05	9.500	37	HD 213519	-0.174	0.038	43
Gl 872B	22:46:42.34	+12:10:20.9	0.234	-0.492	LS05	7.300	14	HD 215648	0.233	-0.492	16
LSPM J2335+3100E	23:35:29.47	+31:00:58.5	0.548	0.256	LS05	8.850	24	HD 221830	0.539	0.254	32
HD 222582B	23:41:45.14	-05:58:14.8	-0.148	-0.117	Sk06/SG03	9.583	30	HD 222582	-0.145	-0.111	41
M0 dwarfs in a CPM pair not used in our metallicity calibration											
Gl 282B	07:40:02.90	-03:36:13.3	0.067	-0.286	H00	5.568	13	HD 61606	0.070	-0.278	14
LSPM J1030+5559	10:30:25.31	+55:59:56.8	-0.181	-0.034	LS05	5.360	13	HD 90839	-0.178	-0.033	12
M dwarfs in a CPM pair where the primary has a metallicity measurement from S09											
LSPM J0315+0103	03:15:00.922	+01:03:08.2	0.362	0.118	LS05	10.85	77	G 77-35	0.362	0.118	79
LSPM J1208+2147N	12:08:55.378	+21:47:31.6	-0.439	0.037	LS05	10.38	83	G 59-1	-0.397	0.036	113:
LSPM J1311+0936	13:11:22.445	+09:36:13.1	-0.517	0.269	LS05	8.86	55	G 63-5	-0.521	0.269	61
PM II6277-0104	16:27:46.699	-01:04:15.4	-0.340	-0.106	LS05	10.57	54	G 17-16	-0.347	-0.102	62:
M dwarfs in a CPM pair that may not be physically associated											
HD 46375B	06:33:12.10	+05:27:53.1	0.114	-0.097	Sk06	7.843	11	HD 46375	0.114	-0.097	33
CE 226	10:46:33.27	-24:35:11.2	-0.141 ^f	-0.109 ^f	Sk06	9.447	31	HD 93380	-0.141	-0.109	20
LP 731-76	10:58:27.99	-10:46:30.5	-0.201	-0.094	Sk06/SG03	8.640	14	BD-103166	-0.186	-0.005	25: ^h
Gl 806.1B	20:46:06.42	+33:58:06.2	0.356	0.330	MEarth	8.7: ⁱ	19:	HD 197989	0.356	0.330	22

Table 2.4—Continued

Secondary	RA ^a (hh:mm:ss)	Dec ^a (dd:mm:ss)	PM _{RA} (as/yr)	PM _{Dec} (as/yr)	Astrom. ^b (Ref.)	K _S ^c (mag)	d _{Sp} ^d (pc)	Primary	PM _{RA} ^e (as/yr)	PM _{Dec} ^e (as/yr)	d ^e (pc)
-----------	-------------------------------	--------------------------------	-----------------------------	------------------------------	--------------------------------	--------------------------------------	--------------------------------------	---------	--	---	------------------------

^aPositions are given in the International Celestial Reference System (ICRS), and have been corrected to epoch 2000.0 where necessary assuming the proper motions given in the table.

^bAstrometry references. If one reference is provided, it applies to both position and proper motion; if two are provided, the first is for position and the second for proper motion.

^cApparent K_S magnitudes are from Sk06.

^dErrors on the distance estimates are 14%.

^eProper motions and distances for primary stars are from Hipparcos (van Leeuwen 2007) except when otherwise noted.

^fFor CE 226 and Gl 376B, the Hipparcos proper motion for the primary was found to be a better match to the observed motion of the secondary from 2MASS to recent epoch MEarth imaging than the proper motion given in Ruiz et al. (2001, for CE 226) or in LSPM-North (for Gl 376B). In these cases, the Hipparcos value has been adopted in the table.

^gLépine, private communication. We resolved this object as a binary. An appended “J” indicates a measurement that was derived for the components jointly. We assume the two components contribute equally to the luminosity in order to estimate their spectroscopic distances.

^hNo parallax was available for the primary. Its distance was estimated assuming an absolute K_S magnitude of 6, typical for an early K dwarf.

ⁱNo K_S magnitude could be found for Gl 806.1B. We estimated a rough magnitude from 2MASS Atlas images using a 4 pixel aperture radius (this value was chosen to reduce contamination from nearby stars), and applied an aperture correction of 0.04 magnitudes, derived from stars of similar K magnitude elsewhere in the field.

References. — H00=Høg et al. (2000); SG03=Salim & Gould (2003); LS05=Lépine & Shara (2005); Sk06=Skrutskie et al. (2006); So09=Sozzetti et al. (2009); LG11=Lépine & Gaidos (2011)

Note. — Object names beginning with “J” are 2MASS identifiers.

Table 2.5. Measured properties of M dwarf common proper motion pairs

Secondary	SpT	EW _{Na} (Å)	EW _{Ca} (Å)	H ₂ O-K2	[Fe/H] (dex)	[Fe/H] _{prim} ^b (dex)	Ref.	RV _{sec} (km/s)	RV _{prim} (km/s)	Ref.
M dwarfs used to calibrate metallicity relation										
LSPM J0045+0015N	M4	5.24 ± 0.15	3.41 ± 0.14	0.868 ± 0.005	+0.08 ± 0.12	+0.02 ± 0.03	VF05	16 ± 5	32.5	VF05
Gl 53.B	M4	6.19 ± 0.16	3.63 ± 0.14	0.894 ± 0.005	+0.22 ± 0.12	+0.07 ± 0.12	B05	16 ± 5	7.0	Cl2
G272-II9	M3	4.13 ± 0.15	3.20 ± 0.15	0.937 ± 0.005	-0.17 ± 0.13	-0.21 ± 0.03	So06	11 ± 5	-1.2	VF05
LSPM J0236+0652	M4	3.96 ± 0.14	2.49 ± 0.17	0.866 ± 0.005	-0.22 ± 0.13	-0.12 ± 0.02	VF05	30 ± 6	26.8	VF05
LSPM J0255+2652W	M4	6.27 ± 0.17	3.83 ± 0.18	0.897 ± 0.005	+0.23 ± 0.12	+0.28 ± 0.03	VF05	33 ± 5	32.5	VF05
GJ 3195B	M3	3.90 ± 0.18	3.29 ± 0.17	0.924 ± 0.005	-0.24 ± 0.13	-0.31 ± 0.04	B05	-1 ± 5	-6.8	VF05
J03480588+4032226	M2	8.07 ± 0.15	5.76 ± 0.15	0.958 ± 0.005	+0.29 ± 0.12	+0.22 ± 0.03	VF05	0 ± 5	-10.6	VF05
Gl 166C	M5	3.99 ± 0.16	2.13 ± 0.21	0.835 ± 0.005	-0.21 ± 0.13	-0.28 ± 0.02	VF05	-37 ± 6	-42.3	VF05
...	-0.33 ± 0.06	B05
LSPM J0455+0440W	M3	5.60 ± 0.15	4.84 ± 0.20	0.965 ± 0.005	+0.15 ± 0.12	+0.05 ± 0.03	VF05	46 ± 5	47.7	VF05
LSPM J0528+1231	M4	5.16 ± 0.20	2.97 ± 0.21	0.870 ± 0.005	+0.07 ± 0.13	-0.22 ± 0.03	VF05	17 ± 5	17.3	VF05
LSPM J0546+0112	M1	7.24 ± 0.17	5.19 ± 0.20	0.982 ± 0.005	+0.30 ± 0.12	+0.45 ± 0.03	VF05	28 ± 5	30.2	VF05
...	+0.40 ± 0.06	Sa04
LSPM J0617+0507	M4	5.23 ± 0.11	3.31 ± 0.17	0.891 ± 0.005	+0.08 ± 0.12	-0.04 ± 0.03	VF05	11 ± 5	12.7	VF05
PM I06523-051I	M2	4.61 ± 0.07	4.17 ± 0.10	0.953 ± 0.005	-0.05 ± 0.12	+0.14 ± 0.03	VF05	-5 ± 5	-5.4	VF05
Gl 297.2B	M2	4.89 ± 0.23	4.15 ± 0.26	0.953 ± 0.005	+0.01 ± 0.13	-0.09 ± 0.09	B05	30 ± 5	37.7	VF05
LSPM J0849+0329W	M4	5.05 ± 0.21	3.23 ± 0.22	0.861 ± 0.005	+0.05 ± 0.13	+0.10 ± 0.03	VF05	12 ± 5	10.8	VF05
LSPM J0852+2818	M4	7.53 ± 0.19	3.60 ± 0.24	0.882 ± 0.005	+0.30 ± 0.12	+0.31 ± 0.01	VF05	31 ± 5	27.8	VF05
...	+0.33 ± 0.07	Sa04
Gl 376B	M7	6.56 ± 0.26	1.74 ± 0.24	0.776 ± 0.005	+0.26 ± 0.12	+0.20 ± 0.02	VF05	52 ± 5	56.0	M08
LSPM J1248+1204	M5	4.46 ± 0.22	2.70 ± 0.21	0.854 ± 0.005	-0.09 ± 0.13	+0.08 ± 0.03	VF05	8 ± 5	3.5	VF05
Gl 505B	M1	3.77 ± 0.08	3.84 ± 0.11	0.995 ± 0.005	-0.27 ± 0.12	-0.25 ± 0.05	B05	1 ± 5	8.5	Cl2
Gl 544B	M5	4.78 ± 0.27	2.45 ± 0.31	0.855 ± 0.005	-0.01 ± 0.13	-0.18 ± 0.03	VF05	6 ± 7	-9.5	VF05
...	-0.20 ± 0.19	B05
PM I14574+2124W	M2	5.31 ± 0.23	4.56 ± 0.22	0.981 ± 0.005	+0.10 ± 0.13	+0.12 ± 0.02	VF05	25 ± 5	26.0	VF05

Table 2.5—Continued

Secondary	SpT	EW _{Na} (Å)	EW _{Ca} (Å)	H ₂ O-K2	[Fe/H] (dex)	[Fe/H] _{prim} ^b (dex)	RV _{sec} (km/s)	RV _{prim} (km/s)	Ref.
...	+0.07 ± 0.10
LSPM J1535+6005E	M5	5.38 ± 0.08	3.94 ± 0.10	0.877 ± 0.005	+0.11 ± 0.12	+0.11 ± 0.03	-4 ± 5	-8.3	VF05
LSPM J1604+3909W	M5	3.03 ± 0.20	1.31 ± 0.16	0.849 ± 0.005	-0.52 ± 0.15	-0.69 ± 0.03	-64 ± 5	-59.0	VF05
PM II7052-0505	M3	3.27 ± 0.13	3.09 ± 0.15	0.940 ± 0.005	-0.44 ± 0.14	-0.62 ± 0.04	24 ± 6	33.6	VF05
J17195815-0553043A	M4	4.17 ± 0.52	1.86 ± 0.65	0.842 ± 0.005	-0.16 ± 0.18	-0.13 ± 0.03	-23 ± 5	-32.3	VF05
J17195815-0553043B	M5	4.02 ± 0.33	2.57 ± 0.27	0.877 ± 0.005	-0.20 ± 0.15	-0.13 ± 0.03	-25 ± 6	-32.3	VF05
LSPM J1800+2933NS	M2	4.78 ± 0.19	3.86 ± 0.18	0.949 ± 0.005	-0.01 ± 0.13	-0.06 ± 0.03	7 ± 5	2.4	VF05
PM II9321-II19	M5	4.70 ± 0.26	3.50 ± 0.25	0.880 ± 0.005	-0.03 ± 0.13	+0.05 ± 0.03	-47 ± 5	-48.3	VF05
...	-0.07 ± 0.03
Gl 768.1B	M4	5.07 ± 0.30	3.35 ± 0.27	0.896 ± 0.005	+0.05 ± 0.13	+0.16 ± 0.02	3 ± 5	1.4	VF05
...	+0.07 ± 0.12
LSPM J2003+2951	M5	5.36 ± 0.21	2.81 ± 0.15	0.847 ± 0.005	+0.10 ± 0.13	+0.21 ± 0.03	-40 ± 5	-44.8	VF05
LSPM J2011+1611E	M5	3.71 ± 0.18	1.97 ± 0.18	0.852 ± 0.005	-0.29 ± 0.13	-0.15 ± 0.03	-45 ± 5	-49.0	VF05
LSPM J2040+1954	M3	3.97 ± 0.13	3.00 ± 0.15	0.913 ± 0.005	-0.21 ± 0.12	-0.09 ± 0.03	-33 ± 5	-35.2	VF05
LSPM J2231+4509	M3	4.89 ± 0.22	3.34 ± 0.29	0.928 ± 0.005	+0.01 ± 0.13	-0.00 ± 0.03	-29 ± 5	-31.5	VF05
Gl 872B	M3	4.01 ± 0.25	3.16 ± 0.26	0.939 ± 0.005	-0.20 ± 0.14	-0.22 ± 0.01	0 ± 5	-4.5	VF05
...	-0.36 ± 0.11
LSPM J2335-3100E	M4	3.09 ± 0.15	2.42 ± 0.19	0.904 ± 0.005	-0.50 ± 0.14	-0.40 ± 0.03	-110 ± 8	-111.8	VF05
HD 222582B	M3	5.03 ± 0.17	2.97 ± 0.15	0.892 ± 0.005	+0.04 ± 0.12	-0.03 ± 0.02	21 ± 5	12.6	VF05
...	+0.05 ± 0.05
...	-0.01 ± 0.01

M0 dwarfs in a CPM pair not used in our metallicity calibration

Gl 282B	M0	3.85 ± 0.12	4.36 ± 0.12	1.044 ± 0.005	-0.25 ± 0.13	+0.07 ± 0.03	-20 ± 5	-17.6	VF05
...	+0.01 ± 0.08
LSPM J1030-5559	M0	3.56 ± 0.18	4.13 ± 0.19	1.049 ± 0.005	-0.34 ± 0.14	-0.07 ± 0.02	10 ± 5	9.4	VF05

Table 2.5—Continued

Secondary	SpT	EW _{Na} (Å)	EW _{Ca} (Å)	H ₂ O-K2	[Fe/H] (dex)	[Fe/H] _{prim} ^b (dex)	RV _{sec} (km/s)	RV _{prim} (km/s)	Ref.
	NIR								
M dwarfs in a CPM pair where the primary has a metallicity measurement from S09									
LSPM J0315-0103	M2	2.09 ± 0.21	1.98 ± 0.27	0.942 ± 0.005	-0.89 ± 0.20	-0.77	87 ± 5	88.1	L02
LSPM J1208-2147N	M2	2.54 ± 0.17	1.97 ± 0.25	0.984 ± 0.005	-0.70 ± 0.17	-1.05	-3 ± 7	-9.9	L02
LSPM J1311-0936	M0	2.90 ± 0.16	3.10 ± 0.16	1.025 ± 0.005	-0.56 ± 0.15	-0.62	27 ± 5	26.8	L02
PM I16277-0104	M3	2.98 ± 0.22	2.01 ± 0.45	0.911 ± 0.005	-0.54 ± 0.22	-0.87	-158 ± 5	-162.4	L02
M dwarfs in a CPM pair that may not to be physically associated									
HD 46375B	M1	6.62 ± 0.19	4.97 ± 0.21	0.988 ± 0.005	+0.26 ± 0.12	+0.25 ± 0.03	0 ± 5	-0.4	VF05
CE 226	M4	3.79 ± 0.17	2.17 ± 0.24	0.905 ± 0.005	-0.27 ± 0.13	-0.72 ± 0.03	-15 ± 5	46.5	VF05
LP 731-76	M5	6.04 ± 0.17	3.09 ± 0.15	0.853 ± 0.005	+0.21 ± 0.12	+0.38 ± 0.03	11 ± 5	27.2	VF05
...	+0.35 ± 0.05
Gl 806.1B	M4	3.93 ± 0.41	3.20 ± 0.48	0.895 ± 0.005	-0.23 ± 0.17	-0.05 ± 0.13	-8 ± 5	44.9	VF05

^aReference for published metallicity of the primary star. If more than one value is available, alternative values are provided in the following row(s). Values from the SPOCS catalog (VF05) are used preferentially.

References. — L02=Latham et al. (2002) Sa04=Santos et al. (2004); B05=Bonfils et al. (2005a); Sa05=Santos et al. (2005); VF05=Valenti & Fischer (2005); So06=Sousa et al. (2006); M08=Massarotti et al. (2008); So09=Sozzetti et al. (2009); C12=Chubak et al. (2012)

Note. — Object names beginning with “J” are 2MASS identifiers.

uncontaminated continuum regions could be defined. These features and the continuum regions, one on either side of each feature, are listed in Table 2.6. To measure the EW of a feature, we first mitigated the effect of finite pixel sizes by linearly interpolating each spectrum onto a ten-times oversampled wavelength grid with uniform spacing in wavelength. The continuum was estimated by linear interpolation between the median fluxes of the two continuum regions. We then applied the trapezoidal rule to numerically integrate the flux within the feature. We also measured ten spectral indices. We considered three indices quantifying the deformation in the continuum due to water absorption: the H₂O-K2 index, introduced in §2.4 (R12), the H₂O-H index (Terrien et al. 2012) and the H₂O-J index (Mann et al. 2013a). We also measured the flux ratios defined by McLean et al. (2003) and used by Cushing et al. (2005). These ratios quantify absorption in several water, FeH and CO bands. The indices we measured are summarized in Table 2.7. Finally, we considered three non-linear combinations of parameters. The non-linear combinations we considered were motivated by previous work: Luhman & Rieke (1999) suggested that $EW_{\text{Na}}/EW_{\text{CO}}$ is temperature-sensitive and R12 used the ratios $EW_{\text{Na}}/(\text{H}_2\text{O-K2})$ and $EW_{\text{Ca}}/(\text{H}_2\text{O-K2})$ to fit their metallicity relation.

We searched for the combination of three parameters that provide the best fit to metallicity, using the forms:

$$\begin{aligned}
 [\text{Fe}/\text{H}] &= A (F_1) + B (F_2) + C (F_3) + D \\
 &= A (F_1) + B (F_1)^2 + C (F_2) + D \\
 &= A (F_1) + B (F_1)^2 + C (F_1)^3 + D
 \end{aligned} \tag{2.6}$$

where F_n is the EW of one of the 27 spectral features in Table 2.6, one of the ten

Table 2.6. Spectral features searched as part of metallicity calibration

Name	Feature (μm)		Blue continuum (μm)		Red continuum (μm)		Source
Na I	0.8180	0.8205	0.8140	0.8170	0.8235	0.8290	Cushing et al. (2005) ^a
FeH	0.9895	0.9943	0.9850	0.9890	1.0150	1.0210	Cushing et al. (2005)
Na I	1.1370	1.1415	1.1270	1.1320	1.1460	1.1580	Cushing et al. (2005)
K I, Fe I	1.1682	1.1700	1.1650	1.1678	1.1710	1.1750	Cushing et al. (2005)
K I, Fe I	1.1765	1.1792	1.1710	1.1750	1.1910	1.1930	Cushing et al. (2005)
Mg I	1.1820	1.1840	1.1710	1.1750	1.1910	1.1930	Cushing et al. (2005)
Fe I	1.1880	1.1900	1.1710	1.1750	1.1910	1.1930	Cushing et al. (2005)
Fe I	1.1970	1.1985	1.1945	1.1970	1.1990	1.2130	Cushing et al. (2005)
K I	1.2425	1.2450	1.2300	1.2380	1.2550	1.2600	Cushing et al. (2005)
K I	1.2518	1.2538	1.2300	1.2380	1.2550	1.2600	Cushing et al. (2005)
Al I	1.3115	1.3165	1.3050	1.3110	1.3200	1.3250	Cushing et al. (2005)
Mg I	1.4872	1.4892	1.4790	1.4850	1.4900	1.4950	Cushing et al. (2005)
Mg I	1.5020	1.5060	1.4957	1.5002	1.5072	1.5117	Covey et al. (2010)
K I	1.5152	1.5192	1.5085	1.5125	1.5210	1.5250	Covey et al. (2010)
Mg I	1.5740	1.5780	1.5640	1.5690	1.5785	1.5815	Cushing et al. (2005)
Si I	1.5875	1.5925	1.5845	1.5875	1.5925	1.5955	Covey et al. (2010)
CO	1.6190	1.6220	1.6120	1.6150	1.6265	1.6295	Covey et al. (2010) ^b
Al I	1.6700	1.6775	1.6550	1.6650	1.6780	1.6820	Cushing et al. (2005)
Feature ^c	1.7060	1.7090	1.7025	1.7055	1.7130	1.7160	Covey et al. (2010)
Mg I	1.7095	1.7130	1.7025	1.7055	1.7130	1.7160	Covey et al. (2010) ^b
Ca I	1.9442	1.9526	1.9350	1.9420	1.9651	1.9701	Cushing et al. (2005)
Ca I	1.9755	1.9885	1.9651	1.9701	1.9952	2.0003	Covey et al. (2010)
Br- γ	2.1650	2.1675	2.1550	2.1600	2.1710	2.1740	Cushing et al. (2005)
Na I	2.2040	2.2110	2.1930	2.1970	2.2140	2.2200	Covey et al. (2010)
Ca I	2.2605	2.2675	2.2557	2.2603	2.2678	2.2722	Covey et al. (2010)
CO	2.2925	2.3150	2.2845	2.2915	2.3165	2.3205	Covey et al. (2010)
CO	2.3440	2.3470	2.3410	2.3440	2.3475	2.3505	Covey et al. (2010)

^aAtomic features were identified in Cushing et al. (2005), but feature and continuum windows were defined based on our observations.

^bFeature and continuum windows were modified from those defined in Covey et al. (2010).

^cAtomic feature not identified.

Table 2.7. Spectral indices searched as part of metallicity calibration

Name	Absorption band	Definition	Source
H ₂ O- <i>J</i>	<i>J</i> -band water deformation	$\frac{\langle 1.210-1.230 \rangle / \langle 1.313-1.333 \rangle}{\langle 1.313-1.333 \rangle / \langle 1.331-1.351 \rangle}$	Mann et al. (2013a)
H ₂ O- <i>H</i>	<i>H</i> -band water deformation	$\frac{\langle 1.595-1.615 \rangle / \langle 1.680-1.700 \rangle}{\langle 1.680-1.700 \rangle / \langle 1.760-1.780 \rangle}$	Terrien et al. (2012)
H ₂ O-K2	<i>K</i> -band water deformation	$\frac{\langle 2.070-2.090 \rangle / \langle 2.235-2.255 \rangle}{\langle 2.235-2.255 \rangle / \langle 2.360-2.380 \rangle}$	Rojas-Ayala et al. (2012)
H ₂ OA	1.35 μ m H ₂ O band	$\langle 1.341 - 1.345 \rangle / \langle 1.311 - 1.315 \rangle$	McLean et al. (2003)
H ₂ OB	1.4 μ m H ₂ O band	$\langle 1.454 - 1.458 \rangle / \langle 1.568 - 1.472 \rangle$	McLean et al. (2003)
H ₂ OC	1.7 μ m H ₂ O band	$\langle 1.786 - 1.790 \rangle / \langle 1.720 - 1.724 \rangle$	McLean et al. (2003)
H ₂ OD	2.0 μ m H ₂ O band	$\langle 1.962 - 1.966 \rangle / \langle 2.073 - 2.077 \rangle$	McLean et al. (2003)
CO	2.29 μ m ¹² CO 2-0 band	$\langle 2.298 - 2.302 \rangle / \langle 2.283 - 2.287 \rangle$	McLean et al. (2003)
<i>J</i> -FeH	1.17 μ m FeH 0-1 band	$\langle 1.198 - 1.202 \rangle / \langle 1.183 - 1.187 \rangle$	McLean et al. (2003)
γ -FeH	0.99 μ m FeH 0-0 band	$\langle 0.990 - 0.994 \rangle / \langle 0.984 - 0.988 \rangle$	McLean et al. (2003)

Note. — Angle brackets denote the median of the wavelength range indicated. All wavelengths are in microns.

indices in Table 2.7, or one of the three non-linear combinations of parameters described above. We used the RMSE as a diagnostic to identify the best potential metallicity relations.

There were a multitude of relations with $\text{RMSE} < 0.14$ dex, of which the majority included the EW of the Na I line at $2.2\mu\text{m}$ as the primary indicator of metallicity (sometimes appearing as $\text{EW}_{\text{Na}}/\text{EW}_{\text{CO}}$ or $\text{EW}_{\text{Na}}/(\text{H}_2\text{O-K2})$) and included a quadratic term. However, we preferred the two-parameter fit $[\text{Fe}/\text{H}] = A(\text{EW}_{\text{Na}}) + B(\text{EW}_{\text{Na}})^2 + C$ because it uses one fewer parameter. Motivated by the clear trend with metallicity seen in EW_{Na} , we also considered functional forms other than a quadratic, including a spline. No other forms tested resulted in a statistically superior fit. We show our result in Figure 2.11.

In performing our final fit, we did not include the two K7/M0V stars. In Figure 2.11 these are evident as having an EW_{Na} lower than other calibrators of similar metallicity. As discussed in §2.6.4, we attempted to find a metallicity relation that was valid through these early spectral types, but did not converge on a suitable result. Our final calibration sample therefore includes 36 M dwarfs with spectral types M1V and later. We address this choice in detail in the following section.

Expressing EWs in \AA , our best fit is given by:

$$[\text{Fe}/\text{H}] = -1.96 \text{ dex} + 0.596 \text{ dex} (\text{EW}_{\text{Na}}) - 0.0392 \text{ dex} (\text{EW}_{\text{Na}})^2 \quad (2.7)$$

It is calibrated for EW_{Na} between 3 and 7.5 \AA , corresponding to metallicities of $-0.6 < [\text{Fe}/\text{H}] < 0.3$ dex, and for NIR spectral types from M1V to M5V. There are indications that EW_{Na} begins to saturate for $[\text{Fe}/\text{H}] > 0.3$ dex and our best fit

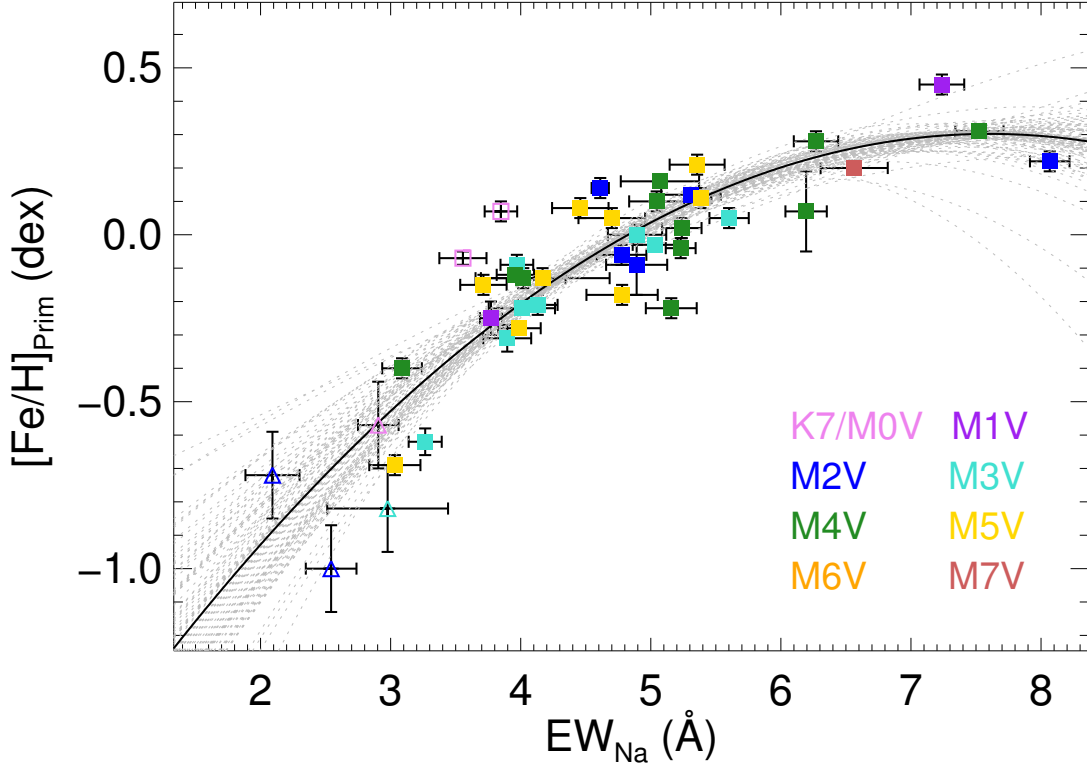


Figure 2.11.— Our best-fitting empirical metallicity relation (solid black line). We used a quadratic to relate the EW of the Na I line at $2.2\mu\text{m}$ to the $[\text{Fe}/\text{H}]$ of an M dwarf. Our relation was calibrated against 36 M dwarfs in wide binaries with an FGK star of known metallicity. The NIR spectral type of each star is indicated by its color. The two K7/M0V stars that were not included in the calibration sample are plotted as open squares. We show an additional four M dwarfs for which the primary star has a metallicity measurement from Sozzetti et al. (2009) as open triangles; we used these stars to validate extrapolation of our relation to lower metallicities. Also shown (as dashed grey lines) are the best fits for 100 bootstrap samples.

becomes multivalued for $EW_{\text{Na}} > 7.5 \text{ \AA}$, so the calibration cannot be extrapolated past this point. The four M dwarfs for which the primary star has a metallicity measured by Sozzetti et al. (2009) objects indicate that our relation appears to be valid when extrapolated to $EW_{\text{Na}} = 2 \text{ \AA}$, corresponding to $[\text{Fe}/\text{H}] = -1.0 \text{ dex}$. In §2.6.5 we confirm the validity of the relation for later NIR spectral types by comparing metallicities estimated for members of CPM M-dwarf multiples with a range of spectral types. While there is only one calibrator later than M5, this object also indicates that the relation can be extrapolated as late as M7.

We estimated the error introduced by our limited number of calibrators by bootstrapping. We randomly selected 36 of our calibrators, allowing repeats, and re-fit our metallicity relation. The standard deviation of the difference between the best fitting metallicities of the M dwarf secondaries and the metallicities of the primaries, averaged over 100 bootstrap samples, was $0.12 \pm 0.01 \text{ dex}$. The correlation coefficient, R_{ap}^2 is often used to evaluate the goodness of fit. The correlation coefficient indicates how well the fit explains the variance present in the data and is given by:

$$R_{ap}^2 = 1 - \frac{(n-1) \sum (y_{i,model} - y_i)^2}{(n-p) \sum (y_i - \bar{y})^2} \quad (2.8)$$

where n is the number of data points and p is the number of parameters. The R_{ap}^2 value for our fit is 0.78 ± 0.07 . The best-fitting metallicities for our calibrators are included in Table 2.5. The errors on metallicity include the errors on EW_{Na} , bootstrap errors and the scatter in our best fit, added in quadrature. We took the bootstrap errors to be the 1σ confidence interval on the resulting metallicities when considering the best fits from 100 bootstrap samples. The intrinsic scatter in the relation (0.12 dex) dominates for all but the lowest metallicity stars.

The scatter in our metallicity relation is similar to those reported by R10, R12, Terrien et al. (2012) and Mann et al. (2013a) despite differences in sample size, lending support to the idea that the scatter is astrophysical in origin. We consider potential temperature and surface gravity effects in §2.6.4. One possibility is variations between the Na I abundance and $[\text{Fe}/\text{H}]$ of the primary solar-type star. We considered whether an M dwarf's EW_{Na} is a better tracer of its primary star's Na I abundance than its Fe abundance. 32 of our calibrators have measured abundances for Na I from VF05. We related the spectral features and indices in Tables 2.6 and 2.7 to the Na I abundance of the primary star. We found several suitable tracers; however, none reduced the scatter.

In Table 2.1, we include the EWs of the Na line at $2.20\mu\text{m}$ and the Ca line at $2.26\mu\text{m}$, the $\text{H}_2\text{O-K2}$ index, our inferred $[\text{Fe}/\text{H}]$, and their associated errors for each of our targets. The corresponding values for the FGK-M CPM pairs can be found in Table 2.5.

2.6.4 Influence of effective temperature and surface gravity on the metallicity calibration

We examine the potential influence of differences in the effective temperature and surface gravity on the metallicity calibration presented in §2.6.3 by computing EW_{Na} for a grid of BT-Settl theoretical spectra for spectral types K5V-M7V, shown in Figure 2.12 (Allard et al. 2011, the behavior of NIR lines in theoretical spectra are discussed in some detail in R12). The spectral type range corresponds to approximately K5V-M6.5V, depending on the adopted temperature scale (we quote the temperature

scale from E. Mamajek, which is available online.²). The BT-Settl theoretical spectra show EW_{Na} varying by 1 Å between M0V and M8V stars (Figure 2.12). We also note that in our *K*-band SpeX spectral sequence (Figure 2.4) the Na I line at $2.2\mu m$ is broader for the latest spectral types.

We plot in Figure 2.13 the median EW_{Na} for each NIR spectral type as a function of H_2O-K_2 , for two subsamples. Our "nearby sample" (§2.2.2) formed the first, and kinematically young stars ($V_{tot} < 50 km/s$) formed the second. We selected the nearby sample to approximate a volume limited sample, which is unlikely to be influenced by selection effects that may exist in the rotation sample. We selected the kinematically young sample in order to isolate stars that are expected to be of similar age and metallicity. We found a similar increase in the median EW_{Na} of mid to late M dwarfs as we noted in the theoretical spectra. This could introduce a systematic error of 0.1 dex in the metallicities of early M dwarfs relative to mid M dwarfs. However, we are uncertain of the origin of this effect, given the differing behavior of our two subsamples and the relative differences in the number of early and late type stars (there are 23 stars with NIR spectral types M0V-M2V and 231 with spectral types M4V-M5V across the two subsamples).

We considered whether an alternative parameterization could account for this potential bias. We show the residuals for our chosen parameterization and three alternatives, including the parameterization from R12, in Figure 2.14. In Figure 2.15, we show the effect that the alternative calibrations have on the metallicities of the sample as a whole. With the R12 parameterization, the inferred metallicities

²http://www.pas.rochester.edu/~mamajek/EEM_dwarf_UBVIJHK_colors_Teff.dat

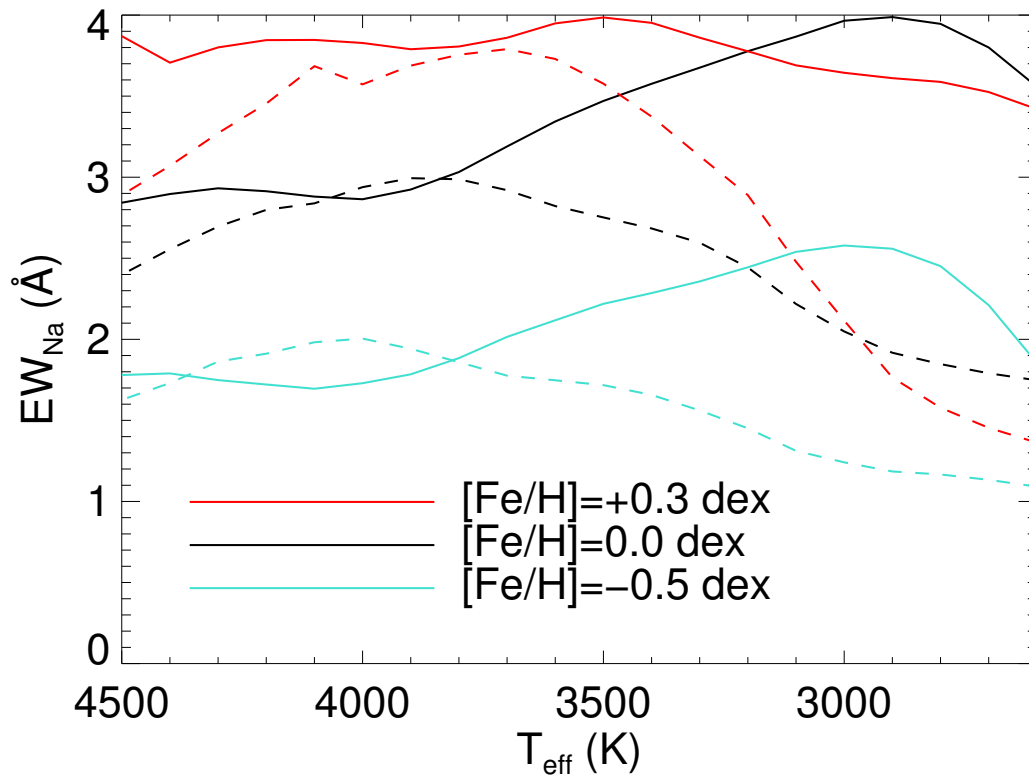


Figure 2.12.— The behavior of the Na I line at $2.2\mu\text{m}$ in the BT-Settl stellar models Al-lard et al. (2011). The horizontal axis is model effective temperature, approximately cor-responding the spectral type range K5V-M6.5V. The vertical axis shows measure EW_{Na} in \AA . Dashed lines indicate theoretical spectra with $\log g = 4$ and solid lines those with $\log g = 5$.

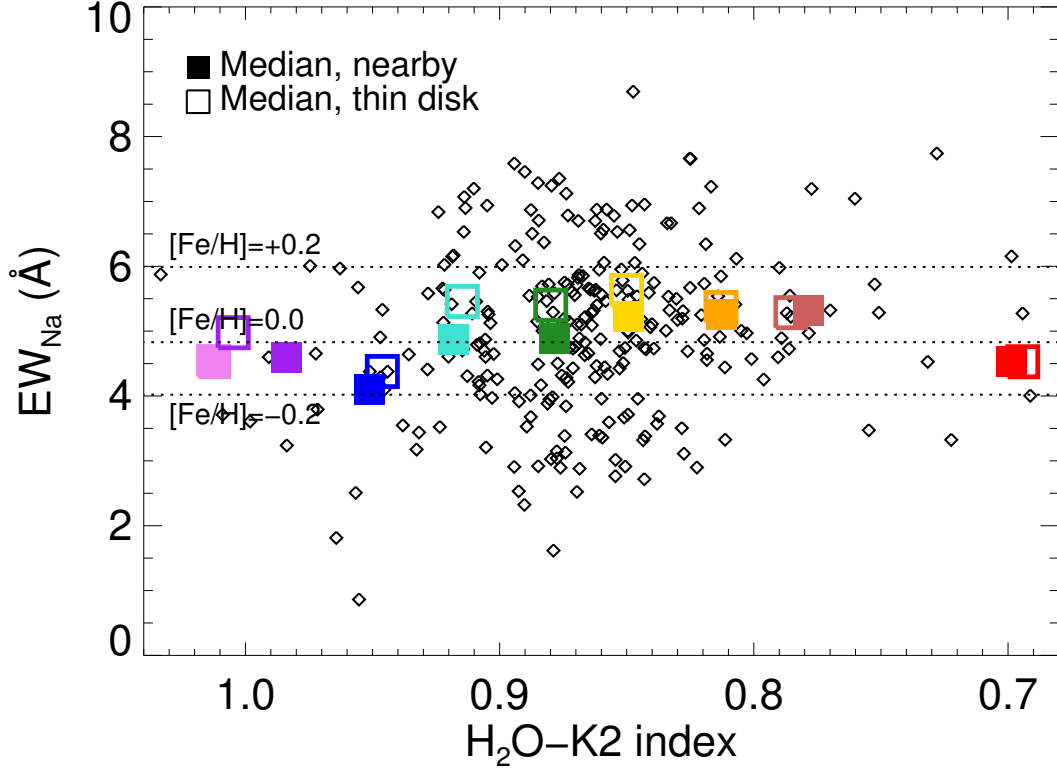


Figure 2.13.— The behavior of EW_{Na} in our observed spectra. We plot the median EW_{Na} against the median H_2O-K2 for each NIR spectral type as shown in Figure 2.11. The medians for two subsamples are shown. Filled squares include only those stars which are in our nearby sample and open squares include only kinematically young stars. Points are colored by their NIR spectral type, from purple for M0V stars to red for M8V stars, as shown in Figure 2.11.

of the latest stars decreased by 0.1 dex and metallicities were consistent across spectral types. However, the metallicities of M5 were lowered relative to those of M4 dwarfs, the spectral range across which our relation is best calibrated. Furthermore, the fit is unconstrained at the latest spectral types where the choice of the R12 parameterization makes the most difference. Including the EW of magnesium or the H₂O-K2 as a third parameter in the metallicity calibration improves the fit for the two K7/M0V calibrators and has only a marginal effect at other spectral types. However, only scatter *above* the best fit plotted in Figure 2.11 was reduced in this case, while the scatter *below* our best fit remained.

When the M0V calibrators were not included in the fit, the addition of these extra parameters makes little difference. Therefore, rather than including an additional parameter to fit these two points at the far end of our spectral type range, we simply limit our calibration to a range of spectral types which appear to be well-fit by a relation depending solely on Na I.

The insensitivity of NIR spectral types to late K dwarfs may be partially responsible for the behavior seen in our two M0V calibrators. The optical spectral type of PM I07400–0336 places it as K6.5V dwarf (Poveda et al. 2009) and LSPM J1030+5559 has been identified previously as a K7V dwarf (Garcia 1989). However, theoretical models indicate that the EW_{Na} should remain constant between late M and mid K dwarfs (with slight dependence on surface gravity), and Mann et al. (2013a) reported a metallicity calibration that is valid from K5V-M5V.

Surface gravity remains one possible explanation for the K7/M0V discrepancy and has yet to be explored in the context of empirical calibrations. Luhman et al.

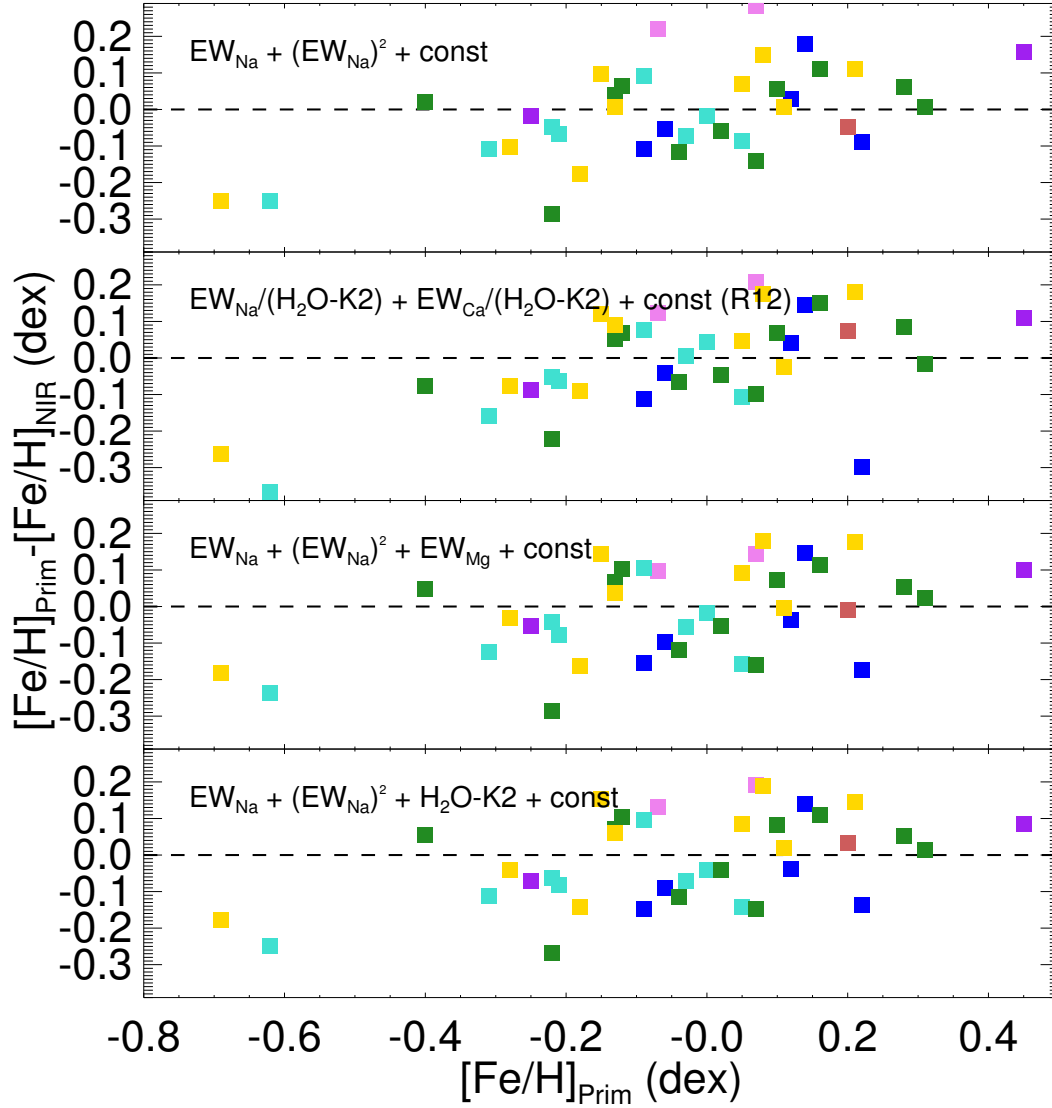


Figure 2.14.— The residuals for the best-fitting metallicity relations for four different parameterizations. We include the K7/M0V calibrators in this analysis. Points are colored by their NIR spectral type, from purple for M0V stars to light red for M7V stars, as shown in Figure 2.11.

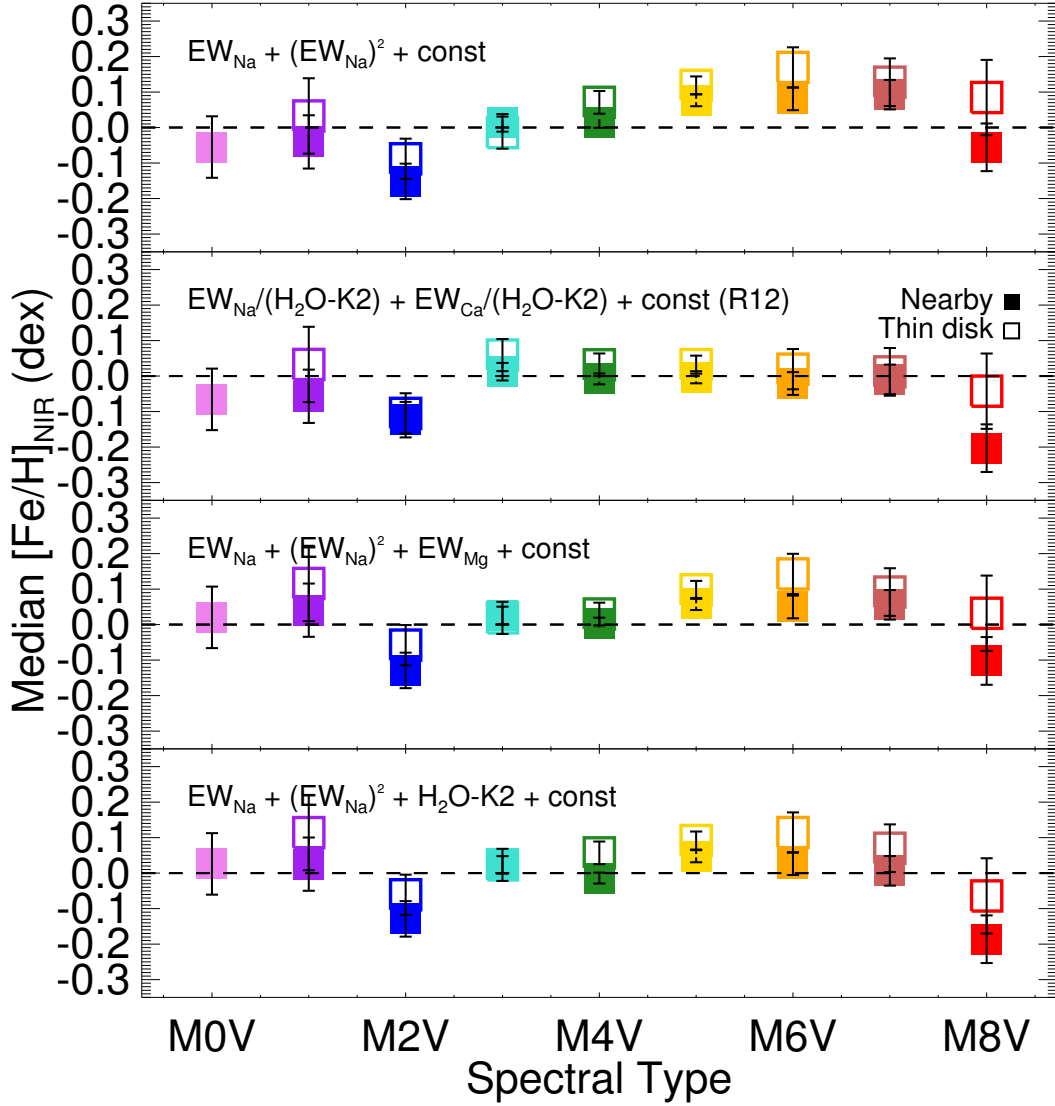


Figure 2.15.— The median metallicity for two subsamples of stars as a function of NIR spectral type. Filled squares indicate median metallicities for stars without measured rotation periods and open squares indicate the median metallicities for kinematically young stars. Points are colored by their NIR spectral type, from purple for M0V stars to red for M8V stars, as shown in Figure 2.11.

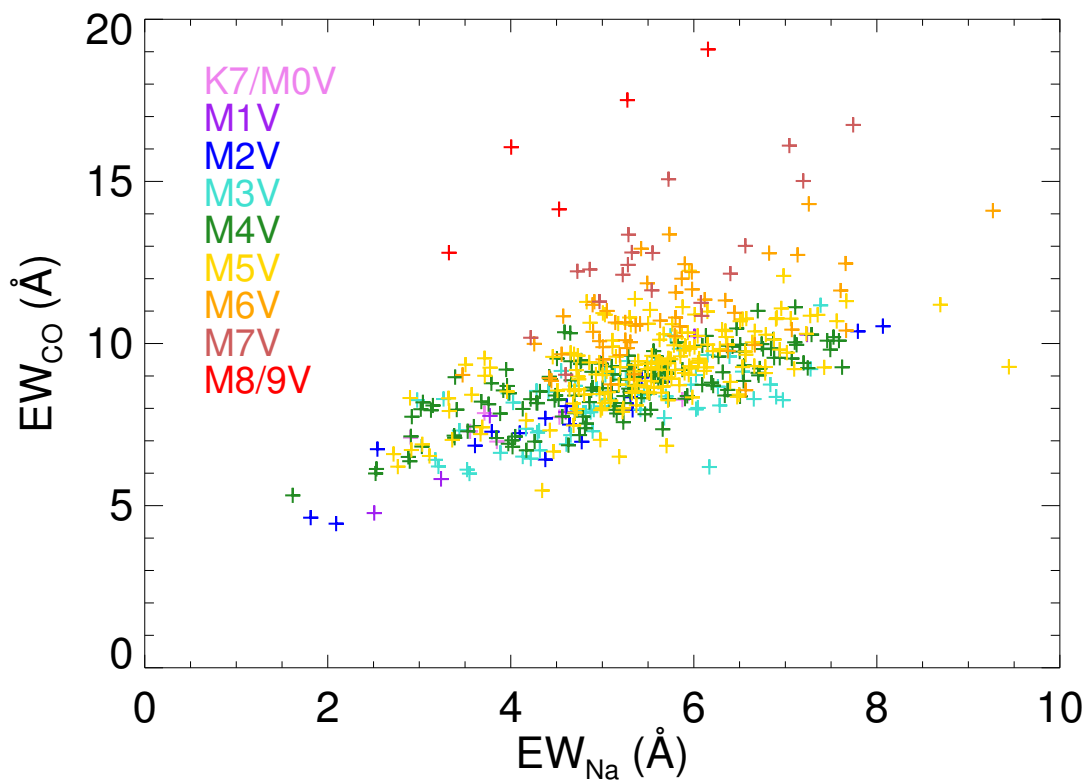


Figure 2.16.— We compare EW_{Na} against EW_{CO} for all stars in our sample. According to Luhman et al. (1998), very young stars would reveal themselves through low EW_{Na} but high EW_{CO} . We have no data in the upper left corner of this plot, indicating it is likely that no very young stars are present in our data.

(1998) demonstrated that in the low surface gravity environments of very young stars, Na I may appear abnormally weak. It is therefore possible that an M dwarf with an age of several Myr could be masquerading as a metal-poor object. The CO band head is sensitive to gravity in the opposite manner and is therefore a useful indicator of youth (Luhman et al. 1998). In Figure 2.16, we plot EW_{Na} against EW_{CO} for all stars in our sample. We found a general positive correlation and spectral dependence, but no object stood apart as having low EW_{Na} but high EW_{CO} . This is not surprising as it is unlikely that we would find a new, bright young star within 25pc.

We considered the potential for other systematics by comparing the difference between our best fitting metallicities and the metallicities of the primaries to the EWs of all other indices. In all cases, we found no significant systematic effects.

2.6.5 Tests of our metallicity relation

As a test of our metallicity calibration, we compared the metallicities we estimated for the components of M dwarf-M dwarf CPM pairs. We have observed 22 such pairs. 11 were placed on the slit together and so share observing conditions, while 11 were observed separately but close in time. In both cases, the two stars were reduced with the same telluric standard. In Figure 2.17 we show the results of this comparison. The mean metallicity difference between the primary and secondary components is -0.01 dex with a standard deviation of 0.05 dex. This is less than the uncertainty of our metallicity measurement by a significant amount, lending support to the idea that most of the scatter in the metallicity relation is astrophysical in origin, as mentioned

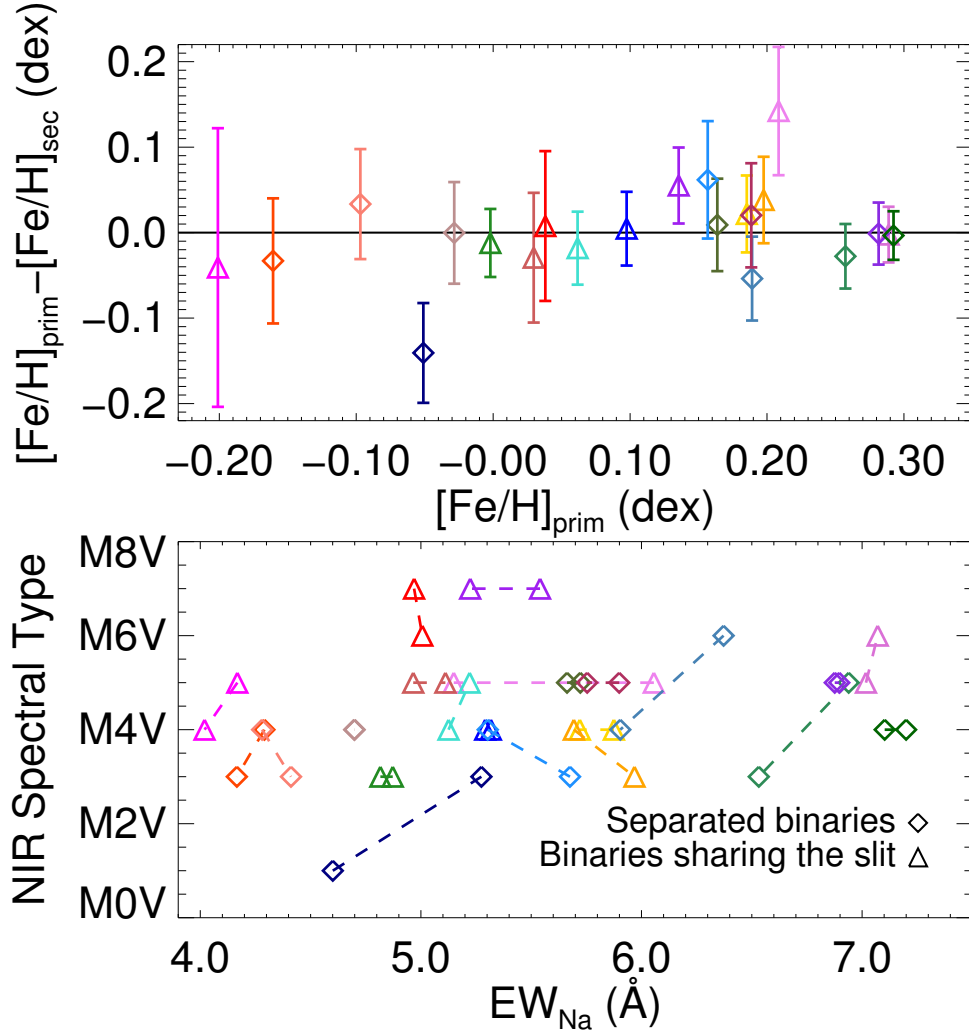


Figure 2.17.— We compare measurements of M dwarf-M dwarf CPM pairs. In the top panel, we plot the $[\text{Fe}/\text{H}]$ difference against the metallicity of the earlier M dwarf in the pair. The mean $[\text{Fe}/\text{H}]$ difference between pairs is -0.01 dex and the standard deviation is 0.05 dex. In the bottom panel, we compare EW_{Na} measurements and spectral types of the binaries. Points are color-coded such that a pair has the same color in the top and bottom panels.

in §2.6.3.

We also compared EW_{Na} measurements for stars that were observed on more than one occasion in Figure 2.1 (see §2.4). We found that our EW_{Na} measurements were consistent even for observations taken in very different conditions and separated in time by months or more. The mean EW_{Na} difference between the observation we elected to keep and the observation we discarded was -0.01 dex with a standard deviation of 0.04 dex.

2.6.6 Inclusion of previous metallicity estimates

R12 published their measurements of EW_{Na} , EW_{Ca} and $[\text{Fe}/\text{H}]$ for 133 M dwarfs using the TripleSpec instrument on Palomar (Herter et al. 2008). To facilitate joint use of our observations and those from R12, we determined the relationship between TripleSpec and SpeX EWs. We compare our EW_{Na} measurements directly in Figure 2.18. We used the following relation to convert from TripleSpec to IRTF EW_{Na} :

$$EW_{\text{Na},\text{N13}} = 0.036 + 0.90 (EW_{\text{Na},\text{R12}}) \quad (2.9)$$

Similarly for the Ca line at $2.26\mu\text{m}$:

$$EW_{\text{Ca},\text{N13}} = 0.22 + 0.88 (EW_{\text{Ca},\text{R12}}) \quad (2.10)$$

We also directly compared our metallicity estimates for the 28 stars in common (excluding metallicity calibrators). As seen in Figure 2.18, the metallicity measurements agreed well for sub-solar metallicities, but for metallicities above solar, the relation in this work gives higher metallicities for late M dwarfs (M5V-M7V).

The difference between our inferred metallicity and that from R12 is 0.0 ± 0.07 dex for M1V-M4V stars and 0.08 ± 0.05 for M5V-M7V stars. This difference is consistent with the effects discussed in §2.6.4, but we note that our relation is most strongly constrained for M4 and M5 dwarfs.

The objects observed by R12 are listed in Table 2.2. We have included EWs updated using Equations 2.9 and 2.10. After applying our EW_{Na} relationship, we can directly compute the metallicities for stars published in R12 using our metallicity calibration. We also present these updated metallicities in Table 2.2.

2.7 Photometric metallicity calibrations

We exploited our sample of M dwarfs with spectroscopically determined NIR metallicities to identify which color-color diagrams are metallicity sensitive and to derive an empirical relationship between an M dwarf's NIR color and its metallicity. In Figure 2.19, we plot JHK_S color-color diagrams for the 444 of our targets with the highest quality 2MASS magnitudes (Skrutskie et al. 2006, `qual_flag=AAA`). The metallicity dependence of these colors was established in Leggett (1992). We also plot the Bessell & Brett (1988) M dwarf main sequence, which coincides with our solar metallicity stars. These diagrams are plotted in the 2MASS photometric system; we used the color transformations updated³ from Carpenter (2001) to transform the colors from Bessell & Brett (1988) to the 2MASS system.

All color combinations discriminated effectively between low and high

³<http://www.astro.caltech.edu/jmc/2mass/v3/transformations/>

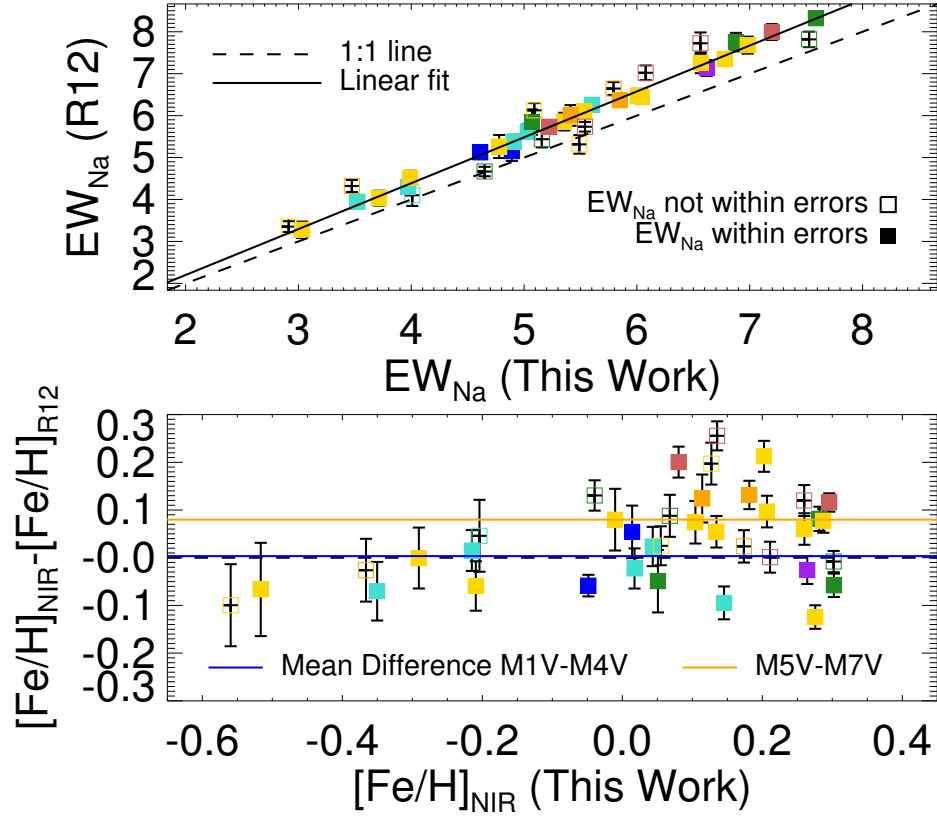


Figure 2.18.— Comparison between our measurements and those from R12. In the top panel, we compare EW_{Na} measured in this work using the SpeX instrument on IRTF to those presented in R12, who used the TripleSpec instrument on Palomar. We show the one-to-one line (dashed line) and our best fit (solid line). In the bottom panel, we compare $[Fe/H]$ estimated in this work directly to that estimated by R12. We over plot the mean metallicity difference for an early subsample (NIR spectral types M1V-M4V) and a late subsample (M5V-M7V). Data are plotted as filled squares if our EW_{Na} measurements agree within the errors and as open squares if the discrepancy is larger than the associated error. In both panels, data are colored by their NIR spectral type, from purple for M0V stars to red for M8V stars, as shown in Figure 2.11.

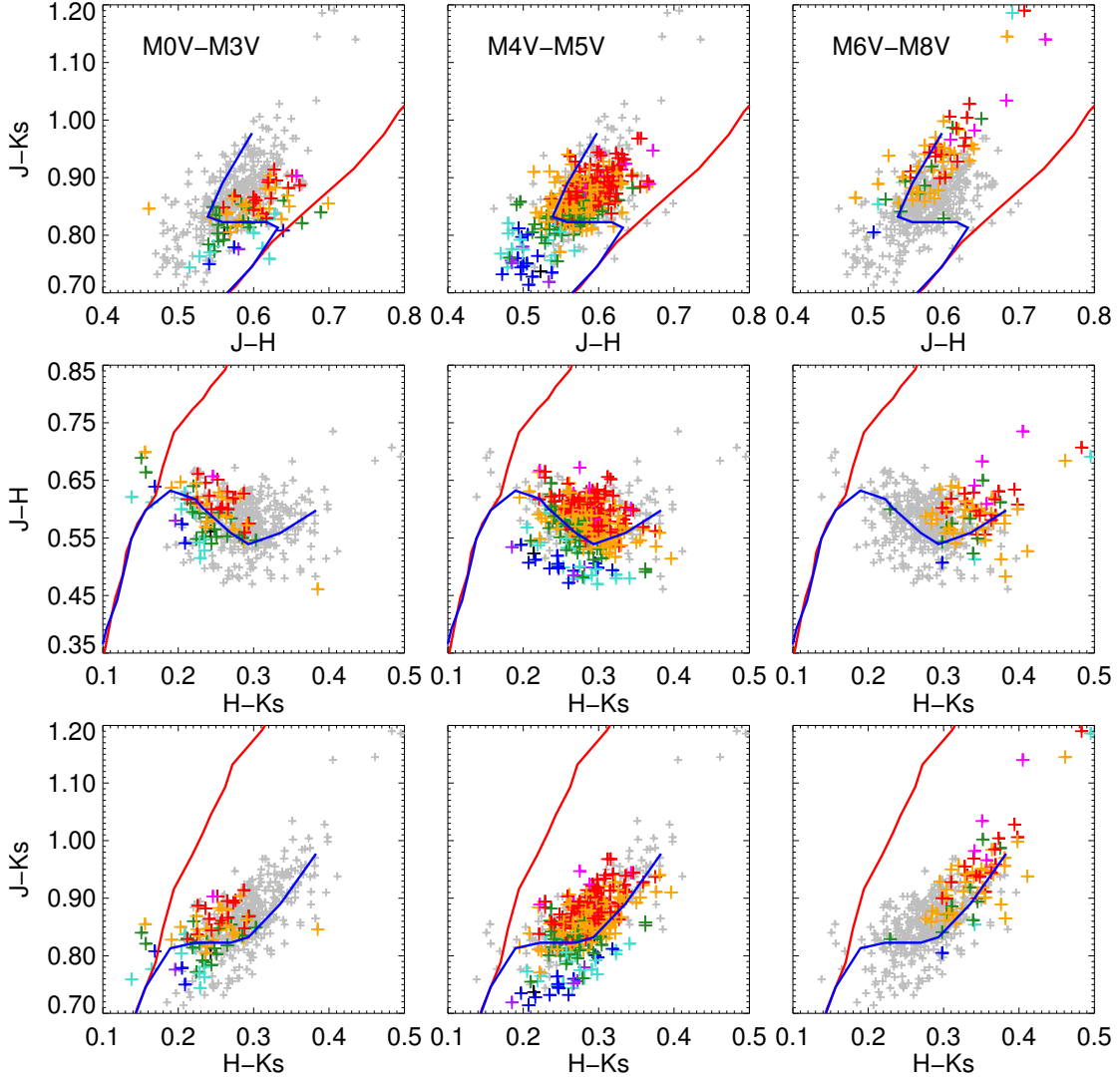


Figure 2.19.— Color-color diagrams for M dwarfs observed with IRTF. Stars are colored by the metallicity we estimated from the NIR. Stars with $EW_{Na} < 2 \text{ \AA}$ are plotted in black. Those with $-1.0 < [Fe/H] < -0.6$ are in purple, with $-0.6 < [Fe/H] < -0.4$ in blue, with $-0.4 < [Fe/H] < -0.2$ in cyan, with $-0.2 < [Fe/H] < 0.0$ in green, with $0.0 < [Fe/H] < +0.2$ in orange, and with $+0.2 < [Fe/H] < +0.3$ in red. Stars with $EW_{Na} > 7.5 \text{ \AA}$ are plotted in magenta. Grey points are stars of other spectral types other than the range indicated in the top panels. Overplotted are the dwarf (blue) and giant (red) tracks from Bessell & Brett (1988), converted to the 2MASS system using the updated color transformations of Carpenter (2001), which are available online.

metallicity stars. Consistent with Johnson et al. (2012), we found that the $J - K_S$ color of an M dwarf is the best single-color diagnostic of its metallicity. We used the vertical ($J - K_S$) distance from the $J - K_S$, $H - K_S$ Bessell & Brett dwarf main sequence (D_{MS}) as the diagnostic for the metallicity of an M dwarf. We considered using D_{MS} to determine both EW_{Na} and $[Fe/H]$ directly (Figure 2.20). We chose to relate D_{MS} to EW_{Na} because the correspondence is linear and because it relates two directly measured quantities.

We determined the relation between EW_{Na} and D_{MS} using those stars with $2.5 < EW_{Na} < 7.5 \text{ \AA}$ and $|D_{MS}| < 0.1$. We binned the data into 0.5 \AA -wide bins and computed the median D_{MS} in each. We then fit a straight line through these points, using the reciprocal square root of the number of data points in each bin as the weights. The best-fitting relation between EW_{Na} (in \AA) and D_{MS} , shown in Figure 2.20 is:

$$EW_{Na} = 4.97 + 31.3 (D_{MS}/\text{mag}) \quad (2.11)$$

The standard deviation is 2.0 \AA and the R_{ap}^2 value is 0.92. We applied Equation 2.7 in order to write metallicity (in dex) as a function of D_{MS} :

$$[Fe/H] = 0.0299 + 6.47 (D_{MS}/\text{mag}) - 38.4 (D_{MS}/\text{mag})^2 \quad (2.12)$$

We show the resulting photometric metallicity calibration in Figure 2.21.

Our calibration is valid from $2.5 < EW_{Na} < 7.5 \text{ \AA}$, corresponding to $-0.7 < [Fe/H] < 0.3$ and for $0.2 < H - K_S < 0.35$. The 1σ uncertainty in EW_{Na} translates to 0.1 dex for $EW_{Na} = 7 \text{ \AA}$ and 0.5 dex for $EW_{Na} = 3 \text{ \AA}$. This calibration is particularly useful because it does not require V magnitudes, which are often

unreliable, or parallaxes, which are often unavailable. In contrast, accurate JHK_S magnitudes are available for the majority of nearby M dwarfs from 2MASS.

2.8 Radial velocities from NIR spectroscopy

Absolute wavelength calibration for moderate resolution NIR spectra are typically determined using a lamp spectrum taken at the same pointing as the science spectrum, as done by Burgasser et al. (2007), who measured the radial velocity of an L dwarf binary to 18 km/s accuracy using SpeX ($R \approx 2000$). An alternative is to take deep sky exposures and use OH emission lines to perform wavelength calibration. This approach was used, for example, by Muirhead et al. (2013), who use the TripleSpec instrument on Palomar ($R \approx 2700$) to measure absolute radial velocities for the eclipsing post common envelope binary KOI-256 with typical errors of 4 km/s.

We acquired Thorium-Argon spectra regularly throughout the night to track instrumental variations, but it was not possible to obtain them at every telescope position due to the exposure times required. We found that this procedure was not adequate for accurate radial velocity work. We therefore used telluric absorption features to supplement the wavelength calibration by adjusting the velocity zero-points for individual observations, then cross-correlated each spectrum with a standard spectrum to measure its absolute RV (§2.8.1). In §2.8.2, we discuss using precisely measured RVs from Chubak et al. (2012) to investigate random and systematic error. We describe further tests of our method in §2.8.3.

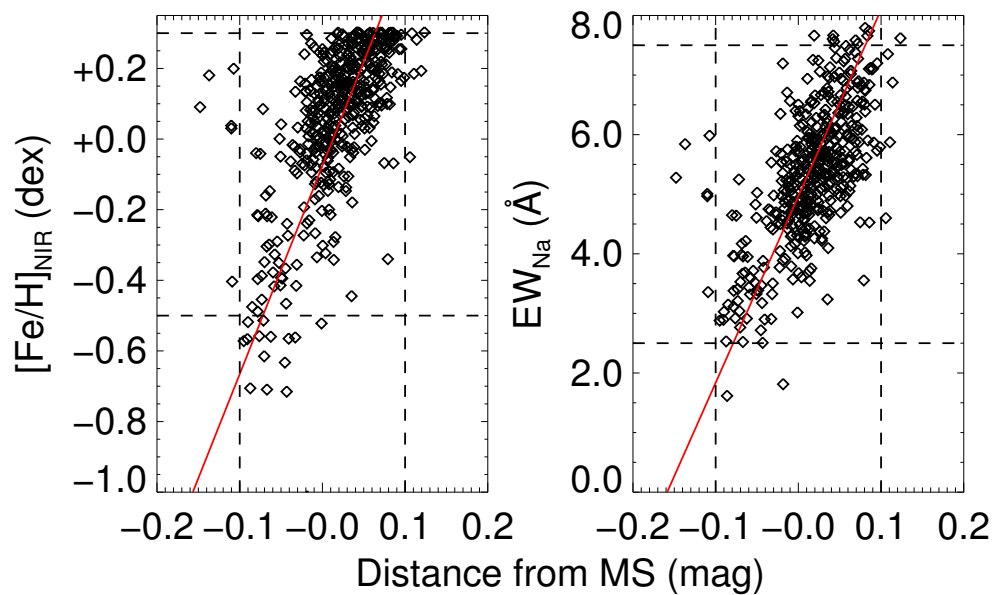


Figure 2.20.— Metallicity (as measured from the NIR; left) and EW_{Na} (right) plotted against distance from the Bessell & Brett main sequence. Our best-fit calibration for an M dwarf’s metallicity or EW_{Na} as a function of the distance from the main sequence is over plotted in red. The range over which the calibration is valid is included as dashed vertical lines.

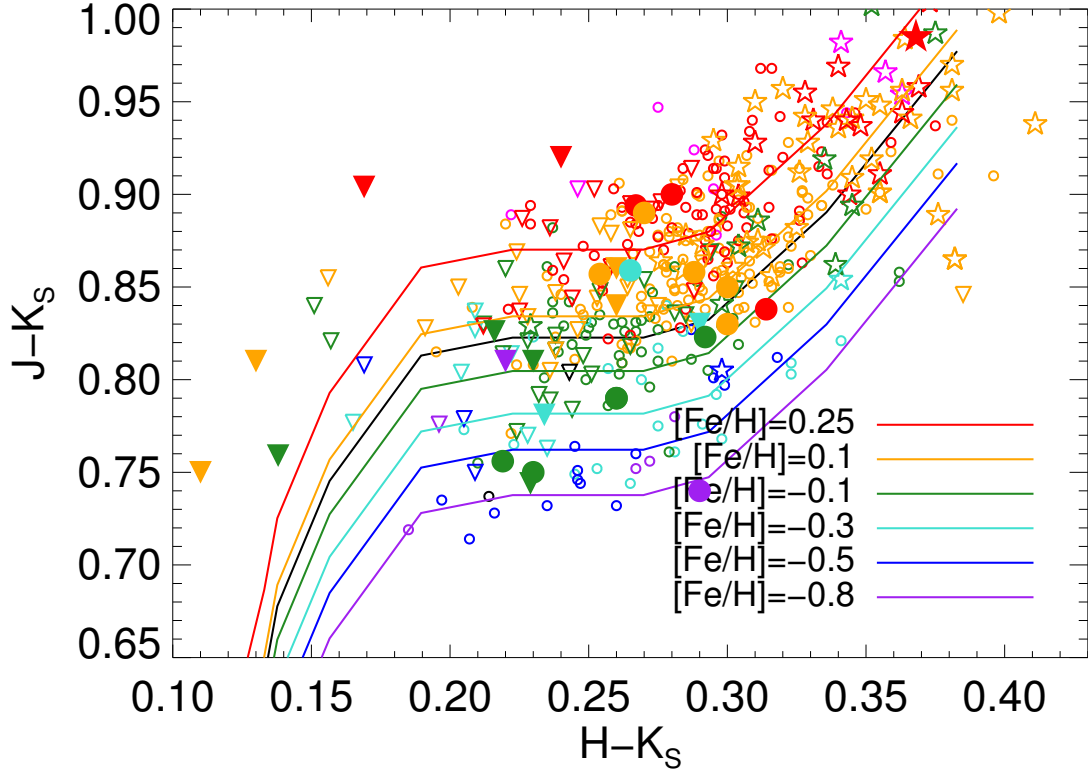


Figure 2.21.— Reproduction of the $J - K_S$, $H - K_S$ color-color diagram for all M dwarfs observed with IRTF. Stars are colored as in Figure 2.19, while symbols indicate NIR spectral type (K7V-M3V as triangles, M4V-M5V as circles, and M6V-M9V as stars). Large filled symbols are our metallicity calibrators. Overplotted are isometallicity contours for our best fit, which relate distance from the main sequence to metallicity via EW_{Na} .

2.8.1 Radial velocity method

Atmospheric absorption features present in our data provided a natural replacement to arc spectra. By correlating the telluric lines in our spectra with a theoretical atmospheric transmission spectrum (hereafter called simply the "transmission spectrum"), we determined the absolute wavelength calibration. The SpeXtool package includes a transmission spectrum created using ATRANS (Lord 1992). This spectrum was created using environmental parameters typical of Mauna Kea and an airmass of 1.2 and has a resolution five times that of SpeX. We used the wavelength calibration determined by SpeX using ThAr arc spectra as our initial wavelength guess for the nontelluric corrected science spectrum. From this wavelength solution, we created a wavelength vector that was oversampled by a factor of six and linearly spaced in wavelength.

We found that excellent continuum removal was required for the wavelength calibration to be determined through direct cross correlation of the science spectrum and the transmission spectrum. However, the large atmospheric features made this difficult. Instead of attempting to remove the continuum from the M dwarf and subsequently finding the offset between the stellar spectrum and the atmospheric spectrum, we tackled these problems simultaneously. We did this by finding the modifications to the transmission spectra that provided the best match the telluric features observed in the science spectrum. There were three differences between the theoretical transmission spectrum and the telluric features as observed in the science spectrum: the continuum, the strength of the telluric features and the pixel offset between the spectra.

CHAPTER 2. A NIR SPECTROSCOPIC SURVEY OF M DWARFS

The first parameter of our model was a Legendre polynomial as a function of pixel by which the transmission spectrum was multiplied in order to replicate the shape of the spectrum. The curvature of the spectrum was affected by both instrumental effects and the M dwarf spectral energy distribution. We used a 3rd or 4th degree Legendre polynomial and fit for the coefficients. We selected the degree of the polynomial by eye for each order, using the lowest degree polynomial required to model several representative M dwarf spectra.

The second parameter was an exponential scaling of the flux, to account for the effects of airmass and atmospheric water vapor on the depths of telluric features. The transmission spectrum represents typical conditions on Mauna Kea, while we observed at air masses from 1.0 to 1.7 with humidity from 85% to less than 15%.

As discussed in Blake et al. (2010), differences in airmass scale the depths of the telluric features (T) as $T = T_0^\tau$ where the optical depth τ scales linearly with airmass. Blake et al. (2010) were able to find a single linear scaling between airmass and τ using a large sample of A0V stars. We attempted to use the same approach, but found substantial scatter and systematic differences in the scaling of different telluric features with airmass. This is likely due to the water absorption features in our spectral region, which are time-variable, and cannot be modeled by a simple function of airmass alone. We therefore chose to take an empirical approach and included the exponential scaling τ as a model parameter.

The third and final parameter was the offset in pixels between the transmission and science spectrum. We modeled the offset as linear in wavelength. To apply the shift, we created a new wavelength vector that was linearly shifted from the original

and interpolated the transmission spectrum onto the new wavelength vector. We constrained the allowable range for the offset because atmospheric features appear at regular spacing and we found that if unconstrained, our fitting program can too often land in a local minimum. We used $0.0008\mu\text{m}$ as the limit, which is larger than any offset we expected. In our full sample, no shifts beyond $0.0006\mu\text{m}$ were found, and very few beyond $0.0004\mu\text{m}$.

We modeled each order of the non-telluric corrected science spectrum independently, minimizing the difference between our model and the science spectrum using a nonlinear least squares approach, implemented through `mpfit` (Markwardt 2009). We determined by trial and error the region of each order to use. Regions with high signal to noise and strong telluric features but uncontaminated by strong stellar features were required for optimal performance. Because of these constraints, this method worked better in the *J*, *H* and *K*-bands than it did in *Y* or *Z*.

Once we determined the absolute wavelength solutions of science target and an RV standard, we interpolated the telluric-corrected spectra onto a common wavelength vector that was oversampled and uniform in the log of the wavelength (such that a radial velocity introduces a constant offset in pixels). The continuum is different in the telluric-corrected spectrum because telluric correction removed instrumental effects, so we used a spline to remove the continuum. We used `xcor1` to cross-correlate the two spectra and determine the offset. We used the same standard star (Luyten's star, also known as Gl 273 or LSPM J0727+0513) throughout because it had an accurately measured absolute radial velocity from Chubak et al. (2012) and a NIR spectral type in the middle of our range (M4V).

We took the final RV for each target to be the median of the RVs measured in the *J*, *H* and *K*-bands and applied the heliocentric correction, implemented through the IDL routine `baryvel` (Stumpff 1980). Our final estimate of the error is the 1σ confidence limit on the RV after 50 trials added in quadrature to 4.4 km/s (our internal measurement error, see §2.8.3). These values are reported in Table 2.1.

This method of measuring radial velocities is applicable to other moderate resolution NIR spectrographs, including TripleSpec, and uses observations of the target star to refine the wavelength calibration. Our method is therefore likely to be useful for instruments where obtaining lamp spectra is expensive.

2.8.2 Using precise RVs to investigate errors and systematics

Chubak et al. (2012) presented absolute, barycentric-corrected RVs for 2046 dwarf stars with spectral types from F to M. M dwarf RVs were measured by comparison to an M3.5V RV standard, offset to agree with the measurements from Nidever et al. (2002). No corrections were made for convective or gravitational effects for M dwarfs, and Chubak et al. (2012) report a systematic error of 0.3 km/s (random errors are at this level or lower in nearly all cases). Ten of their M dwarfs are in our sample. We chose one of these, LSPM J0727+0513, as our standard star. For the other nine stars, we compare our measurements to those from Chubak et al. (2012) in Figure 2.22. Considering the RV measured in each order separately, we found that the bluest two bands (*Z* and *Y*) systematically underestimate (*Z*-band) or overestimate (*Y*-band) the RV. The wavelength calibration is also subject to failure in those bands. We suggest that this is because in these two orders, the strongest stellar features overlap with the

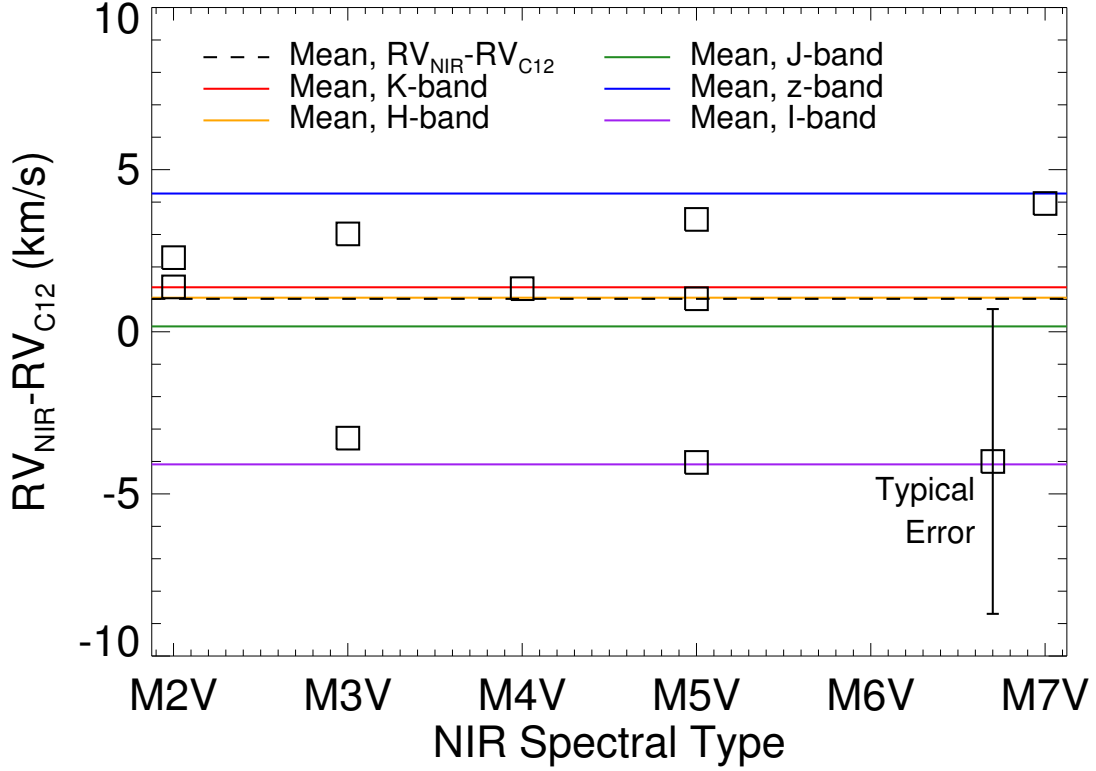


Figure 2.22.— We compare our RV measurements to those from Chubak et al. (2012), with NIR spectral type on the horizontal axis. Data points show the difference between our adopted RV for each star, which is the median of the RV measured in each of the *J*, *H*, and *K*-bands, and that reported in Chubak et al. (2012). The dashed line shows the mean difference between our measurements and those from Chubak et al. (2012). We also look at how well the RV measured from a single band compares to the values from Chubak et al. (2012); the mean difference for each band is plotted as a colored line. The *Y* and *Z*-bands tend to over- and underestimate the RV. A -2.6 km/s offset has been applied.

strongest telluric features, compromising the wavelength calibration and therefore the velocity measurement. They were also the orders with the lowest S/N. The RVs reported in this paper are the median of the J , H , and K -band measurements.

We measured RVs for all our targets using each of the ten RV standards from Chubak et al. (2012) in order to determine our internal error and systematic RV offset. The typical standard deviation of RVs measured against an alternative standard relative to that measured against LSPM J0727+0513 was 4.2 km/s. We used this value as our internal random error. RVs measured using LSPM J0727+0513 were systematically higher than those measured using other RV standards. Considering M3V-M5V standards, the median offset was 2.6 km/s with a standard deviation of 1.5 km/s. The values reported in this paper include a -2.6 km/s systematic RV correction. Our total internal measurement error is 4.4 km/s, which is our internal random error (4.2 km/s) added in quadrature to our internal systematic error (1.5 km/s).

Our choice of a single, mid-M RV standard does not appear to systematically affect the RV measurements or errors of early and late M dwarfs at this level of precision. We investigated the effect of the standard spectral type by comparing the results using LSPM J0727+0513 with using an M2V star, PM I06523-0511 (Gl 250), to measure the RVs of early M-dwarfs, and an M7V star, J1056+0700 (Gl 406), to measure the RVs of late M-dwarfs, finding that these choices did not appear to systematically affect the measured RVs, and that the scatter remained consistent with our estimated uncertainties.

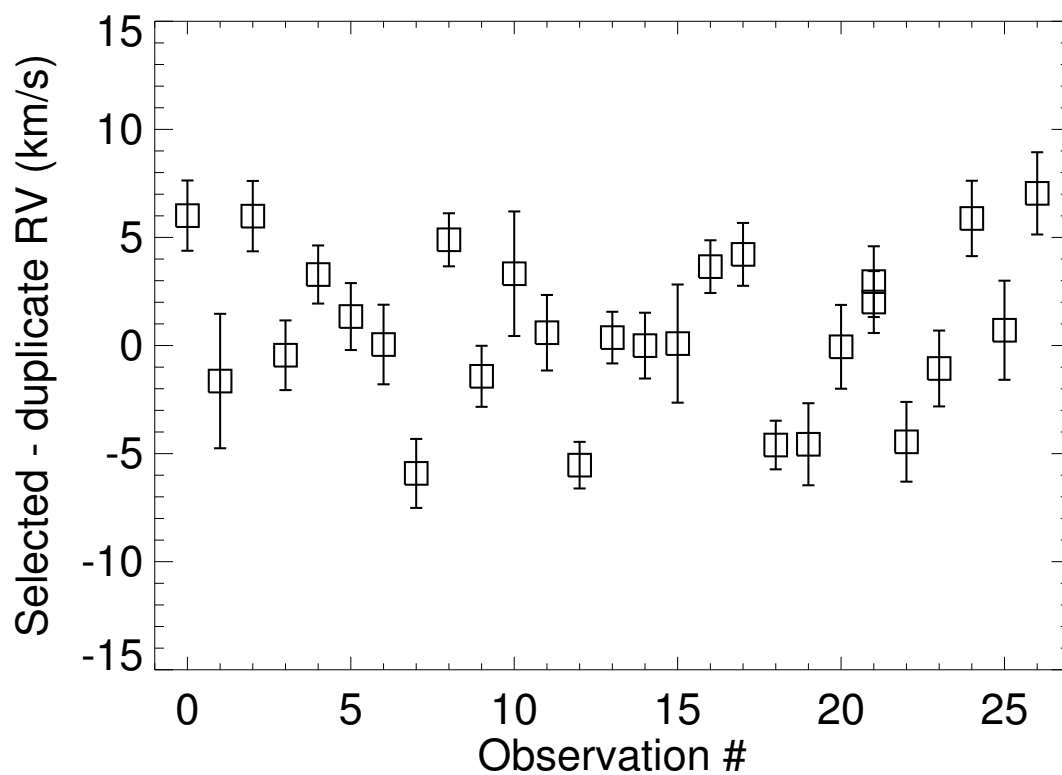


Figure 2.23.— We compare RV measurements for 26 stars which we observed multiple times. For each star, we plot the difference between the RV measured from the observation we elected to keep and the observation we did not use. The error bars plotted are the 1σ confidence intervals after 100 trials.

2.8.3 Validating the use of SpeX for radial velocities

To determine the precision of our wavelength calibration method, we used the transmission spectrum to create simulated data in each order, which we then calibrated. We simulated stellar absorption lines of random widths, depths and locations on top of the transmission spectrum and multiplied by a polynomial (drawn from a random distribution) to curve the data. We then offset the spectrum and monitored how well we could recover that offset. The accuracy declined as more stellar absorption lines were added to the spectrum. With 50 added lines, accuracy was better than 5 km/s in all orders and better than 1 km/s in *H*-band.

We have multiple observations for 26 stars at different epochs. The time between observations ranges from days to months to years. We compared our RVs for these stars (Figure 2.23). The mean difference between the observation we elected to keep and the observation we chose to discard with 0.08 km/s with a standard deviation of 4 km/s, consistent with our calculation of the error.

Finally, we compared the RVs of CPM pairs (Figure 2.24). 11 of these stars are separated and were observed independently and 11 were observed together on the slit. These observations were taken close in time, at near-identical conditions and were reduced using the same wavelength calibration and telluric standard. The mean RV difference between the primary and secondary components is 0.2 km/s with a standard deviation of 2 km/s.

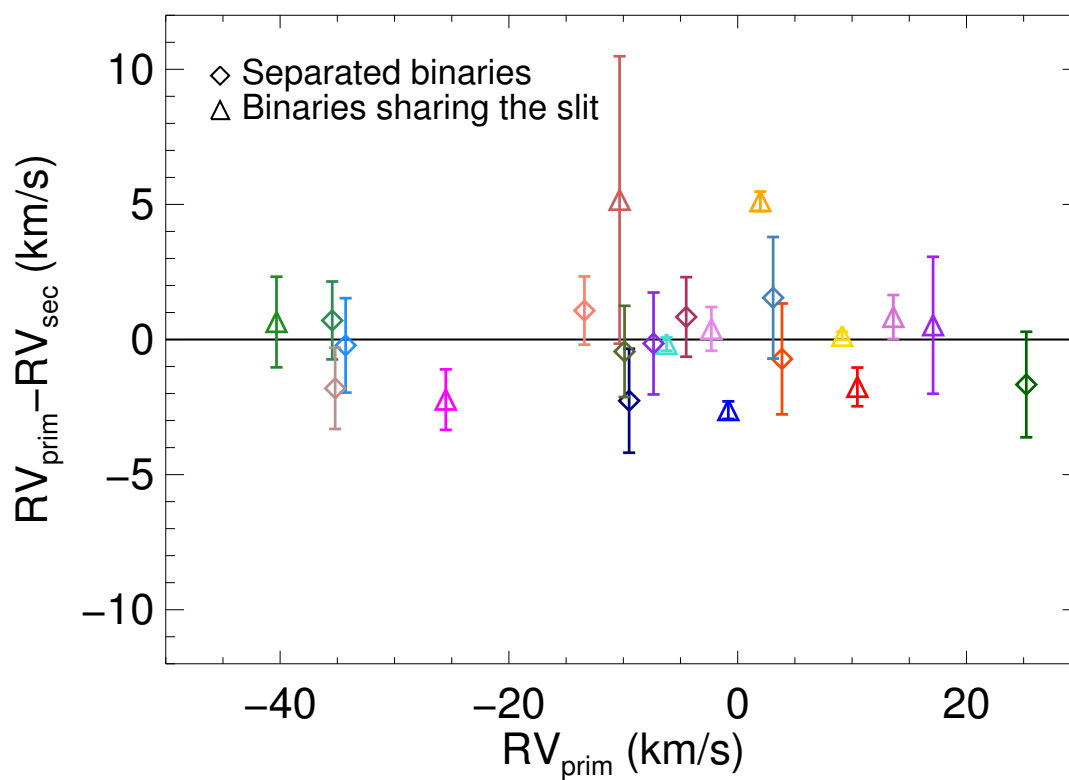


Figure 2.24.— We compare RV measurements for binary stars, 11 of which were observed independently and 11 of which were observed together on the slit. The error bars are the 1σ confidence limits in the RV after 100 trials. Colors uniquely identify pairs in this figure and in Figure 2.17.

2.9 Conclusions

The MEarth team and collaborators are creating a well-studied sample of nearby M dwarfs which will be the basis for future studies investigating their fundamental properties, their evolution, and the exoplanets orbiting them. The data set being assembled is diverse, with photometric rotation periods, parallaxes, and optical spectra. In this work, we presented metallicities, NIR spectral types and radial velocities for a fifth of MEarth M dwarfs.

We created a NIR spectral typing routine, determined by-eye spectral types and presented spectral standards for M1V-M8/9V dwarfs. We related NIR spectral type to PMSU spectral type, finding the conversion to be metallicity-sensitive. We calibrated a new spectroscopic distance relation using NIR spectral type or H₂O-K2, which can be used to estimate distances to 22%.

We used M dwarfs in CPM pairs with an F, G or K star of known metallicity to calibrate an empirical metallicity relation. We validated the physical association of these pairs using proper motions, radial velocities and distances (making use of our RV measurements and spectroscopic distance estimates for the secondaries). We explored the NIR for combinations of EWs that effectively trace stellar metallicity, and found that the EW of the Na I line at $2.2\mu\text{m}$ is sufficient. Our metallicity calibration has a standard deviation of 0.12 dex and $R_{ap} = 0.78$. It is calibrated using 36 M dwarfs with NIR spectral types from M1V to M5V and $-0.6 < [\text{Fe}/\text{H}] < 0.3$, and can be extrapolated to $[\text{Fe}/\text{H}] = -1.0$ dex. We found no evidence that the calibration breaks down for M dwarfs as late as M7V.

CHAPTER 2. A NIR SPECTROSCOPIC SURVEY OF M DWARFS

Using our EW_{Na} measurements of 447 M dwarfs and the $J - H$, $H - K_S$ color-color diagram, we calibrated a relationship between an M dwarf's distance from the Bessell & Brett main sequence and its sodium equivalent width. It is valid from $2.5 < EW_{\text{Na}} < 7.5 \text{ \AA}$. The standard deviation of our fit is 2 \AA and has an R_{ap}^2 value of 0.92. Metal-rich M dwarfs can be selected by taking those M dwarfs whose $J - K_S$ colors are redder than the Bessell & Brett (1988) M dwarf track in the $J - H$, $H - K_S$ color-color diagram.

We developed a method to wavelength calibrate SpeX M dwarf spectra using telluric features present in the data, and we measured absolute radial velocities for the stars in our sample at a precision of 4.4 km/s. We used synthetic spectra, M dwarfs with precise radial velocities from Chubak et al. (2012) and M dwarf-M dwarf binaries to validate our method. Because telluric absorption features are strong in even short exposure data, our method for determining the absolute wavelength calibration requires no information beyond the science spectrum itself. This opens up the possibility of measuring radial velocities for stars with an extant moderate resolution NIR spectrum.

Our measurements, including NIR spectral types, EWs, radial velocities, and spectroscopic distance estimates are presented in Table 2.1. We also include distances estimated from parallaxes, and radial velocities from PMSU. To facilitate joint use of our datasets, we reproduce spectral measurements for M dwarfs observed by R12 in Table 2.2, with EWs modified to account for differences between their TripleSpec and our IRTF measurements and $[\text{Fe}/\text{H}]$ inferred using our calibration; we also include PMSU spectral types and RVs, and the parallaxes reported in R12.

CHAPTER 2. A NIR SPECTROSCOPIC SURVEY OF M DWARFS

In future work, will continue to explore the use of the NIR as a diagnostic of intrinsic stellar properties, investigating how metallicity relates to rotation period, tracers of magnetic activity, and galactic kinematics.

Chapter 3

An Empirical Calibration to Estimate Cool Dwarf Fundamental Parameters from H -band Spectra

E. R. Newton, D. Charbonneau, J. Irwin, *and* A.W. Mann

The Astrophysical Journal, Volume 800, Issue 2, Article 85, 2015

3.1 Introduction

Our understanding of planets is often limited by our knowledge of the stars they orbit. Stellar characterization is not yet as reliable for cooler dwarfs as it is for F, G and K dwarfs, for which fundamental stellar parameters can be determined with reasonable precision and accuracy (e.g. Valenti & Fischer 2005). The interpretation of

observables for cooler dwarfs is complicated by uncertain sources of opacity and the appearance of complex molecules in their atmospheres, and by discrepancies between their observed and theoretical properties. For this reason, empirical calibrations remain an important component of our understanding of M dwarfs.

Empirically-derived relations between basic stellar parameters provide the basis for determining the physical properties of field M dwarfs. For stars with parallaxes, masses can be estimated using the mass to absolute *K*-band magnitude relation of Delfosse et al. (2000), and radii can then be calculated using a mass-radius relation (e.g., Bayless & Orosz 2006; Boyajian et al. 2012). The mass-magnitude and mass-radius relations are determined from double-lined eclipsing binaries and have precisions of about 10%. Johnson et al. (2012) circumvented the lack of a distance for *Kepler* Object of Interest (KOI) 254 by constraining the mass and radius of this star using four separate empirical relationships between photometric quantities, mass, radius, and [Fe/H]. Another technique that can be used is the infrared flux method (IRFM; Blackwell & Shallis 1977; Blackwell et al. 1979, 1980), which was extended to M dwarfs by Casagrande et al. (2008). The IRFM uses the ratio of infrared to bolometric flux and a grid of stellar models to determine the effective temperature (T_{eff}) and bolometric flux (F_{bol}) of a star.

Planet surveys have driven many authors to investigate methods to estimate the stellar parameters of cool dwarfs without parallaxes, which are predominantly based on fitting observations to grids of stellar models. This has proved particularly fruitful for M dwarfs targeted by the *Kepler* survey, some of which host confirmed or candidate planets – including several likely to be Earth-sized and in their stars' habitable zone. Dressing & Charbonneau (2013) matched observed colors to

CHAPTER 3. EMPIRICAL TEMPERATURES AND RADII FOR COOL STARS

Dartmouth stellar isochrones (Dotter et al. 2008; Feiden et al. 2011). Mann et al. (2012) and Mann et al. (2013b) matched optical spectra to synthetic BT-Settl and PHOENIX spectra, respectively. Muirhead et al. (2012a) and Muirhead et al. (2014) used moderate resolution *K*-band spectra to determine T_{eff} and metallicity for 103 cool KOIs, which they interpolated onto Dartmouth isochrones to infer the stars' radii.

The methods described above rely on relationships derived from binary stars or on matching observed properties to stellar models. While there is reasonable agreement between predicted and observed masses and radii (or luminosities), the observed radii of M dwarfs at a given T_{eff} are larger than expected from models. This was first noted for binary stars (e.g. Popper 1997; Torres & Ribas 2002; Berger et al. 2006; Lopez-Morales 2007; Chabrier et al. 2007), but has been demonstrated in stars with interferometric radii measurements (e.g. Berger et al. 2006; Boyajian et al. 2012). Additionally, if magnetic activity is responsible for the inflated radii, as discussed in Lopez-Morales & Ribas (2005), Ribas (2006), Lopez-Morales (2007), and Chabrier et al. (2007), a mass-radius-*activity* relationship would be required to accurately determine the radii of field dwarfs. On the theoretical side, synthetic spectra – though they have been improved significantly over the last two decades – suffer from incomplete line lists for the molecules that blanket the spectra, particularly for TiO, VO, metal hydrides, and water vapor (e.g. Valenti et al. 1998; Allard et al. 2000; Leggett et al. 2000; Bean et al. 2006a; Önehag et al. 2012; Rajpurohit et al. 2013).

The use of proxies – stars with directly measured parameters that are similar to the star of interest – enable parameters of a field dwarf to be inferred with limited reliance on stellar models. Muirhead et al. (2012b) used Barnard's star to anchor

stellar models to direct measurements and inferred the properties of a similar M dwarf, KOI 961/*Kepler*-42. Building on the method used by Muirhead et al. (2012b), Ballard et al. (2013) used four stars with interferometric radii as proxies to infer the stellar properties of *Kepler*-61. As discussed by Ballard et al. (2013), the use of proxies fills a particularly crucial niche: while the temperature-sensitive index used by Muirhead et al. (2012a,b, 2014) saturates $T_{\text{eff}} > 3800$ K, the *Kepler* sample is rich in planets orbiting early M and late K dwarfs. Ballard et al. (2013) did not use models in their derivation of stellar parameters, instead directly using the interferometric radii. However, their method assumes that the properties of *Kepler*-61 match those of stars with the same spectral type, and M dwarf spectral types represent a coarse binning in stellar properties. It has also been shown that late-type dwarfs may have different spectral types in the optical and infrared (e.g. Rojas-Ayala et al. 2012; Pecaut & Mamajek 2013; Newton et al. 2014).

The idea of proxies naturally extends to the identification of empirical tracers of stellar parameters, and the development of such tracers is the motivation for this work. We develop methods to estimate stellar temperatures, radii, and luminosities that do not require parallaxes or stellar models, that are precise, accurate and extensible, and that can be applied to the large body of moderate-resolution near-infrared (NIR) spectra presently available. This idea was also used by Mann et al. (2013b), who used the sample of stars with interferometric measurements to derive index-based calibrations for T_{eff} in the visible, *J*, *H*, and *K* bands (although they use model-fitting for the stellar parameters reported therein). Our approach is also based on spectra of the interferometric sample but differs from their work in several ways. We utilize the NIR, which is not as strongly blanketed as the optical

by molecular bands that are often sensitive to metallicity. Instead of spectral indices, we use equivalent widths (EWs), which do not require flux-calibrated spectra and are less sensitive to instrument characterization and atmospheric dispersion. Due to ongoing discussions in the literature on measurements of T_{eff} , we opt to directly calibrate relations for T_{eff} , radius, and luminosity, rather than inferring one property and using additional relations to determine the others. Finally, we have the benefit of three new interferometric measurements from von Braun et al. (2014), and include Gl 725B, which was excluded from the analysis in Mann et al. (2013b), in our radius calibration.

In this paper, we present purely empirical relations between the EWs of NIR features and a cool dwarf's T_{eff} , radius, and luminosity. These calibrations are based on what we refer to as the interferometric sample: the set of stars with interferometrically-measured angular diameters and for which bolometric fluxes and distances have been measured, thereby allowing their effective temperatures and luminosities to be determined. We discuss our observations and measurements in §3.2. In §3.3, we discuss the behavior of H -band spectral features and present our new calibrations, including discussion of systematic errors. We then apply our calibrations to MEarth M dwarfs in §3.4 and consider the behavior of inferred stellar parameters with absolute K magnitude. We also address the applicability of NIR metallicity calibrations from Mann et al. (2013a), Newton et al. (2014), and Mann et al. (2014) to mid and late M dwarfs. We consider the cool KOIs in §4.4.2, and compare our stellar and planetary parameters to those derived using other techniques. In §3.6, we summarize our findings.

3.2 Observations and measurements

Our observations and data reduction were carried out as discussed in Newton et al. (2014), which we summarize briefly here. We used the SpeX instrument on IRTF with the $0.3 \times 15''$ slit, yielding spectra from $0.8 - 2.4\mu\text{m}$ with $R = 2000$. Four observations were acquired of each object, with two observations at each of two nod positions. Telluric standards were observed directly before or after observations of the interferometry stars used in this work. Flats (using an internal quartz lamp) and wavelength calibrations (using internal Thorium-Argon lamps) were taken throughout the night, at roughly one hour intervals or after large slews.

We reduced our data using Spextool (Cushing et al. 2004) and used xtellcor to perform telluric corrections (Vacca et al. 2003). We determined absolute radial velocities using the method described in Newton et al. (2014), using telluric features to provide an absolute wavelength calibration. We then shifted the spectra to rest wavelengths.¹

To measure EWs, we defined a wavelength range for the feature and nearby continuum regions on either side. We oversampled the data and numerically integrated the flux within the feature. We estimated errors on the radial velocities and equivalent widths by creating 50 realizations of our data, taking into account correlated noise for the high S/N observations of the interferometry and MEarth samples. We measured the EWs of 26 spectral features and 13 spectral indices in the NIR, primarily the same lines as examined by Newton et al. (2014). Our

¹An error resulted in the barycentric correction not being applied. Corrections are a small fraction of a pixel and results in EWs that differ by only tenths of 1σ .

H-band features are included in Table 3.1². We measure the temperature-sensitive indices used in Mann et al. (2013b) and the H₂O-K2 index (Rojas-Ayala et al. 2012). Wavelengths are given in vacuum.

3.2.1 Stars with interferometric measurements

Our calibration sample comprises 25 stars with interferometrically-measured radii. We preferentially use the interferometric measurements from Boyajian et al. (2012) and incorporate the measurements they collected from the literature. Where more than one such literature measurement is available, we use the weighted average. The literature sources for measurements are: Ségransan et al. (2003); Boyajian et al. (2008); Demory et al. (2009); Boyajian et al. (2012) and von Braun et al. (2012). We also include newer measurements from von Braun et al. (2014).

We observed 20 M dwarfs with interferometrically-measured radii from the sample described above. We supplement this sample with the five remaining: spectra for Gl 581 and Gl 892 are available in the IRTF spectral library (Cushing et al. 2005; Rayner et al. 2009)³ and we include spectra of Gl 876, Gl 649, and Gl 176 that were observed by Mann et al. (2013b). We cross-correlated these spectra with the RV standard we use in the rest of our work in order to assure agreement between our wavelength calibrations.

²The feature windows in this table have been corrected from the values in the published version of this paper.

³http://irtfweb.ifa.hawaii.edu/~spex/IRTF_Spectral_Library/

Table 3.1. *H*-band spectral features

Feature	Feature window		Blue continuum		Red continuum	
	μm	μm	μm	μm	μm	μm
Mg (1.48 μm)	1.4870	1.4900	1.4820	1.4850	1.4920	1.4950
Mg (1.50 μm)	1.5015	1.5070	1.4965	1.5000	1.5070	1.5120
K (1.51 μm)	1.5160	1.5185	1.5105	1.5135	1.5185	1.5210
Mg (1.57 μm)	1.5738	1.5790	1.5640	1.5680	1.5790	1.5815
Si (1.58 μm)	1.5880	1.5930	1.5860	1.5880	1.5930	1.5950
CO (1.61 μm)	1.6150	1.6175	1.6120	1.6150	1.6275	1.6300
CO (1.62 μm)	1.6190	1.6225	1.6120	1.6150	1.6275	1.6300
Al-a (1.67 μm)	1.6714	1.6741	1.6580	1.6630	1.6780	1.6815
Al-b (1.67 μm)	1.6743	1.6778	1.6580	1.6630	1.6780	1.6815
Mg (1.71 μm)	1.7095	1.7130	1.7025	1.7055	1.7130	1.7160

Note. — All wavelengths are given in vacuum. The feature windows in this table have been corrected from the values in the published version of these paper.

CHAPTER 3. EMPIRICAL TEMPERATURES AND RADII FOR COOL STARS

The bolometric fluxes and luminosities (F_{bol} and L_{bol}) for the stars from Boyajian et al. (2012) were re-measured using spectra and photometry by Mann et al. (2013b). To measure F_{bol} , Boyajian et al. (2012) use multicolor photometry to select best-fitting template spectra from the Pickles (1998) catalog, which they extrapolate to the NIR using photometry. Mann et al. (2013b) demonstrated that the fluxes extrapolated beyond $1.1\mu\text{m}$ do not match their observed spectra and instead used optical and infrared spectra that they obtained for each star. They use models to cover gaps in the spectra and assume Wein's and Rayleigh-Jeans' laws at shorter and longer wavelengths than covered by their spectra. They then adjust the overall flux level using a correction factor calculated by comparing photometric fluxes to the fluxes measured from the spectra. Mann et al. (2013b) measure T_{eff} systematically higher than Boyajian et al. (2012) by 1%.

We use the updated parameters from Mann et al. (2013b) in this work, but note that the radii measured are insensitive to these changes in temperature. We apply the method from Mann et al. (2013b), described above, to the three new objects from von Braun et al. (2014) that we include in this paper. We provide updated parameters for Gl 176, Gl 649, and Gl 876 in Table 4.5. We also use the $[\text{Fe}/\text{H}]$ calibration from Mann et al. (2013a) to estimate the iron abundances of these stars (see §3.4.1 for discussion of NIR metallicity calibrations).

Included in the table are the reduced χ^2 (χ_{red}^2) of the photometric corrections applied to each spectrum. Large χ_{red}^2 indicate that errors in the photometry or spectrum are underestimated or that there are systematic offsets between the two. The χ_{red}^2 for the three stars presented here are typical of those reported by Mann et al. (2013b).

Table 3.2. Updated parameters for new interferometry stars

Object	F_{bol} (ergs/s/cm ² × 10 ⁻⁸)	T_{eff} (K)	L_{bol} (L_{\odot})	R (R_{\odot})	χ^2_{red} ^a	[Fe/H] ^b (dex)
Gl 176	1.2544 ± 0.0099	3701 ± 90	0.03352 ± 0.00027	0.4525 ± 0.0221	0.36	+0.17
Gl 649	1.3171 ± 0.0071	3604 ± 46	0.04379 ± 0.00023	0.5387 ± 0.0157	1.94	+0.05
Gl 876	1.8863 ± 0.0115	3176 ± 20	0.01290 ± 0.00008	0.3761 ± 0.0059	0.78	+0.35

^a χ^2_{red} describes the goodness of fit as described in the text and in Mann et al. (2013b).

^b[Fe/H] estimated from Equation 16 from Mann et al. (2013a).

Mann et al. (2013b) excluded Gl 725B (GJ 725B in their work) due to its atypically large χ_{red}^2 (7.9). This indicates a large disagreement between this star’s photometry and spectrum, which affects its F_{bol} in an unknown manner. Therefore, we also exclude Gl 725B from our analysis of T_{eff} and L_{bol} , both of which are subject to this uncertainty. However, we include Gl 725B in our analysis of radius: while changing a star’s temperature affects the interferometrically-measured radius through the adopted limb darkening model, the effect is small (see Boyajian et al. 2012). Finally, we note that while Gl 725B has an unusually cool temperature given its radius, Gl 876 has similar properties; Gl 876 has $\chi_{red}^2 = 0.78$, typical of the values in Mann et al. (2013b), and is not excluded from any part of our analysis.

3.2.2 MEarth M dwarfs

Newton et al. (2014) obtained spectra of 447 mid to late M dwarfs in the solar neighborhood that are targets of the MEarth transiting planet survey (Berta et al. 2012; Irwin et al. 2015). Half of these M dwarfs had previously published parallaxes, which were compiled in Newton et al. (2014). Dittmann et al. (2014) measured parallaxes for most of these stars from MEarth astrometry; with the parallaxes from Dittmann et al. (2014), we have distances to 388 of these M dwarfs.

We note that LSPM J0035+5241S is improperly matched in Newton et al. (2014), who identified it as LSPM J0035+5241N. It is identified properly in this work as LSPM J0035+5241S.

3.2.3 Cool KOIs

Muirhead et al. (2012a) and Muirhead et al. (2014) presented H - and K -band spectra for 103 KOIs with $r - J > 2$, which implies they have temperatures below 4000K. They obtained spectra using the TripleSpec instrument on the Palomar 200-inch (5.1m) Hale telescope (Herter et al. 2008), which simultaneously obtains $R = 2700$ spectra in J -, H -, and K -band. We convolved the spectra with a Gaussian of fixed width to degrade the resolution to that of IRTF. We then cross-correlated each spectrum with that of our RV standard to place them on the same wavelength calibration as our observations.

Measurements of EWs should not depend on the resolution of the spectrograph. However, most lines in the NIR spectra of a cool dwarf are not free of contaminating features at moderate resolution. We found systematic differences of 0.1\AA between the EWs of some features measured at $R = 2000$ and at $R = 2700$, so we stress the importance of accounting for even moderate differences in spectral resolution.

While the subtraction of sky emission lines in IRTF spectra is very robust, it is more difficult for TripleSpec spectra: because of the tilt of the slit, the removal of sky background requires that illumination be very well characterized. Sky emission features persist in some of the KOI spectra and contaminate many spectral features of interest, necessitating the removal of the affected spectra from our analysis. We first identified contaminated spectra by eye, then developed the following quantitative method to remove spectra based on scatter between the EWs of the components of doublets.

We compared the EWs of the two components of the Mg doublet at $1.50\mu\text{m}$, of

the Mg I doublet at $1.57\mu\text{m}$, and of the Al I doublet at $1.67\mu\text{m}$. One component in each of the $1.50\mu\text{m}$ Mg doublet and the Al doublet is contaminated by sky emission. Neither component is contaminated in the $1.57\mu\text{m}$ Mg doublet. We found that in the spectra of the MEarth and interferometry stars, for which sky emission is not prevalent, the EWs of the doublet components are linearly correlated with little scatter. For the $1.57\mu\text{m}$ Mg doublet, which is free of sky emission, there is also little scatter for the KOIs. However, a fraction of the KOIs show inconsistencies in the EWs of the components of the contaminated doublets. The stars that show scatter tend to be those that we determined by eye to contain sky emission.

For each of the two doublets contaminated by sky emission, we used the interferometric sample to determine a linear correlation between the doublet components. Objects deviating from the best-fitting line by more than 0.75\AA for Mg at $1.50\mu\text{m}$ or 0.5\AA for Al at $1.67\mu\text{m}$ were discarded. These limits replicate the contamination we determined by eye and the amount of scatter expected based on observations of the MEarth and interferometry stars. Our final sample of KOIs includes 66 stars. The number of spectra excluded by our cuts does not depend sensitively on the limits we adopt.

3.3 Inferring stellar parameters

The interferometric sample, which we use to calibrate our empirical relationships, consists of 25 cool stars with radii directly measured using interferometry. We discussed observations of these stars in §3.2.1. Typical H -band spectra, with our EW measurements indicated, are shown in Figure 3.1.

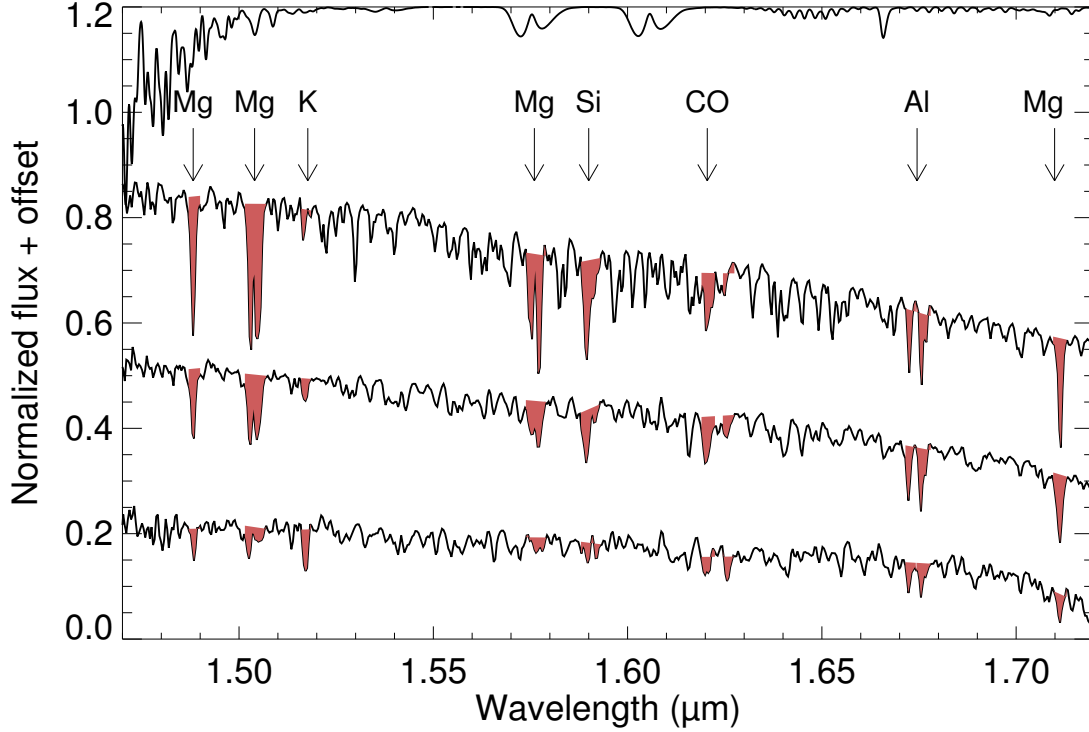


Figure 3.1.— Representative *H*-band spectra of cool dwarfs spanning the temperature range of our calibration. From the top down: a K4V from the IRTF spectral library, an M2V composite spectrum, and an M5V composite spectrum. The composite spectra are from Newton et al. (2014). We indicate the EW measurements with red shading and the elements that dominate the major absorption features. Along the top, we show a typical atmospheric transmission spectrum for Mauna Kea, from Lord (1992).

3.3.1 Behavior of *H*-band spectral features as a function of effective temperature

In Figures 3.2-3.3, we plot selected EWs, EW ratios, and spectral indices for the interferometric calibration sample against the measured T_{eff} . Included in these plots are all *H*-band EW measurements, the two EW ratios used in our final analysis (each of which is Mg I / Al I, involving different atomic transitions), and one EW ratio that we found to have a strong temperature dependence for mid M dwarfs. This last EW ratio, K I / Si I, may be useful for studies focusing on later objects. The data points in these figures are colored by their $[\text{Fe}/\text{H}]$, using the iron abundance calibration from Mann et al. (2013a).

We measured the same spectral features in BT-Settl model spectra (Allard 2014, available online⁴) as we do in our observed spectra. We used models based on the Asplund et al. (2009) solar abundances and degraded their resolution to that of SpeX by convolving the spectra with a fixed-width Gaussian. We then measured EWs numerically using the same technique that we used with our observed spectra. Figures 3.2-3.3 include the EWs, EW ratios, and spectral features that we measured for a suite of synthetic spectra. We show temperature tracks for three surface gravities, using solar metallicity: $\log g = 5, 4.5$, and 4 . Late dwarfs have long main sequence lifetimes, so age does not strongly affect $\log g$. For $\log g = 5$, we also show temperature tracks for two non-solar metallicities, $[\text{Fe}/\text{H}] = -0.5$ and $[\text{Fe}/\text{H}] = +0.3$, which roughly spans the metallicity range of the interferometric sample. The synthetic spectra with $[\text{Fe}/\text{H}] = -0.5$ have an alpha enhancement of

⁴<http://phoenix.ens-lyon.fr/Grids/BT-Settl/>

CHAPTER 3. EMPIRICAL TEMPERATURES AND RADII FOR COOL STARS

+0.2; the remainder have no alpha enhancement. The EW measurements of M dwarfs should most closely match the theoretical $\log g = 5$ temperature track. The surface gravities of the late K dwarfs ($T_{\text{eff}} > 4000$ K) decrease with increasing temperature, reaching $\log g = 4.5$ for the hottest star in our sample. Observed EWs for the late K dwarfs are therefore expected to most closely match the temperature track with that surface gravity.

Spectral features that show the smallest metallicity dependence show the most agreement between the EWs measured in the synthetic spectra and in our observed spectra. The Mg I EWs show the best agreement (though the slight metallicity dependence in the models is not evident in our data). For the M dwarfs, the EWs closely follow the temperature tracks for stars with $\log g = 5$, as expected. For the four K dwarfs, the EWs drop due to the lower surface gravities of these objects. For the Mg I features at $1.50\mu\text{m}$ and $1.71\mu\text{m}$, the EWs of K dwarfs closely follow the temperature tracks for $\log g = 4.5$; however for those at $1.48\mu\text{m}$ and $1.57\mu\text{m}$, the EWs are smaller than expected for stars with their temperatures and surface gravities. The EWs of the Si I feature at $1.58\mu\text{m}$ and the CO feature at $1.62\mu\text{m}$ both show tight trends with T_{eff} , albeit ones that deviate from those expected from synthetic spectra.

The EWs we observe deviate most strongly from the EWs we calculate from synthetic spectra for features where the models indicate a strong metallicity dependence in the EWs: K I at $1.52\mu\text{m}$, Si I at $1.58\mu\text{m}$, CO at $1.61\mu\text{m}$, and the components of the Al I doublet at $1.67\mu\text{m}$. The EWs of our observed spectra match neither the strength of the features in the synthetic spectra, nor the amplitude of their metallicity dependence. This result is similar to what was found by Rojas-Ayala et al. (2012), who noted disagreement between EWs measured from synthetic and

observed spectra for two metallicity-sensitive K -band features, Na I at $2.21\mu\text{m}$ and Ca I at $2.26\mu\text{m}$. This suggests that there may be issue with the treatment of metal abundances in M dwarf atmosphere models.

Lastly, we note that the K -band spectral indices we measure in our observed spectra are broadly in agreement with those in the synthetic spectra.

3.3.2 Empirical calibrations for stellar parameters using spectral features

We first conducted a principal component analysis (PCA), looking for the strongest correlations between the EW measurements of our calibration sample. We then fit for T_{eff} , radius, and luminosity using a linear combination of between one and five principal components. These fits were not better than the simple functions we tried later, and we required line ratios to best fit the full temperature range. The PCA was also hampered by the limited metallicity range of the interferometry stars, but may be a more useful tool in the future.

We investigate simple parameterizations of two or three EWs or EW ratios and simple functions of one EW. The multi-line functions we test (using x , y , and z to represent an EW measurement or ratio of measurements) are $ax + by$, $ax + by + cz$ and $ax + bx^2 + cy$. The single-line functions we test are $ax + b/x$, $ax + b\sqrt{x}$, and $ax + bx^2$. We restrict our fits to a single NIR band, and perform a comprehensive search across the possible combinations of features. We use least-squares regression to determine the best-fitting parameters for each combination and the Bayesian

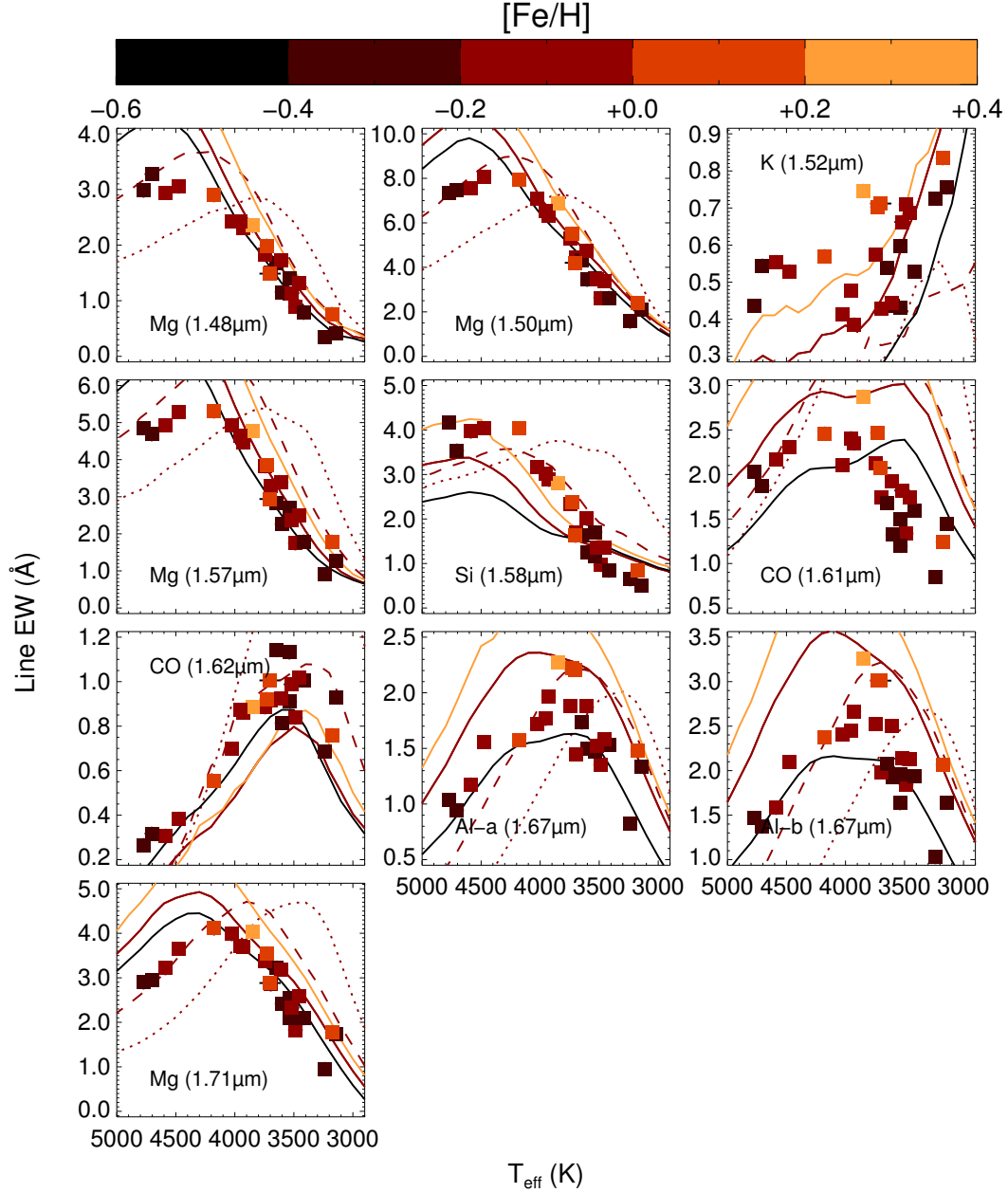


Figure 3.2.— EWs of H -band spectral features plotted against measured T_{eff} for stars in our interferometric sample. We use the updated temperatures from Mann et al. (2013b) and adopt iron abundances using the Mann et al. (2013a) calibration. The EWs measured from BT-Settl model spectra (Allard 2014) are also plotted. Solid lines are $\log g = 5$, dashed lines for $\log g = 4.5$, and dotted lines for $\log g = 4$, all with solar metallicity. For $\log g = 5$, we show three metallicities: -0.5 dex (black), $+0.0$ dex (red), and $+0.3$ dex (orange).

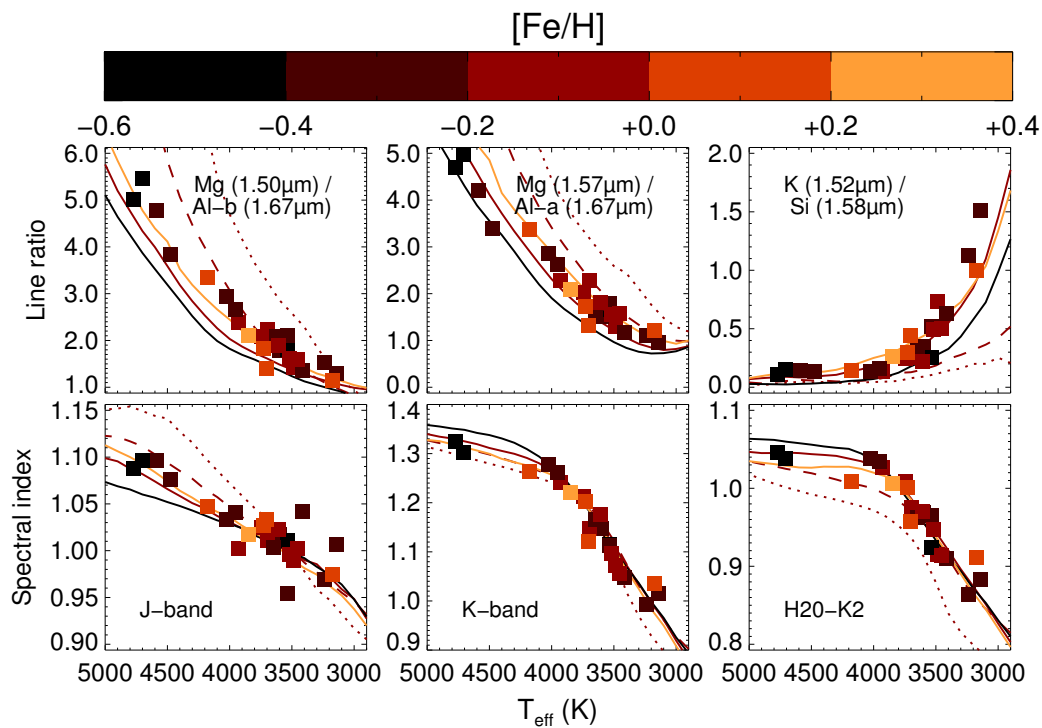


Figure 3.3.— Same as Figure 3.2 but plotting select EW ratios and spectral indices against T_{eff} , using the updated temperatures from Mann et al. (2013b).

Information Criterion (BIC) to quantitatively compare each fit. After removing fits that qualitatively show systematics in the residuals, we select the fit with the lowest BIC. Our best fits are shown in Figure 3.4.

We found no viable *K*-band relationship and the only viable *J*-band relationship has significantly higher scatter than our adopted *H*-band relation. Combining features from different regions of the spectrum also did not result in significant improvement. We excluded the Si I, K I, and CO ($1.62\mu\text{m}$) features from our fits because the behavior of these features as observed in our larger samples of MEarth and *Kepler* M dwarfs is not well-represented by the behavior of these features in the interferometric sample, which may be due to metallicity. While empirically these lines can be used to fit stellar parameters as well as those we do use, such fits would have more limited applicability.

In the following equations, we use the element responsible for the spectral feature to indicate an EW measurement, for example, Al-a($1.67\mu\text{m}$) represents the EW measurement of the blue component of the Al doublet at $1.67\mu\text{m}$. All EWs are in Ångstroms. After each equation, we indicate the standard deviation of the residuals

(σ) and the mean absolute deviation (MAD). Our best fitting relationships are⁵:

$$\begin{aligned}
 T_{\text{eff}}/\text{K} &= + 261.9 \times \text{Al-a}(1.67\mu\text{m}) \\
 &+ 413.8 \times \text{Mg}(1.50\mu\text{m}) / \text{Al-b}(1.67\mu\text{m}) \\
 &+ 2402 \\
 \sigma_{T_{\text{eff}}/\text{K}} &= 73 \\
 \text{MAD}/\text{K} &= 55
 \end{aligned} \tag{3.1}$$

$$\begin{aligned}
 R/R_{\odot} &= - 0.0503 \times \text{Mg}(1.57\mu\text{m}) \\
 &+ 0.283 \times \text{Al-a}(1.67\mu\text{m}) \\
 &+ 0.206 \times \text{Mg}(1.57\mu\text{m}) / \text{Al-a}(1.67\mu\text{m}) \\
 &- 0.235 \\
 \sigma_{R/R_{\odot}} &= 0.027 \\
 \text{MAD}/R_{\odot} &= 0.020
 \end{aligned} \tag{3.2}$$

⁵The equations presented have been updated from those in the published paper following fixing the application of the barycentric correction. Applying the new relations to the MEarth sample indicates that there are no significant differences between the published EWs and relations and the corrected EWs and relations. For T_{eff} , the median difference between the new and old values is 4 K with a standard deviation of 9 K. For R , the difference is $0.005 R_{\odot}$ with a standard deviation of $0.006 R_{\odot}$. For $\log L$, the difference is 0.002 dex with a standard deviation of 0.016 dex.

$$\log L/L_{\odot} = +0.783 \times \text{Mg}(1.71\mu\text{m}) \quad (3.3)$$

$$-0.169 \times [\text{Mg}(1.71\mu\text{m})]^2$$

$$+0.267 \times \text{Mg}(1.50\mu\text{m})$$

$$-3.417$$

$$\sigma_{\log L/L_{\odot}} = 0.049$$

$$\text{MAD/dex} = 0.039$$

We show our best fits in Figure 3.4. We present the stellar parameters we estimate for the interferometric calibration sample in Table 3.3; our EW measurements are included in Table 3.4. These fits are calibrated from our sample of 24 calibrators (25 for our radius fit, for which Gl 725B is included, see §3.2.1). They are valid for stars with $3200 < T_{\text{eff}} < 4800$ K, $0.18 < R < 0.8 R_{\odot}$, and $-2.5 < \log L/L_{\odot} < -0.5$.

We note that these calibrations depend on some of the same spectral features. More fundamentally, spectral features are determined by a star’s T_{eff} , $\log g$, and $[\text{Fe}/\text{H}]$ – not by its radius and L_{bol} . It could be argued that it is only appropriate to derive T_{eff} , $\log g$, and $[\text{Fe}/\text{H}]$ from spectral features, which could then be used to determine radius or L_{bol} . We opt to present relations calibrated directly to radius and L_{bol} for several reasons: we do not have masses for these stars or other constraints on $\log g$, efforts are currently underway that will revise the temperatures and luminosities of our calibration sample, and disagreement continues over T_{eff} scales (e.g. Casagrande et al. 2014).

3.3.3 Systematic uncertainties in the calibrations

To assess systematic uncertainties in our calibrations, we performed two bootstrap analyses with 1000 samples each. In each case, we randomly created a new realization of our calibration sample and re-fit our relations using each new realization. In the first bootstrap analysis, we randomly drew stars from our calibration sample, allowing calibrators to be sampled repeatedly. Despite the limited number of calibrators, our fits are well-constrained at the limits of our calibration. In the second bootstrap analysis, we randomly permuted the residuals from our best fit, assigning each residual to a new data point. This probes the effect of deviations from our best fit that are not captured in the errors on the measured stellar parameters. We find no systematic deviation in T_{eff} . For radius and L_{bol} , small systematic errors are evident in the difference between the stellar parameters we infer from our bootstrapped fits and those we infer from our fiducial fit. For radius, the difference is $0.006 R_{\odot}$. For luminosity, the difference is -0.014 dex for the coolest stars ($\log L/L_{\odot} = -2.5$ dex) and reaches -0.021 dex for the hottest ($\log L/L_{\odot} > -1.3$ dex). We adopt systematic uncertainties of $0.006 R_{\odot}$ for radius and 0.02 dex for $\log L/L_{\odot}$.

We additionally demonstrate the robustness of our calibrations for small stars by removing Gl 699 (Barnard’s star), which anchors the radius and luminosity fits, and refit our relations. The effect on the parameters we infer for other stars is negligible, and the relations also provide a good fit if we extrapolate them to Gl 699. Extrapolation gives a radius of $0.21 R_{\odot}$ (the measured value is $0.19 R_{\odot}$) and a log luminosity of -2.36 dex (measured: -2.47 dex) for Gl 699.

T_{eff} , radius and L_{bol} are not independent parameters and our calibrations

should produce consistent values. Looking at the difference between $\log L/L_{\odot}$ and $2\log R/R_{\odot} + 4\log T/5777\text{K}$, the scatter is 0.1 dex with a systematic offset of -0.06 dex. This corresponds to a 7% difference in radius – if the entire systematic offset is assigned to the radius calibration – or a 3.5% difference in T_{eff} – if it is assigned to the temperature calibration.

3.4 Application to M dwarfs from MEarth

We applied our calibrations for T_{eff} , radius and luminosity to the sample of MEarth M dwarfs observed by Newton et al. (2014).

We present measurements of the EWs used in our best fits, the K -band temperature index from Mann et al. (2013b), and our inferred stellar parameters in Table 3.5. The quoted errors on our stellar parameters are random errors (propagated from EW errors) added in quadrature to the standard deviation of the residuals in our best fits. The errors do not include our adopted systematic uncertainties, which are $0.006 R_{\odot}$ for radius, and 0.02 dex for $\log L/L_{\odot}$. We found no evidence of systematic uncertainties for T_{eff} .

The latest spectral type represented in our interferometry calibration sample is M4V (Gl 699, Barnard’s star). The MEarth targets predominantly have temperatures and radii at the extreme end of the calibration range, while close to half of sample have EWs that indicate that they are cooler than Gl 699. While our calibrations are not valid for these cool stars, they remain well-behaved for late M dwarfs and are useful diagnostics of stellar properties. We therefore report estimated stellar properties for

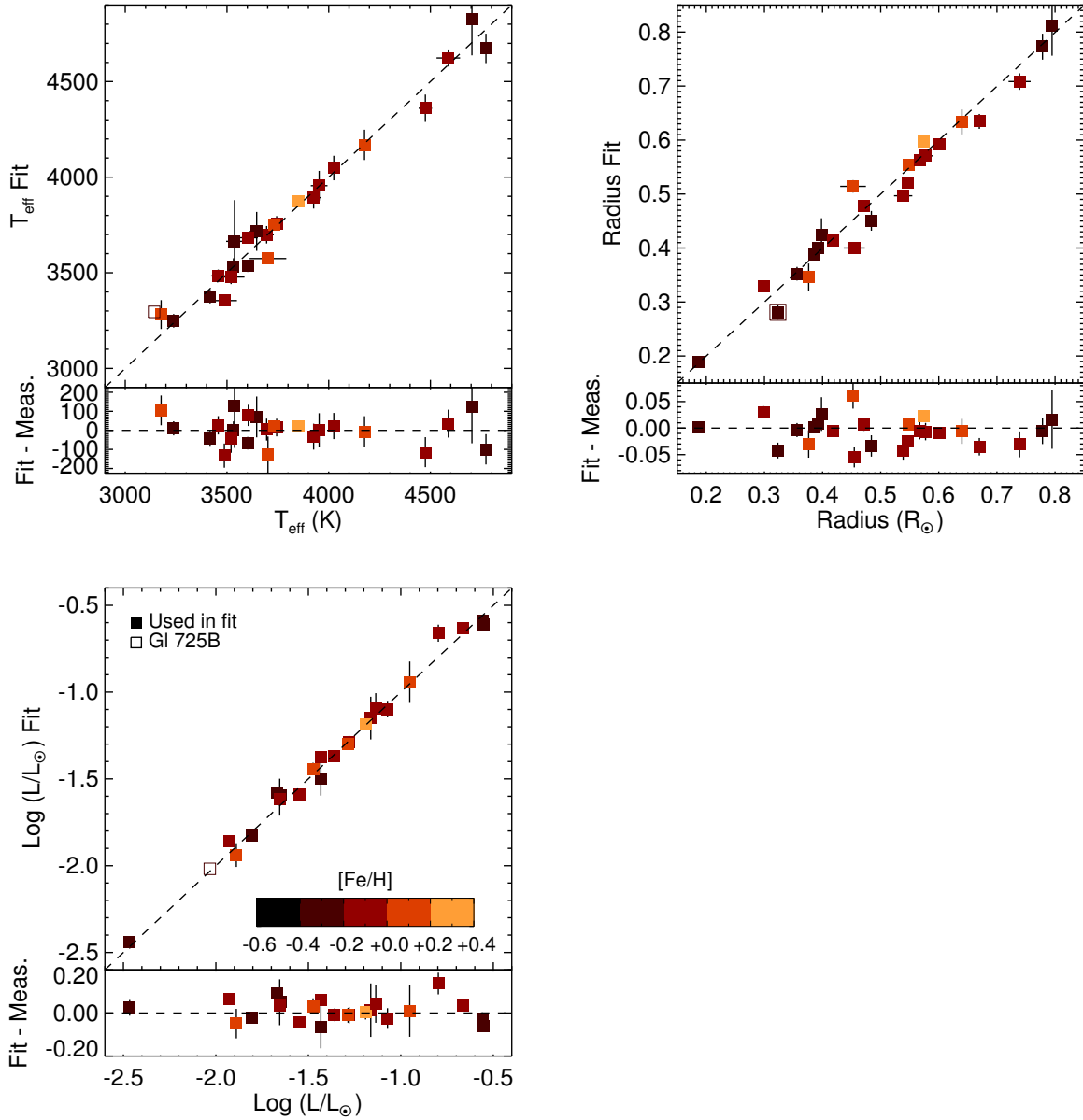


Figure 3.4.— Our best-fitting relationships and the residuals for T_{eff} (top left), radius (top right), and L_{bol} (bottom left). The horizontal axes shows the directly-measured stellar parameter, using the updated values from Mann et al. (2013b). In the top plot of each panel, the vertical axis shows the stellar parameter we infer from our best fits; in the bottom plot, the vertical axis shows the residuals between our best-fitting values and the directly-measured values. The $[\text{Fe}/\text{H}]$ is indicated by the color of each data point. GI 725B - used only in our radius fit - is indicated by an open square.

Table 3.3. Inferred parameters for the interferometric sample

Star	Measured parameters			Inferred parameters		
	$T_{\text{eff}}^{\text{a}}$ (K)	Radius ^b (R_{\odot})	$L_{\text{bol}}^{\text{a}}$ ($\log L/L_{\odot}$)	$T_{\text{eff}}^{\text{c}}$ (K)	Radius ^d (R_{\odot})	$L_{\text{bol}}^{\text{e}}$ ($\log L/L_{\odot}$)
Gl 725B ^f	3142 ± 29	0.3232 ± 0.0061	-2.0329 ± 0.0052	(3295 ± 81)	0.281 ± 0.030	(-2.02 ± 0.06)
Gl 876 ^g	3176 ± 20	0.3761 ± 0.0059	-1.8893 ± 0.0027	3281 ± 105	0.346 ± 0.037	-1.94 ± 0.08
Gl 699	3238 ± 11	0.1869 ± 0.0012	-2.4660 ± 0.0038	3248 ± 81	0.188 ± 0.029	-2.44 ± 0.06
Gl 725A	3417 ± 17	0.3561 ± 0.0039	-1.8033 ± 0.0052	3375 ± 81	0.352 ± 0.030	-1.82 ± 0.05
Gl 687	3457 ± 35	0.4183 ± 0.0070	-1.6521 ± 0.0086	3483 ± 80	0.413 ± 0.028	-1.62 ± 0.05
Gl 581	3487 ± 62	0.2990 ± 0.0100	-1.9278 ± 0.0077	3354 ± 74	0.329 ± 0.027	-1.86 ± 0.05
Gl 436	3520 ± 66	0.4546 ± 0.0182	-1.5476 ± 0.0110	3477 ± 81	0.400 ± 0.028	-1.59 ± 0.05
Gl 411	3532 ± 17	0.3924 ± 0.0033	-1.6708 ± 0.0061	3532 ± 85	0.401 ± 0.029	-1.58 ± 0.05
Gl 412A	3537 ± 41	0.3982 ± 0.0091	-1.6548 ± 0.0047	3664 ± 227	0.425 ± 0.041	-1.61 ± 0.12
Gl 15A	3602 ± 13	0.3863 ± 0.0021	-1.6467 ± 0.0052	3534 ± 79	0.388 ± 0.028	-1.60 ± 0.05
Gl 649 ^g	3604 ± 46	0.5387 ± 0.0157	-1.3586 ± 0.0023	3683 ± 79	0.497 ± 0.028	-1.37 ± 0.06
Gl 526	3646 ± 34	0.4840 ± 0.0084	-1.4325 ± 0.0060	3716 ± 125	0.450 ± 0.033	-1.50 ± 0.11
Gl 887	3695 ± 35	0.4712 ± 0.0086	-1.4325 ± 0.0088	3698 ± 86	0.478 ± 0.028	-1.37 ± 0.05
Gl 176 ^g	3701 ± 90	0.4525 ± 0.0221	-1.4746 ± 0.0034	3574 ± 78	0.514 ± 0.029	-1.44 ± 0.06
Gl 880	3731 ± 16	0.5477 ± 0.0048	-1.2856 ± 0.0049	3749 ± 76	0.555 ± 0.028	-1.30 ± 0.06
Gl 809	3744 ± 27	0.5472 ± 0.0067	-1.2798 ± 0.0057	3758 ± 82	0.522 ± 0.028	-1.29 ± 0.06
Gl 205	3850 ± 22	0.5735 ± 0.0044	-1.1905 ± 0.0094	3872 ± 75	0.597 ± 0.027	-1.19 ± 0.06
Gl 338B	3926 ± 37	0.5673 ± 0.0137	-1.1627 ± 0.0145	3892 ± 92	0.562 ± 0.028	-1.15 ± 0.13
Gl 338A	3953 ± 41	0.5773 ± 0.0131	-1.1357 ± 0.0164	3955 ± 106	0.571 ± 0.029	-1.09 ± 0.10
Gl 820B	4025 ± 24	0.6010 ± 0.0072	-1.0722 ± 0.0064	4047 ± 97	0.591 ± 0.028	-1.10 ± 0.07
Gl 380	4176 ± 19	0.6398 ± 0.0046	-0.9518 ± 0.0065	4168 ± 107	0.634 ± 0.036	-0.94 ± 0.13
Gl 702B	4475 ± 33	0.6697 ± 0.0089	-0.7972 ± 0.0108	4360 ± 102	0.635 ± 0.030	-0.66 ± 0.07
Gl 570A	4588 ± 58	0.7390 ± 0.0190	-0.6654 ± 0.0064	4623 ± 85	0.708 ± 0.031	-0.63 ± 0.05
Gl 105A	4704 ± 21	0.7949 ± 0.0062	-0.5589 ± 0.0056	4825 ± 202	0.811 ± 0.061	-0.59 ± 0.06
Gl 892	4773 ± 20	0.7784 ± 0.0053	-0.5521 ± 0.0060	4673 ± 106	0.773 ± 0.036	-0.61 ± 0.05

^aCalculated from the interferometric radius and bolometric flux as describe in §3.2.1. Values are from Mann et al. (2013b) Table 1 unless otherwise noted.

^bMeasured from interferometry; see Boyajian et al. (2012) Table 6 for references unless otherwise noted.

^cInferred from EWs using Equation 3.1; fit shown in Figure 3.4, top left.

^dInferred from EWs using Equation 3.2; fit shown in Figure 3.4, top right.

^eInferred from EWs using Equation 3.3; fit shown in Figure 3.4, bottom left.

^fGl 725B was excluded from our T_{eff} and L_{bol} calibrations, as discussed in §3.2.1. The T_{eff} and L_{bol} we infer from Equations 3.1 and 3.3 for this star are nevertheless included in this table.

^gValues for interferometric radii are from von Braun et al. (2014); updated T_{eff} and L_{bol} from this work.

Table 3.4. Measured quantities for the interferometric sample

star	Mg 1.48 μ m Å	Mg 1.50 μ m Å	K 1.51 μ m Å	Mg 1.58 μ m Å	Si 1.58 μ m Å	CO 1.61 μ m Å	CO 1.62 μ m Å	Al-a 1.67 μ m Å	Al-b 1.67 μ m Å	Mg 1.71 μ m Å	J-a band ^a K ²	H-a band ^a K ²	K-a band ^a K ²	H ₂ O- K ² ^b
Gl 725B	0.42 ± 0.07	2.11 ± 0.08	0.75 ± 0.06	1.28 ± 0.11	0.50 ± 0.08	1.45 ± 0.08	0.93 ± 0.06	1.34 ± 0.06	1.64 ± 0.08	1.74 ± 0.10	1.01	0.80	1.02	0.88
Gl 876	0.76 ± 0.18	2.38 ± 0.20	0.83 ± 0.11	1.79 ± 0.19	0.83 ± 0.19	1.24 ± 0.22	0.76 ± 0.13	1.48 ± 0.17	2.07 ± 0.21	1.77 ± 0.20	0.97	0.86	1.04	0.91
Gl 699	0.34 ± 0.03	1.57 ± 0.05	0.73 ± 0.03	0.91 ± 0.05	0.64 ± 0.04	0.85 ± 0.04	0.69 ± 0.04	0.82 ± 0.03	1.03 ± 0.05	0.95 ± 0.07	0.97	0.73	0.99	0.86
Gl 725A	0.78 ± 0.08	2.63 ± 0.09	0.53 ± 0.06	1.79 ± 0.09	0.84 ± 0.09	1.59 ± 0.06	1.01 ± 0.07	1.53 ± 0.09	1.94 ± 0.07	2.09 ± 0.10	1.04	0.85	1.05	0.91
Gl 687	1.32 ± 0.07	3.39 ± 0.09	0.69 ± 0.05	2.49 ± 0.08	1.36 ± 0.08	1.74 ± 0.05	1.02 ± 0.05	1.58 ± 0.06	2.13 ± 0.08	2.59 ± 0.09	1.00	0.79	1.06	0.91
Gl 581	0.89 ± 0.02	2.63 ± 0.03	0.71 ± 0.02	1.74 ± 0.04	0.96 ± 0.03	1.34 ± 0.03	0.84 ± 0.02	1.35 ± 0.03	1.84 ± 0.03	1.83 ± 0.05	0.99	0.83	1.07	0.92
Gl 436	1.14 ± 0.06	3.46 ± 0.08	0.66 ± 0.06	2.38 ± 0.07	1.35 ± 0.08	1.82 ± 0.08	0.99 ± 0.05	1.53 ± 0.06	2.13 ± 0.10	2.33 ± 0.10	1.00	0.87	1.10	0.95
Gl 411	1.40 ± 0.09	3.52 ± 0.08	0.43 ± 0.05	2.43 ± 0.11	1.70 ± 0.10	1.20 ± 0.09	0.91 ± 0.08	1.47 ± 0.07	1.96 ± 0.10	2.53 ± 0.15	1.01	0.80	1.11	0.92
Gl 412A	1.14 ± 0.29	3.46 ± 0.39	0.60 ± 0.19	2.69 ± 0.34	1.15 ± 0.41	1.49 ± 0.29	1.13 ± 0.27	1.50 ± 0.25	1.63 ± 0.36	2.09 ± 0.29	0.95	0.84	1.11	0.97
Gl 15A	1.15 ± 0.04	3.44 ± 0.07	0.44 ± 0.05	2.26 ± 0.06	1.25 ± 0.06	1.33 ± 0.06	0.81 ± 0.05	1.50 ± 0.05	1.93 ± 0.06	2.42 ± 0.05	1.02	0.90	1.15	0.97
Gl 649	1.72 ± 0.05	4.76 ± 0.07	0.44 ± 0.04	3.39 ± 0.11	2.01 ± 0.08	1.93 ± 0.06	0.93 ± 0.06	1.88 ± 0.06	2.50 ± 0.08	3.18 ± 0.08	1.02	0.87	1.18	0.97
Gl 526	1.67 ± 0.17	4.32 ± 0.23	0.54 ± 0.10	2.84 ± 0.21	1.63 ± 0.18	1.68 ± 0.12	1.14 ± 0.13	1.73 ± 0.14	2.07 ± 0.21	3.23 ± 0.25	1.00	0.87	1.17	0.96
Gl 887	1.50 ± 0.07	4.45 ± 0.07	0.43 ± 0.05	3.30 ± 0.09	1.69 ± 0.08	1.74 ± 0.07	0.91 ± 0.06	1.44 ± 0.06	1.98 ± 0.09	2.85 ± 0.08	1.01	0.85	1.15	0.98
Gl 176	1.49 ± 0.10	4.20 ± 0.11	0.71 ± 0.06	2.94 ± 0.10	1.62 ± 0.12	2.07 ± 0.09	1.01 ± 0.08	2.21 ± 0.07	3.01 ± 0.10	2.88 ± 0.12	1.03	0.91	1.12	0.96
Gl 880	1.99 ± 0.04	5.52 ± 0.08	0.70 ± 0.04	3.85 ± 0.06	2.38 ± 0.07	2.47 ± 0.06	0.92 ± 0.05	2.22 ± 0.07	3.02 ± 0.05	3.55 ± 0.06	1.03	0.91	1.20	1.00
Gl 809	1.83 ± 0.05	5.29 ± 0.09	0.57 ± 0.05	3.82 ± 0.09	2.34 ± 0.06	2.12 ± 0.06	0.88 ± 0.05	1.88 ± 0.07	2.53 ± 0.09	3.38 ± 0.08	1.02	0.89	1.21	1.01
Gl 205	2.35 ± 0.05	6.88 ± 0.05	0.75 ± 0.04	4.77 ± 0.06	2.81 ± 0.06	2.88 ± 0.05	0.89 ± 0.06	2.27 ± 0.04	3.26 ± 0.06	4.05 ± 0.05	1.02	0.89	1.22	1.01
Gl 338B	2.31 ± 0.11	6.32 ± 0.14	0.39 ± 0.08	4.48 ± 0.14	2.88 ± 0.10	2.35 ± 0.13	0.86 ± 0.09	1.97 ± 0.13	2.66 ± 0.12	3.70 ± 0.25	1.00	0.87	1.24	1.03
Gl 338A	2.42 ± 0.11	6.55 ± 0.13	0.48 ± 0.10	4.65 ± 0.15	3.01 ± 0.13	2.41 ± 0.12	0.87 ± 0.10	1.77 ± 0.10	2.45 ± 0.16	3.71 ± 0.17	1.04	0.88	1.26	1.03
Gl 820B	2.43 ± 0.05	7.07 ± 0.08	0.41 ± 0.05	4.94 ± 0.10	3.17 ± 0.08	2.11 ± 0.08	0.70 ± 0.08	1.72 ± 0.09	2.41 ± 0.12	3.98 ± 0.07	1.03	0.90	1.28	1.04
Gl 380	2.90 ± 0.10	7.95 ± 0.17	0.57 ± 0.08	5.30 ± 0.14	4.05 ± 0.09	2.46 ± 0.08	0.55 ± 0.10	1.57 ± 0.13	2.37 ± 0.12	4.11 ± 0.18	1.05	0.87	1.26	1.01
Gl 702B ^c	3.05 ± 0.06	8.07 ± 0.07	0.53 ± 0.05	5.28 ± 0.09	4.05 ± 0.07	2.31 ± 0.09	0.38 ± 0.09	1.56 ± 0.07	2.10 ± 0.09	3.65 ± 0.10	1.08
Gl 570A ^c	2.93 ± 0.03	7.56 ± 0.03	0.55 ± 0.02	4.94 ± 0.04	3.97 ± 0.03	2.17 ± 0.04	0.31 ± 0.04	1.18 ± 0.03	1.58 ± 0.04	3.22 ± 0.03	1.10
Gl 105A	3.28 ± 0.06	7.48 ± 0.09	0.54 ± 0.04	4.69 ± 0.08	3.54 ± 0.08	1.87 ± 0.07	0.32 ± 0.06	0.94 ± 0.07	1.37 ± 0.12	2.95 ± 0.08	1.10	0.86	1.30	1.04
Gl 892	2.98 ± 0.03	7.34 ± 0.05	0.44 ± 0.02	4.86 ± 0.04	4.16 ± 0.04	2.03 ± 0.04	0.27 ± 0.04	1.03 ± 0.04	1.47 ± 0.06	2.90 ± 0.06	1.09	0.96	1.32	1.05

Note. — EW definitions given in Table 3.1

^aTemperature-sensitive indices from Mann et al. (2013b)

^bTemperature-sensitive index from Covey et al. (2010); Rojas-Ayala et al. (2012)

^cSpectral windows for the K-band indices fall outside of calibrated wavelength range.

Table 3.5. Measured quantities and inferred stellar parameters for M dwarfs in the MEarth sample

LSPM Name	Comp	Mg (1.50 μ m) Å	Mg (1.58 μ m) Å	Al-a (1.67 μ m) Å	Al-b (1.67 μ m) Å	Mg (1.71 μ m) Å	K-a band ^a	T_{eff}^b K	Radius ^c R_{\odot}	$\log L/L_{\odot}^d$ dex	Parallax mas	Ref. ^e [Fe/H] ^f (M13) dex	[Fe/H] ^f (M14) dex
LSPM J0001+0659		0.59 ± 0.11	-0.10 ± 0.16	0.48 ± 0.08	0.86 ± 0.14	0.40 ± 0.13	0.94	-3.03 ± 0.11	57.1 ± 2.6	D14	-0.05
LSPM J0007+0800		2.10 ± 0.12	1.56 ± 0.12	1.05 ± 0.05	1.10 ± 0.09	1.67 ± 0.12	1.03	...	0.295 ± 0.032	-2.04 ± 0.06	44.0 ± 6.3	N14	-0.71
LSPM J0008+2050		1.36 ± 0.05	0.66 ± 0.09	0.84 ± 0.04	1.09 ± 0.07	1.03 ± 0.10	0.95	3147 ± 82	0.140 ± 0.032	-2.46 ± 0.07	67.5 ± 2.7	D14	+0.02
LSPM J0015+4344		2.05 ± 0.13	1.27 ± 0.15	1.07 ± 0.07	1.32 ± 0.08	1.33 ± 0.13	0.95	3328 ± 93	0.255 ± 0.034	-2.15 ± 0.08	35.1 ± 1.5	D14	+0.22
LSPM J0015+1333		1.58 ± 0.07	0.92 ± 0.11	0.94 ± 0.06	1.19 ± 0.07	1.34 ± 0.09	1.02	3201 ± 83	0.194 ± 0.033	-2.27 ± 0.06	99.8 ± 4.0	D14	-0.22

Note. — For binaries that were not resolved in the LSPM catalogs but which we resolve, we use the appropriate LSPM name in the first column and identify the components in the second column. Only a portion of this table is shown here to demonstrate its form and content. Machine-readable and Virtual Observatory (VO) versions of the full table are available.

^aTemperature-sensitive K-band index from Mann et al. (2013b).

^bInferred from EWs using Equation 3.1; fit shown in Figure 3.4, top left.

^cInferred from EWs using Equation 3.2; fit shown in Figure 3.4, top right.

^dInferred from EWs using Equation 3.3; fit shown in Figure 3.4, bottom left.

^eD14 = parallax from Dittmann et al. (2014); N14 = parallax compiled from the literature by Newton et al. (2014). For parallaxes compiled from the literature, we refer the reader to Newton et al. (2014) for the reference.

^f[Fe/H] using the Mann et al. (2013a) calibration, appropriate for early M dwarfs ($\log L/L_{\odot} > -2.25$).

^g[Fe/H] using the Mann et al. (2014) calibration, appropriate for late M dwarfs ($\log L/L_{\odot} < -2.25$).

stars beyond the limits of our calibration, but caution that these values may only be used to assess the properties of stars relative to one another.

We limit application of our temperature calibration to objects with small uncertainties in the EWs: when EW uncertainties are a large fraction of the measurement, their ratios have asymmetric error distributions, and we find that the temperatures of cool stars with large errors are systematically hotter than those of similar stars with small errors. Therefore, we do not report estimated temperatures for stars for which the contribution from EW uncertainties (random error) to the total error exceeds 100K. We found no evidence for similar effects in our radius and luminosity calibrations.

3.4.1 Using luminosities to revisit the metallicities of the M_{Earth} sample

Newton et al. (2014) estimated the metallicities of the M dwarfs in our sample from the EW of the Na I feature at $2.2\mu\text{m}$ in the *K*-band of IRTF spectra (see also Rojas-Ayala et al. 2010, 2012; Terrien et al. 2012). Their empirical relation was based on M dwarfs with NIR spectral types M5V and earlier. Mann et al. (2013a) constructed a similar calibration for K5-M5 dwarfs, using a combination of the Na feature and other NIR spectral features. Mann et al. (2014) used early-late M dwarf pairs to bootstrap a calibration valid for M dwarfs with spectral types M4V-M9V and showed that Newton et al. (2014) and other previous works either over- or underestimated the metallicities of M7 to M9 dwarfs. In the following, we make use of our estimated stellar luminosities to investigate the best metallicity calibration to

use on our sample of stars.

Newton et al. (2014) looked for systematic trends in the metallicities of stars with spectral type, which they determined by matching each NIR spectrum to that of a spectral standard. They found that the M5-M7 dwarfs in their sample appeared metal-rich by 0.1 dex relative to earlier stars (Figure 13 in their work). Because M5 dwarfs comprised a quarter of their metallicity calibration sample, they assumed the metallicities of the MEarth M5 dwarfs - and by extension the M6 and M7 dwarfs - were estimated accurately. However, M spectral types are a coarse binning in stellar parameters. In Figure 3.5, we show that while the M4V metallicity calibrators used by Newton et al. (2014) are typical of the M4 dwarfs in the MEarth sample, 70% of the M5 dwarfs have luminosities lower than the median luminosity of the M5V metallicity calibrators. The calibration from Newton et al. (2014) may not be valid for all M dwarfs assigned an M5V spectral type.

In Figure 3.6, we compare $[\text{Fe}/\text{H}]$ values measured for the MEarth M dwarfs using the calibrations from Newton et al. (2014), Mann et al. (2013a), and Mann et al. (2014). We only show M dwarfs whose metallicities, as estimated from the Newton et al. (2014) calibration, are less than 0.25 dex, because the Newton et al. (2014) calibration saturates for more metal-rich stars. This demonstrates that while the Newton et al. (2014) calibration is generally valid for M2-M4V stars, it over- and under-estimates the metallicities of later and earlier stars, respectively.

We compare the Newton et al. (2014) calibration to the Mann et al. (2014) calibration, which is applicable to late M dwarfs, in the top panel of Figure 3.6. This demonstrates that Newton et al. (2014) overestimates the metallicities of M dwarfs

with $\log L/L_{\odot} < -2.25$, which includes the majority of stars M5V and later. The two calibrations agree for stars with $-2.25 < \log L/L_{\odot} < -1.75$ (approximately M4V), with a median offset of 0.03 dex. For hotter stars, the Mann et al. (2014) calibration is not applicable, and the estimated metallicities deviate significantly. In the bottom panel of Figure 3.6, we find an almost linear trend with luminosity when we compare the Newton et al. (2014) to the Mann et al. (2013a) calibration, which is applicable to early M dwarfs. The two calibrations agree most closely for $-2.0 < \log L/L_{\odot} < -1.5$, (approximately M2V-M3V). For earlier stars, the Newton et al. (2014) calibration underestimates metallicities, a finding anticipated in that work.

We update the metallicities of the MEarth M dwarfs by stitching together the Mann et al. (2013a) and Mann et al. (2014) relations. For stars with $\log L/L_{\odot} < -1.75$, we use the Mann et al. (2014) relation, which was calibrated specifically for late-type dwarfs. For stars with $\log L/L_{\odot} > -1.75$, we use the Mann et al. (2013a) relation, for which the calibration was dominated by early M dwarfs. We use the code provided by A. Mann⁶ to calculate metallicities. We note that the method we use to measure EWs (over-sampling and using the trapezoidal rule to numerically integrate the flux beneath the pseudo-continuum), while more robust than the IDL routines TOTAL or SUM without over-sampling, produces different (typically larger) EW measurements.

⁶<https://github.com/awmann/metal>

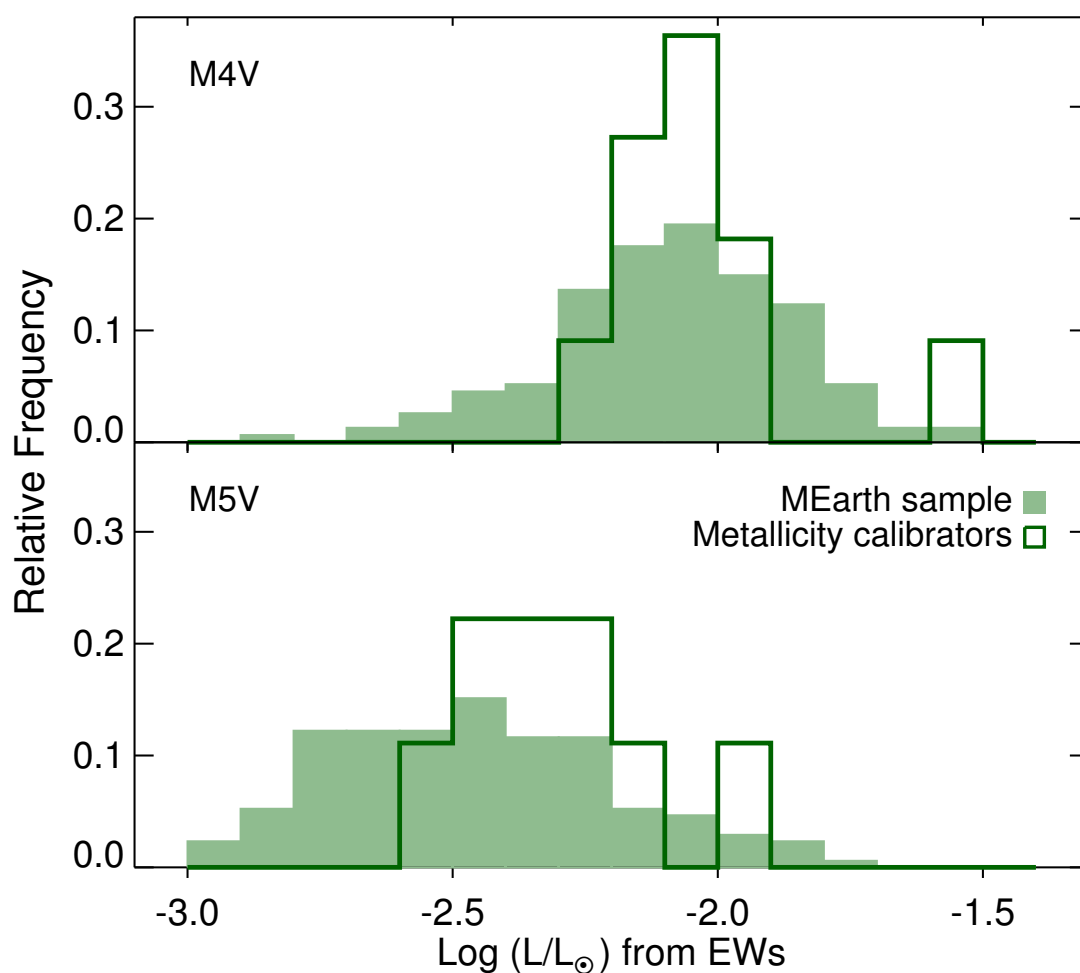


Figure 3.5.— The distribution of inferred luminosities for M4 dwarfs (top panel) and for M5 dwarfs (bottom panel). M dwarfs in the MEarth sample are represented by the light green shaded histogram. The M dwarfs in the Newton et al. (2014) metallicity calibration sample are represented by the dark green histogram.

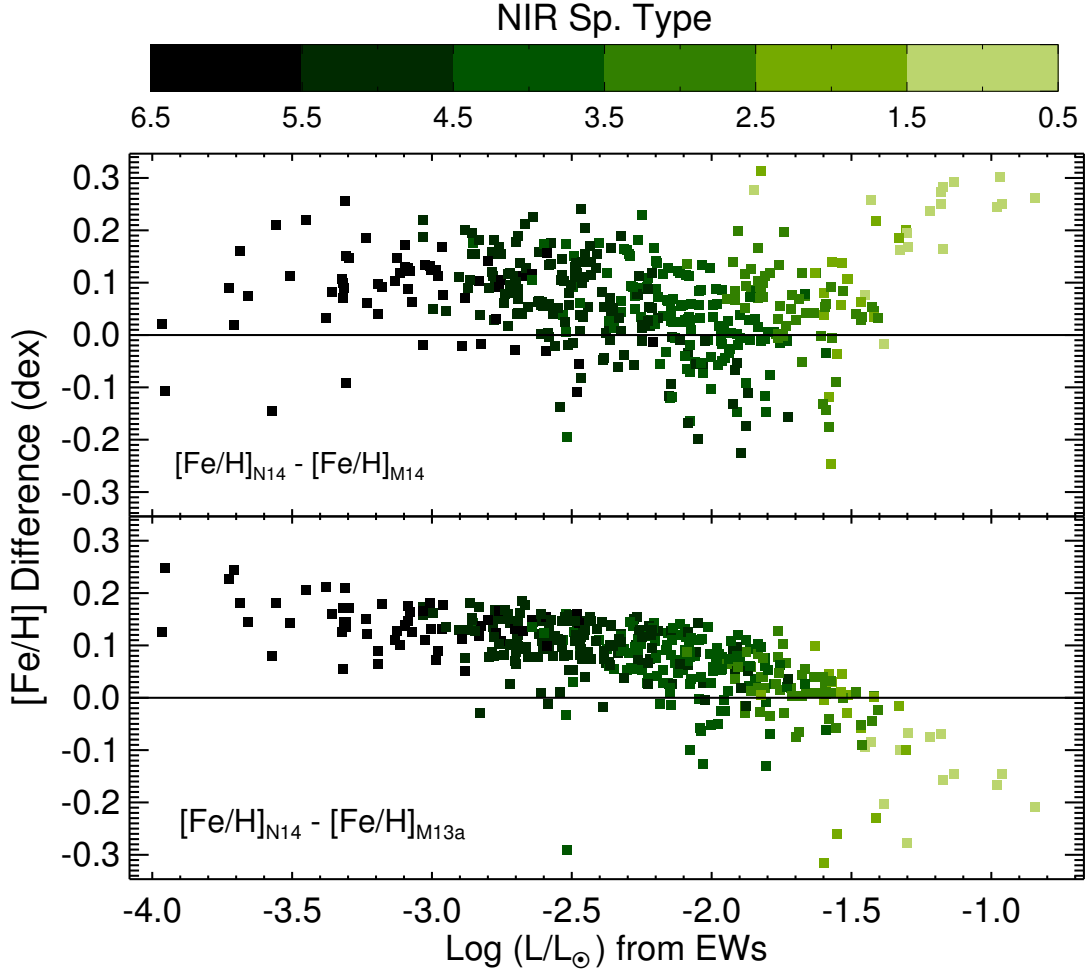


Figure 3.6.— The difference between literature $[\text{Fe}/\text{H}]$ values versus stellar luminosity. We use relations from three works: Mann et al. (2013a, M13a), Newton et al. (2014, N14), and Mann et al. (2014, M14). The Mann et al. (2013a) relation is calibrated for M4V stars and earlier, while the Mann et al. (2014) relation is calibrated for stars M4V and later. Points are colored by the NIR spectral type assigned by eye by Newton et al. (2014).

3.4.2 Comparison to the Mann et al. temperature and radius calibrations

Mann et al. (2013b) developed empirical relations for cool dwarf temperatures that are based on spectral indices in visual and infrared bands. As we have done in this work, they used stars with interferometric measurements to calibrate the relationships. The temperature-sensitive indices are ratios between the median flux in three wavelength windows (Equation 13 in their paper) and quantify the curvature of the spectrum in each band. Mann et al. (2013b) chose the continuum windows to minimize the scatter in the resulting temperature calibration.

We compare the stellar parameters we estimated for the MEarth M dwarfs to those we calculated using the Mann et al. (2013b) J -, H -, and K -band T_{eff} calibrations in Figure 3.7. We then applied their temperature-radius polynomial (Equation 6 in their work) to convert the K -band temperatures to radii. Accurate transformation requires additional significant figures, included here for completeness:

$$\begin{aligned} R/R_{\odot} = & -16.883175 + 1.1835396 \times 10^{-2} \times (T_{\text{eff}}/K) \\ & - 2.7087196 \times 10^{-6} \times (T_{\text{eff}}/K)^2 \\ & + 2.1050281 \times 10^{-10} \times (T_{\text{eff}}/K)^3 \end{aligned} \tag{3.4}$$

We limit our comparison to those stars within the limits of the calibrations in question; only these objects are included in Figure 3.7. We note that the Mann et al. (2013b) K -band calibration saturates for stars with $T_{\text{eff}} < 3300$ K, so there is a minimum value for the temperatures derived from this relation.

The Mann et al. (2013b) J - and H -band indices are not good predictors of T_{eff} .

CHAPTER 3. EMPIRICAL TEMPERATURES AND RADII FOR COOL STARS

The differences between the T_{eff} inferred from our two calibrations have standard deviations ($\sigma_{\Delta T}$) larger than expected from the errors in the calibrations: $\sigma_{\Delta T} = 140$ K for the J -band calibration and 170 K for the H -band calibration. This is because the wavelength windows for these indices fall in regions with strong telluric absorption. Temperatures from the K -band index and our EW-based calibration agree within the errors of the calibrations, with $\sigma_{\Delta T} = 90$ K, although for $3500 < T_{\text{eff}} < 3800$ K, the median temperature we infer from EWs is 40 K hotter.

The radii we infer directly from EWs and the radii calculated from the K -band using the temperature-radius relation have $\sigma_{\Delta R} = 0.05 R_{\odot}$. However, there is evidence for a systematic offset for stars with $0.3 < R/R_{\odot} < 0.4$, where the median offset is $0.045 R_{\odot}$ (12%), with radii calculated from EWs being larger. We believe this is due to systematics in the Mann et al. (2013b) relations: the K -band temperature relation predicts temperatures that are too cool by 50 – 100K for the three interferometry stars with temperatures around 3500K (Figure 11 in their work). Because the slope of the temperature-radius relation is steep for stars of this size, temperatures that are 50-100K too cool result in radii that are 0.03 - $0.06 R_{\odot}$ (15%) too small. This is consistent with the differences we find and supports the temperatures and radii we infer from EWs. Additionally, the temperature-radius relation has larger scatter for stars of this size relative to hotter/larger stars (Figure 4 in their work).

Intriguingly, we find that stars with $[\text{Fe}/\text{H}] < -0.2$ dex are assigned larger radii by the Mann et al. (2013b) relations than stars are with $[\text{Fe}/\text{H}] > +0.2$ dex. The mean difference is $0.05 R_{\odot}$. The effect persists when applying the temperature-radius relation to temperatures inferred using our EW relations, so the difference must either be a result of the Mann et al. (2013b) temperature-radius relation or of our radius

calibration. We suggest that the root cause is the temperature-radius relation for two reasons: (1) we expect a metallicity dependence in the temperature-radius relation from theory (one has yet to present itself in observations of the interferometry stars, but the metallicity range spanned by these data is narrow) and (2) we do not see a metallicity dependence when we consider inferred radius as a function of M_K (§3.4.3).

3.4.3 Trends between absolute M_K and inferred stellar parameters

We consider the relationship between M_K and the T_{eff} , radius, or L_{bol} estimated from EWs in Figure 3.8. NIR photometry is from 2MASS (Skrutskie et al. 2006). We exclude 53 objects with $\sigma_{M_K} > 0.2$ and 9 objects lacking high quality magnitudes from 2MASS (for which the `qual_flag` is anything other than AAA). For T_{eff} , we also exclude those objects that have random errors on $T_{\text{eff}} > 100$ K as discussed at the beginning of §3.4. We fit a quadratic for M_K as a function of stellar temperature, radius, or log luminosity; the standard deviation in M_K is about 0.5 mag for each fit. Because M_K is an independent indicator of stellar parameters – for example, it was tied to stellar mass by Delfosse et al. (2000) – the existence of a clear relationship between M_K and the T_{eff} , radii, and L_{bol} we infer provides additional validation of our method.

Visually, our plot of M_K versus T_{eff} shows the largest scatter. Large variations in T_{eff} and M_K are also seen in the Dartmouth models (Dotter et al. 2008; Feiden et al. 2011) which predict that a star with $[\text{Fe}/\text{H}] = -0.5$ dex and $T_{\text{eff}} = 3400$ will be 1 magnitude fainter than a star with the same temperature but with $[\text{Fe}/\text{H}] = +0.3$

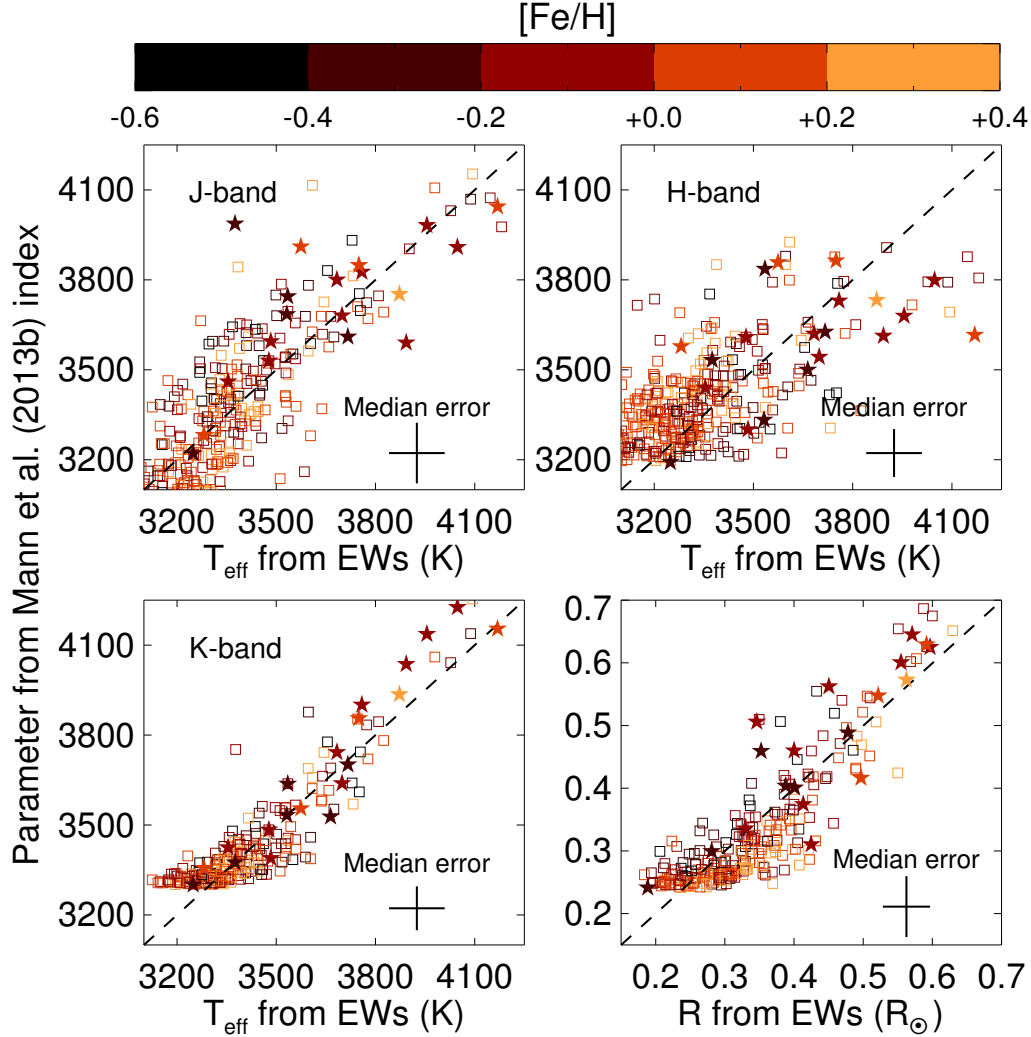


Figure 3.7.— A comparison of the calibrations from Mann et al. (2013b) and from this work, showing the T_{eff} and radii estimated for the M dwarfs from Newton et al. (2014). On the horizontal axis, we show the parameters we infer using the EW-based methods we develop in this work. On the vertical axis, we show the parameters we infer using the index-based methods from Mann et al. (2013b). We use the polynomial presented in that work to convert temperatures estimated from the K -band index to radii. The color of the points indicate the stars' metallicities.

dex. While neither our T_{eff} estimates nor the interferometric measurements indicate such a metallicity dependence, the models still demonstrate the strong influence atmospheric opacities can have on T_{eff} (they predict less sensitivity for M_K versus radius or L_{bol}). Unresolved binaries also contribute significantly to the scatter, which we discuss in §3.4.4.

3.4.4 Identifying over-luminous objects

An object that is an unresolved multiple will have an M_K smaller than that of a single star with the same value of L_{bol} predicted from our Equation 3.3: the EWs of spectral features are largely unchanged by the object’s multiplicity (though for very tight binaries features might appear broadened), while the object appears brighter. Our sample contains binaries that are unresolved in 2MASS but for which independent spectra of the components were obtained: when two stars could be identified in the SpeX guider, Newton et al. (2014) aligned the slit along both components and extracted each object separately. As expected, many of these objects are brighter than single stars with similar spectrally-inferred stellar parameters. The diagram of M_K versus L_{bol} shows the excess scatter at brighter magnitudes most clearly.

To quantify the likelihood of an object being a multiple, we calculate the significance of the magnitude offset (S) between the object and a quadratic that describes our empirical M_K -luminosity sequence. We fit M_K as a function of $\log L/L_{\odot}$ for stars with $\log L/L_{\odot} > -2.5$, which is the limit of our calibration, using σ_{M_K} as our measurement error. We then exclude those objects whose magnitudes are brighter than the best-fitting magnitude by more than the 0.52 mag, which is the standard

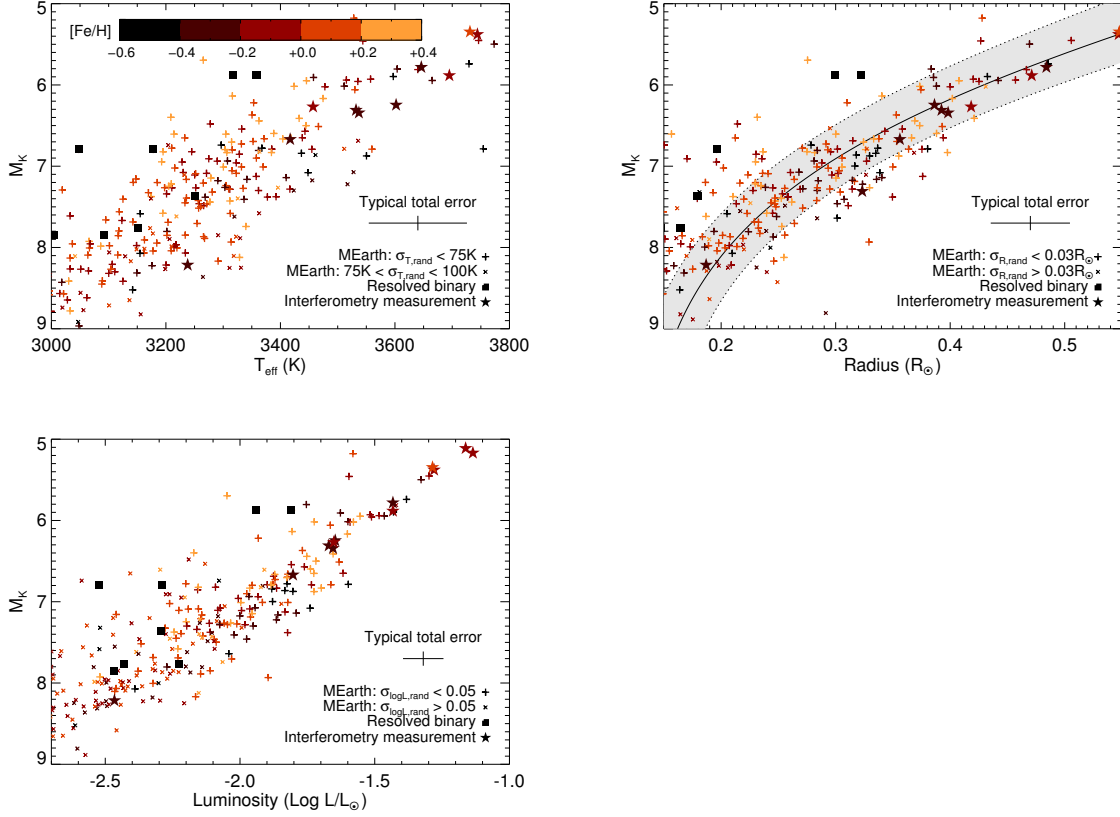


Figure 3.8.— Absolute K magnitude versus inferred T_{eff} , radius, or L_{bol} for M-dwarfs from Newton et al. (2014). Included are stars with $\sigma_{M_K} < 0.2$ mag; the symbol indicates the size of the error on stellar parameter (plus symbols for smaller errors, crosses for larger errors). We over-plot the properties of the interferometry stars (filled stars); we show the measured radii and the temperatures and luminosities calculated in Mann et al. (2013b) and in this work. The $[\text{Fe}/\text{H}]$ of each data point is indicated by its color. We also indicate binaries that are unresolved in 2MASS but resolved in our IRTF observations (filled black squares). In the radius plot (upper right), we also include an M_K -radius relation, calculated from the Delfosse et al. (2000) M_K -mass relation and the Boyajian et al. (2012) mass-radius relation. The shaded region indicates $\pm 15\%$.

deviation in the residuals, and re-fit the data. We extrapolate the fit to stars with fainter luminosities. S is then given by:

$$S = \frac{M_K - M_{K,\text{fit}}}{\sqrt{\sigma_{M_K}^2 + \sigma_{M_{K,\text{fit}}}^2}} \quad (3.5)$$

We show the distribution of S -values in Figure 3.9, which is well-modeled by a Gaussian with a width of $\sigma = 1.5$. An obvious feature is an overabundance of stars that appear too bright for the L_{bol} we infer (objects with $S < 0$), and we identify objects with very negative S -values as potential multiples. We note that the width of the Gaussian indicates that our estimates of the errors do not account for all of the scatter in the relation. One possible contributor is binaries with more extreme mass ratios, as the secondary would increase the combined brightness by a lesser amount.

We select those stars with $S < -3.76$ (-2.5σ) as candidate multiples. We include the list of candidates in Table 3.6, which we note does not include the systems identified as visual binaries by Newton et al. (2014), which can be found in that work. 18 of these stars are in fact known binaries that were not resolved in our IRTF observations, as indicated in the table. Others may be previously-unidentified multiples. While youth is another possibility for explaining their brightnesses, a candidate over-luminous object would need to be younger than several hundred Myr to show an enhanced K -band magnitude, which is unlikely for a field M dwarf.

3.5 Applications to *Kepler* Objects of Interest

We apply our calibrations to the high fidelity sample of 66 KOIs selected as described in Section 3.2.3. The KOIs are primarily early M to mid K dwarfs, with a small

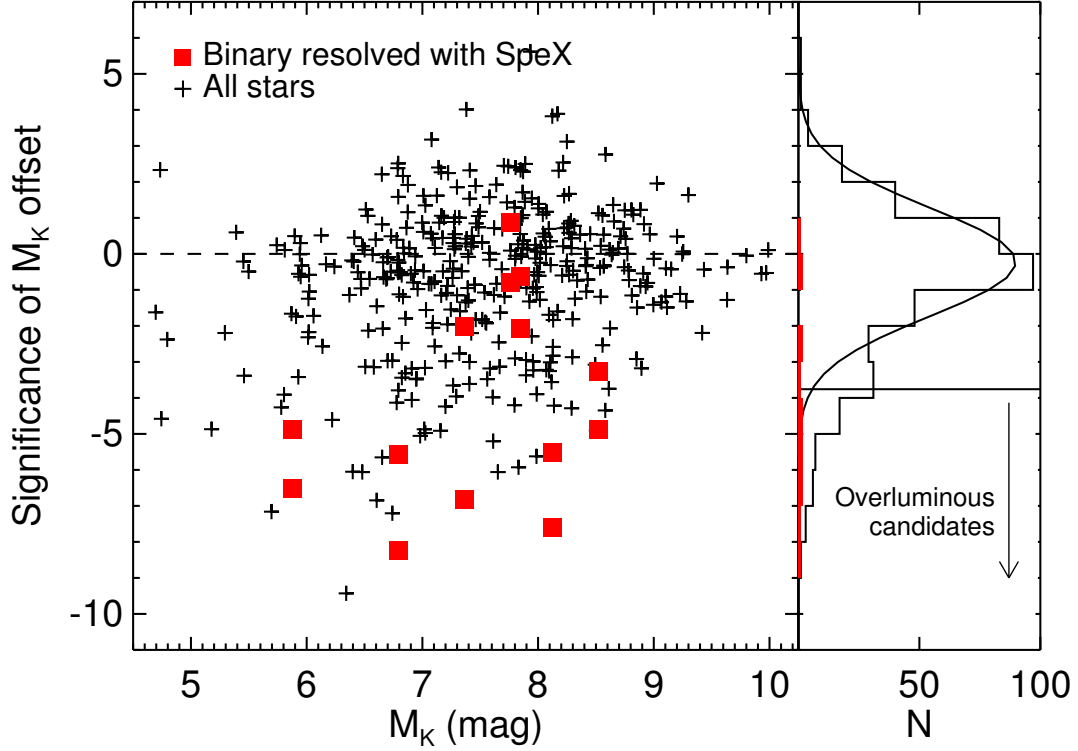


Figure 3.9.— Significance S versus absolute K magnitude for the MEarth M dwarfs. S is the offset in magnitudes from our empirical M_K -log luminosity main sequence divided by the error, which includes the error in absolute magnitude and in inferred luminosity. On the right side of the figure, we include a histogram of the significances for our entire sample (black histogram) and the best-fitting Gaussian, which has a width of 1.5 (solid curve). We also show the histogram of significances for the IRTF-resolved binaries (solid red histogram). In the histogram panel, we indicate the 2.5σ cut we use to select candidate overluminous objects, which are listed in Table 3.6.

Table 3.6. Candidate overluminous objects

Object	$ S ^a$	Binary Ref. ^b	Binary Type ^c
LSPM J0008+2050	4.8	B04	VB
LSPM J0028+5022	4.1	D07	VB
LSPM J0105+2829	4.1
LSPM J0111+1526	4.9	B04	VB
LSPM J0159+0331E	4.6	S10	SB2
LSPM J0259+3855	3.9	L08	VB
LSPM J0409+0546	4.1	L08	VB
LSPM J0438+2813	4.0	B04	VB
LSPM J0528+1231	6.0
LSPM J0540+2448	5.4	D76	VB
LSPM J0711+4329	4.2	M06	VB
LSPM J0736+0704	5.1	H97	VB
LSPM J0810+0109	3.9
LSPM J0835+1408	6.0
LSPM J0918+6037W	4.1
LSPM J1000+3155	4.7
LSPM J1233+0901	5.7	WDS ^d	VB
LSPM J1331+2916	7.1	G02	SB2
		B04	VB
LSPM J1332+3059	4.2
LSPM J1419+0254	3.7
LSPM J1547+2241	5.6
LSPM J1555+3512	4.2	M01	VB
LSPM J1604+2331	5.0
LSPM J1616+5839	4.8
LSPM J1707+0722	3.8	P05	VB
LSPM J1733+1655	5.9
LSPM J1841+2447S	6.8	G96	SB2
LSPM J2010+0632	4.6	S10	SB2
LSPM J2040+1954	3.9	WDS ^e	VB
LSPM J2117+6402	7.1
LSPM J2223+3227	4.8	W60	VB

Table 3.6—Continued

Object	$ S ^a$	Binary Ref. ^b	Binary Type ^c
--------	---------	--------------------------	--------------------------

^aAbsolute value of the significance of the magnitude offset from our empirical main sequence as defined by Equation 3.5. All objects are over-luminous given their inferred luminosities.

^bReference for previous discovery of the object as binary. If no reference is listed, our literature search did not identify that the object is known to be binary. References: W60 = Worley (1960); D76 = Dahn et al. (1976); G96 = Gizis & Reid (1996); H97 = Henry et al. (1997b); M01 = McCarthy et al. (2001); G02 = Gizis et al. (2002); B04 = Beuzit et al. (2004); P05 = Pravdo et al. (2005); M06 = Montagnier et al. (2006); D07 = Daemgen et al. (2007); L08 = Law et al. (2008); S10 = Shkolnik et al. (2010)

^cType of binary: VB = visual binary; SB2 = double-lined spectroscopic binary

^dThis object is the well-known binary Wolf 424 (Gl 473AB), which is identified in the Washington Double Star catalog. We confirmed that its original discovery was by Reuyl (1938).

^eThis object is listed in the Washington Double Star Catalog as a visual binary, discovered by Riddle et al. (in prep) using Robo-AO, who indicate that it is a chance alignment.

number of mid M dwarfs. Muirhead et al. (2014) identified three KOIs as visual binaries (two of which meet our sky emission cuts) and KOI 256 as a white dwarf-M dwarf eclipsing binary, which we exclude from this analysis. Unlike for the MEarth objects, the EWs for the KOIs do not approach zero and it is therefore not necessary to use the limits on the errors we adopted for the MEarth objects. However, for ease of comparison, we restrict the discussion in this section to those KOIs with random errors less of than 150K on T_{eff} . This leaves us with 51 non-visual binaries in our KOI sample.

The cool KOI sample has been the subject of several recent works, and as part of this work, we compare the stellar parameters we infer to those presented in Dressing & Charbonneau (2013), Mann et al. (2013b), and Muirhead et al. (2014). Dressing & Charbonneau (2013) matched observed colors to Dartmouth models of different ages, metallicities, and masses. From the best-fitting model, they revised the temperatures and radii for all the M dwarfs in *Kepler* with formal errors typically between 50 to 100 K for T_{eff} and $0.06 R_{\odot}$ for radius. Mann et al. (2013b) fit flux-calibrated optical spectra to PHOENIX models to determine the T_{eff} of *Kepler* M dwarfs with an estimated error of 57 K, and used relations derived from stars with interferometric measurements to calculate radius and luminosity from T_{eff} . Their radius and luminosity errors are 7% and 13%, respectively. They refined and tested their method using the interferometric sample, which is also the basis for our work. We note that when fitting spectra without continuum removal, the spectral shape – and therefore the color – is an important determinant. Muirhead et al. (2014) followed the method developed in Muirhead et al. (2012a), using moderate resolution *K*-band spectra to determine temperatures and metallicities for 103 cool KOIs. Their temperatures are based on the

H₂O-K2 index (Covey et al. 2010), which was calibrated by Rojas-Ayala et al. (2012) as a tracer of T_{eff} using measurements of BT-Settl model spectra. Typical formal errors for T_{eff} are 65K. The authors then inferred the stars' radii by interpolating the T_{eff} and metallicities onto Dartmouth isochrones, achieving a median formal error on stellar radius of $0.06 R_{\odot}$. We note that Muirhead et al. (2014) used new stellar models, and provided updated parameters for those objects that were first presented in Muirhead et al. (2012b).

3.5.1 Comparison to previous work

We compare our inferred temperatures and radii to those from previous works in Figures 3.10 and 3.11. The literature sources we query are Mann et al. (2013b), Muirhead et al. (2014), and Dressing & Charbonneau (2013). We also apply the K-band calibration from Mann et al. (2013b) to the KOI spectra to estimate T_{eff} , after which we use their temperature-radius relation to estimate radii (see §3.4.2). We adopt the metallicities from Muirhead et al. (2014).

We cannot make statements about temperature differences above 3900K. The literature sources we query have their own target selection criteria, each of which places an upper limit of roughly 4000K on the temperatures of the stars in their sample. This is particularly important for the sample from Dressing & Charbonneau (2013), whose sample is strictly limited to stars with updated temperatures of less than 4000K. Mann et al. (2013b) and Muirhead et al. (2014) both use color cuts to select red objects, which could also bias the resulting temperatures since their methods are related to spectral colors. Finally, the H₂O-K2 index used by Muirhead

et al. (2014) saturates for $T_{\text{eff}} > 3800\text{K}$.

The temperatures we find generally agree well with those from other works. They are cooler than those inferred from previous spectra-based approaches: the median temperature difference is $80 \pm 90\text{K}$ considering the K -band index, $10 \pm 60\text{K}$ considering Mann et al. (2013b), and $30 \pm 70\text{K}$ considering Muirhead et al. (2014). Compared to Dressing & Charbonneau (2013), the temperatures we infer are hotter by a median of $40 \pm 90\text{K}$. The errors we quote are the median absolute deviations in the temperature differences.

The radii we infer are larger than those found by Mann et al. (2013b), with a median difference of $0.02 R_{\odot}$ and a median absolute deviation of $0.04 R_{\odot}$. This difference may be due to their use of a temperature-radius relation, which assumes that all stars at a given temperature have the same radius, but is within reasonable systematic uncertainties for the calibrations.

Our radii are also larger than the radii estimated using methods based on model isochrones, by $0.05 \pm 0.03 R_{\odot}$ relative to Muirhead et al. (2014) and $0.09 \pm 0.04 R_{\odot}$ relative to Dressing & Charbonneau (2013). Because our temperatures are in agreement, the difference in the radii must result from their use of models to estimate radius from temperature. Indeed, Boyajian et al. (2012, Figure 14) found that for stars with interferometrically-measured radii between $0.4 < R/R_{\odot} < 0.6$, the model radii – predicted by interpolating each stars' T_{eff} onto Dartmouth models – are smaller than the measured radii by about 10%, or $0.05 R_{\odot}$. We illustrate the disagreement between observations and models by comparing the temperatures and radii of the interferometric sample to Dartmouth isochrones in Figure 3.12. This effect is

sufficient to explain the differences between our radii and those from Muirhead et al. (2014).

The discrepancy between models and observations also affects the radii from Dressing & Charbonneau (2013). However, the difference between our radii and those from Dressing & Charbonneau (2013) is larger because of the metallicities they estimate. In the Dartmouth models, an M dwarf with $[\text{Fe}/\text{H}] = -0.2$ is about $0.04 R_{\odot}$ smaller than a solar-metallicity dwarf of the same temperature; such a metallicity dependence is not seen in the temperatures and radii of the interferometry stars. Dressing & Charbonneau (2013) estimated sub-solar metallicities for most of the KOIs, whereas the metallicities from Muirhead et al. (2014) are closer to solar (see Figure 7 in Dressing & Charbonneau) and Dressing & Charbonneau (2013) therefore find smaller radii. This can also be seen in Figure 3.12. The overall offset between the observed and theoretical temperatures and radii, and the sub-solar metallicities they estimated are what cause our inferred radii to be substantially larger than those reported in Dressing & Charbonneau (2013).

3.5.2 Updated stellar and planetary parameters

We use the data available on the NASA Exoplanet Archive⁷ to update the properties of the planet candidates orbiting the cool KOIs. We compare the planets properties that we get using our stellar parameters to those that one would infer using the stellar parameters in the catalog from Huber et al. (2014). Huber et al. (2014) synthesized stellar parameters available in the literature for objects in the *Kepler* Input Catalog.

⁷<http://exoplanetarchive.ipac.caltech.edu/>, accessed 2014/06/10

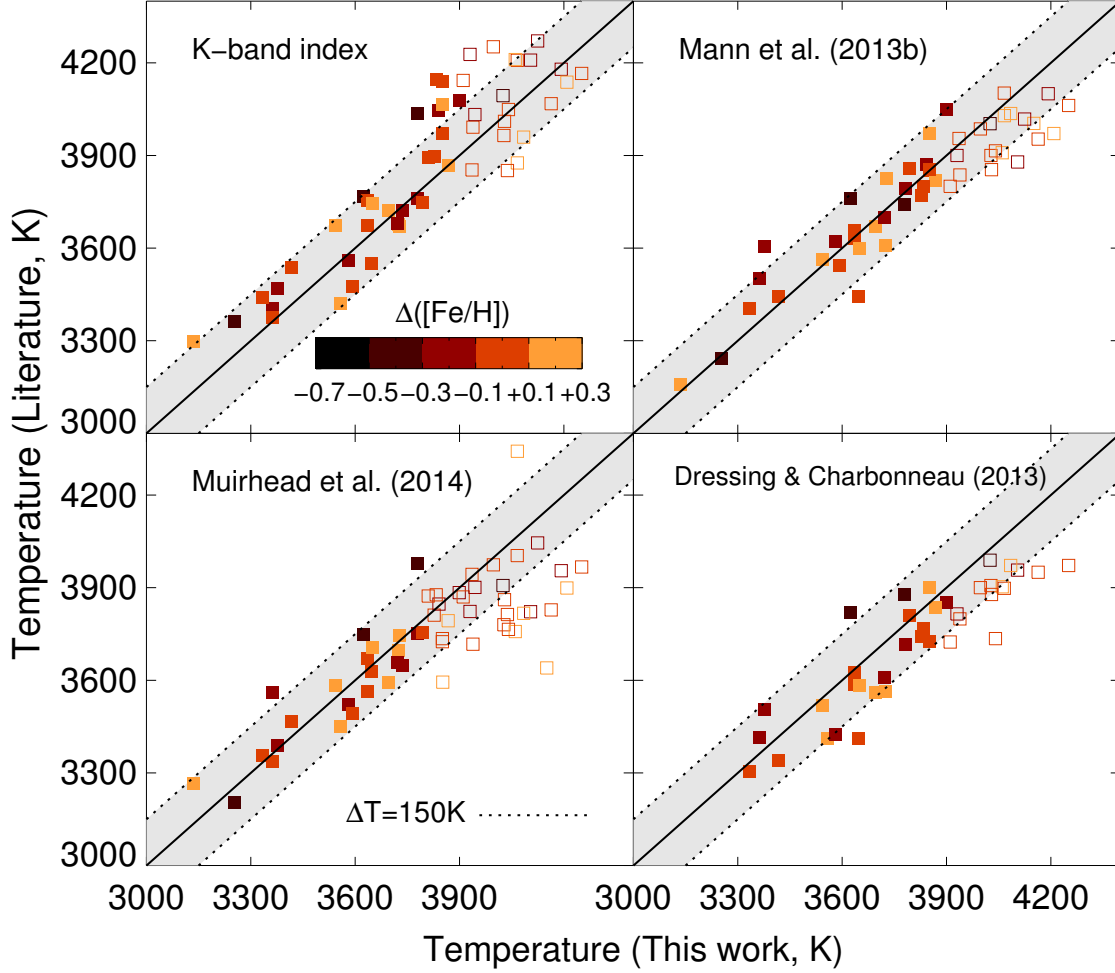


Figure 3.10.— Comparison between the temperatures we infer for the KOIs and those inferred from previous works. Our estimates are on the horizontal axis, and those from the literature are on the vertical axis. The literature works are indicated on each panel. We show the one-to-one line and indicate $\pm 150\text{K}$ as the shaded region. Stars with $T_{\text{eff}} > 3900\text{ K}$ ($T_{\text{eff}} > 3800\text{ K}$ for Muirhead et al. 2014) are shown as open squares; due to selection effects, we limit our discussion to cooler stars.

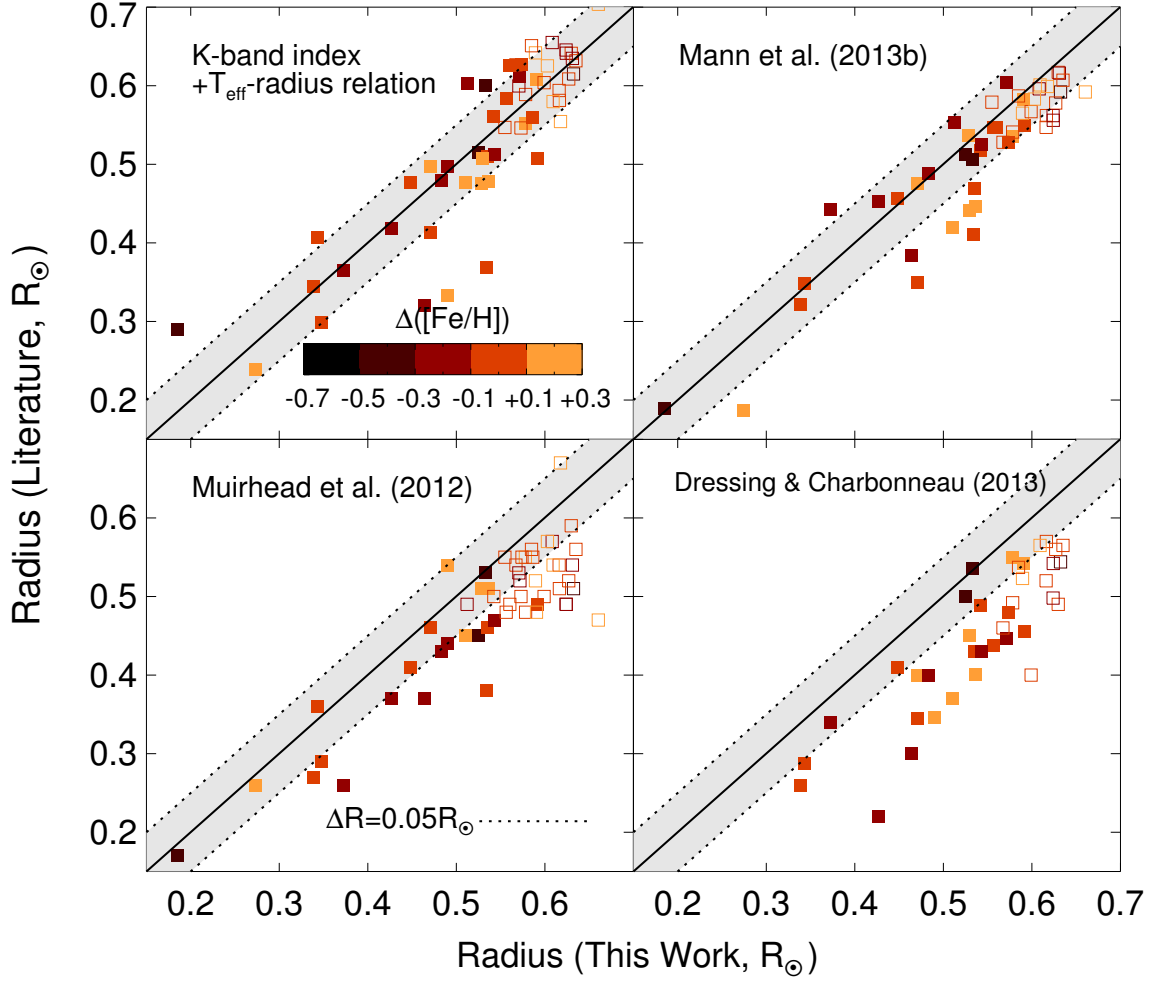


Figure 3.11.— Comparison between the radii we infer for the KOIs and those inferred from previous works. Our estimates are on the horizontal axis, and those from the literature on the vertical axis. The literature works are indicated on each panel. We show the one-to-one line and indicate $\pm 0.05 R_{\odot}$ using the shaded region. Stars with $T_{\text{eff}} > 3900$ K (> 3800 K for Muirhead et al. (2014)) are shown as open squares; due to selection effects, we limit our discussion to cooler stars.

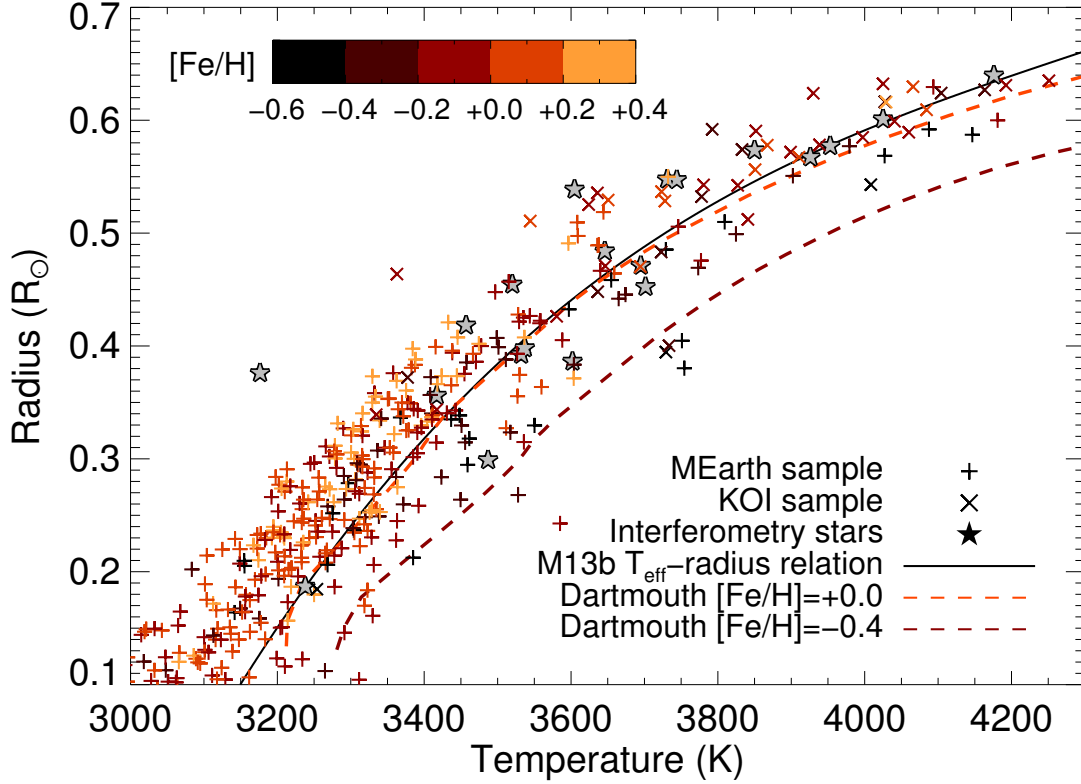


Figure 3.12.— Temperature-radius diagram for the stars in this work, showing the measured values for the interferometric sample (gray stars) and the values we infer using EWs for the MEarth sample (plus symbols) and the KOIs (crosses). We color the MEarth and KOI samples by their estimated metallicities. For MEarth, we estimate metallicities using relations from Mann et al. (2013a) and Mann et al. (2014), and for the KOIs we use the metallicities from Muirhead et al. (2014). We also include the Mann et al. (2013b) temperature-radius relation (solid black line) and 5 Gyr, solar alpha-enhancement Dartmouth isochrones for $[\text{Fe}/\text{H}] = 0.0$ dex (dashed orange line) and $[\text{Fe}/\text{H}] = -0.4$ dex (dashed dark red line). Gl 725B (measured $T_{\text{eff}} = 3142$ K, $R = 0.32 R_{\odot}$) was used to calibrate our radius relation but not our temperature relation, and is not shown. The largest outlier from the interferometric sample is Gl 876 (measured $T_{\text{eff}} = 3176$ K, $R = 0.38 R_{\odot}$).

For the M dwarfs, measurements primarily come from Muirhead et al. (2012b) and Dressing & Charbonneau (2013).

To update the planetary radii we use the planet-to-star radius ratio (r/R_*) and calculate r using either our new stellar radius or that from Huber et al. (2014). To update planet equilibrium temperatures (T_{eq}), we assume that the planet radiates the same amount of heat as it receives, that heat is distributed isotropically, that the planet has an albedo of $a = 0.3$, and that the star and planet radiate as blackbodies. This gives the familiar equation $T_{eq} = T_{\odot} \times (1 - a)^{1/4} \sqrt{R_*/2d}$. The ratio between the planet-star distance and the stellar radius (d/R_*) is another directly measured transit parameter. We calculate T_{eq} using either our new stellar effective temperature or that from Huber et al. (2014).

We present our updated stellar and planetary parameters in Table 3.7. In Figure 3.13, we show how the planet radii and equilibrium temperatures change when using our updated parameters. The difference in equilibrium temperature is largely negligible, but our new stellar radii have a significant effect on the radii of orbiting planets: the typical planet is 15% larger with our stellar parameters than with those in Huber et al. (2014).

3.5.3 Comments on individual systems

Two KOIs stand out because our new radii are smaller than those in Huber et al. (2014). These are the candidate planets orbiting KOI 2715, for which the previous best stellar parameters come from the *Kepler* Input Catalog (Brown et al. 2011).

Three *Kepler* targets in our sample have previously received significant attention. KOI 961 (*Kepler*-42) hosts a suite of sub-Earth-sized planets and was analyzed by Muirhead et al. (2012a), who inferred this star’s properties by tying models to Barnard’s star, which has a directly measured radius. While the temperature we estimate is nearly 200 K hotter than the temperature from their analysis, the two estimates are consistent (3068 ± 174 K versus 3254 ± 110 K). The radii are also in very good agreement: $0.17 \pm 0.04 R_{\odot}$ in their analysis versus 0.19 ± 0.04 in this work.

Johnson et al. (2012) presented KOI 254 (*Kepler*-45), an early M dwarf hosting a hot Jupiter, and found $R = 0.55 \pm 0.11 R_{\odot}$ and $T_{\text{eff}} = 3820 \pm 90$ K, again consistent with our results of $R = 0.58 \pm 0.03 R_{\odot}$ and $T_{\text{eff}} = 3870 \pm 80$ K.

KOI 571 (*Kepler*-186) was recently announced as hosting an Earth-sized planet in its habitable zone (*Kepler*-186f, Quintana et al. 2014). The stellar parameters listed for this star in Huber et al. (2014) and in our Table 3.7 are from Muirhead et al. (2012b). Quintana et al. (2014) separately determined the radius for this star by finding the Dartmouth model best matching the mean stellar density, determined from transit photometry, and the metallicity and T_{eff} from Muirhead et al. (2012b). Their radius of $0.47 \pm 0.05 R_{\odot}$ is smaller than our estimate of $0.53 \pm 0.03 R_{\odot}$, but is consistent. We also revise the radius of *Kepler*-186f upward, from $1.02 R_{\oplus}$ to $1.17 R_{\oplus}$; a planet of this size is still likely to be rocky (e.g. Rogers 2015). The T_{eff} (3624 ± 80 K) and luminosity ($0.048 \pm 0.008 L_{\odot}$) we infer for this object are also consistent with the properties from Quintana et al. (2014), who estimated $T_{\text{eff}} = 3788 \pm 54$ K and $L = 0.041 \pm 0.009 L_{\odot}$. Therefore, our results support the conclusion that *Kepler*-186f is a rocky, habitable-zone planet.

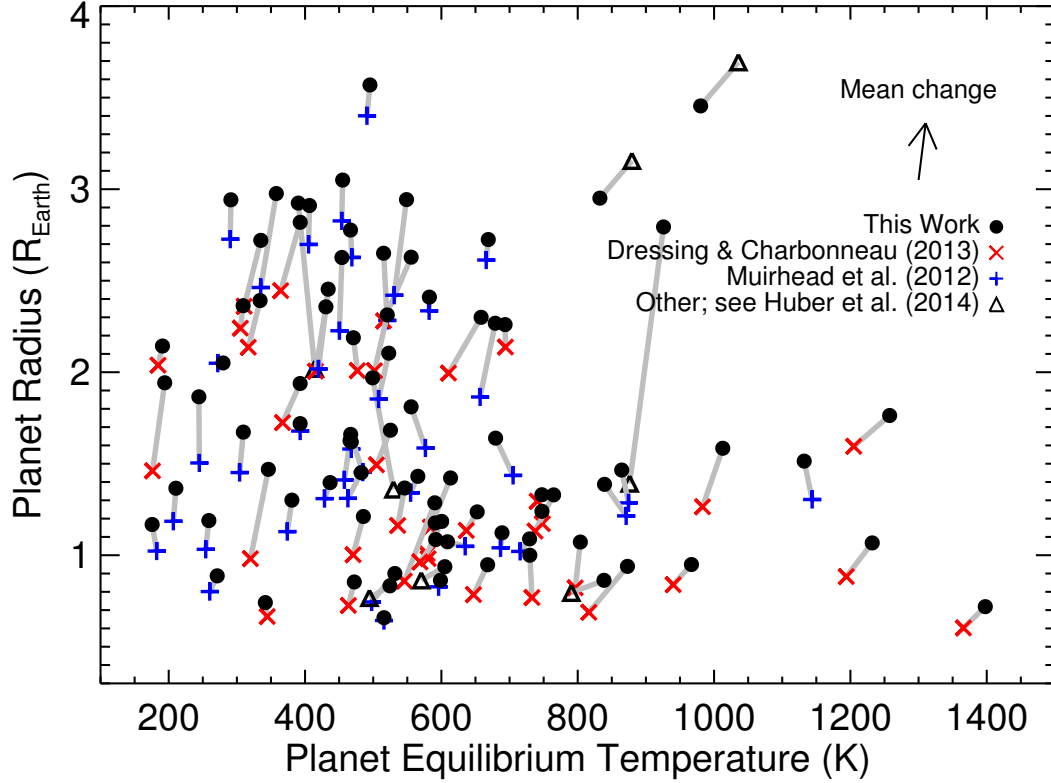


Figure 3.13.— Planet radius versus planet equilibrium temperature, when using stellar properties from Huber et al. (2014) or updated parameters from this work (filled circles). The Huber et al. (2014) catalog primarily draws M dwarf stellar parameters from Dressing & Charbonneau (2013, red crosses) and from Muirhead et al. (2012b, blue pluses), with small numbers of objects from other works (black open triangles). We use planet properties from the NExSci database (accessed 2014/06/10). Gray lines connect the previous and updated values for each planet.

3.6 Summary

We presented empirical calibrations for the effective temperatures, radii, and luminosities of cool dwarfs. We used 24 M dwarfs with interferometrically-measured parameters (25 for our radius calibration) to calibrate our relationships, which are based on EWs of *H*-band spectral features. Our relationships are applicable to dwarfs with $3100 < T_{\text{eff}}/\text{K} < 4800$, $0.2 < R/R_{\odot} < 0.8$, and $-2.5 < \log L/L_{\odot} < -0.5$. The standard deviations in the residuals of the best-fits are 73 K, $0.027 R_{\odot}$, and 0.049 dex (11%). From our bootstrap analysis, our luminosity calibration is the only one for which systematic error is important, but comparing temperature, radius, and luminosities indicates that there may be additional sources of systematic uncertainty. Our calibrations can be applied to stars without parallaxes and to non-flux calibrated spectra, and can be used very effectively for early M dwarfs with $3700 < T_{\text{eff}}/\text{K} < 4000$, where the $\text{H}_2\text{O-K2}$ index used by Muirhead et al. (2012a) and Muirhead et al. (2014) to estimate temperature saturates. This is an important regime for understanding planets orbiting cool stars, because these are the late-type dwarfs with the greatest representation in *Kepler*. Figure 3.12 summarizes our results: we show the measured parameters for the interferometric stars on which the calibration is based, and the properties we infer for the MEarth and *Kepler* samples.

Our investigation of *H*-band spectral features also revealed that the EWs we measure of features in our observed spectra that are not strongly dependent on metallicity – in particular, Mg I features – show the best agreement with the EWs we measure from synthetic spectra. Conversely, the EWs we measure for features for which a metallicity dependence is apparent are the most discrepant.

CHAPTER 3. EMPIRICAL TEMPERATURES AND RADII FOR COOL STARS

We applied our calibrations to the MEarth sample of M dwarfs and validated the stellar parameters we infer by demonstrating that they display a clear relationship with M_K , which is an independent tracer of the stars' underlying physical properties. By comparing M_K to inferred stellar luminosity, we identified 31 candidate multiples. 18 of the objects we identified in this manner are known binaries. We also used the luminosities we estimated to demonstrate that the Newton et al. (2014) metallicity calibration over-estimates the metallicities of late M dwarfs, and updated the metallicities of the sample using the calibrations from Mann et al. (2013a) and Mann et al. (2014).

Using spectra from Muirhead et al. (2014), we applied our calibration to the cool stars from *Kepler* that host candidate planets. The temperatures that we find agree remarkably well with the temperatures reported in previous works, particularly given the different methods used, while our new stellar radii are larger. The largest discrepancy (median difference $0.09 R_\odot$) arises when we compare our radii to Dressing & Charbonneau (2013), who fit photometry to Dartmouth models to estimate stellar parameters. The primary cause of the discrepancy is that at a given T_{eff} , the interferometrically-measured radii are larger than those predicted by models by about 10% (Boyajian et al. 2012), so the model-based radii from Dressing & Charbonneau (2013) are too small. The sub-solar metallicities they infer for the KOIs also contribute. Using our new stellar parameters, we updated the properties of the candidate planets, finding that the typical planet is larger than what one would calculate using the recent catalog from Huber et al. (2014) by 15%. The properties we infer for KOIs 961 (*Kepler*-42), KOI 254 (*Kepler*-45), and KOI 571 (*Kepler*-186) are consistent with the results from previously-published in-depth studies of those

objects.

Our new calibrations have the benefit of being independent of stellar models. Because of the discrepancies between theoretical and observed stellar parameters, methods that rely on fixing stellar parameters to models will be subject to systematic errors. We note two important considerations that were discussed by Boyajian et al. (2012). First, stellar radii for these low-mass stars generally are measured to be larger than predicted. Second, the effect of metallicity on radius does not appear to be as strong in the interferometric sample as is predicted by models, so metal-poor M dwarfs may be particularly misrepresented by such methods. We note, however, that we see some evidence of a metallicity dependence in the temperature-radius plane when considering the larger sample of stars to which we have applied our calibrations (see §3.4.2 and Figure 3.12). Additional interferometric measurements – particularly of mid-to-late M dwarfs and stars of extreme metallicity – would improve both our empirical calibrations and our general understanding of the physical properties of low-mass stars.

CHAPTER 3. EMPIRICAL TEMPERATURES AND RADII FOR COOL STARS

Table 3.7. Stellar parameters of cool Kepler Objects of Interest with high-fidelity spectra

KOI	<i>Kepler</i> ID	Huber et al. (2014)			T_{eff} (K)	This work		Lit. ^c		This work	
		T_{eff}^a (K)	Radius ^a R_{\odot}	Ref. ^b		Radius R_{\odot}	Luminosity $\log L/L_{\odot}$	R_p R_{\oplus}	T_{eq} K	R_p R_{\oplus}	T_{eq} K
247.01	11852982	3741	0.49	SPE5	3850 ± 75	0.556 ± 0.027	-1.18 ± 0.06	1.85	507	2.10	522
250.01	9757613	3887	0.53	SPE5	3899 ± 100	0.572 ± 0.028	-1.10 ± 0.14	2.83	453	3.05	455
250.02	9757613	3887	0.53	SPE5	3899 ± 100	0.572 ± 0.028	-1.10 ± 0.14	2.70	405	2.91	406
250.03	9757613	3887	0.53	SPE5	3899 ± 100	0.572 ± 0.028	-1.10 ± 0.14	1.04	686	1.12	688
250.04	9757613	3887	0.53	SPE5	3899 ± 100	0.572 ± 0.028	-1.10 ± 0.14	2.73	290	2.94	291
251.01	10489206	3810	0.52	SPE5	3827 ± 84	0.542 ± 0.029	-1.20 ± 0.07	2.61	665	2.72	668
251.02	10489206	3810	0.52	SPE5	3827 ± 84	0.542 ± 0.029	-1.20 ± 0.07	0.83	595	0.86	598
254.01	5794240	3820	0.55	SPE43	3867 ± 82	0.578 ± 0.028	-0.97 ± 0.10	10.23	691	10.71	700
255.01	7021681	3770	0.51	SPE5	4027 ± 81	0.616 ± 0.027	-1.01 ± 0.12	2.46	334	2.98	357
255.02	7021681	3770	0.51	SPE5	4027 ± 81	0.616 ± 0.027	-1.01 ± 0.12	0.74	497	0.90	531
314.01	7603200	3841	0.50	SPE5	3841 ± 73	0.512 ± 0.027	-1.33 ± 0.05	1.58	467	1.62	467
314.02	7603200	3841	0.50	SPE5	3841 ± 73	0.512 ± 0.027	-1.33 ± 0.05	1.68	392	1.72	392
314.03	7603200	3841	0.50	SPE5	3841 ± 73	0.512 ± 0.027	-1.33 ± 0.05	0.64	515	0.66	515
463.01	8845205	3387	0.30	SPE5	3377 ± 79	0.372 ± 0.028	-1.71 ± 0.06	1.50	244	1.87	244
478.01	10990886	3744	0.50	SPE5	3727 ± 74	0.529 ± 0.027	-1.27 ± 0.06	2.63	468	2.78	466
531.01	10395543	4030	0.60	SPE5	4065 ± 76	0.630 ± 0.028	-0.92 ± 0.07	3.40	490	3.57	495
571.01	8120608	3761	0.46	SPE5	3624 ± 79	0.525 ± 0.029	-1.32 ± 0.07	1.44	705	1.64	679
571.02	8120608	3761	0.46	SPE5	3624 ± 79	0.525 ± 0.029	-1.32 ± 0.07	1.59	576	1.81	555
571.03	8120608	3761	0.46	SPE5	3624 ± 79	0.525 ± 0.029	-1.32 ± 0.07	1.21	870	1.39	839
571.04	8120608	3761	0.46	SPE5	3624 ± 79	0.525 ± 0.029	-1.32 ± 0.07	1.45	484	1.66	466
571.05	8120608	3761	0.46	SPE5	3624 ± 79	0.525 ± 0.029	-1.32 ± 0.07	1.02	182	1.17	175
596.01	10388286	3678	0.47	SPE5	3635 ± 78	0.536 ± 0.028	-1.35 ± 0.08	1.29	874	1.47	864
818.01	4913852	3721	0.52	SPE5	3723 ± 86	0.537 ± 0.028	-1.36 ± 0.10	2.34	581	2.41	582
854.01	6435936	3593	0.47	SPE5	3694 ± 85	0.470 ± 0.032	-1.12 ± 0.06	2.05	271	2.05	279
898.01	7870390	3893	0.52	SPE5	4025 ± 99	0.632 ± 0.038	-0.71 ± 0.09	2.42	530	2.94	548
898.02	7870390	3893	0.52	SPE5	4025 ± 99	0.632 ± 0.038	-0.71 ± 0.09	1.86	656	2.27	679
898.03	7870390	3893	0.52	SPE5	4025 ± 99	0.632 ± 0.038	-0.71 ± 0.09	2.02	419	2.45	433
899.01	7907423	3568	0.42	SPE5	3636 ± 77	0.448 ± 0.030	-1.28 ± 0.06	1.34	554	1.43	565
899.02	7907423	3568	0.42	SPE5	3636 ± 77	0.448 ± 0.030	-1.28 ± 0.06	1.02	715	1.09	729
899.03	7907423	3568	0.42	SPE5	3636 ± 77	0.448 ± 0.030	-1.28 ± 0.06	1.31	428	1.40	436
936.01	9388479	3581	0.44	SPE5	3544 ± 78	0.511 ± 0.028	-1.40 ± 0.07	2.28	520	2.65	515
936.02	9388479	3581	0.44	SPE5	3544 ± 78	0.511 ± 0.028	-1.40 ± 0.07	1.30	1143	1.51	1132
947.01	9710326	3750	0.46	SPE5	3780 ± 92	0.543 ± 0.034	-1.24 ± 0.07	2.23	450	2.63	454
961.01	8561063	3068	0.17	SPE41	3254 ± 106	0.185 ± 0.043	-2.73 ± 0.07	0.86	570	0.94	605
961.02	8561063	3068	0.17	SPE41	3254 ± 106	0.185 ± 0.043	-2.73 ± 0.07	0.79	790	0.86	838
961.03	8561063	3068	0.17	SPE41	3254 ± 106	0.185 ± 0.043	-2.73 ± 0.07	0.77	494	0.83	524
1085.01	10118816	3939	0.52	SPE5	3777 ± 97	0.532 ± 0.030	-1.07 ± 0.09	1.05	634	1.07	608

CHAPTER 3. EMPIRICAL TEMPERATURES AND RADII FOR COOL STARS

Table 3.7—Continued

KOI	<i>Kepler</i> ID	Huber et al. (2014)			T_{eff} (K)	This work		Lit. ^c		This work	
		$T_{\text{eff}}^{\text{a}}$ (K)	Radius ^a R_{\odot}	Ref. ^b		Radius R_{\odot}	Luminosity $\log L/L_{\odot}$	R_{p} R_{\oplus}	T_{eq} K	R_{p} R_{\oplus}	T_{eq} K
1397.01	9427402	3957	0.54	PHO2	4104 ± 107	0.624 ± 0.032	-1.21 ± 0.16	2.01	501	2.31	520
1408.01	9150827	4023	0.57	SPE5	4192 ± 84	0.631 ± 0.029	-0.78 ± 0.07	1.31	462	1.45	482
1408.02	9150827	4023	0.57	SPE5	4192 ± 84	0.631 ± 0.029	-0.78 ± 0.07	0.80	260	0.89	271
1422.01	11497958	3517	0.37	SPE5	3580 ± 98	0.426 ± 0.031	-1.50 ± 0.08	1.41	457	1.63	465
1422.02	11497958	3517	0.37	SPE5	3580 ± 98	0.426 ± 0.031	-1.50 ± 0.08	1.45	303	1.67	309
1422.03	11497958	3517	0.37	SPE5	3580 ± 98	0.426 ± 0.031	-1.50 ± 0.08	1.13	373	1.30	380
1422.04	11497958	3517	0.37	SPE5	3580 ± 98	0.426 ± 0.031	-1.50 ± 0.08	1.19	206	1.37	210
1422.05	11497958	3517	0.37	SPE5	3580 ± 98	0.426 ± 0.031	-1.50 ± 0.08	1.03	254	1.19	258
1649.01	11337141	3767	0.48	PHO2	3833 ± 102	0.574 ± 0.030	-1.29 ± 0.13	0.98	580	1.18	590
1681.01	5531953	3608	0.40	PHO2	3722 ± 132	0.483 ± 0.033	-1.46 ± 0.09	1.00	470	1.21	485
1681.02	5531953	3608	0.40	PHO2	3722 ± 132	0.483 ± 0.033	-1.46 ± 0.09	0.88	1193	1.07	1231
1681.03	5531953	3608	0.40	PHO2	3722 ± 132	0.483 ± 0.033	-1.46 ± 0.09	0.78	647	0.95	667
1702.01	7304449	3304	0.26	PHO2	3334 ± 99	0.339 ± 0.031	-1.91 ± 0.08	0.82	796	1.07	803
1843.01	5080636	3584	0.45	PHO2	3650 ± 92	0.529 ± 0.031	-1.40 ± 0.09	1.16	536	1.37	546
1843.02	5080636	3584	0.45	PHO2	3650 ± 92	0.529 ± 0.031	-1.40 ± 0.09	0.73	463	0.85	472
1867.01	8167996	3799	0.49	PHO2	3938 ± 112	0.578 ± 0.029	-1.20 ± 0.12	1.13	737	1.33	764
1867.02	8167996	3799	0.49	PHO2	3938 ± 112	0.578 ± 0.029	-1.20 ± 0.12	2.01	415	2.36	430
1867.03	8167996	3799	0.49	PHO2	3938 ± 112	0.578 ± 0.029	-1.20 ± 0.12	1.01	579	1.18	600
1868.01	6773862	3950	0.56	PHO2	4163 ± 133	0.627 ± 0.035	-0.94 ± 0.12	2.14	316	2.39	334
1902.01	5809954	3763	0.46	PHO16	3737 ± 114	0.490 ± 0.032	-1.36 ± 0.12	18.43	172	19.77	171
1907.01	7094486	3901	0.54	PHO2	3851 ± 109	0.591 ± 0.033	-1.24 ± 0.17	2.01	476	2.19	470
2006.01	10525027	3809	0.46	PHO2	3792 ± 93	0.592 ± 0.030	-1.24 ± 0.10	0.77	732	1.00	729
2036.01	6382217	3903	0.52	PHO2	4060 ± 112	0.589 ± 0.031	-1.03 ± 0.15	1.49	504	1.68	525
2036.02	6382217	3903	0.52	PHO2	4060 ± 112	0.589 ± 0.031	-1.03 ± 0.15	0.96	568	1.09	591
2057.01	9573685	3900	0.54	PHO2	3997 ± 118	0.585 ± 0.029	-1.02 ± 0.11	1.14	636	1.24	652
2130.01	2161536	3972	0.56	PHO2	4251 ± 130	0.635 ± 0.037	-0.75 ± 0.09	1.72	367	1.94	392
2191.01	5601258	3724	0.46	PHO2	3910 ± 107	0.567 ± 0.030	-1.24 ± 0.11	1.15	584	1.42	613
2306.01	6666233	3878	0.52	PHO2	4029 ± 89	0.616 ± 0.029	-0.92 ± 0.10	0.94	1546	1.11	1607
2329.01	11192235	3815	0.50	PHO2	3929 ± 135	0.624 ± 0.036	-1.32 ± 0.13	1.26	983	1.58	1012
2347.01	8235924	3972	0.56	PHO2	4084 ± 108	0.609 ± 0.029	-1.25 ± 0.14	1.07	1637	1.16	1684
2542.01	6183511	3339	0.29	PHO2	3417 ± 113	0.344 ± 0.041	-1.65 ± 0.11	0.60	1365	0.72	1397
2650.01	8890150	3735	0.40	PHO2	4040 ± 102	0.599 ± 0.028	-1.12 ± 0.10	0.98	319	1.47	346
2650.02	8890150	3735	0.40	PHO2	4040 ± 102	0.599 ± 0.028	-1.12 ± 0.10	0.86	545	1.29	590
2662.01	3426367	3410	0.34	PHO2	3646 ± 128	0.471 ± 0.031	-1.30 ± 0.11	0.69	816	0.94	872
2704.01	9730163	3327	0.19	PHO54	3134 ± 102	0.274 ± 0.034	-2.17 ± 0.10	2.02	414	2.92	390
2704.02	9730163	3327	0.19	PHO54	3134 ± 102	0.274 ± 0.034	-2.17 ± 0.10	1.36	529	1.97	499
2705.01	11453592	3400	0.27	PHO54	3592 ± 134	0.534 ± 0.044	-1.52 ± 0.18	1.39	876	2.79	925

Table 3.7—Continued

KOI	<i>Kepler</i> ID	Huber et al. (2014)			This work			Lit. ^c		This work	
		$T_{\text{eff}}^{\text{a}}$	Radius ^a	Ref. ^b	T_{eff}	Radius	Luminosity	R_{p}	T_{eq}	R_{p}	T_{eq}
		(K)	R_{\odot}		(K)	R_{\odot}	$\log L/L_{\odot}$	R_{\oplus}	K	R_{\oplus}	K
2715.01	9837661	4385	0.71	KIC0	4150 ± 129	0.660 ± 0.029	-0.90 ± 0.22	6.83	588	6.38	557
2715.02	9837661	4385	0.71	KIC0	4150 ± 129	0.660 ± 0.029	-0.90 ± 0.22	3.69	1035	3.45	980
2715.03	9837661	4385	0.71	KIC0	4150 ± 129	0.660 ± 0.029	-0.90 ± 0.22	3.16	879	2.95	832
2764.01	10073672	3952	0.55	PHO2	4124 ± 117	0.608 ± 0.029	-1.02 ± 0.15	1.59	1204	1.76	1257
2839.01	6186964	3900	0.54	PHO2	3935 ± 136	0.555 ± 0.031	-1.13 ± 0.14	1.29	740	1.33	747
2845.01	10591855	3954	0.55	PHO2	4066 ± 146	0.618 ± 0.031	-0.78 ± 0.22	0.84	940	0.95	966
2926.01	10122538	3903	0.52	PHO2	4208 ± 157	0.603 ± 0.034	-0.95 ± 0.16	2.28	515	2.63	555
2926.02	10122538	3903	0.52	PHO2	4208 ± 157	0.603 ± 0.034	-0.95 ± 0.16	2.00	610	2.30	658
2926.03	10122538	3903	0.52	PHO2	4208 ± 157	0.603 ± 0.034	-0.95 ± 0.16	2.45	364	2.82	392
2926.04	10122538	3903	0.52	PHO2	4208 ± 157	0.603 ± 0.034	-0.95 ± 0.16	2.36	310	2.72	335
2992.01	8509442	3952	0.55	PHO2	4088 ± 141	0.578 ± 0.034	-0.90 ± 0.19	2.04	184	2.14	190
3090.01	6609270	3854	0.53	PHO2	3850 ± 128	0.560 ± 0.030	-1.29 ± 0.16	1.17	748	1.24	747
3090.02	6609270	3854	0.53	PHO2	3850 ± 128	0.560 ± 0.030	-1.29 ± 0.16	2.14	694	2.26	693
3282.01	12066569	3894	0.54	PHO2	3944 ± 127	0.571 ± 0.031	-1.23 ± 0.13	2.24	305	2.36	309
3414.01	6023859	3900	0.54	PHO2	3834 ± 159	0.563 ± 0.039	-1.32 ± 0.16	18.48	239	19.37	235
3749.01	11547869	3311	0.22	PHO2	3362 ± 112	0.348 ± 0.039	-1.81 ± 0.10	8.17	314	12.62	319
4252.01	10525049	3842	0.53	PHO2	3809 ± 117	0.586 ± 0.033	-1.36 ± 0.22	0.67	344	0.74	341
4427.01	4172805	3668	0.43	PHO2	4037 ± 155	0.573 ± 0.050	-1.20 ± 0.14	1.46	176	1.94	194

^aStellar parameter in catalog from Huber et al. (2014)

^bReference for Huber et al. (2014) data. Data primarily come from: SPE5 = (Muirhead et al. 2014); PHO2 = (Dressing & Charbonneau 2013); SPE41=Muirhead et al. (2012b)

^cPlanet properties one infers using the stellar parameters from Huber et al. (2014) and the planet parameters from the NASA Exoplanet Archive

Chapter 4

The Rotation and Galactic Kinematics of Mid M dwarfs in the Solar Neighborhood

E R. Newton, J. Irwin, D. Charbonneau, Z.K. Berta-Thompson, J.A. Dittmann,
A.A. West

The Astrophysical Journal, Volume 821, Issue 2, Article 93, 2016

4.1 Introduction

Rotation is one of the few directly observable stellar properties, and these observations provide constraints on the angular momentum evolution of stars. Late-time angular momentum loss is governed by magnetized stellar winds, which

depend on the magnetic field topology. Stellar rotation therefore provides empirical insight into both the stellar wind and magnetic field. These interlinked properties are also relevant to the detection and characterization of their planetary systems. Stellar winds and magnetic fields affect habitability, potentially stripping the planetary atmosphere (Cohen et al. 2014). Rapidly-rotating, active stars are also difficult targets for exoplanet surveys. Line broadening from the most rapidly-rotating stars and radial velocity signals induced by stellar activity pose challenges for radial velocity surveys (Saar & Donahue 1997; Saar et al. 1998). In transit surveys, periodic modulations from star spots can cause confounding signals (e.g. Berta et al. 2012).

The rotation of fully convective stars (with $M < 0.35 M_{\odot}$; Chabrier & Baraffe 1997) and of those that have an outer convective envelope is both age- and mass-dependent. Stars spin up as they approach the zero-age main sequence, a consequence of Kelvin-Helmholtz contraction and late-stage accretion, and the conservation of angular momentum. To match the rotation periods observed in the youngest clusters, pre-main sequence stars must also experience early angular momentum losses (e.g. Hartmann & Stauffer 1989; Bouvier et al. 1997b). This is thought to be the result of star-disk interactions (e.g. Koenigl 1991; Collier Cameron et al. 1995; Matt & Pudritz 2005). After reaching the main sequence, angular momentum loss is dominated by magnetized stellar winds, the strength of which may depend on mass. By the age of the Hyades, the rotation periods of solar-type dwarfs have reached a narrow range and subsequently obey a Skumanich-type relation (Skumanich 1972) between angular velocity (ω), mass, and age (t), where $\omega \propto t^{-1/2}$. The well-defined rotation-age relation and the lack of dependence on initial conditions gives rise to the concept of gyrochronology (Barnes 2003).

The convergence of stellar rotation periods can be described by a parametrized wind-loss model (Kawaler 1988; Reiners & Mohanty 2012), in which more rapid rotators spin down faster. The rate of angular momentum loss is thought to saturate for stars with angular velocities faster than some mass-dependent critical value ω_{sat} . This is typically modeled as a change in how the angular momentum loss rate depends on rotation rate, which occurs when the angular velocity drops below the critical value. This leads to a change in the time dependence of the rotation rate itself. In the most common prescription (e.g. Bouvier et al. 1997b), during the saturated regime (rapid rotation), ω decreases exponentially with time, and in the unsaturated regime, ω follows the Skumanich law. This behavior causes the rotation periods to converge as the stars evolve from the saturated to unsaturated regime. The well-behaved relationship between rotation, age, and color for solar-type stars with ages older than roughly 650 Myr can be used to infer ages of isolated field stars through gyrochronology, by measuring their rotation period and color.

For solar-type stars, angular momentum evolution can be modeled with reasonable success using presently-available observations. However, these models may not be able to simultaneously fit the evolution of the lowest mass dwarfs (e.g. Irwin et al. 2011a; Reiners & Mohanty 2012). This could arise from a different magnetic dynamo in fully-convective stars. Models of the solar magnetic dynamo indicate the importance of stellar rotation in the generation of the solar magnetic field (see Charbonneau 2005, for a review). The tachocline, the interface between the radiative and convective zone, has also been thought to be key. In some solar dynamo models, the tachocline is where the strengthening and organization of the solar magnetic field occurs. The tachocline is not present in fully-convective stars;

nevertheless, strong magnetic fields appear to be prevalent amongst these low-mass stars (Johns-Krull & Valenti 1996; Reiners & Basri 2010). Theoretical models of magnetic dynamos in fully-convective stars focus on how rotation and convection can maintain a magnetic field in the absence of a tachocline (e.g. Chabrier & Küker 2006; Dobler et al. 2006; Browning 2008; Yadav et al. 2015a).

Measurements of stellar rotation provide insight into angular momentum evolution and the magnetic dynamo. Observational constraints at young ages come predominantly from open clusters and moving groups, with ages of a few Myr (e.g. the Orion Nebular Cluster) to the Hyades and Praesepe (650 Myr; Perryman et al. 1998; Gáspár et al. 2009; Bell et al. 2014). The Sun and the old stellar clusters NGC 6811 (1 Gyr) and NGC 6819 (2.5 Gyr) provide anchors at older ages for stars around solar mass (Meibom et al. 2011, 2015). While solar-mass stars have converged to a narrowly-constrained mass-rotation relation by 650 Myr, M dwarfs still show a broad range of rotation rates at this age and continue to undergo substantial angular momentum evolution at field ages. Observations of *field* M dwarfs are therefore particularly important for constraining their angular momentum evolution. Substantial observational progress has been made in recent years, with many new measurements of rotation periods for field M dwarfs, notably by Kiraga & Stepień (2007), Norton et al. (2007), Hartman et al. (2011), Irwin et al. (2011a), Kiraga (2012), Goulding et al. (2013), Kiraga & Stepień (2013), and McQuillan et al. (2013).

Determining the ages of field stars is important for enabling their use in modeling rotational evolution. M dwarf radii and effective temperatures remain mostly unchanged once they reach the main sequence and therefore do not provide robust constraints on their ages. Galactic kinematics provide one possible avenue:

CHAPTER 4. THE ROTATION AND KINEMATICS OF NEARBY M DWARFS

The motions of stars through the solar neighborhood bear signatures of their past dynamical interactions. Stars form in dense clusters with kinematics generally constrained to a co-rotating disk with a small scale height and a small velocity dispersion. After their formation, there are two primary effects on the stars' kinematics: the clusters dissipate, and stars undergo dynamical heating. Most clusters are not gravitationally bound and evaporate over time, although some physically-associated, coeval stellar populations persist as the young moving groups and open clusters mentioned previously. Dynamical interactions increase the velocity dispersion of a group of stars over time. This mechanism acts within the kinematically cold stellar population known as the "thin disk," and also is thought to have produced the population of kinematically hotter stars often referred to as the "thick disk". Whether the thick disk should be described by a single population or a superposition of many mono-age or mono-abundance populations has recently been called into question (Bovy et al. 2012; Minchev et al. 2015), but it is composed of stars generally older than, and with different chemical abundances from, the canonical thin disk (Bensby et al. 2005). Within the thin/young disk, the velocity dispersion of a group of stars increases with time. Relationships between age and velocity dispersion have calibrated for stars in the Solar Neighborhood (e.g. Wielen 1977; Nordstrom et al. 2004). Kinematics can therefore shed light on the ages of *populations* of stars.

Irwin et al. (2011a) contributed a substantial number of the currently-available measurements for fully-convective stars, with rotation periods for 41 M dwarfs from the MEarth transit survey (Berta et al. 2012; Irwin et al. 2015) that had published trigonometric parallaxes. By assigning stars to the thin/young and thick/old disk based on their space velocities, we showed that the rapidly-rotating M dwarfs were

on average younger than the slowly-rotating stars.

In this work, we extend the analysis of Irwin et al. (2011a) to the full Northern sample of M dwarfs observed by MEarth. Our sample is particularly of interest due to the large body of observations that our team has gathered on these stars. We measured parallaxes for 1507 of the MEarth targets using MEarth astrometry (Dittmann et al. 2014) and calibrated the MEarth photometric bandpass to provide optical magnitudes for every target (Dittmann et al. 2016). In Newton et al. (2014), we obtained low-resolution near-infrared spectra of 447 MEarth targets, measuring their absolute radial velocities and estimating their iron abundances ($[\text{Fe}/\text{H}]$). Using the $\text{H}\alpha$ line to trace magnetic activity and additional rotation periods derived from MEarth data, we found that the fraction of active stars continues to decrease with increasing rotation period out to the longest rotation periods in the MEarth sample (West et al. 2015).

4.2 Photometry from MEarth

The MEarth Project is an all-sky transit survey searching for planets around approximately 3000 nearby, mid-to-late M dwarfs (Berta et al. 2012; Irwin et al. 2015). MEarth-North is located at the Fred Lawrence Whipple Observatory, on Mount Hopkins, Arizona, and has been operational since 2008 September. MEarth-South, at Cerro Tololo Inter-American Observatory (CTIO) in Chile, was commissioned in January 2014. Each installation consists of eight 40cm telescopes on German Equatorial Mounts, equipped with CCD cameras. This work uses data from only MEarth-North.

CHAPTER 4. THE ROTATION AND KINEMATICS OF NEARBY M DWARFS

Nutzman & Charbonneau (2008) selected the Northern MEarth targets from the Lépine & Shara (2005) Northern proper motion catalog, which includes stars with proper motions $> 0''.15 \text{ yr}^{-1}$. MEarth exclusively targets nearby, mid-to-late M dwarfs: at the time of selection, all stars had parallaxes or distance estimates (spectroscopic or photometric; Lépine 2005) placing them within 33 pc, and estimated stellar radii less than $0.33 R_{\odot}$. Trigonometric parallaxes are now available for the majority of stars in the Northern sample (Dittmann et al. 2014).

MEarth targets are spread across the sky and must therefore be targeted individually; targets are visited at a cadence of 20–30 minutes for observations taken as part of the main planetary transit search. Additional observations of all targets have been taken at a cadence of approximately 10 days since September 2011 for the astrometric program (Dittmann et al. 2014). We also include these data in the analysis presented here. Exposure times are set for each object such that a 2 Earth-radius planet transit would be detected in each datum at 3σ , and therefore depend on the estimated stellar radii. We use the Delfosse et al. (2000) mass- M_K relation to estimate stellar masses, then the Bayless & Orosz (2006) mass-radius polynomial to estimate stellar radii. Our current exposure time calculations also use the trigonometric distances from Dittmann et al. (2014). We did not adjust the exposure time of individual images when we updated the stellar parameters in order to avoid changing the effect of non-linearity on our photometry; instead, we co-add exposures to reach the requisite sensitivity when necessary. Each visit to a star may therefore contain multiple exposures.

Northern target stars are typically observed at the 20–30 minute cadence for one to two observing seasons, with each season lasting from mid-September of one year

to mid-July of the following year. During southern Arizona’s summer monsoons, MEarth-North is shut down completely.

For the 2008–2009 and 2009–2010 observing seasons, we used long-pass filters composed of 5 mm thick Schott RG715 glass. In 2010–2011, in an attempt to mitigate color-dependent systematics (discussed at the close of this section and in Irwin et al. 2006), we switched to a custom filter with a sharp interference cutoff at the red end, approximating the Cousins I-band. Finding that this increased the level of systematics rather than mitigating them, from 2011–2012 onwards we reverted to RG715 filters, but with 3 mm thickness.

We do not attempt to stitch observations taken with different filters or different telescopes together, so the data on each star may be composed of multiple light curves, where we define a *light curve* as the set of observations from a single MEarth telescope with a single filter setup. A single light curve will therefore contain data from one of the 2008–2010, 2010–2011, or 2011–2015 intervals. Each object is usually assigned to a single telescope for the entirety of its observations; however, starting in the 2012–2013 season, two telescopes were assigned to a subset of the targets (see Berta et al. 2012). A small number of targets also appear in multiple fields (where there are multiple targets within the field of view) so may have more light curves.

For our data reduction, we follow the methodology of Irwin et al. (2006), modified for the specifics of the MEarth data as detailed in Berta et al. (2012). We highlight here several systematics that affect our ability to detect rotation periods:

1. Irwin et al. (2011a) noted weather-dependent effects in the differential magnitudes of the target M dwarfs, which result from variations in telluric

water vapor absorption in the bandpass of the RG715 filter, or humidity dependence of the interference cutoff in the interference filters used in 2010–2011. Because our targets are typically the only M dwarfs in the field, the reference stars predominantly have bluer colors. Therefore, the observed fluxes of the targets and reference stars are affected differently by the varying telluric absorption or humidity when integrated over the filter bandpass. This effect cannot be corrected with standard differential photometry procedures, and we note that the resulting systematic effects are dominated by the time variability of the driving quantity (precipitable water vapor or humidity) and are not strongly correlated with airmass, so cannot be corrected by standard methods for removing atmospheric extinction. Instead, the differential magnitudes of all of the M dwarfs being observed within a half-hour window are combined to produce a lower cadence comparison light curve, which we call the "common mode," that measures any residual photometric variations that are common to the target M dwarfs. Due to differences in the target spectral types, it is necessary to scale the common mode by a factor that varies for each object. This scale factor has proved difficult to calculate, so it is fit empirically from the light curve.

2. The MEarth telescopes use German Equatorial Mounts, which require the telescope tube to be flipped over the pier when the target crosses the meridian, resulting in rotation of the focal plane relative to the sky by 180° , and causing stars to sample two distinct regions of the detector. Residual flat-fielding errors result in offsets in the differential magnitudes between the two locations. To correct for this, we assign a different baseline magnitude to observations taken

at these two rotation angles. Additional flat fielding errors are inevitably introduced whenever the cameras are removed from the telescopes for repair, so we introduce a new pair of baseline magnitudes each time this is done. We refer to the set of data taken between these camera removals on a single side of the meridian as a light curve "segment", where each segment is modeled with its own baseline magnitude when producing differential photometry.

3. The large-scale structure of our flat field evolves on timescales of several years. We take nightly twilight flats, but because the illumination is dominated by scattered light, we filter out all of the large-scale structure. To account for the large-scale flat field structure, we observe a star field in the Galactic plane dithered randomly inside a one square degree box, and use photometry to obtain the large scale flat field pattern. These observations require a substantial amount of telescope time during photometric conditions, so are repeated only intermittently. We have used a single large-scale correction for each of the 2008–2010, 2010–2011, and 2011–2015 data sets, in order to avoid introducing spurious signals when there are sudden changes in this correction. However, there are several instances where rapid evolution in the flat-field is evident, which we account for by introducing additional segments with new baseline magnitudes.

We discuss our treatment of these systematics during rotation period determination in the following section.

4.3 Determining rotation periods

We attempt to identify rotation periods in each of the 1883 targets observed with MEarth-North, including data obtained through 16 August 2015.

4.3.1 Period detection

We apply the method used by Irwin et al. (2011a), which is based on Irwin et al. (2006), to fit simultaneously for terms needed to account for both our systematics, and for rotational modulation. For each light curve, we fit both a null hypothesis, which assumes that the light curve has no astrophysical variability and can be fit with systematics alone, and an alternate hypothesis that includes a sinusoid.

Our models include two terms to address the systematics discussed in the previous section: the common mode, and the baseline magnitude in each segment of the light curve.

The null model takes the form:

$$m_{\text{null}}(t) = m_i + k c(t) \quad (4.1)$$

where i is the segment number, and m_i is the baseline magnitude for light curve segment i , t is time and k scales the common mode $c(t)$. We only include as many m_i constants as there are segments containing data points, so for example if a target was observed only on one side of the meridian, only a single baseline magnitude is fit. This model corresponds to a constant intrinsic magnitude (above the Earth's atmosphere) for the target M dwarf, modulated by the atmospheric and instrumental systematics.

The alternate model additionally includes a sinusoid:

$$m_{\text{alt}}(t) = m_{\text{null}}(t) + a \sin(\omega t + \phi) \quad (4.2)$$

where a is the semi-amplitude (in magnitudes), ϕ is the phase, and ω is the angular frequency $\omega = 2\pi/P$, where the rotation period is given by P . For fitting purposes, we rewrite the sine term on the right-hand side of this equation using standard trigonometric identities to replace the non-linear ϕ parameter with a pair of linear semi-amplitudes a_s and a_c :

$$m_{\text{alt}}(t) = m_{\text{null}}(t) + a_s \sin(\omega t) + a_c \cos(\omega t) \quad (4.3)$$

Observations of a star may comprise several separate light curves. These are fit simultaneously, enforcing a common period over all light curves. The common mode scaling, baseline magnitudes, and the amplitude and phase of the sinusoid are independent. Before fitting, we remove data deviating from the median by more than 5σ , where we use the median absolute deviation scaled to the Gaussian-equivalent RMS (Hoaglin et al. 1983) to define σ . Clipping is done to remove flares and (in some cases) eclipses, rather than to iteratively improve our fit by removing outliers. We do not use outlier removal in our fits because we are comparing models at different periods – each model could clip different data, and the χ^2 of poorly-fitting models would be artificially reduced.

We use a maximum likelihood method to find the best-fitting rotation period under the assumption of the alternate hypothesis. We step through a uniformly spaced grid of frequencies corresponding to periods ranging from 0.1 to 1500 days, performing a linear least-squares fit of Eq. (4.3) to the remaining variables at

each frequency. As the null hypothesis is nested within the alternate, an F-test is appropriate for determining whether the addition of a sinusoid is warranted. We therefore calculate the F-test statistic (which measures the amount of variance that is explained by the additional parameters in the alternate model) at each frequency and select the one with the highest statistic as the candidate frequency. The set of F-test statistic values as a function of frequency are analogous to a periodogram.

We then visually inspect the light curves for each M dwarf, looking at the data with the common mode and varying baseline magnitudes removed. We look at differential magnitude as a function of time and at the data phased to the candidate frequency from the F-test. For some objects, multiple exposures were acquired at each visit in order to achieve the S/N we require for planet detection. While fitting is performed on un-binned data, we visually examine the data both binned by visit and un-binned.

We assess the validity of the candidate period by posing a series of questions developed after early exploration of the data, but emphasize that the criteria we use in deciding whether a period is detected are fundamentally qualitative. The questions we ask are:

- Can the candidate periodic rotation signal be seen by eye in the binned, phase-folded data?
- Are two or more complete, near-consecutive rotation cycles seen? An important factor are the baseline magnitudes, which can allow data at disparate times to be offset arbitrarily; thus, data spanning multiple segments must be considered carefully.

- Is the candidate rotation signal uncorrelated with systematics included in the model (baseline magnitude offsets and the common mode) and with the FWHM of the image?
- If the candidate period is < 10 days, can the variability be seen during single, well-sampled nights?
- If there are simultaneously-observed light curves, do the concurrent data agree?

After considering these questions, we classify objects as either "rotators" or "non-rotators". Rotators are objects that we consider to have secure detections of periodic photometric modulation that we assume to be attributable to stellar rotation. We further assign rotators a rating of "grade A" (274 stars) or "grade B" (113 stars). Grade A means that we are confident that we have identified a sinusoidal photometric modulation that can be attributed to an astrophysical source; the answer to all posed questions must be "yes". Grade B means that a modulation has been detected that we believe to be real, but that the signal does not pass all of our tests. Most grade B rotators fail only one criterion, and fall into one of the following categories: 1) two complete cycles are not seen, but the variability that is detected strongly suggests periodic modulation, 2) the only data available are from our astrometric program so the candidate periodicity is not sampled at high-cadence, 3) a convincing period is detected, but the noise level is comparable to amplitude of modulation.

Representative examples of grade A and B rotators are shown in Fig. 4.1. The median of the phased data in ten equally-spaced bins is also included. The sample scatter about the median (1.48 times the median absolute deviation) is shown, but is typically smaller than the data points.

CHAPTER 4. THE ROTATION AND KINEMATICS OF NEARBY M DWARFS

We assign non-rotators a rating of either "possible/uncertain" (239 stars) or "no detection" (1260 stars). If we detect a candidate signal, but are not confident enough in its veracity to consider the object a rotator, we assign it a "possible" rating. A "no detection" rating indicates that we cannot positively identify a periodic modulation. Importantly, "no detection" does not mean that object is not rotating.

While we do not require a specific value for the F-test statistic, our rotators comprise most of the statistically-significant peaks (Fig. 4.2).

We present rotation period measurements for rotators with grade A and B ratings in Table 4.1. We do not attempt to assign errors in these periods (for example, based on the width of the periodogram peak) because there are usually multiple peaks in the periodogram, and an estimate based only on the dispersion about one particular peak would be misleading. We refer the reader to Irwin et al. (2011a) for details of signal injection and recovery tests which can be used to gauge approximate period errors.

We include estimates of stellar mass and radius in Table 4.1. Our stellar masses are estimated from the absolute K magnitude, using the relation from Delfosse et al. (2000), which we modified to allow extrapolation past the limits of the calibration. The relation is unphysical beyond the calibration range of $4.5 < M_K < 9.5$, and a number of our stars are fainter than this limit. Our modification simply enforces a constant value and first derivative slope at the boundaries, and produces a physically reasonable result. For stellar radii, we use the mass-radius relation from Boyajian et al. (2012).

We also include non-rotators with "possible" or "no detection" ratings in Table

4.1, listing the period of the strongest peak in the periodogram. We caution that these periods should not be interpreted as detections. Additional data would be useful for confirming or disproving the listed periods.

The rotation periods and ratings in this paper supersede those reported previously in Irwin et al. (2011a) and West et al. (2015).

4.3.2 Identifying multiples

The multiplicity fraction amongst mid M dwarfs is around 30% (see e.g. Winters 2015, for a review). Close companions can affect a star’s rotation through tidal synchronization or disruption of the protostellar disk (e.g. Meibom & Mathieu 2005; Morgan et al. 2012). Unresolved multiples or background objects could also result in spurious period detections. Our tables note objects identified as multiples in the literature or by visual inspection, and any objects where the MEarth photometric aperture contained known background sources. Including both bright and faint companions, 230 objects in our sample have a nearby, physically-associated companion and 449 have a source in the background. We additionally note objects identified as potentially over-luminous in our previous work. These were identified by Newton et al. (2015), on the basis of their absolute magnitudes and spectroscopically-derived luminosities, or by Dittmann et al. (2016), using their absolute magnitudes and colors.

The analysis in this paper excludes the objects that have bright, unresolved companions (regardless of whether they are common proper motion or background objects, contamination flag 1), or have been identified as over-luminous (flag 4). This

Table 4.1. Kinematics and rotation periods for all rotators and non-rotators (table format)

Column	Format	Units	Description
1	A1	...	Source type: A = Grade A rotators; B = Grade B rotators; U = Possible or uncertain detection; N = Non-detection or undetermined detection.
2	A17	...	2MASS identifier
3	A11	...	LSPM identifier
4	F10.6	deg	RA in decimal degrees (J2000)
5	F11.8	deg	Dec. in decimal degrees (J2000)
6	F6.4	arcsec	Parallax
7	F6.4	arcsec	Uncertainty in parallax
8	A19	...	ADS bibliography code reference for parallax
9	F7.4	arcsec/yr	Proper motion along RA
10	F7.4	arcsec/yr	Proper motion along Dec.
11	F6.1	km/s	Radial velocity
12	F4.1	km/s	Uncertainty in radial velocity
13	A19	...	ADS bibliography code reference for RV
14	F6.1	km/s	Velocity towards Galactic center (U)
15	F6.1	km/s	Velocity in direction of galactic rotation (V)
16	F6.1	km/s	Velocity toward the North Galactic Pole (W)
17	F8.3	days	Photometric rotation period
18	F6.4	mag	Semi-amplitude of variability
19	F6.4	mag	Uncertainty in semi-amplitude
20	F5.3	M_{\odot}	Stellar mass
21	F5.3	R_{\odot}	Stellar radius
22	F5.1	km/s	Rotational velocity
23	I1	...	Flag indicating known or suspected contamination by a common proper motion companion or background source: 1 = Bright contaminant; 2 = Faint contaminant; 3 = Very faint contaminant; 4 = Potentially overluminous.
24	I4	...	Number of data points
25	F6.4	mag	Median photometric error
26	I6	...	F-test statistic

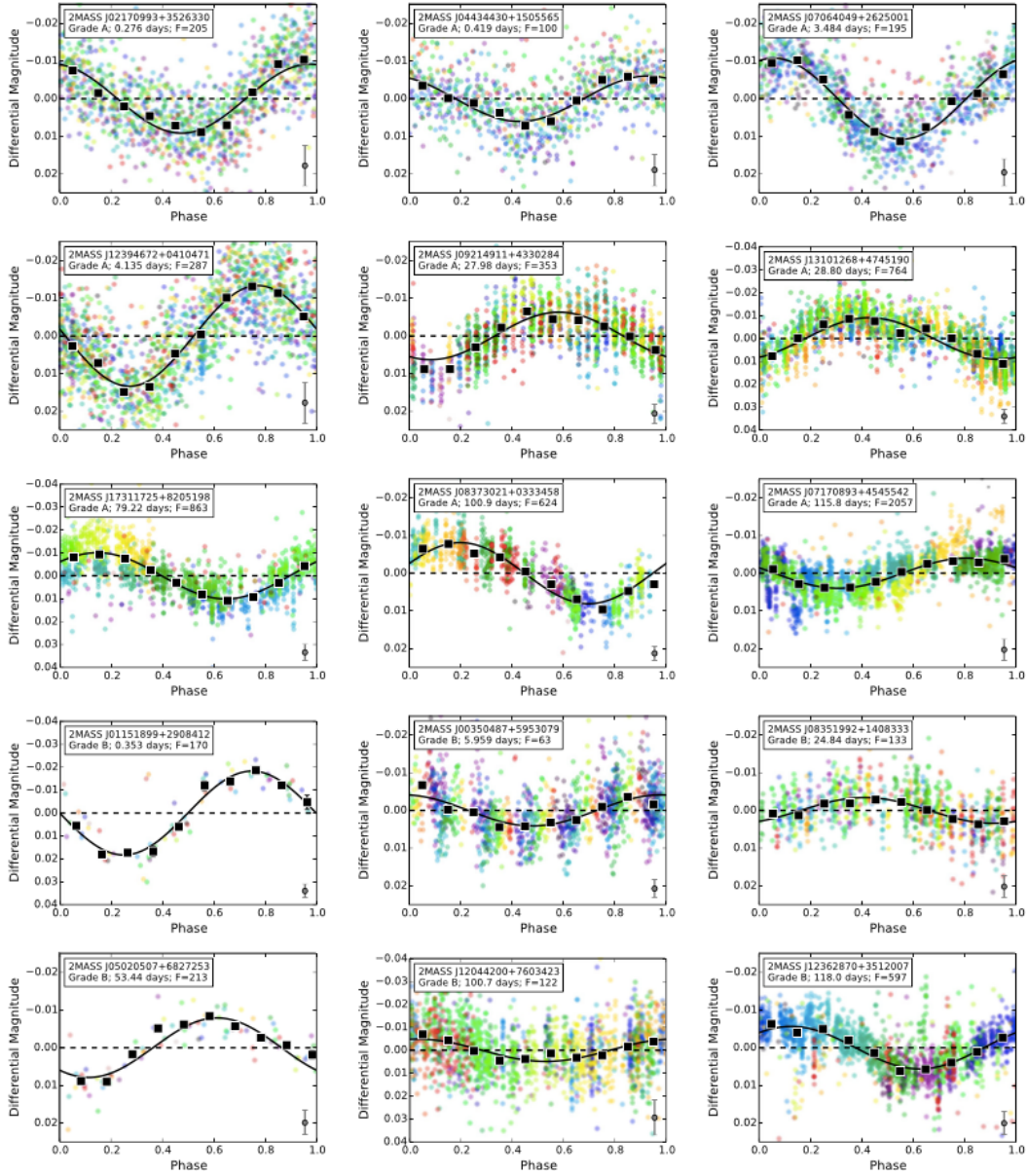


Figure 4.1.— Examples of typical rotators, randomly selected from our sample. The top three rows show grade A rotators, and the bottom two rows show grade B rotators. Data points are colored according to the observation number, and the median error is indicated in the bottom right corner. The earliest data points are purple, the latest are red. We also show the median magnitude in ten uniformly spaced bins in phase; the sample scatter about the median is plotted but typically smaller than the plotting symbol. The label indicates the rating (grade A or B), the rotation period, and the F-test statistic (F). Phased light curves for all grade A and B rotators and for the candidate rotators are available in the electronic edition of the *Astrophysical Journal*.

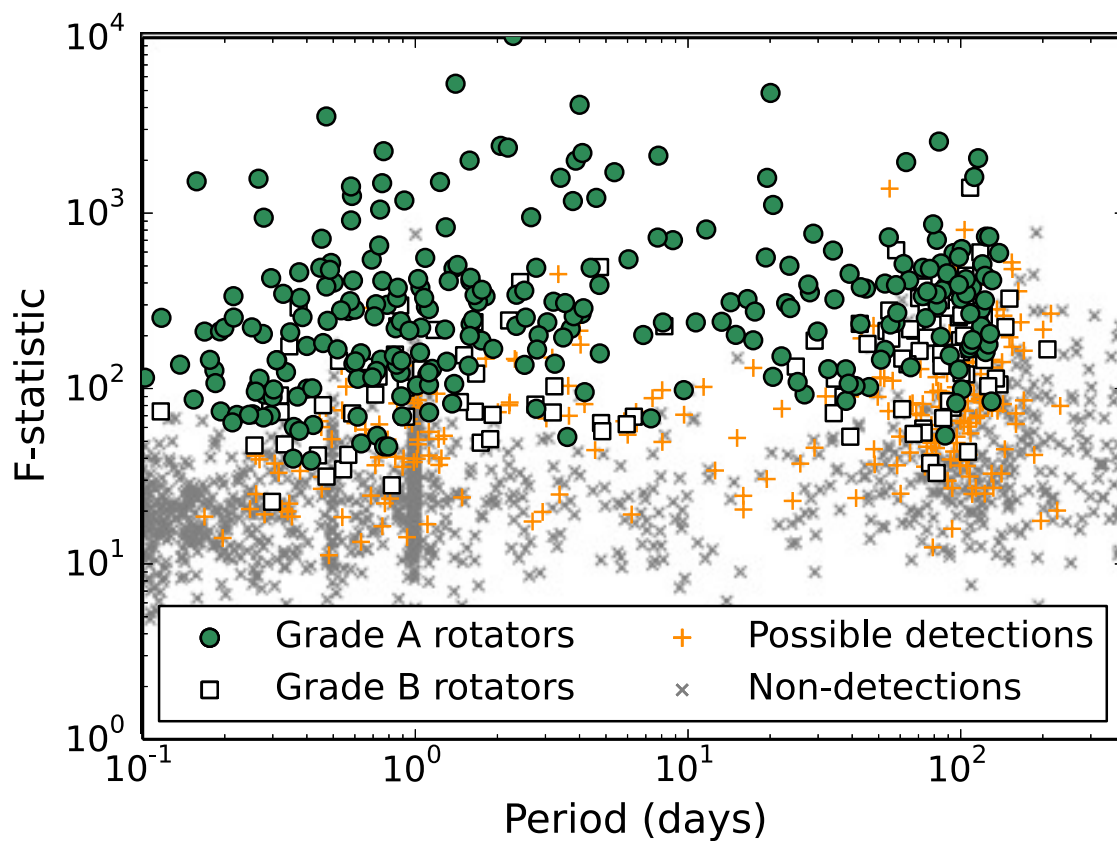


Figure 4.2.— F-test statistic as a function of rotation period for grade A (filled circles) and grade B (open squares) rotators, "possible" detections (plus symbols), and non-detections (crosses).

excludes 211 of the 230 objects with a nearby, physically-associated companion (12% of the full sample). The contaminants are distributed proportionally across the four possible period detection ratings. Objects with faint companions are not excluded.

2MASS J11470543+7001588 (G 236-81) is one such multiple, and is the only object in which we clearly detect two unrelated periods. The periods are 3.49 days and 5.37 days.

4.3.3 Defining a statistical sample

For questions that seek to address how the rotators are different from the non-rotators, we need to know whether or not we could have detected rotation with a certain period and amplitude in a given star. The full Monte Carlo simulation necessary to adequately address period recovery is computationally intensive, so we instead use global properties of the light curves to define a "statistical sample" of stars for which we believe we could have detected long rotation periods. We find that a combination of the number of visits (n_{visits}) to an object and the typical error (σ) of each visit is strongly predictive of whether or not we detected a rotation period, leading us to define the statistical sample as all stars with $n_{\text{visits}} > 1200$ and $\sigma < 0.005$ mag, where σ is the median theoretical error divided by the square root of the number of exposures per visit. There are 311 stars in the statistical sample.

We show the distribution of periods in the statistical sample in Figure 4.3. The grade A rotators are biased towards shorter periods, which are easier to positively identify as being the result of stellar variability even within the statistical sample. The primary reason is that a short-period rotator undergoes more rotation cycles

in a given amount of time than does a long-period rotator. The multiple rotation cycles seen for short periods helps to confirm low-amplitude signals in noisy data, and causes a greater fraction of stars to have enough data to satisfy our requirement of two cycles of modulation (see §4.3.1). The tendency for the grade B rotators and candidate rotators to have long periods is therefore due to the incompleteness of grade A rotators at long periods. Non-detections favor non-astrophysical periods near 1 day or that are very long (1000 days).

We see a relative lack of stars with intermediate rotation periods around 30 days, which we suggest is astrophysical in origin. In the statistical sample, the distribution of best-fitting periods for all stars (including possible detections and stars with no detection) does not indicate a large population of intermediate rotators. This lends support to the idea that our by-eye classification is not lacking sensitivity to intermediate-period rotators.

4.4 Comparison to previous period measurements

A few dozen of our stars have been the targets of other surveys. In this section, we take a closer look at these objects. We first compare our work to that of other ground-based photometric surveys (§4.4.1). In §4.4.2, we look at the few MEarth objects with photometry from the *Kepler* space telescope. The rotational broadening of spectral features provides another means to determine stellar rotation, and we present a comparison to those studies in §4.4.3.

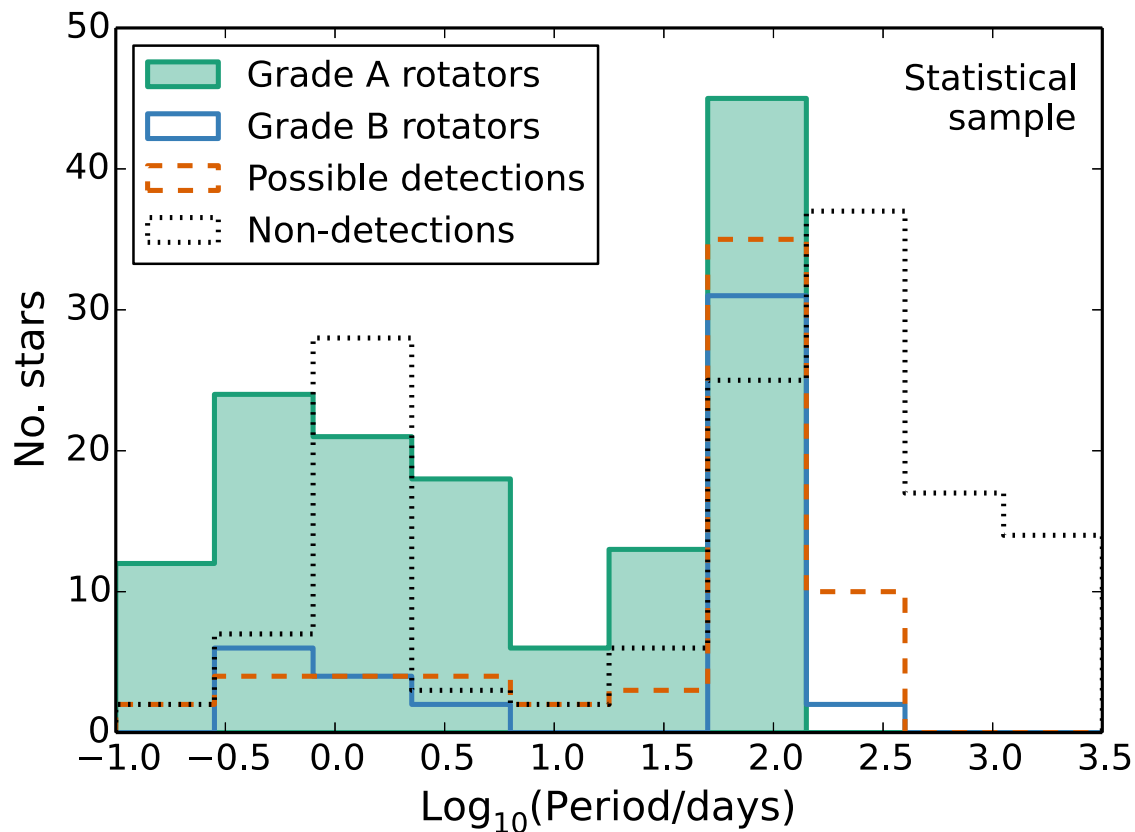


Figure 4.3.— Distribution of best-fitting periods for the grade A and grade B rotators, and uncertain detections in our statistical sample. The lack of grade A rotators at long periods is likely a result of incompleteness. We see a relative lack of stars with intermediate rotation periods, which we suggest is astrophysical in origin.

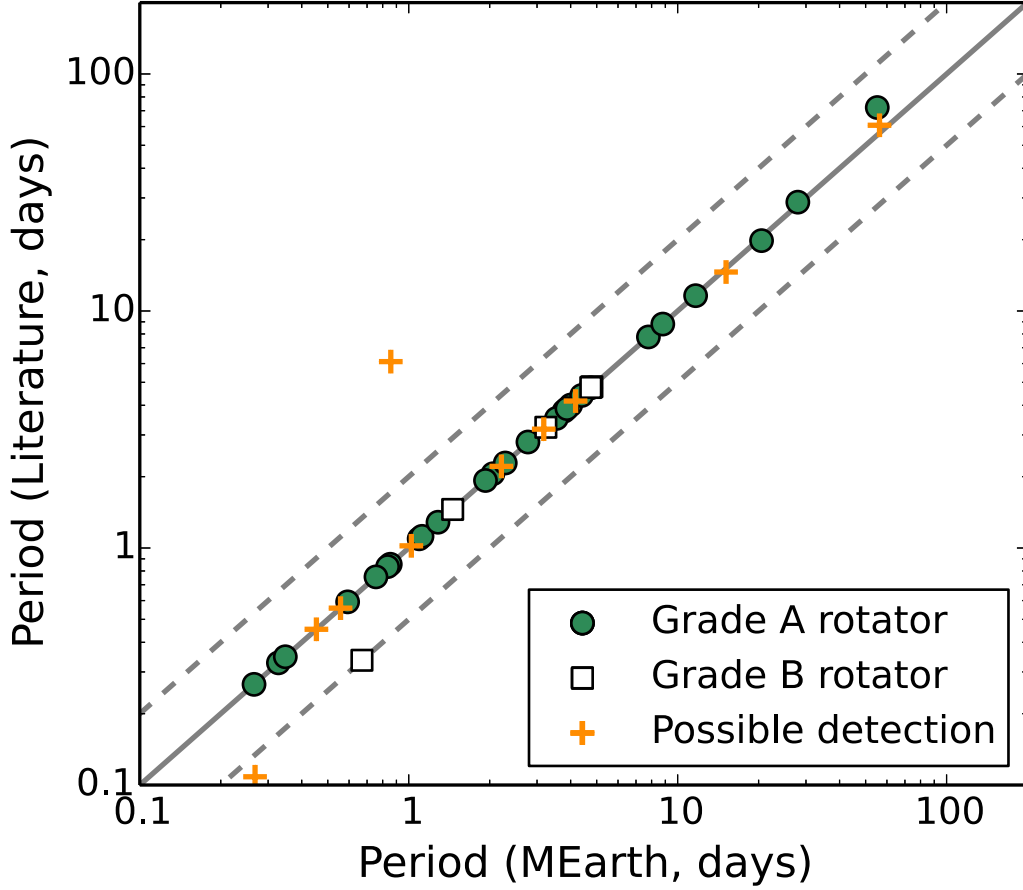


Figure 4.4.— Comparison between photometric period measurements from this work (horizontal axis) and literature sources (vertical axis). We indicate the MEarth period rating assigned for each star with different symbols: grade A rotators (filled circles), grade B rotators (open squares), and possible detections (plus symbols). The solid line indicates exact agreement, while the dashed lines indicate periods twice or half of what we measure. The strong outlier with a literature period at 6.11 days likely results from the daily sampling alias.

4.4.1 Comparison to ground-based photometry

We compare our grade A and B rotators to those with photometric periods from the literature. We additionally show objects with "possible" ratings. Including known multiples, we have overlap with Alekseev & Bondar (1998, 1 star in common), Norton et al. (2007, 5 stars), Hartman et al. (2010, 3 stars), Shkolnik et al. (2010, 2 stars), and Hartman et al. (2011, 25 stars).

Hartman et al. (2011), our primary source for literature measurements, used data from HATNet that spanned time baselines of 45 days to 2.5 years. They searched for rotation periods between 0.1 and 100 days amongst all field K and M dwarfs using analysis of variance (AoV), which tries to find the period that minimizes the scatter in the phased light curve. They decorrelate against external parameters ("EPD" light curves), then against templates built from other objects in the field ("TFA" light curves), and report a quality flag for each detection. We exclude quality flags of 2, and by default use the TFA-based detections. We adopt the EPD-based detections if they have a better quality flag. We noticed that for 2MASS J17195298+2630026 (Gl 669 B), the two algorithms resulted in different periods. The TFA analysis gives $P = 1.45$ days, which agrees with the period we detect. The EPD analysis gives $P = 20$ days, the same period as both we and Hartman et al. (2011) determine for the common proper motion companion 2MASS J17195422+2630030 (Gl 669 A). Although the EPD period had the higher quality flag, we adopt the TFA period for this object.

We find excellent agreement between the periods measured from these surveys and the periods we measure from MEarth (Figure 4.4). Three objects are discrepant. For grade A rotator 2MASS J13505181+3644168 (LHS 6261), our period is 55.7 days

while that from Hartman et al. (2011) is 72.2 days. We also detect a second strong frequency in this object with a period of 93 days. Our frequencies evenly bracket the Hartman et al. detection, so we suspect our periodogram peak has been split as a result of the window function of the MEarth data. For our "possible"-rated object 2MASS J14545496+4108480 (LP 222-15), we find a period of 0.858 days, while Hartman et al. (2011) measure a period of 6.11 days. There is a peak in our periodogram at 6.2 days, and 0.858 is close to the one-day sampling alias of this signal. For our "possible"-rated object 2MASS J13314666+2916368 (DG CVn), we measure $P = 0.268$ days, while Robb et al. (1999) measure 0.108 days. Our candidate signal is affected both by the sparse data set and the baseline magnitude changes.

4.4.2 Comparison to *Kepler*

The *Kepler* space telescope gathered multi-year photometry on approximately 150000 stars, including several thousand M dwarfs, most of which are early Ms (Borucki et al. 2010; Koch et al. 2010). We downloaded *Kepler* light curves for the objects with simultaneous data from MEarth from the Mikulski Archive for Space Telescopes (MAST). We use the PDCSAP_FLUX data; this reduction was intended to remove instrumental systematics while retaining astrophysical variability (Stumpe et al. 2012; Smith et al. 2012). Ten targets in our sample also have data from *Kepler*. We examine the two that have periodic modulations in the *Kepler* data that are detectable by eye (Figure 4.5). We have not detected periods in the remaining objects, though we note that for KIC 6117602, we have a candidate detection of 80 days which is at odds with the 0.67 day period reported by Rappaport et al. (2014).

Table 4.2. Objects with ground-based photometric periods from the literature

2MASS ID	Grade ^a	MEarth P (days)	Lit P (days)	Ref. ^b
Rotators				
J00285391+5022330	A	1.093	1.09332	H11
J02024428+1334335	A	4.003	4.01	S10
J03223165+2858291	A	1.929	1.92673	H11
J03364083+0329194	A	0.328	0.32766	K12
J03425325+2326495	A	0.834	0.834379	H10
J07382951+2400088	A	3.875	3.87463	H11
J07444018+0333089	A	2.775	2.8	A98
J08065532+4217333	A	8.804	8.80699	H11
J09214911+4330284	A	27.984	28.7811	H11
J09441580+4725546	A	4.395	4.40041	H11
J09591880+4350256	A	0.755	0.7554	H11
J10512059+3607255	A	3.782	3.77885	H11
J11031000+3639085	A	2.056	2.05692	H11
J11115176+3332111	A	7.785	7.77026	H11
J11474074+0015201	A	11.662	11.603	K12
J13505181+3644168	A	55.239	72.1768	H11
J15553178+3512028	A	3.542	3.52093	H11
J17195422+2630030	A	20.511	19.8077	N07
J17335314+1655129	A	0.266	0.2659	N07
J18130657+2601519	A	2.285	2.2838	N07
J19510930+4628598	A	0.593	0.592578	H11
J20103444+0632140	A	1.121	1.12	S10
J21322198+2433419	A	4.747	4.7358	N07
J22232904+3227334	A	0.854	0.854	M11
J23025250+4338157	A	0.348	0.347704	H11
J23050871+4517318	A	1.285	1.28447	H11
J00161455+1951385	B	4.798	4.7901	N07
J03284958+2629122	B	3.235	3.23062	H10
J04381255+2813001	B	0.670	0.335985	H11

Table 4.2—Continued

2MASS ID	Grade ^a	MEarth P (days)	Lit P (days)	Ref. ^b
J17195298+2630026	B	1.457	1.454184	H11 ^c
J23545147+3831363	B	4.755	4.757	K13
Candidates				
J02253841+3732339	U	15.135	14.6016	H11
J03264495+1914402	U	0.454	0.454016	H10
J10235185+4353332	U	56.311	60.7517	H11
J10382981+4831449	U	3.178	3.17243	H11
J13314666+2916368	U	0.268	0.10835	R99
J13374043+4807542	U	0.558	0.55754	H11
J14545496+4108480	U	0.858	6.11491	H11
J14592508+3618321	U	4.173	4.16904	H11
J15040626+4858538	U	1.022	1.02136	H11
J15192126+3403431	U	2.211	2.21031	H11

^aMEarth period rating, see description in text.

^bReference for literature photometric period. A98 = Alekseev & Bondar (1998); R99 = Robb et al. (1999); N07 = Norton et al. (2007); H10 = Hartman et al. (2010); S10 = Shkolnik et al. (2010); H11 = Hartman et al. (2011); M11 = Messina et al. (2011); K12 = Kiraga (2012); K13 = Kiraga & Stępień (2013)

^cPeriod from TFA light curve, see text for discussion.

For KIC 9726699 (GJ 1243, Figure 4.5, top panel), we detect a period at 0.59 days, which we assigned grade A. The period, including the indications of asymmetry, is easily identifiable in *Kepler* photometry. For KIC 9201463 (Figure 4.5, bottom panel), for which the *Kepler* light curve has a clear 5.5 day signal, we did not detect a rotation period in the MEarth data alone. However, the MEarth data has power at this frequency, and the modulation matches the phase of *Kepler* signal. The MEarth bandpass is redder than that of *Kepler*, so we expect the amplitude to be lower in our data. The relatively small amplitude (0.5% in the *Kepler* bandpass), somewhat non-sinusoidal modulation, and the frequent flaring are also likely to contribute to our inability to detect the signal independently in MEarth.

4.4.3 Comparison with $v \sin i$ measurements

The rate at which a star spins can also be inferred by measuring the broadening of spectral features due to the rotational velocity (v) of its photosphere. Due to the unknown inclination i only $v \sin i$ can usually be determined. We searched the literature for previous measurements of $v \sin i$ for M dwarfs in the Nutzman & Charbonneau (2008) sample. The papers in which we looked for matches are listed in Table 4.3. We first compare $v \sin i$ measurements directly to other $v \sin i$ measurements from the literature (§4.4.3), and use lessons from this analysis in our comparison of $v \sin i$ and photometric rotation period (§4.4.3).

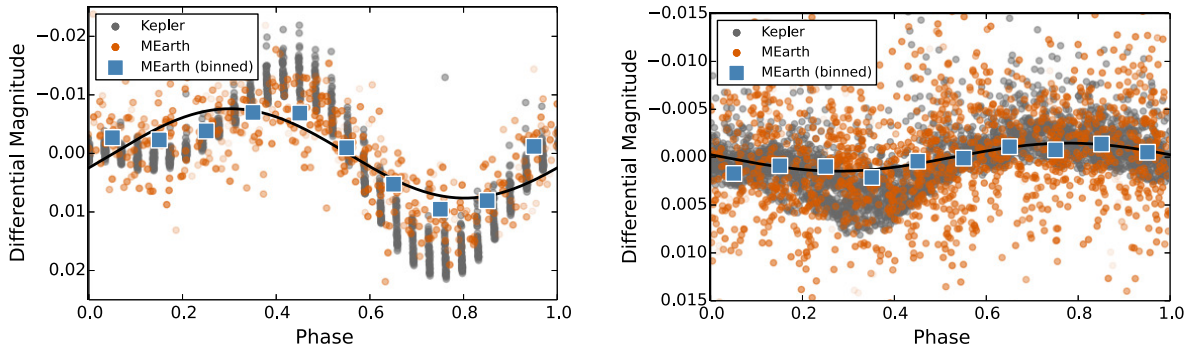


Figure 4.5.— Phased light curves for objects in common between the MEarth and *Kepler* samples, for which a rotation period was detectable by eye in *Kepler*. For KIC 9726699 (top), the rotation period is the best-fitting one found by our analysis. For KIC 9201463 (bottom), the period was identified first in the *Kepler* light curve, after which we found the closest-fitting peak in the periodogram of the MEarth data. Grey points show a subset of the *Kepler* data, MEarth data from the same period of time are shown in orange (with increasing transparency indicating data with larger errors), and the binned MEarth data in blue. The black curve is the sinusoid that best fits the MEarth data.

Table 4.3. Sources for $v \sin i$ compilation

Abbreviation	Reference	Resolving power ($R/1000$)
V83	Vogt et al. (1983)	115
SH86	Stauffer & Hartmann (1986)	20
S87	Stauffer et al. (1987)	20
MC92	Marcy & Chen (1992)	40
T92	Tokovinin (1992)	18
JV96	Johns-Krull & Valenti (1996)	120
S97	Stauffer et al. (1997b)	44
D98	Delfosse et al. (1998)	42
TR98	Tinney & Reid (1998)	19
B00	Basri et al. (2000)	31
S01	Schweitzer et al. (2001)	34/45
G02	Gizis et al. (2002)	19
R02	Reid et al. (2002)	33
MB03	Mohanty & Basri (2003)	31
B04	Bailer-Jones (2004)	39
FS04	Fuhrmeister & Schmitt (2004)	45
J05	Jones et al. (2005)	42
Z05	Zickgraf et al. (2005)	20/22/34
T06	Torres et al. (2006)	50
Z06	Zapatero Osorio et al. (2006)	20
R07	Reiners & Basri (2007)	200
RB07	Reiners & Basri (2007)	31
H07	Houdebine (2008)	45
RB08	Reiners & Basri (2008)	31/33
J09	Jenkins et al. (2009)	37
WB09	West & Basri (2009)	31
B10	Blake et al. (2010)	25
H10	Houdebine (2010)	40/42/75
RB10	Reiners & Basri (2010)	31/32
B10	Browning et al. (2010)	60
R12	Reiners et al. (2012)	40/48

Table 4.3—Continued

Abbreviation	Reference	Resolving power ($R/1000$)
Ba12	Bailey et al. (2012)	30
Bar12	Barnes et al. (2012)	35
D12	Deshpande et al. (2012)	20
H12	Houdebine (2012)	75/115
K12	Konopacky et al. (2012)	30
T12	Tanner et al. (2012)	24
D13	Deshpande et al. (2013)	22.5
M13	Mamajek et al. (2013)	100
B14	Barnes et al. (2014)	54
M14	Malo et al. (2014)	50/52/68/80
D15	Davison et al. (2015)	57
HM15	Houdebine & Mullan (2015)	75/115

Comparison between literature $v \sin i$ measurements

Several of the surveys with $v \sin i$ measurements for our targets used spectrographs with resolving powers ($R \equiv \lambda / \Delta \lambda$) of 20000 to 40000. At these resolutions, the rotational broadening of all but the most rapid rotators falls below the resolution of the spectrograph, and disentangling non-astrophysical sources of broadening from rotational broadening is challenging.

We directly compare $v \sin i$ for M dwarfs from different literature sources, regardless of whether the star was observed by MEarth, in Figure 4.7. Since we do not know the true $v \sin i$, we consider the value measured by the highest-spectral resolution survey (which we call the "primary" survey) and compare it to values measured by lower-spectral resolution ("secondary") surveys. We require that the primary survey resolution be greater than 40000.

For $v \sin i > 20$ km/s, the primary and secondary surveys do not deviate systematically, but there are significant discrepancies for smaller values of $v \sin i$. We find that when inferring $v \sin i$ broadening that is below the spectral resolution, the secondary surveys tend to determine higher values for $v \sin i$ than the primary survey, and the magnitude of the discrepancy varies with the significance of the reported detection. Here we define the $v \sin i$ significance as the $v \sin i$ measured by the primary survey divided by the resolving power in km/s of the spectrograph used in the secondary survey. We find discrepancies in many $v \sin i$ detections with significances less than about 0.8. We therefore arrive at a similar conclusion to Reiners et al. (2012), who found evidence that some detections of $v \sin i$ are spurious.¹ Improved treatment

¹ Houdebine & Mullan (2015) carried out a comparison of $v \sin i$ values and found their measurements and

of $v \sin i$ detection limits, as well as additional or repeated $v \sin i$ measurements at higher resolving power, would be beneficial.

Comparison between $v \sin i$ and photometric measurements

We compare the equatorial rotational velocities (v_{eq}) we infer from the photometric rotation period to the measured $v \sin i$ in Figure 4.6 and Table 4.4. This comparison includes our grade A and B rotators. v_{eq} is calculated from the estimated stellar radius (R) and the rotation period (P) by:

$$v_{\text{eq}} = \frac{2\pi R}{P} \quad (4.4)$$

We do not calculate errors on the rotation period, so for this comparison we assume a 10% error on period (Irwin et al. 2011a) and a 10% error on stellar radius (Delfosse et al. 2000; Boyajian et al. 2012). If the photometric rotation period, stellar radius, and the $v \sin i$ are correct, $v_{\text{eq}} > v \sin i$. Significance is defined as before: the reported $v \sin i$ measurement divided by the resolving power of the spectrograph used.

We first note the stars with reported $v \sin i$ detections at low significance, for which the $v \sin i$ broadening is less than the resolving power of the spectrograph used (brown circles and squares in Figure 4.6). This includes the three objects for which we measured long photometric rotation periods but that have $v \sin i$ measurements indicating rapid rotation. Based on the analysis we presented previously in Figure 4.7, these low-significance $v \sin i$ detections may be incorrect, and we suggest this is the cause of the disagreement with our results.

other surveys agreed well. However, their comparison did not include all of the lower-resolution surveys we considered.

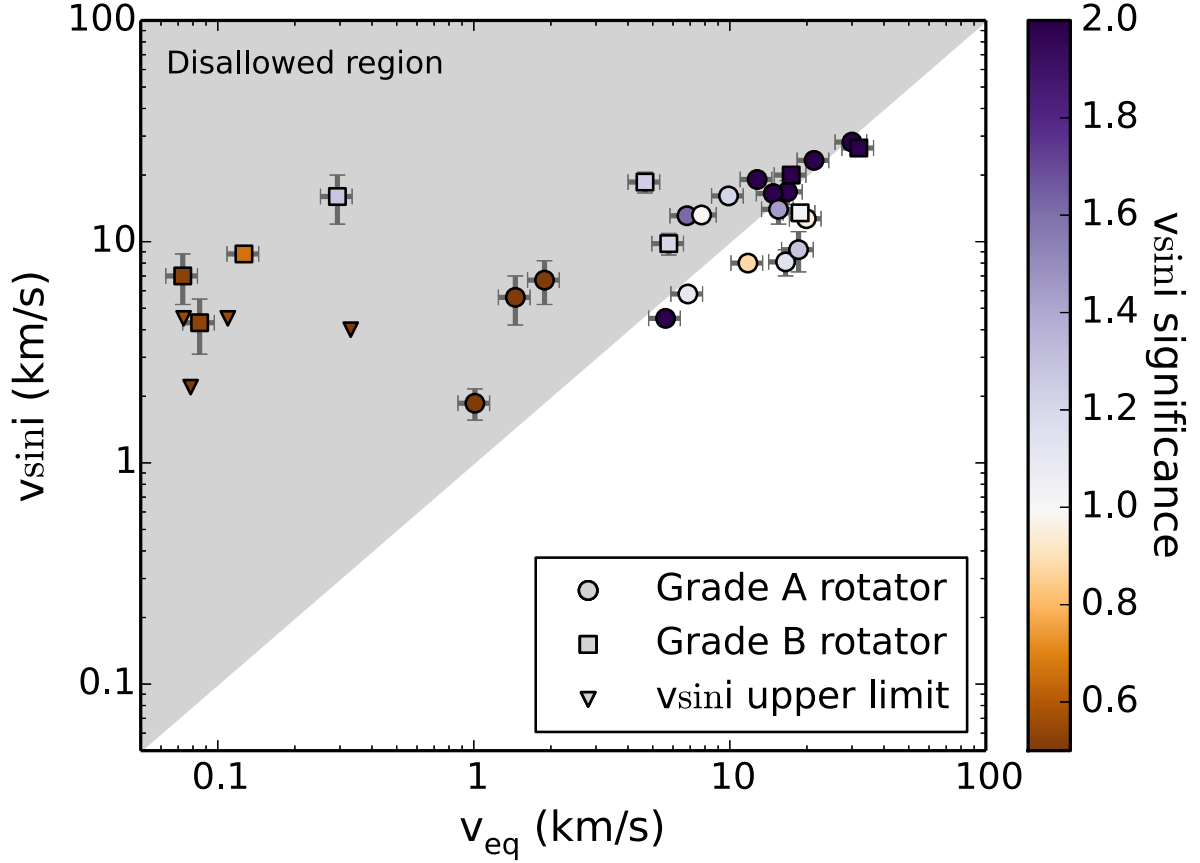


Figure 4.6.— Comparison of estimated equatorial rotation velocities (horizontal axis) and $v \sin i$ measurements from the literature. The color indicates our estimate of the significance of the detection, assuming the $v \sin i$ reported and the resolution of the spectrograph used; smaller values (brown) are less significant, while larger values (purple) are more so. Solid circles (for grade A rotators) and squares (for grade B rotations) indicate $v \sin i$ detections, while triangles indicate an upper limit. Errors on $v \sin i$ are included where available, and we have estimated errors for v_{eq} . The gray shaded region indicates the region where $v \sin i > v_{\text{eq}}$; no detections should fall in this region.

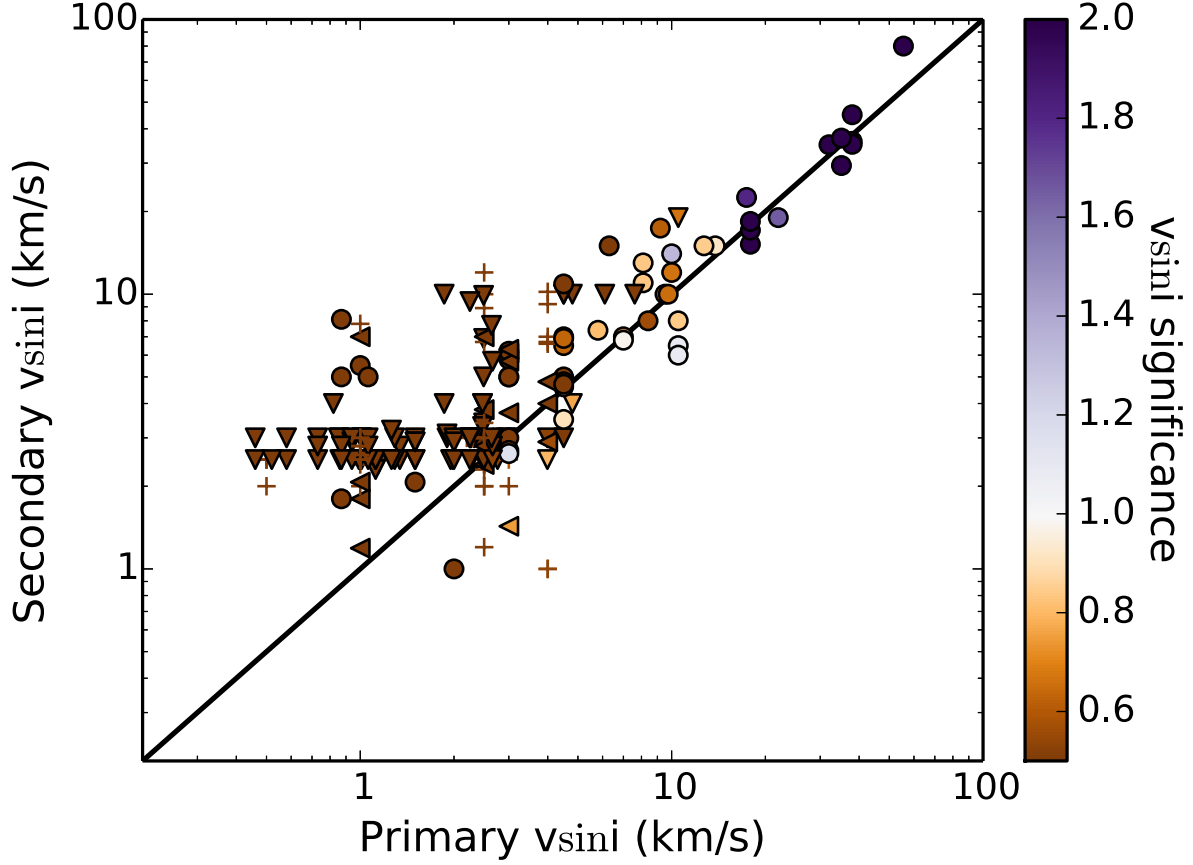


Figure 4.7.— Comparison of $v \sin i$ measurements from the literature for M dwarfs in our database. The horizontal axis shows the $v \sin i$ measured by the highest-spectral resolution survey (requiring $R > 40000$, called the "primary" survey), while the vertical axis shows the $v \sin i$ measured from other ("secondary") surveys. The color indicates our estimate of the significance of the detection; smaller values (brown) are less significant, while larger values (purple) are more so. The symbol shape indicates whether the reported value is a detection or an upper limit: Solid circles indicate detections reported by both the primary and secondary surveys. Triangles pointed downwards indicate that the secondary survey reported an upper limit, while triangles pointed towards the left indicate that the primary survey reported an upper limit. Plus symbols indicate that both the primary and secondary survey report upper limits.

Table 4.4. Rotators with $v \sin i$ measurements

2MASS ID	Grade	P^a (days)	v_{eq}^b (km/s)	$v \sin i$ (km/s)	$R/1000^c$	Ref. ^d
J02170993+3526330	A	0.3	30.0 ± 4.2	28.2 ± 0.7	37	J09
J02204625+0258375	A	0.5	21.3 ± 3.0	23.3 ± 0.7	37	J09
J03205965+1854233	A	0.6	11.8 ± 1.7	$8.0 \pm \dots$	33	R02
J03425325+2326495	A	0.8	19.9 ± 2.8	12.7 ± 0.5	22.5	D13
J06000351+0242236	A	1.8	6.9 ± 1.0	5.8 ± 0.3	57	D15
J07444018+0333089	A	2.8	5.6 ± 0.8	$4.5 \pm \dots$	200	R07
J08294949+2646348	A	0.5	16.5 ± 2.3	8.1 ± 1.1	42	D98
J08505062+5253462	A	1.8	6.8 ± 1.0	13.1 ± 0.7	37	J09
J09301445+2630250	A	10.7	1.9 ± 0.3	6.7 ± 1.5	22.5	D13
J09535523+2056460	A	0.6	14.8 ± 2.1	16.5 ± 0.4	37	J09
J10163470+2751497	A	22.0	0.33 ± 0.05	< 4.0	33	R02
J10521423+0555098	A	0.7	12.8 ± 1.8	19.1 ± 0.2	37	J09
J11474074+0015201	A	11.7	1.5 ± 0.2	5.6 ± 1.4	22.5	D13
J12185939+1107338	A	0.5	18.6 ± 2.6	9.2 ± 1.9	42	D98
J13003350+0541081	A	0.6	16.8 ± 2.4	16.8 ± 2.1	42	D98
J13564148+4342587	A	0.5	15.5 ± 2.2	14.0 ± 2.0	31	R10
J17195422+2630030	A	20.5	1.0 ± 0.1	1.9 ± 0.3	75	H12
J18024624+3731048	A	123.8	0.07 ± 0.01	< 4.5	37	J09
J18452147+0711584	A	0.8	9.9 ± 1.4	16.1 ± 0.1	22.5	D13
J19173151+2833147	A	1.1	7.8 ± 1.1	13.2 ± 0.5	22.5	D13
J22245593+5200190	A	81.8	0.11 ± 0.02	< 4.5	37	J09
J03132299+0446293	B	126.2	0.08 ± 0.01	< 2.2	42	D98
J05011802+2237015	B	70.7	0.13 ± 0.02	8.8 ± 0.3	22.5	D13
J06022918+4951561	B	104.6	0.08 ± 0.01	4.3 ± 1.2	37	J09
J09002359+2150054	B	0.4	17.4 ± 2.5	20.0 ± 0.6	37	J09
J11005043+1204108	B	0.3	31.9 ± 4.5	26.5 ± 0.8	22.5	D13
J12265737+2700536	B	0.7	18.8 ± 2.7	13.5 ± 0.6	22.5	D13

Table 4.4—Continued

2MASS ID	Grade	P^a (days)	v_{eq}^b (km/s)	$v \sin i$ (km/s)	$R/1000^c$	Ref. ^d
J16370146+3535456	B	100.4	0.07 ± 0.01	7.0 ± 1.8	22.5	D13
J22081254+1036420	B	2.4	4.7 ± 0.7	18.6 ± 2.0	20	D12
J23134727+2117294	B	34.5	0.29 ± 0.04	16.0 ± 4.0	24	T12
J23354132+0611205	B	1.7	5.8 ± 0.8	9.8 ± 1.1	37	J09

^aRotation period determined from MEarth photometry in this work.

^bEquatorial rotation velocity and error calculated from the MEarth rotation period and the estimated stellar radius, assuming 10% errors on both the radius and the period.

^cResolving power of the spectrograph used in the $v \sin i$ study, divided by 1000.

^dReference code for $v \sin i$ measurement. See Table 4.3.

We will now consider only $v \sin i$ detections at higher significance (white and purple points in Figure 4.6). Our photometric periods concur with the detection of rapid spin from rotational broadening. However, $v \sin i$ still exceeds v_{eq} in some cases, so one or more of the $v \sin i$, our photometric period, or the radius estimate must be in error. In some cases, the highest peak in the periodogram may represent an alias or harmonic of the true period of the star. The most extreme example is 2MASS J23134727+2117294 (LP 462-11), with $v \sin i = 16$ km/s and $P = 34.5$ days ($v_{\text{eq}} = 0.3$ km/s). Our light curve for this object is relatively sparse (which engendered it a grade B rating); and although the strongest signal in the periodogram is at $P = 34.5$, a rotation period of close to one day also provides a reasonable fit to the data. Table 4.5 considers stars with $v \sin i > v_{\text{eq}}$ and provides the strongest signal at periods shorter than the best-fitting period.

4.5 Spot characteristics

We consider different aspects of starspots in this section. First, we investigate the relationship between semi-amplitude and rotation period (§4.5.1), then consider spot patterns and the stability of the photometric modulations (§4.5.2). In §4.5.3, we compare the fraction of stars that we detect to be rotating to the recovery rates of photometric and $v \sin i$ surveys.

Table 4.5. Alternate short-period signals for stars with $v \sin i > v_{eq}$

2MASS ID	Grade	MEarth P^a (days)	v_{eq}^a (km/s)	F-stat	Alt. P^b (days)	Alt. v_{eq} (km/s)	Alt. F-stat	$v \sin i$ (km/s)
J02204625+0258375	A	0.5	21.4	270	0.33	32.4	180	28.2
J08505062+5253462	A	1.8	6.8	250	0.64	19.1	140	13.1
J09301445+2630250	A	10.7	1.9	160	0.91	22.3	100	6.7
J09535523+2056460	A	0.6	14.8	75	0.38	23.4	60	16.5
J10521423+0555098	A	0.7	12.8	360	0.41	21.9	250	19.1
J11474074+0015201	A	11.7	1.5	540	1.09	16.1	340	5.6
J17195422+2630030	A	20.5	1.0	740	1.05	19.5	540	1.9
J18452147+0711584	A	0.8	9.9	150	0.46	17.2	110	16.1
J19173151+2833147	A	1.1	7.8	80	0.53	16.2	50	13.2
J22081254+1036420	B	2.4	4.7	180	0.7	16.1	180	18.6
J23134727+2117294	B	34.5	0.3	80	1.03	10.0	50	16.0
J23354132+0611205	B	1.7	5.8	40	0.62	15.9	30	9.8

^aRotation period and v_{eq} determined from MEarth photometry, reproduced from Table 4.4 for clarity.

^bAlternative periods with power in the MEarth data. These periods are less significant than the adopted period.

4.5.1 Amplitude of variability

The amplitude of the photometric modulation is derived from the combined effect of the contrast between the spotted and unspotted stellar photosphere and the longitudinal inhomogeneity in the distribution of spots. Starspots, in turn, are surface manifestations of a star's magnetic field. Because rotation, magnetic fields, and starspots are closely related, we might therefore expect a correlation between rotation period and amplitude.

Hartman et al. (2011) found that the rotation periods and amplitudes of K and early- to mid-M dwarfs are uncorrelated for periods less than 30 days (see Figure 16 in their work), and that amplitude decreases with increasing rotation period for $P > 30$ days. For later M dwarfs, Hartman et al. (2011) similarly found no correlation between amplitude and period for periods of up to 30 days, but their sample contained few objects at longer periods. An anti-correlation was also seen by McQuillan et al. (2014) for M dwarfs in the *Kepler* sample; this sample is dominated by early M dwarfs and considered all stars with $T_{\text{eff}} < 4000$ K together. McQuillan et al. (2014) also identified a population of rotators with periods < 15 days and high variability at a range of effective temperatures; examining Figure 14 in their work, the amplitude and period for this population appears uncorrelated. They postulate that these objects are binaries.

We use semi-amplitudes in this analysis, where the semi-amplitude is defined as the coefficient of the best-fitting sinusoid (a in Eq. 4.2). Data on a single star may include several light curves whose semi-amplitudes are fit independently; the values we use are those from the light curve with the most observations. We derive

errors using the covariance matrix from our least-squares fit, which does not include uncertainty in the period (see §4.3). The median amplitude error is 0.002 magnitudes, and is independent of rotation period and the rating we have assigned for the period. Note that if the light curve is evolving or shows non-sinusoidal behavior, the semi-amplitude is suppressed relative to the peak-to-peak amplitude.

In Figure 4.8, we plot the semi-amplitude of variability versus rotation period for higher-mass ($0.25 < M \lesssim 0.5 M_{\odot}$) and lower-mass ($0.08 \lesssim M < 0.25 M_{\odot}$) M dwarfs in MEarth. Our mass limits approximate the $V - K$ color limits used by Hartman et al. (2011). We show the divisions based on both stellar mass (estimated from absolute K magnitudes) and color (using $MEarth - K$). We use our statistical sample in this analysis to avoid bias because high-amplitude, rapid rotators can be detected in many light curves where we are not sensitive to lower-amplitude or longer-period variables.

We find a negative correlation between period and semi-amplitude for the higher-mass M dwarfs, but no correlation for mid M dwarfs, consistent with previous results. We use a Spearman rank correlation analysis to test the statistical significance of these results, and calculate the p-value for a two-sided hypothesis test with the null hypothesis that the data are uncorrelated, using the SciPy stats package. Smaller p-values indicate higher confidence that the correlation is not due to chance. The correlation coefficient including both the grade A and B rotators is -0.43 ± 0.07 for $M > 0.25 M_{\odot}$ ($p = 0.01$) and -0.01 ± 0.03 for $M < 0.25 M_{\odot}$ ($p = 0.5$). Values reported are the median and 68% confidence limits from a Monte Carlo simulation where we resampled with perturbation as suggested by Curran (2014). The lack of correlation for the lower mass stars also persists if we consider narrower ranges in

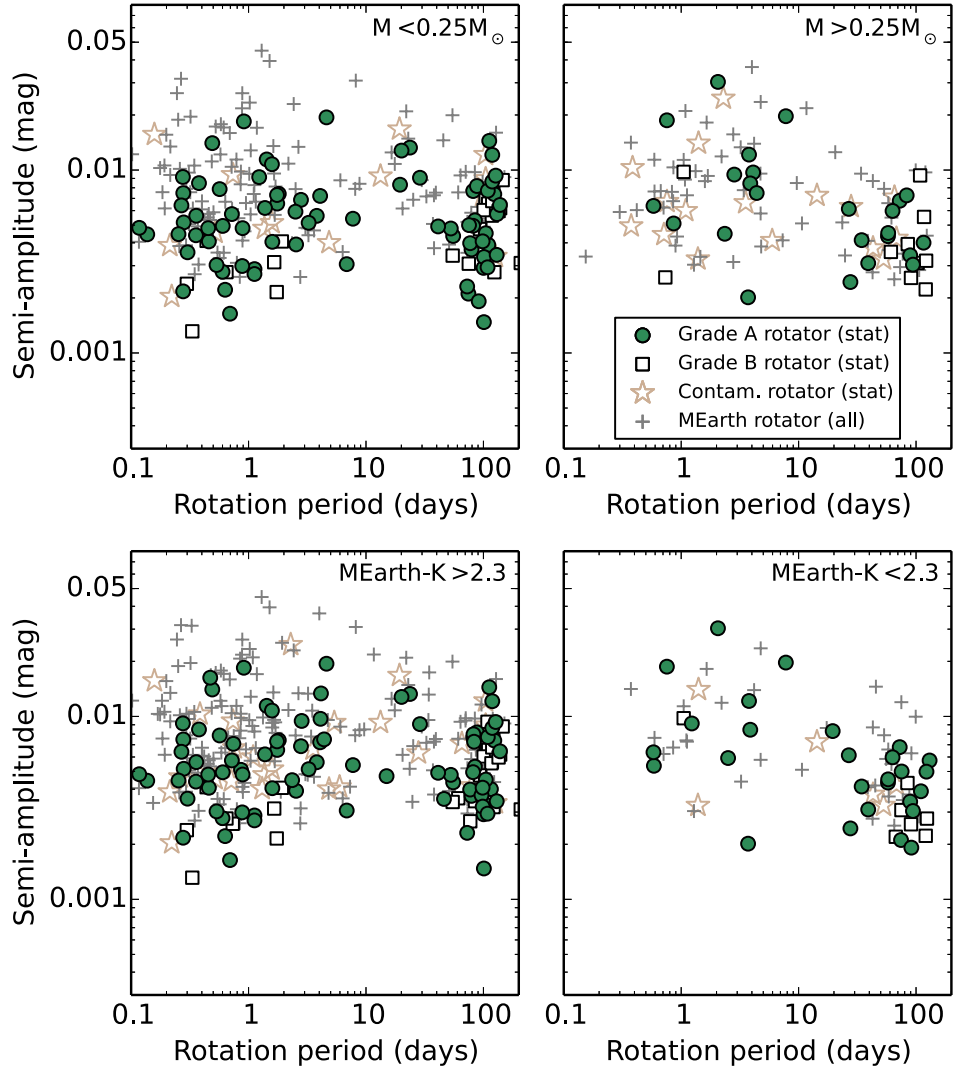


Figure 4.8.— Semi-amplitude of variability (defined as the coefficient of the sinusoid in our best fit) versus photometric rotation period, for $M < 0.25 M_{\odot}$ (left panel) and $M > 0.25 M_{\odot}$ (right panel). The median error on semi-amplitude is 0.002 magnitudes. We caution that due to our use of absolute magnitudes to estimate stellar mass, a greater proportion of objects assigned to the higher mass bin are likely to be unresolved multiples. For objects in our statistical sample, we plot the grade A rotators (filled circles) and B rotators (open squares), and rotators with unresolved companions or that appear over-luminous (open stars). We also show, for reference, all rotators not in the statistical sample (plus signs). Our sensitivity to high-amplitude, short-period rotators in sparse data sets can be seen in the over-abundance of these objects in our full sample.

mass.

4.5.2 Spot patterns and stability

In keeping with our finding of the lack of a correlation between rotation and semi-amplitude, we find that most of our detected rotators show phase-folded light curves with qualitatively similar morphologies. At the precision of our data, they are usually sinusoidal in appearance. This could imply that the photometric modulations are the result of many spots acting in concert, or of a long-lived polar or high-latitude spots viewed at high inclination. Considering the former scenario, Jackson & Jeffries (2013) demonstrated that photometric modulations of the amplitude we see can be produced by a large number of randomly distributed spots. The latter scenario is reflected in the prevalence of poloidal, axisymmetric large-scale fields recovered by Zeeman Doppler Imaging for fully-convective stars (e.g. Morin et al. 2008a), and in spot models from time series photometry or spectroscopy (e.g. Davenport et al. 2015; Barnes et al. 2015). These patterns tend to be stable over multiple rotation cycles, and in some cases over more than a year.

Aided by our visual inspections of the data, we are able to detect objects with evolving spot patterns. We highlight 2MASS J23254016+5308056 (LHS 543a) as the star demonstrating the strongest spot evolution in our sample. Light curves for this star, which we classify as a grade A rotator with a rotation period of 23.5 days, are shown in Figure 4.9. The patterns seem stable for about two rotation cycles, and show evolution over roughly 200 days. We stress, however, that we expect our period detection method to be less effective for stars on which the spot patterns evolve on

timescales comparable to the stellar rotation period.

Zeeman Doppler imaging measurements of late M dwarfs indicate that the magnetic field topologies of these stars can be very different for stars with similar properties. Donati et al. (2008) found that some late M dwarfs had axisymmetric, mostly dipolar fields (similar to earlier M dwarfs), while some are weaker, with more energy at small scales. We do not see any obvious dichotomy amongst the patterns of variability, but it is possible that one of the magnetic field topologies is more effective at producing spot contrast than the other.

4.5.3 Recovery fractions

Previous photometric surveys have found a high fraction of fully-convective stars to be photometrically variable. McQuillan et al. (2014) find that approximately 80% of the latest M dwarfs in *Kepler* have periods detected from their autocorrelation analysis, noting that their recovery of periods for these stars is not limited by the amplitude of variability. The recovery fraction of ground-based surveys is usually lower due to the cadence and precision of the observations. Hartman et al. (2011), correcting for incompleteness using signal injection, estimate that 50% of the stars with $M \lesssim 0.2 M_{\odot}$ are variable at semi-amplitudes $\gtrsim 0.005$ mag in their bandpass (Cousins I_C and R_C).

Our recovery rate of grade A and B rotators in the statistical sample is $47 \pm 5\%$, with no significant difference between the low- and high-mass populations. Considering $P < 100$ days to match the period range studied by Hartman et al. (2011), our recovery rate is $36 \pm 3\%$. The amplitude sensitivity of the two surveys is

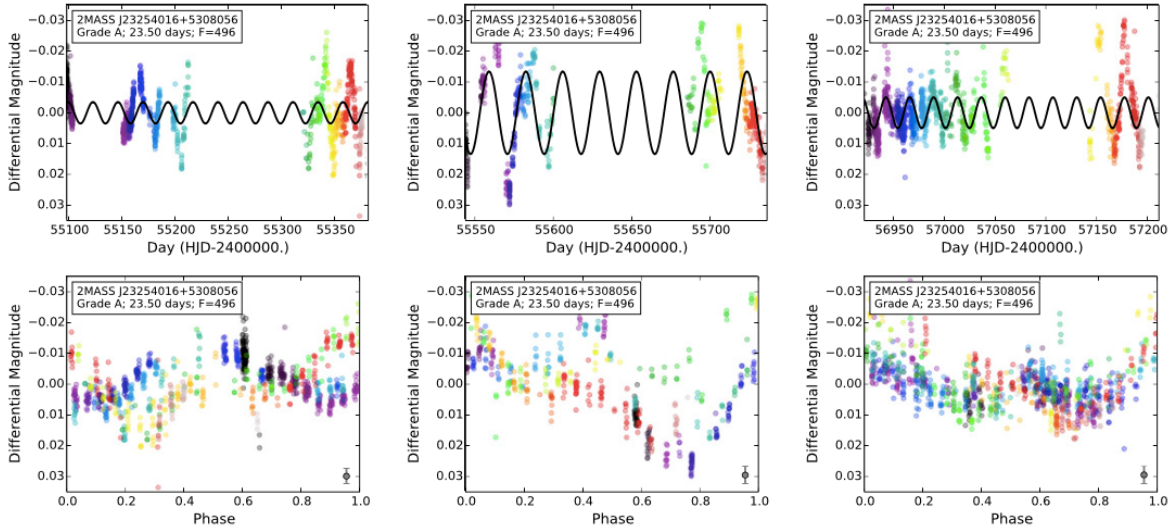


Figure 4.9.— Light curves of 2MASS J23254016+5308056 (LHS 543a) from 2008-2010 (left), 2010-2011 (center), and 2011-2015 (right). The top panels show the brightness as a function of time, with the best-fitting sinusoidal model over-plotted; the bottom panels show the light curves phase-folded to the best period. This object has the strongest and most rapid spot evolution of the stars in which we detect rotation periods. As in Figure 4.1, the color of the data points indicates the observation epoch. The median error is represented in the bottom corner.

similar, but HATnet uses bluer photometric bandpasses where the contrast between the stellar photosphere and cooler spots is higher. We have also not modeled the incompleteness of our survey, though our use of the statistical sample mitigates the larger part of this effect for stars with $P < 100$ days.

Surveys of $v \sin i$ indicate a larger fraction of fully-convective stars are rotating rapidly than does our work. In a volume-limited survey, Delfosse et al. (1998) found that 50% of field mid-M dwarfs (roughly M4V–M5V) are rotating rapidly enough to have detectable $v \sin i$. Mohanty & Basri (2003), using new measurements and including those from Delfosse et al. (1998), similarly found that half of their mid-M dwarf population (M4V–M5.5V) had detectable $v \sin i$. In another survey, Browning et al. (2010) found that 30% of M4.5V–M6V stars had detectable $v \sin i$. For a $0.2 R_{\odot}$ star and a detection limit of 3 km/s (typical for the two $v \sin i$ studies discussed here), this implies a period of less than 3.3 days. We find that only $18 \pm 2\%$ of stars in our statistical are grade A or B rotators with $P < 3.3$ days.

The stellar samples selected by these surveys may not be comparable. For example, as the MEarth sample is proper motion selected, we are missing a larger fraction of stars with lower tangential velocities. These kinematically-cold stars are likely to be preferentially younger and therefore faster rotators (see §4.6.1). We estimate that our sample represents 85 to 90% of the kinematically-unbiased sample (see §4.6.1). If we add an additional 15% of stars to our sample and assume that all are rotating at $P < 3.3$ days, we can increase the fraction of rapid rotators to 30%. This would bring our results into agreement with those from Browning et al. (2010), but still falls below the fractions reported by Delfosse et al. (1998) and Mohanty & Basri (2003).

Our photometric survey could have missed a population of short-period rotators: First, we know from KIC 9201463 that we are not able to detect all short-period rotators. Second, our method for period detection is not sensitive to stars whose spots evolve on timescales comparable the stellar rotation period. The roughly 30% of rapid rotators we would need to have missed could be a population of rapidly-rotating stars with spot patterns that are not stable or that do not provide variability amplitudes high enough for us to detect. Aliasing of periods near 1 day could also contribute (see §4.4.3).

4.6 Kinematics and metallicities of the rotators

To study kinematics, we require information on both the stars' positions and their motions through the Galaxy. As our targets were selected from a proper motion survey (Lépine & Shara 2005), all have measured proper motions. The majority of our targets also have parallaxes from MEarth astrometry measured by Dittmann et al. (2014), though we use more precise measurements from the literature if available. We also gather radial velocities (RVs) from the literature, many of which come from Newton et al. (2014), in which we used $R \approx 2000$ near-infrared spectra to measure absolute RVs to 4 km/s. This survey targeted many of the MEarth rotators that had been identified by the time of observation, but the availability of RVs still limits the fraction of stars for which we have kinematic information.

With all six phase space dimensions, we then calculate the U (radial, positive is towards the Galactic center), V (azimuthal), and W (vertical) velocity components and their errors using an implementation of the method of Johnson & Soderblom

(1987), updated to ICRS using the Galactic coordinate system defined in Perryman et al. (1997, vol. 1, part 1, sec. 1.5.3). These velocities are measured relative to the Solar System barycenter. When we consider velocities relative to the local standard of rest, we will denote these velocities using the subscript LSR. We use solar velocities from Schönrich et al. (2010), adopting $(U_{\odot\text{LSR}}, V_{\odot\text{LSR}}, W_{\odot\text{LSR}}) = (11, 12, 7)$ km/s. The median error in each of components is 3 km/s, with the error in radial velocity typically dominating.

4.6.1 De-biasing the kinematics

The MEarth sample was selected from a proper motion survey with a lower limit of $0''.15/\text{yr}$, and are therefore preferentially missing some stars with low tangential velocities. We simulate the stars that we missed due to proper motion limits by drawing velocities and distances from a model thin disk. We consider only the thin disk, because kinematically-hotter stars are a small fraction of the solar neighborhood and less likely to be missed due to proper motion selection.

We draw U_{LSR} , V_{LSR} , and W_{LSR} from Gaussian distributions with standard deviations of 35 km/s, 20 km/s, and 16 km/s, respectively (Bensby et al. 2003). We draw distances and positions uniformly in volume. We also tested drawing from the observed distribution of the MEarth sample, and found little difference in the resulting simulated sample, consistent with the conclusions of Dittmann et al. (2014). We then compute proper motions and apply the $0''.15/\text{yr}$ selection criterion.

Out to a distance of 25pc, we find that 11% of stars were missed due to the proper motion limits. Adding in the missing stars, the resulting velocity distributions

for MEarth are similar to the distributions for volume-limited samples of more massive stars (e.g. Holmberg et al. 2009).

4.6.2 General kinematic properties of the sample

In Figure 4.10 we show the U and V velocity components of the Northern MEarth M dwarfs within 25pc that have estimated masses less than $0.25 M_{\odot}$. We place these limits to mitigate the likelihood of unresolved multiples contaminating the sample. We also show, for comparison, the G and K dwarfs from the Geneva-Copenhagen survey (GCS; Nordstrom et al. 2004; Holmberg et al. 2009) that are within 40pc. The kinematic substructures that have been identified for higher mass stars are clearly seen in our mid-to-late M dwarfs as well, most notably the arc at $U \approx -37$ km/s, $V \approx -17$ km/s that has been called the Hyades supercluster, the Hyades stream, and the Hyades moving group (Eggen 1958), not to be confused with the 650 Myr-old Hyades open cluster.

The Hyades supercluster has similar kinematics to the Hyades and Pleiades open clusters, and at one time the supercluster was proposed to be a stream of stars evaporating from the Hyades open cluster, or at least composed of several coeval groups (Eggen 1992; Chereul et al. 1998, 1999) though this was not universally agreed upon (Dehnen 1998). However, recent theoretical work shows that spiral structure can dynamically create co-moving groups like the supercluster (De Simone et al. 2004; Quillen & Minchev 2005) and dynamical evolution is thought to be responsible for the larger kinematic structures in the solar neighborhood. For the Hyades supercluster, the dynamical origin of the kinematic association has been

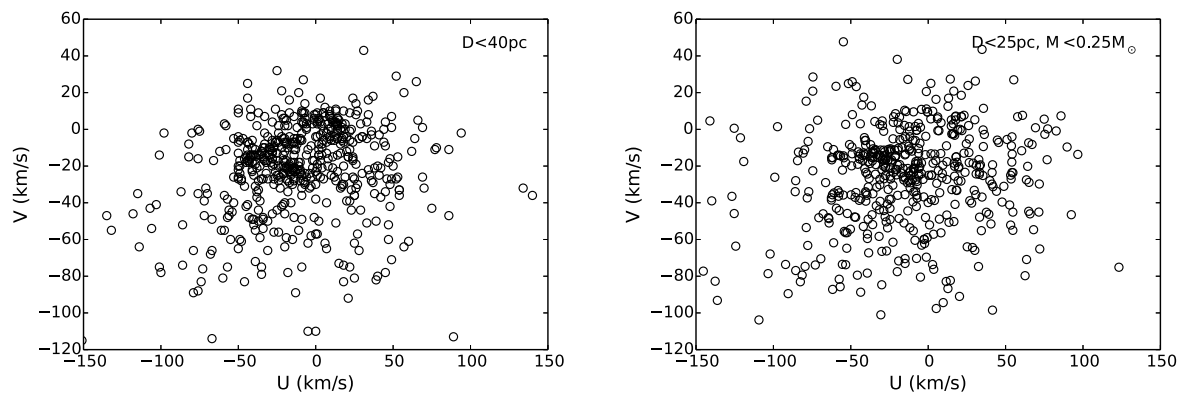


Figure 4.10.— U and V velocities (relative to the Sun rather than the local standard of rest) for G and K dwarfs within 40 pc from the Geneva-Copenhagen Survey (GCS, left) and for mid-to-late M dwarfs within 25 pc from MEarth (right). The kinematic substructure evident in the GCS is also clearly seen in the nearby M dwarfs; most notable is the Hyades supercluster. The typical error on each component is 3 km/s.

demonstrated observationally as well, through analysis of the chemical abundances and the mass function of stars in the proposed supercluster (Famaey et al. 2005, 2007, 2008; Bovy & Hogg 2010).

4.6.3 Disk membership

Stars can be broadly grouped by their kinematics into the thin/young disk, the dynamically-heated thick/old disk, and the even hotter halo population. We assign disk membership using the same method as Bensby et al. (2003), which takes into account the velocity dispersions in U_{LSR} , V_{LSR} , and W_{LSR} and the relative number densities of the different stellar populations. The values we use for the velocity dispersions of the thin disk, thick disk, and halo are also from Bensby et al. (2003). We assume that 89% of the stars in the solar neighborhood are in the thin disk, 10.6% in the thick disk, and 0.4% for the halo (Jurić et al. 2008). We do not consider membership in stellar streams.

In Figure 4.11, we plot the probability of an object being in the thick disk, $P(\text{thick})$, divided by the probability of that object being in the thin disk, $P(\text{thin})$, for the stars in the statistical sample. Out of 163 stars in the statistical sample that have UVW kinematic information, 23 ($14 \pm 3\%$) have $P(\text{thick}) > P(\text{thin})$, and 7 have $P(\text{thick}) > 10 \times P(\text{thin})$. Out of the 87 grade A and B rotators, 6 ($7 \pm 3\%$) have kinematics that potentially place them in the thick/old disk, while none have $P(\text{thick}) > 10 \times P(\text{thin})$. Overall, the rotators have kinematics typical of the Solar Neighborhood and are therefore generally members of the thin disk. Rapid rotators, however, are from a dynamically cold population. The p-value for a k-sample

Anderson-Darling test (Scholz & Stephens 1987) to check whether the rotators are drawn from the field M dwarf population is $p = 10^{-5}$ for rotators with $P < 10$ days.

Our results differ from those of Irwin et al. (2011a), who assigned approximately half of the MEarth rotators in their sample to the thick/old disk based on how closely the objects' kinematics matched those expected for each disk. This difference is primarily due to our inclusion of the thin-thick disk normalization.

The fraction of stars with detected periods depends on the kinematic subsample. We divide our statistical sample at $P(\text{thick}) = 0.1 \times P(\text{thin})$ to ensure enough stars in the kinematically-older subsample. Our recovery fraction for kinematically-young stars with $M < 0.25 M_{\odot}$ is $58 \pm 8\%$, while for the kinematically-old stars it is $16 \pm 8\%$. This may be the result of stars in the kinematically-old subsample generally having longer periods, to which we believe we are less sensitive (§4.5.3). Changing spot patterns or variability amplitude could also contribute, though we do not see any such trends amongst the sample of stars for which we do detect rotation periods.

4.6.4 Metallicities of the rotators

Newton et al. (2014, 2015) estimated $[\text{Fe}/\text{H}]$ for nearly 450 MEarth M dwarfs from near-infrared spectra. Figure 4.12, we show $[\text{Fe}/\text{H}]$ as a function of photometric rotation period. There is not a clear trend with rotation, with a Spearman rank correlation of 0.00 ± 0.03 (see §4.5.1). This is consistent with the interpretation that the rotators are typical Solar Neighborhood stars: within the thin disk, there is no evidence for an age-metallicity relation, and stars may have a range of metallicities (e.g. Nordstrom et al. 2004).

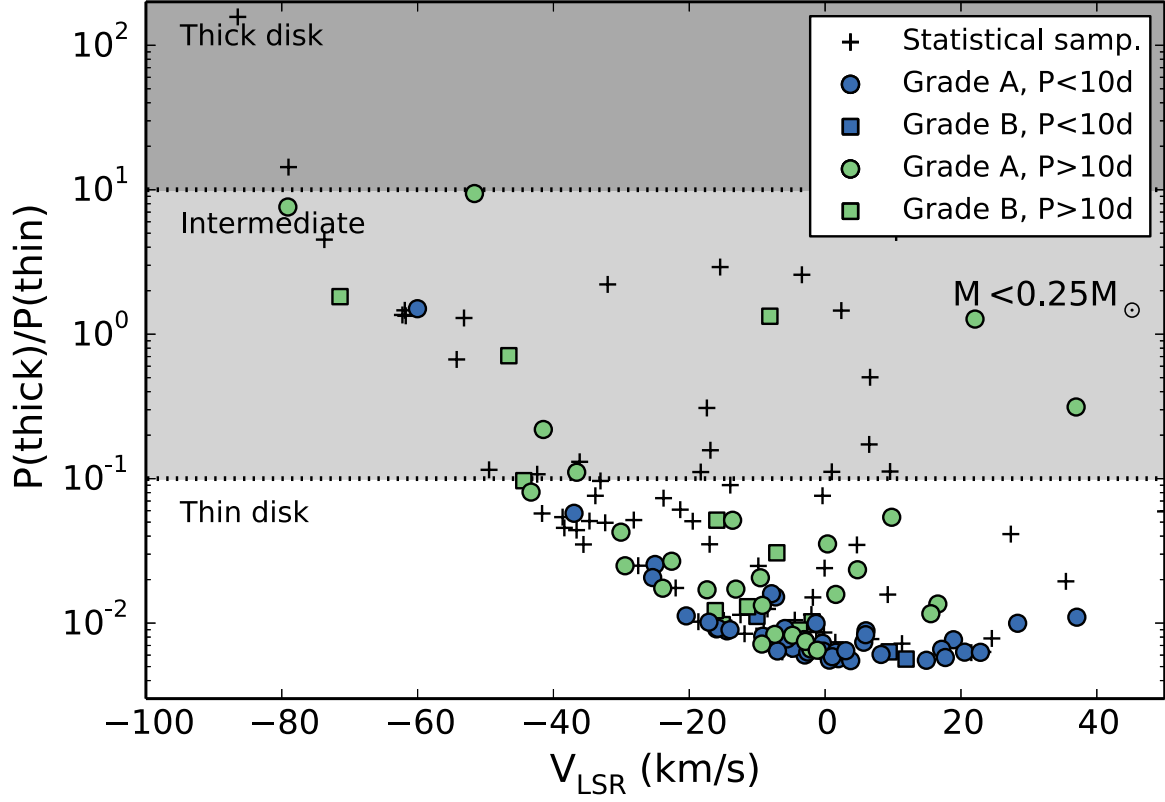


Figure 4.11.— Probability (P) of an object being in the thick/old disk relative to the probability of it being in the thin/young disk, plotted against V_{LSR} . $P_{\text{thick}}/P_{\text{thin}} = 1$ indicates an equal probability of the object being in either disk. Shaded regions denote disk assignments: $P > 10$ are thick/old disk members, $0.1 < P < 10$ are intermediate, and $P < 0.1$ are thin/young disk members. Only stars in our statistical sample are shown. Non-detections are plus symbols, grade A rotators are filled circles, and grade B rotators are filled squares. Blue indicates stars with periods shorter than 10 days, green those with periods longer than 10 days.

The rotators do not appear significantly more metal-rich than the full sample (Anderson-Darling $p = 0.15^{+0.17}_{-0.09}$). We also do not see a correlation between metallicity and period (Spearman correlation coefficient = $-0.02^{+0.03}_{-0.02}$, $p = 0.5 \pm 0.2$), nor between metallicity and amplitude (coefficient = $0.02^{+0.07}_{-0.08}$, $p = 0.5 \pm 0.2$).

There is one star with unusually large (and unphysical) estimated metallicity of 0.7 dex: 2MASS J06052936+6049231 (LHS 1817). This star also has large U and W velocities. Two other rotators in our sample have estimated metallicities this high, and both were removed due to known or suspected multiplicity. All three of these objects were also identified as candidate young objects by Shkolnik et al. (2010), but are not the *only* stars in our sample that are potentially young. Although Shkolnik et al. (2010) have a high-resolution spectrum and did not identify 2MASS J06052936+6049231 as a multiple, its radial velocity (> 100 km/s) makes it unusual in their sample as well.

4.7 The age-rotation relation

Because low-mass main sequence stars spin down with time, it is expected that slow rotators are older than their more rapidly-rotating counterparts. While clusters can constrain the rotational evolution at young ages, there are no reliable methods to determine the ages of isolated field M dwarfs – once they reach the main sequence, their physical properties remain essentially unchanged over a Hubble time. As discussed in the introduction, galactic kinematics provide a means to probe the ages of groups of stars. For example, Irwin et al. (2011a) used the total space velocities of 41 MEarth M dwarfs to classify the stars into the thin/young ($\lesssim 3$ Gyr), intermediate

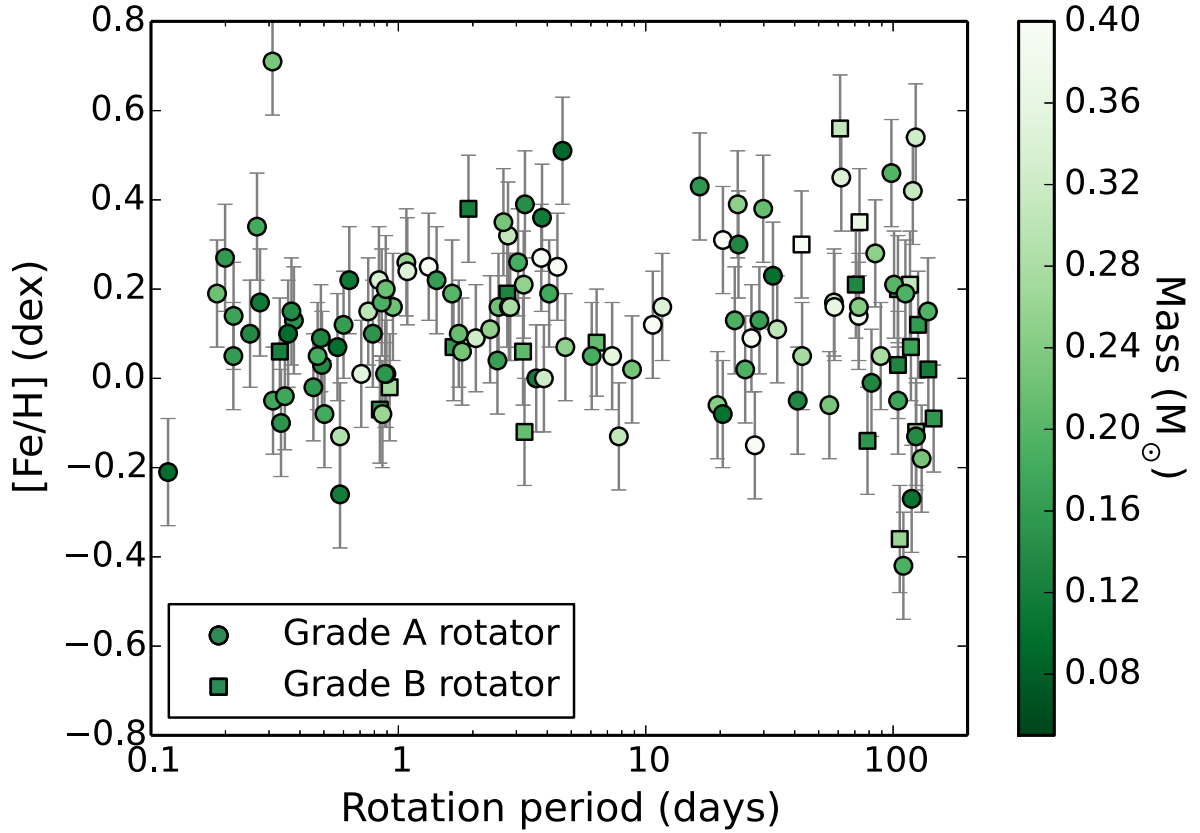


Figure 4.12.— $[\text{Fe}/\text{H}]$, estimated from near-infrared spectra, as a function of measured photometric rotation period. The typical error on $[\text{Fe}/\text{H}]$ is 0.12 dex. The color of the points indicates their stellar mass as estimated from their absolute K magnitudes using our modified version of the Delfosse et al. (2000) relation. We do not see a clear trend between metallicity and rotation.

(3 – 7 Gyr), and thick/old ($\gtrsim 7$ Gyr) disks. Irwin et al. (2011a) found that the young disk objects were entirely fast rotators, while the old disk objects were predominantly slow rotators.

We very clearly see the signatures of age-rotation relation in the distribution of total space velocities as a function of photometric rotation period (Figure 4.13). There is an increase in dynamic hotness of the stellar population with rotation period, a trend which spans the entire period range that we probe. This is evidenced in the Spearman rank correlation coefficient for total space velocity and rotation period, which is 0.18 ± 0.03 ($p = 0.002^{+0.007}_{-0.002}$). We emphasize, however, that it is the velocity *dispersion* that increases with age. Stars with rotation periods of around a day have space velocities narrowly constrained, as would be expected for a very young stellar population. Stars with rotation periods around 100 days have a wide dispersion in space velocities, as expected for an older stellar population that has been dynamically heated.

Decomposing the space velocities into the individual components (Figure 4.14), we see the same signatures of aging: the velocity dispersion of each component increases with rotation period. We also see evidence of asymmetric drift: the V velocities become more negative with increasing rotation period. As noted by West et al. (2015), the magnitude of asymmetric drift is much less than what is seen in more distant, older populations of M dwarfs.

The existence of a relationship between velocity dispersion and age amongst members of the thin disk is well-established (e.g. Wielen 1977), though the exact form of the age-velocity relation is a matter of debate. Nordstrom et al. (2004) and

Holmberg et al. (2009), using data from the GCS fit to a power law, find that velocity dispersion increases smoothly at least to 10 Gyr. In contrast, Soubiran et al. (2008) find an age-velocity relation with a shallower slope that saturates around 5 Gyr, using more distant clump giants. They also find significantly higher velocity dispersions, in contrast to studies of the solar neighborhood. Seabroke & Gilmore (2007) found that the data could not constrain whether the age-velocity relationship saturated beyond 5 Gyr using the data from Nordstrom et al. (2004).

Previous kinematic studies of low-mass stars have used the Wielen (1977) age-velocity relations² (Schmidt et al. 2007; Faherty et al. 2009; Reiners & Basri 2009a, 2010). We refer the reader to Reiners & Basri (2009a) for comments on the usage of the equations. These studies relied on the total velocity dispersion. As discussed by Seabroke & Gilmore (2007), kinematic substructures such as the Hyades supercluster make the U and V velocity distributions non-Gaussian (see also §4.6.2). Therefore, we use the W velocity dispersion (σ_W) for kinematic age assignment.

In general, we find that the different functional forms and coefficients of age-velocity relations in the literature give consistent results for ages between 1 and 5 Gyr. The results diverge for older and younger populations. However, the age-velocity relationship is not appropriate for the youngest stars (as their kinematics are unrelaxed) and not well-constrained at later ages (where it may saturate). Thus, the choice of age-velocity relation is not paramount. We adopt the results from Aumer & Binney (2009, see Table 6), who modeled the star formation history to

²Note that Ofek (2009) re-fit the original equations using data from Nordstrom et al. (2004).

arrive at the age-velocity relationship:

$$\sigma_W(\tau) = \sigma_{W,10} \left(\frac{\tau + \tau_1}{10 \text{ Gyr} + \tau_1} \right)^\beta \quad (4.5)$$

$$\sigma_{W,10} = 23.8 \text{ km/s}$$

$$\tau_1 = 0.001 \text{ Gyr}$$

$$\beta = 0.445$$

The velocity dispersion at 10 Gyr is described by the parameters $\sigma_{W,10}$ and τ_1 , while the exponent β characterizes the heating rate.

To apply the age-velocity relation, we first need the dispersion of the W velocity component, σ_W . To determine the σ_W that underlies our data, we take the Bayesian approach of West et al. (2015), and maximize the posterior probability $p(\sigma_W|D)$, where our data D are our measurements of W_{LSR} . Using Bayes theorem, the posterior probability is the product of the likelihood, $p(D|\sigma_W)$, and the prior, $p(\sigma_W)$:

$$p(\sigma_W|D) \propto p(D|\sigma_W) \times p(\sigma_W) \quad (4.6)$$

We use a Jeffreys prior, which is appropriate as an uninformative prior: $p(\sigma_W) \propto 1/\sigma_W$. The likelihood is the product of the probabilities of obtaining each measurement given the model. The underlying model to which we fit our data is a Gaussian distribution $\mathcal{N}(\mu_W, \sigma_W)$. We use a Cauchy distribution $\mathcal{C}(d_i, \sigma_i)$ to represent our measurement errors. The latter is centered at the measured value and has a standard deviation given by the error (σ_i) on each datum (d_i). This gives:

$$p(D|\sigma_W) = \prod_i V(d_i - \mu_W; \sigma_W, \sigma_i) \quad (4.7)$$

where $V(W; \sigma_W, \sigma_i)$ is the probability density function (PDF) of a zero-mean Voigt profile, and can be written as the convolution of the PDFs of the Gaussian and

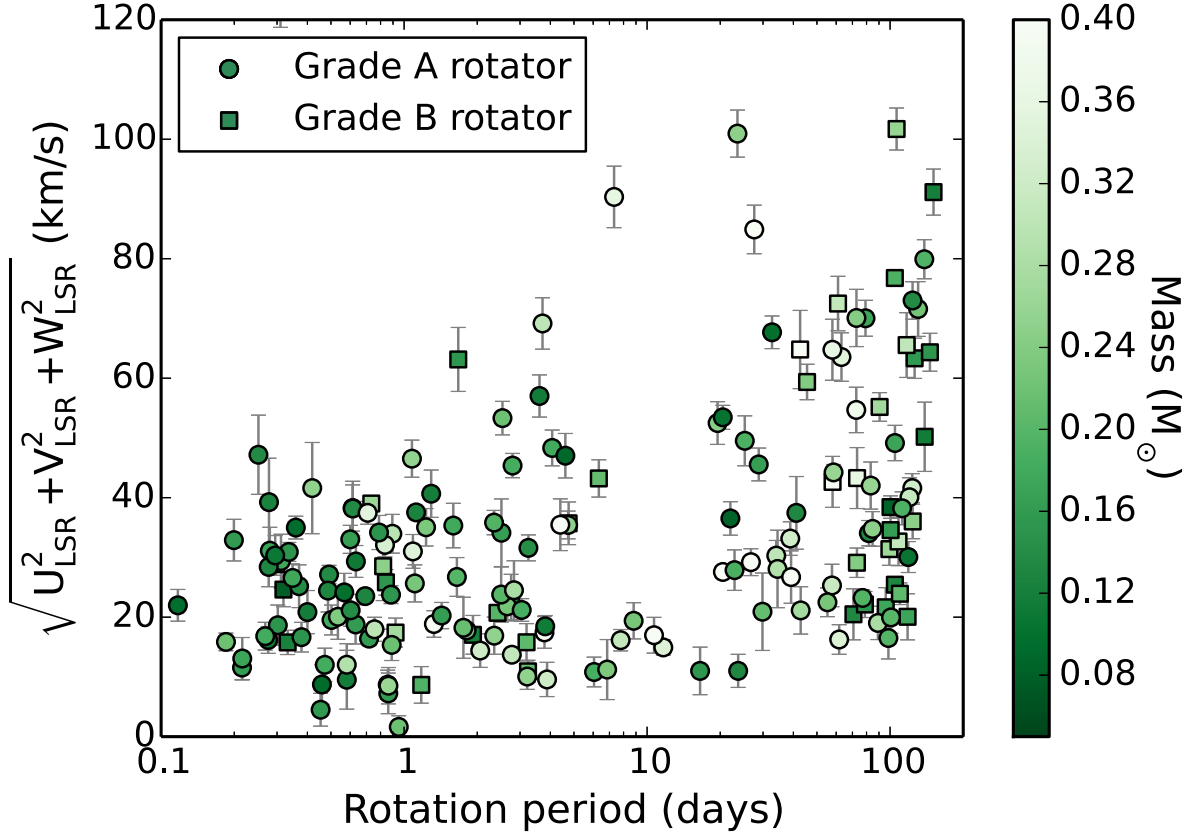


Figure 4.13.— Total space velocity as a function of measured photometric rotation period. The color of the points indicates their stellar mass as estimated from their absolute K magnitudes using our modified version of the Delfosse et al. (2000) relation. The velocity dispersion increases with rotation period, as expected if the ages of stars are increasing with rotation period.

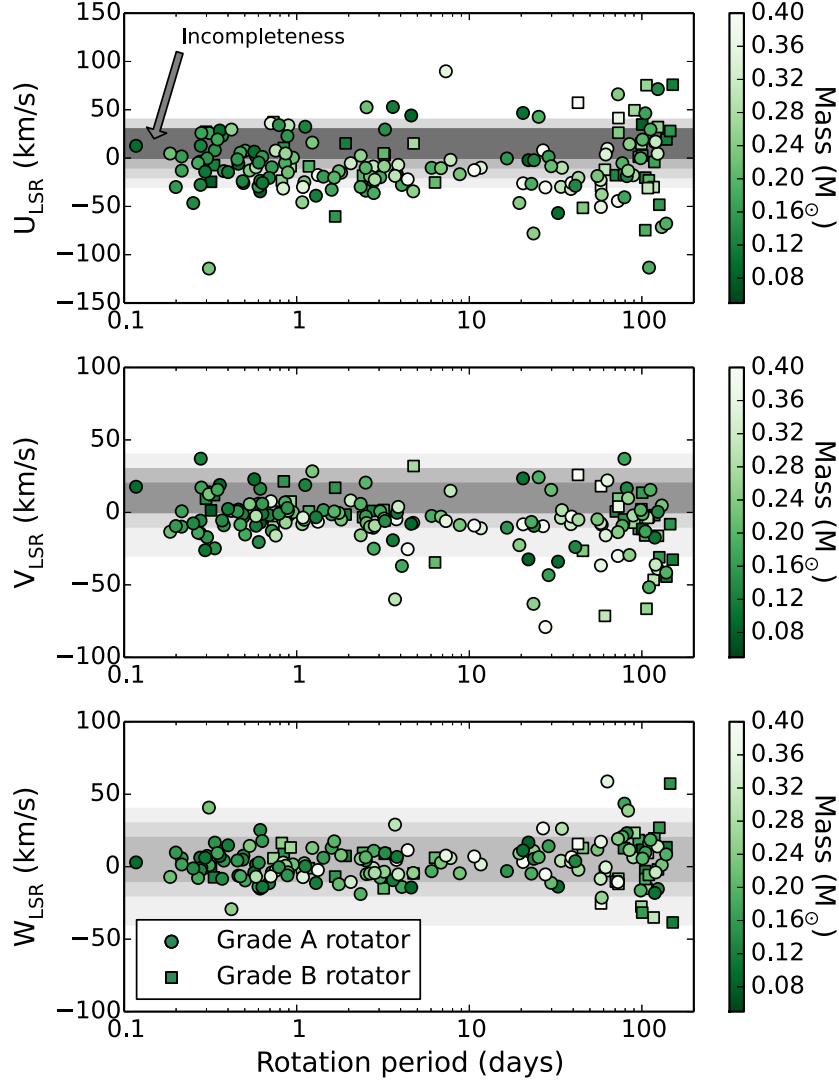


Figure 4.14.— Individual components of space velocity as a function of measured photometric rotation period. The color of the points indicates their stellar mass as estimated from their absolute K magnitudes using our modified version of the Delfosse et al. (2000) relation. The velocity dispersion of each component increases with rotation period, as expected if the ages of stars are increasing with rotation period. The V component also becomes increasingly negative (asymmetric drift), which is also a sign of an older stellar population. The gray shaded regions show the percent of stars that were missed in simulations as a result of our selection criteria. We show increments of 5%, up to 25%, e.g., the darkest gray band shows that at U velocities similar to the Sun, 25% of stars are missing from the MEarth sample. The darkest bands in V and W correspond to 20% and 15%, respectively.

Cauchy distributions $N(W; \mu, \sigma)$ and $C(W; \mu, \sigma)$ as:

$$V(W; \sigma_W, \sigma_i) = N(W; 0, \sigma_W) * C(W; 0, \sigma_i) \quad (4.8)$$

The work on higher mass stars on which we base this analysis shows that the average W velocity (μ_W) remains 0 km/s as the population is dynamically heated. For our sample, μ_W is close to 0 km/s as well (Table 4.6). Due to the small number of objects in our long-period bins, we fix $\mu_W = 0$. We choose a Cauchy over a Gaussian distribution to represent measurement errors in order to decrease the sensitivity of the model to outliers (a measurement might be an outlier if, for example, our period measurement is erroneous or if the object is an unidentified multiple).

We approximate the Voigt PDF following Thompson et al. (1987) as $(1 - \eta) N(W; 0, \Gamma) + \eta C(W; 0, \Gamma)$. The parameters η and Γ depend on σ_W and σ_i ; they are given in Thompson et al. (1987) and also reproduced in Ida et al. (2000). The likelihood is then an analytic function that we evaluate at each datum.

We calculate the log of $p(D|\sigma_W)$ for a grid of σ_W in step sizes of 0.1 km/s, and select the σ_W that results in the highest posterior probability. We use a bootstrap analysis to estimate errors, sampling with replacement from our data over 100 iterations.

Our approach should be insensitive to the stars missing from our sample due to MEarth's selection criteria. To test this, we also fit a generative, non-analytic model. In this case, our model is the binned distribution of a random sample of 200000 stars drawn as discussed in §4.6.1 and subject to the MEarth proper motion limit. While we are interested only in σ_W , the velocity dispersions of the other

velocity components are not independent so we fix σ_U and σ_V in the ratios of the thin disk. After drawing our sample, we apply the $0''.15/\text{yr}$ proper motion limit. As we demonstrated in §4.6.1, the selection of our sample using proper motions causes our sample to be missing 11% of the stars, but the fraction of stars missing will be larger when the velocity dispersion is smaller. We then convolve the resulting PDF with a Cauchy distribution to account for the errors on each datum. The results from this approach are similar to those from the simpler method we adopt.

We divide the sample into bins in period, $P < 1$ day, $1 < P < 10$ days, $10 < P < 70$ days, and $P > 70$ days, considering only objects with $0.1 < M < 0.25 M_\odot$. Considering all rotators (both grade A and B), we infer mean ages of (0.5, 0.7, 0.6, 5.1) Gyr in these bins, respectively. We arrive at similar results using $2.3 < M_{\text{Earth}} - K < 3.3$ to select our low-mass sample.

We also apply the Wielen (1977) relation as described in Reiners & Basri (2009a). 2MASS J06052936+6049231, the rapidly rotating star with a very negative U velocity seen in Fig. 4.14, strongly affected the results and was excluded. The ages we infer considering all rotators for the four bins defined above are (0.7, 1.7, 3.1, 5.4) Gyr. These ages *are* affected by our proper motion bias since they rely on calculating the dispersions of the observed sample.

We present our results in Table 4.6. Within the errors, stars with $P < 10$ days have $\sigma_W \lesssim 10$ km/s, implying ages of < 1 Gyr according to our chosen age-velocity relation. This is younger than the youngest bin used in the calibration, and the distribution of velocities in the GCS is fairly constant from 1 to 2 Gyr. We therefore assign this population of stars mean ages of $\lesssim 2$ Gyr. Our results for $10 < P < 70$

days are not robust: there are relatively few stars at these periods, there is a strong dependence on the upper period boundary, and the total space velocities indicate an older population than the W component alone. For the longest-period rotators, with $P > 70$ days, we adopt a mean age of 5^{+4}_{-2} Gyr.

The velocity dispersions we determine are slightly lower than those from West et al. (2015), which is also based on the sample of MEarth rotators, and therefore we obtain slightly younger ages than one would infer from their work. Due to the mass dependence of rotational evolution (see §4.8), we restricted the range of masses used in this analysis. If we include rotators regardless of mass, we arrive at slightly larger velocity dispersions. Our work also includes a compilation of other published radial velocities, so more precise measurements are available for some objects, and we have made efforts to remove possible multiples, which may have velocities or periods uncharacteristic of otherwise similar stars. We also only use stars with trigonometric distance measurements.

4.8 The mass-period relation

Rotation is found to be strongly mass-dependent in young open clusters, with the lowest-mass stars reaching the fastest rotation rates and maintaining rapid rotation for longer. Rotational evolution at field ages is also mass dependent. Lower-mass stars spin down more slowly than higher-mass stars on the main sequence, but eventually reach longer rotation periods. This mass dependence in the upper envelope of rotation periods is clearly seen in Irwin et al. (2011a, mid and late M dwarfs from MEarth) and McQuillan et al. (2013, 2014, early M dwarfs from *Kepler*).

Table 4.6. Velocity dispersions and ages for stars with detected rotation periods

Period bin (days)	N stars	Mean P (days)	Mean W_{LSR} (km/s)	σ_W (km/s)	Est. age (Gyr)
Grade A					
$0 < P < 1$	39	0.5	3	$6.0^{+1.8}_{-1.0}$	$0.5^{+0.4}_{-0.2}$
$1 < P < 10$	23	2.9	0	$7.4^{+1.8}_{-1.8}$	$0.7^{+0.5}_{-0.3}$
$10 < P < 70$	10	28.3	4	$6.5^{+1.6}_{-1.5}$...
$P > 70$	14	102.4	9	$16.7^{+5.3}_{-4.5}$	$4.5^{+3.9}_{-2.3}$
Grade A+B					
$0 < P < 1$	43	0.5	3	$6.3^{+1.6}_{-1.3}$	$0.5^{+0.3}_{-0.2}$
$1 < P < 10$	31	2.9	1	$7.3^{+1.4}_{-1.4}$	$0.7^{+0.3}_{-0.3}$
$10 < P < 70$	11	29.9	5	$6.9^{+1.6}_{-1.8}$...
$P > 70$	28	106.2	6	$17.7^{+5.4}_{-4.7}$	$5.1^{+4.2}_{-2.6}$

We draw on the large sample of M dwarf photometric rotation periods measured from the *Kepler* survey by McQuillan et al. (2013) to explore the rotation period distribution across the M dwarf spectral class. We downloaded additional data on these stars from the Kepler Input Catalog (Brown et al. 2011, KIC) from the MAST.

Absolute magnitudes provide the best way to estimate masses for single M dwarfs, and we use parallaxes to obtain absolute K magnitudes for the MEarth rotators as described in §4.3.1. Parallaxes are not available for the majority of M dwarfs targeted by *Kepler*, so we instead use masses estimated by Dressing & Charbonneau (2013), who matched broadband photometry to Dartmouth stellar models.³ Because the masses for MEarth and *Kepler* are determined using different methods, there may be an offset between the two mass scales. MEarth stars were selected to have $R < 0.33 R_{\odot}$, so any star with a mass greater than about $0.3 M_{\odot}$ is brighter than expected and more likely to be an unresolved multiple. Figure 4.15 plots photometric period versus estimated mass across the entire M spectral class.

Because we are interested in the mass-period relation, it is important that we have a uniform basis on which to compare the MEarth and *Kepler* samples. We therefore turn to photometric colors. The only reliable optical magnitude available for all MEarth M dwarfs is the apparent magnitude in the MEarth bandpass, which was calibrated by Dittmann et al. (2016), so we use $MEarth - K$ colors. The MEarth bandpass comprises most of i and all of z , so it is possible to estimate *MEarth* magnitudes for the *Kepler* stars from the KIC photometry with reasonable accuracy. We use an empirical relation derived from presently-unpublished observations we

³The requisite multicolor photometry for this method is not available for the brighter MEarth M dwarfs

have obtained of a number of MEarth targets in the SDSS filters:

$$MEarth = (i + 2 \times z) / 3 - 0.20 \quad (4.9)$$

This relation has a scatter of about 5%. Masses from Dressing & Charbonneau (2013) account for reddening; our color transformation does not. Figure 4.15 also plots photometric rotation period versus color.

The long rotation periods we find for the mid M dwarfs are consistent with the previous MEarth results from Irwin et al. (2011a), who found that the lower the mass of the star, the longer the period to which it spins down. It is challenging to infer the shape of the upper period envelope due to the lack of overlap between the stellar populations probed by *Kepler* and by MEarth. McQuillan et al. (2013) did not detect rotation periods longer than 70 days in any of their objects, although periods up to 155 days were searched.⁴ However, it is possible that *Kepler's* systematics, particularly differences between *Kepler's* data quarters, affect the recovery of longer rotation periods.

The lower envelope of the period distribution (shortest period seen at a given mass) is also mass-dependent, with the most rapid rotators having shorter periods at lower masses, particularly below the full convection limit. This feature is also seen in the Hyades and Praesepe open clusters (e.g. Agüeros et al. 2011) and in *vsini* studies of field late M and brown dwarfs (Mohanty & Basri 2003; Jenkins et al. 2009).

We find stars with intermediate rotation periods less often than more slowly-rotating stars, and that the gap between "slow" and "fast" rotators increases with

⁴In McQuillan et al. (2014) they place an upper limit of 70 days on the periods searched, but they do not in this earlier work.

decreasing mass. Using 41 light curves from the 2008-2010 seasons of MEarth data, we showed in Irwin et al. (2011a) that completeness was independent of rotation period for $P < 100$ days. This implies that the gap is astrophysical. Returning to Figure 4.3, which shows the distribution of periods for stars in our statistical sample, the lack of stars at intermediate periods is clear in the grade A and grade B rotators, as well as in the candidate periods for the "possible" detections. A similar gap has been seen in activity studies of M dwarfs (Herbst & Miller 1989; Gizis et al. 2002; Cardini & Cassatella 2007; Browning et al. 2010).

We suggest that the most likely explanation for the gap is that these mid M dwarfs spin down rapidly from "fast" to "slow" rotation rates. Under this hypothesis, M dwarfs spend comparatively little time at intermediate rotation periods, making it unlikely we would catch them there by chance in a field population with a wide range of ages.

4.9 Summary

We have searched for photometric rotation periods in every star that has been observed by the Northern MEarth transit survey. The rotation periods and ratings we present here supersede those reported previously in Irwin et al. (2011a) and West et al. (2015). The comparison of our rotation periods to other photometric periods from the literature and to $v \sin i$ measurements lends support to the periods we have detected, although we refer the reader to §4.4 for further discussion.

The rotation periods we detect range from 0.1 days to 140 days. Due to our

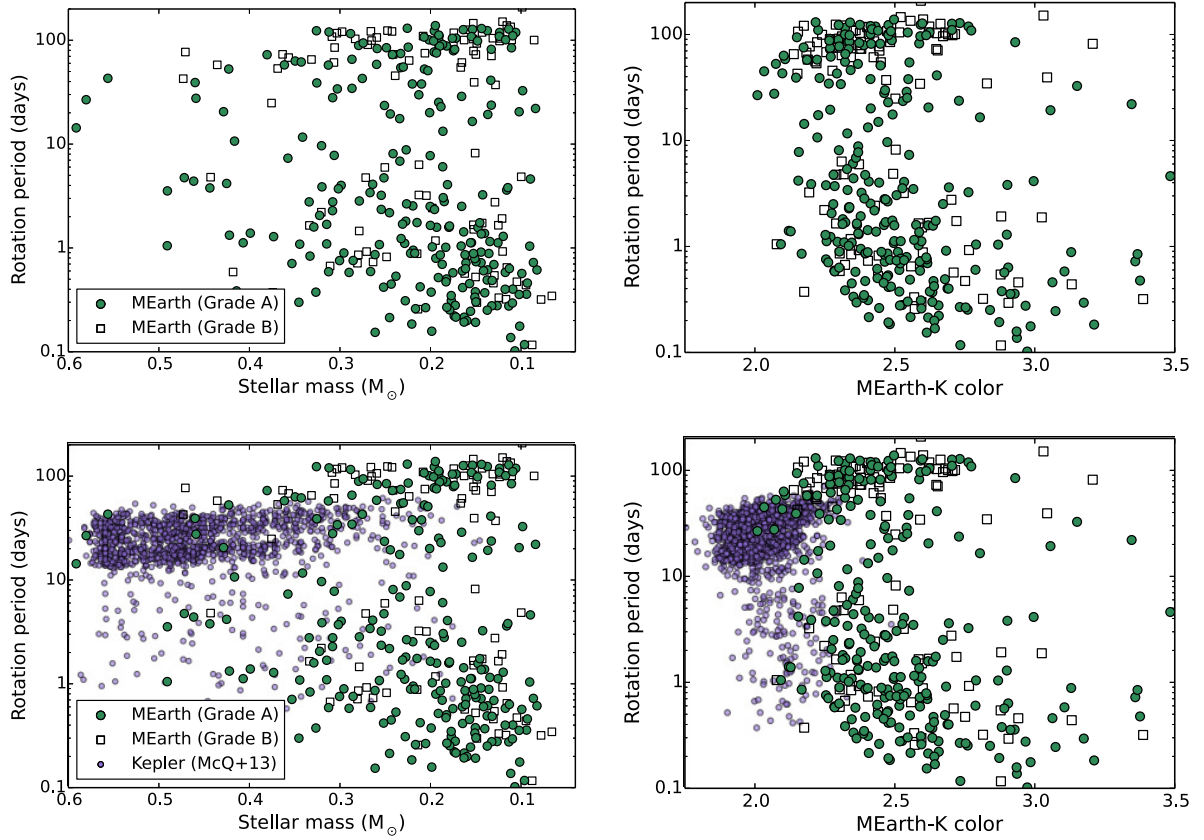


Figure 4.15.— Period versus stellar mass (left panels) and versus color (right panels). Only MEarth rotators from this work are shown in the upper panels, while in the lower panels we include *Kepler* rotators from McQuillan et al. (2013) and MEarth rotators. The masses of the *Kepler* stars are estimated from broadband colors and stellar models, while the masses for the MEarth stars are estimated from absolute K magnitudes. We use a linear combination of i and z magnitudes to estimate the magnitude of the *Kepler* stars in the MEarth bandpass. We have removed known and suspected multiples from these plots, but the MEarth stars with $M > 0.3 M_{\odot}$ are more likely to be unresolved multiples due to MEarth’s selection criteria. We see evidence for both a lower and upper envelope on the detected periods in the MEarth sample, and a lack of stars with intermediate rotation periods.

requirement that the photometric modulation be repeated, we expect that we may not be able to detect periods longer than 140 days (about half of the longest possible observing season), so this limit may simply reflect the longest period to which we are sensitive. For fully-convective stars with detected rotation periods, the amplitude of variability is independent of the rotation period, and we find no correlation between metallicity and rotation period or amplitude. Amongst rapid rotators, we find an abundance of stable, sinusoidal modulations. Our recovery rate in the subset of best-observed stars is $47 \pm 5\%$, and is higher for kinematically-young stars than it is for kinematically-old stars.

We used the variety of data that our team has collected on these stars to probe the Galactic kinematics of mid M stars in the Solar Neighborhood and of rotators in particular. Accounting for the selection criteria for the MEarth sample, we found that the nearby mid M dwarfs have kinematics consistent with those of higher-mass stars. We found evidence of the substructure seen in the kinematics of higher-mass stars amongst the M dwarfs as well, in particular the dynamically-created Hyades supercluster. These substructures, which most strongly affect the U and V components of the space velocities, are important to consider when drawing conclusions about the kinematics of local groups of stars.

There is clear evidence for a rotation-age relation in all three velocity components. Using the dispersion in the W velocity component and established age-velocity relationships, we estimated the mean ages for different populations of rotators. Considering M dwarfs with $0.1 < M < 0.25 M_{\odot}$, we found that stars with rotation periods less than 10 days are on average less than 2 Gyr old, while the slowest rotators we estimate to have an average age of 5^{+4}_{-2} Gyr. We find that most rotators

are likely members of the thin/young disk.

The mass-period relationship, as traced by the M_{Earth} and *Kepler* M dwarfs, confirms that mid M dwarfs spin down to longer periods than earlier M dwarfs. The fastest rotation periods we found amongst the field stars decrease with decreasing mass. We also see a lack of stars with intermediate rotation periods.

4.10 Conclusions

Our results are consistent with a scenario in which mid-type M dwarfs maintain rapid rotation (and enhanced magnetic activity) for the first several billion years of their life. At the age of the Hyades and Praesepe, M dwarfs have a range of rotation rates, with the latest-type M dwarfs having periods of < 1 day (Scholz & Eisloffel 2007). Our field M dwarfs with periods < 10 days are likely not much older than these clusters, given their low velocity dispersion. These stars do not appear to have converged to the same narrow mass-period relationship on which more massive stars are found. Convergence erases the dependence of rotation periods on the initial conditions, which is a prerequisite for gyrochronology.

We see an increase in the dispersion of total space velocity for increasingly longer periods, demonstrating that gyrochronology is potentially feasible for mid M dwarfs at old ages and rotation periods of about 100 days, if convergence can be established. Our current sample only allows us to determine that the mean age of those M dwarfs with $P > 70$ days is about 5 Gyr. This may represent a sample that is continuing to spin down slowly, and for which rotation period increases with age.

More precise constraints on the age-rotation relation at long periods are required.

We have demonstrated that Galactic kinematics is a useful tool for studying the age-rotation relation, and with a larger sample of stars will provide further constraints. However, the use of kinematics is limited by our understanding of the age-velocity relation, which at present is best calibrated from 1 to 5 Gyr. Due to the population-level approach our analysis requires, kinematics may not be able to establish whether the rotation periods of mid M stars converge. M dwarfs in multiple systems with stars of determined ages, such as white dwarfs, provide another promising avenue (e.g. Morgan et al. 2012; Rebassa-Mansergas et al. 2013; Dhital et al. 2013). Observations of M dwarfs in older clusters, while potentially quite useful, are technically challenging due to the greater distances at which these clusters are found, the relative faintness of the M dwarf members, and the need to establish cluster membership, but may become feasible with future observational advances.

McQuillan et al. (2013), using *Kepler* photometry, found that early-type M dwarfs with periods less than 10 days had high amplitudes of variability and stable spot patterns. They postulated that these objects were binaries, which could also explain why no candidate planets have been found around them. Extrapolation of the period distribution of the rapidly-rotating mid-type M dwarfs from MEarth indicates that the young, early-type field M dwarfs should have periods of 1 – 10 days. The stability that McQuillan et al. (2013) saw is also reminiscent of the well-behaved sinusoids we see in rapidly-rotating, lower-mass M dwarfs. This suggests that young field stars could be a substantial component of the rapidly-rotating *Kepler* M dwarf sample.

The relative lack of field mid M dwarfs with intermediate rotation periods –

between about 10 and 70 days – supports the suggestion of Irwin et al. (2011a) that spin-down occurs rapidly. The gap in periods is similar to that seen in the distribution of magnetic activity levels, and may be the result of the same underlying physical mechanism. The rapid evolution may occur when the stars reaches a critical condition, which could be a certain rotation rate or magnetic flux. It could also relate to a change in magnetic field topology, which more effectively couples the stellar wind and magnetic field (see e.g. Garraffo et al. 2015). The mass-period relation shown in Figure 4.15 suggests that the critical condition may be mass-dependent, as the gap appears to narrow at earlier spectral types. Using the mean age of our rapid and slow rotators as the lower and upper bounds, we suggest that this occurs between 2 and 5 Gyr.

The active lifetime of mid and late M dwarfs is plausibly associated with the rapid evolution we discuss above. West et al. (2015) found the fraction of active stars (as traced through $H\alpha$ emission) decreases significantly for the longest-period rotators in the MEarth sample. West et al. (2008) determined that activity lifetime is about 5 Gyr for M4V stars, and 7 Gyr for M5V stars (a large jump in active lifetime is seen between M3V and M5V, which these authors associate with the fully-convective boundary). Our work implies a somewhat shorter active lifetime, but this may be the result of the different age-velocity relationship used by West et al. (2008), which assumes a steeper power law and no saturation.

Stars with rotation periods of around 100 days are not generally found to be magnetically active (West et al. 2015). Nevertheless, many slowly-rotating mid-to-late M dwarfs show variability amplitudes of half a percent or more, implying that they have maintained strong enough magnetic fields to produce the requisite spot

contrasts. The lack of correlation between rotation period and amplitude for these stars indicates that the spot contrast is not changing significantly, even while they undergo substantial spin-down.

We are collecting additional $H\alpha$ measurements and radial velocities to further improve our understanding of the connection of magnetic activity and kinematics to rotation, and using the MEarth-South data to search for new rotators amongst the nearby M dwarfs in the Southern hemisphere. Our goal is to further constrain the age-rotation-activity relation, particularly at intermediate and long periods.

Chapter 5

The Impact of Stellar Rotation on the Detectability of Habitable Planets Around M Dwarfs

E R. Newton, J. Irwin, D. Charbonneau, Z.K. Berta-Thompson, *and* J.A. Dittmann
The Astrophysical Journal, Volume 821, Issue 1, Article L19, 2016

5.1 Introduction

Radial velocities are a powerful tool for the discovery and characterization of exoplanetary systems. However, stellar magnetic activity and rotation affect the measured radial velocities, as surface inhomogeneities cross the stellar surface and change with time. Starspots diminish light received from the limbs of a rotating

star, causing changes in spectral line centroid (e.g. Saar & Donahue 1997). Plages have a similar influence, but with the opposite sign (e.g. Meunier et al. 2010). Strong localized magnetic fields, typically associated with spots, modify convective flows and cause a net blueshift (e.g. Gray 2009; Meunier et al. 2010). Disentangling these stellar activity signals from the planetary reflex motion is challenging, and typically requires modeling activity-induced changes in the spectral line profiles (e.g. Queloz et al. 2009; Boisse et al. 2011; Dumusque et al. 2011, 2012; Rajpaul et al. 2015). This is particularly pertinent for M dwarf stars, which retain high levels of magnetic activity for longer than Sun-like stars. Studies of exoplanets around the nearby M dwarfs Gl 581, Gl 667C, and Gl 191 (Kapteyn’s star) have recently highlighted this concern.

Gl 581 is an M3V (Henry et al. 1997a)¹ star. Bonfils et al. (2005b) first discovered the hot Neptune Gl 581 b orbiting this star, while Udry et al. (2007) identified a second short-period planet, Gl 581 c. The number of additional planets that orbit this star has been a matter of recent debate. Udry et al. (2007) further identified planet d, and Mayor et al. (2009) planet e. Vogt et al. (2010) found evidence for a long-period planet f, and a potentially habitable planet g. Analyses by other groups quickly cast doubt on planets f (Tuomi 2011; Forveille et al. 2011) and g (Gregory 2011; Baluev 2012; Hatzes 2013). Baluev (2012) also raised concerns about planet d. Robertson et al. (2014) looked at the H α line, a magnetic activity indicator. They found support for the existence of the three innermost planets (b, c, and e), but indications that the outer planets (d, g, and f) are the result of stellar activity and rotation.

Bonfils et al. (2013) identified a super-Earth around Gl 667C, with a second

¹Included in the RECONS compilation: <http://www.recons.org/TOP100.posted.htm>

found by Anglada-Escudé et al. (2012b) and Delfosse et al. (2013). Anglada-Escudé et al. (2013b) identified a total of six Keplerian signals at a range of periods. Though long-period signals were seen by Delfosse et al. (2013) and by Makarov & Berghea (2014), they were postulated to be related to the ~ 105 day stellar rotation period. Independent analyses by Feroz & Hobson (2013) and Robertson & Mahadevan (2014) did not find evidence for planets exterior to Gl 667C b and c.

Anglada-Escudé et al. (2014) reported two planets with periods of 48 and 120 days around Gl 191. Robertson et al. (2015b) showed that the 48 day signal is correlated with stellar activity, and suggested a non-planetary origin. They also express concern that the period of the outer planet is close to the 143 day stellar rotation period.

These examples illustrate that stellar activity signals, which appear at the stellar rotation period and its harmonics, can mimic the effect of a planet at or near these orbital periods. The typical rotation periods of field-age dwarf stars varies by almost an order of magnitude across the lower main sequence, increasing from about 25 days for early G stars (Barnes 2007), to greater than 100 days for mid-to-late M dwarfs (Newton et al. 2016). Over the same stellar mass range, the orbital period corresponding to a habitable planet decreases from approximately 365 days to 10 days. There thus exists a range of stellar masses where the stellar rotation and planetary habitable-zone periods overlap. This came to our team's attention in pursuit of follow-up observations of K2-3, an early M dwarf with three confirmed transiting super-Earths (Crossfield et al. 2015): we noted that the stellar rotation period of ~ 40 days is very close to the 44 day orbital period of K2-3d, which is near the inner edge of the planetary habitable zone.

There are several current and near-future radial velocity surveys committed to finding planets around M dwarf stars, including CARMENES (Quirrenbach et al. 2014), HPF (Mahadevan et al. 2012), and SPIRou (Artigau et al. 2014). It is therefore critical that we understand how stellar rotation may impact the discovery of the potentially habitable planets around these stars. In this Letter, we leverage new rotation periods of mid-to-late M dwarfs in the solar neighborhood from our recent work in Newton et al. (2016) to investigate this problem for stars across the M spectral class.

5.2 Stellar rotation periods and masses across the main sequence

To assess stellar rotation across the main sequence, we compile literature measurements for the rotation periods of field stars, using data from Baliunas et al. (1996), Kiraga & Stepien (2007), Hartman et al. (2011), Suárez Mascareño et al. (2015), and Newton et al. (2016). The latter supplies most of the rotation period measurements for mid and late M dwarfs, and results from our analysis of photometry from the MEarth-North transit survey (Berta et al. 2012; Irwin et al. 2015). The rotation periods from Hartman et al. (2011) and Kiraga & Stepien (2007) also come from broadband optical or red-optical photometry. On the other hand, Baliunas et al. (1996) and Suárez Mascareño et al. (2015) measure periodicities in chromospheric activity features.

We use stellar mass (M_*) as the independent parameter for this study. For G

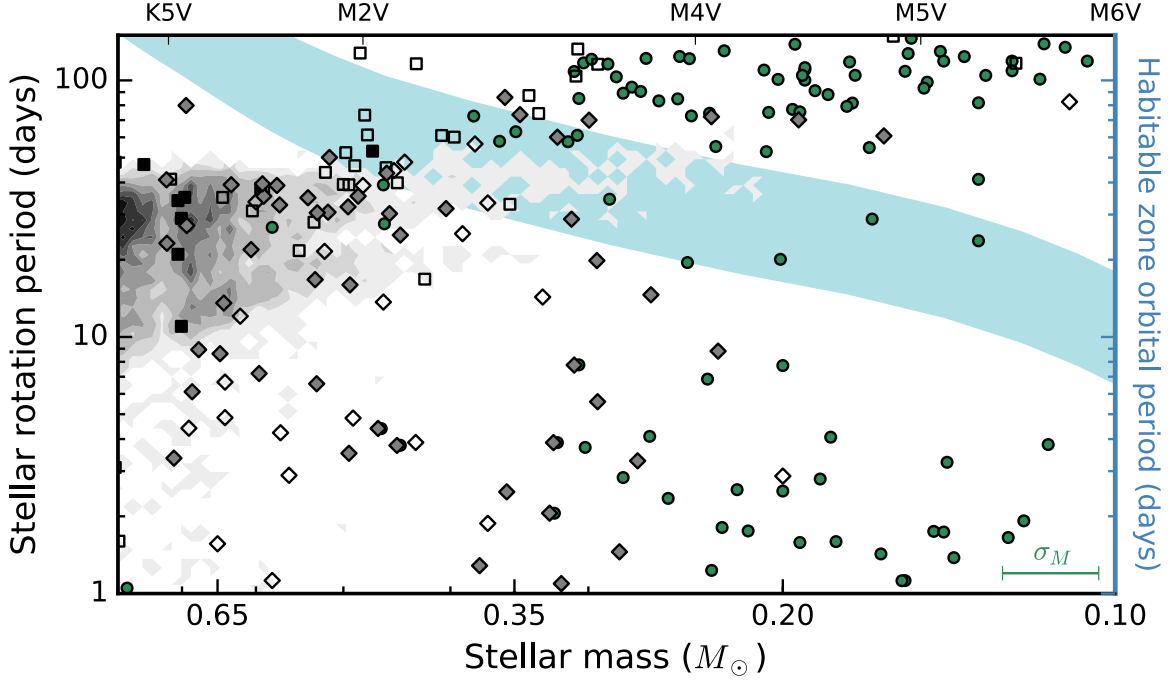


Figure 5.1.— Stellar rotation period as a function of stellar mass and its relation to the planetary habitable zone. Gray shading shows the rotation period distribution from McQuillan et al. (2014), who analyzed data from *Kepler*. Filled black squares are from Baliunas et al. (1996), and open black squares are from Suárez Mascareño et al. (2015). Open diamonds are from Kiraga & Stepien (2007), and filled diamonds are from Hartman et al. (2011). Green circles are M dwarf rotators from the Newton et al. (2016) statistical sample. The upper envelope indicates the rotation periods of typical, older field stars. The error bar in the lower right indicates the 10% scatter in the empirical M_K -mass relation used to infer stellar mass for the M and late K dwarfs (Delfosse et al. 2000). The blue shaded region shows the habitable zone as a function of stellar mass from Kopparapu et al. (2013). For early M dwarfs, the habitable zone period overlaps with the rotation periods of typical stars, both of which are about 40 days. This coincidence complicates the radial velocity detection of habitable planets around early M dwarfs, but not for mid-to-late M dwarfs, or for G and K dwarfs.

and early K dwarfs, we use $B - V$ colors to estimate effective temperature (T_{eff}), and then use isochrones to infer M_* . We use the $B - V$ colors provided by Baliunas et al. (1996) and Suárez Mascareño et al. (2015) in their works. We use the empirical relation between $B - V$ color and T_{eff} from Boyajian et al. (2013) to determine T_{eff} . We adopt the 2 Gyr solar-metallicity isochrones from Baraffe et al. (2015).

For late K and M dwarfs, there are known discrepancies between the theoretical and observed stellar temperatures and masses (e.g. Boyajian et al. 2012). For stars with $B - V > 1$, we therefore use the M_K -mass relation from Delfosse et al. (2000), which we have modified to allow extrapolation as described in Newton et al. (2016). Delfosse et al. (2000) calibrated an empirical relation to determine stellar mass by relating the dynamical masses measured from binary orbits to the stars' absolute CIT K magnitudes (M_K). The scatter in the relation is about 10%. We restrict the K and M dwarfs included in this study to those with trigonometric distances. We use NIR magnitudes from 2MASS (Cutri et al. 2003, , requiring `qual_flag = AAA`), or alternatively CIT magnitudes from Leggett (1992).

We also include the rotation periods measured from *Kepler* photometry by McQuillan et al. (2014). Most *Kepler* stars do not have parallaxes and they may be subject to interstellar reddening. Therefore, we use the T_{eff} listed in McQuillan et al. (2014). These T_{eff} are adopted from the *Kepler* Input Catalog (KIC; Brown et al. 2011) or, where available, from Dressing & Charbonneau (2013). We then interpolate T_{eff} onto the 2 Gyr solar-metallicity isochrones from Baraffe et al. (2015) to infer stellar mass. The difference in the way masses are estimated for the *Kepler* sample may result in an offset relative to the masses of K and M dwarfs estimated from M_K (e.g. Newton et al. 2015).

Figure 5.1 shows stellar rotation period as a function of stellar mass for late-type stars in the field. Given the uncertainties in the stellar parameters for the *Kepler* sample, we treat these as an ensemble and plot the distribution instead of the individual measurements. The sensitivity of the McQuillan et al. (2014) analysis may be limited by *Kepler*'s quarterly flux offsets; the other surveys included in this compilation detected periods out to 100 days or longer.

Figure 5.1 includes stars of a range of ages. As single stars age, they lose angular momentum and their rotation periods increase. Angular momentum loss is mass dependent, with lower-mass stars taking longer to spin down, but eventually reaching longer rotation periods. The long-period envelope of the rotation period distribution is thought to represent an old field population, and the fast rotators at a given mass will eventually evolve toward these long periods². The envelope comprises stars of similar age to the Sun and older, which was established by Skumanich (1972) and Barnes (2003) for Sun-like stars. We quantified this for M dwarfs by using galactic kinematics to estimate that mid M dwarfs with rotation periods around 100 days are on average 5 Gyr old (Newton et al. 2016).

5.3 Stellar rotation and the habitable zone

When radial velocity variations induced by stellar rotation and activity coincide with the planetary orbital period, it can be difficult to identify the planetary signal. This

²There are handful of early M dwarfs with rotation periods of around 100 days, which stand out as lying above this envelope. Though intriguing, discussion is beyond the scope of this paper.

stellar signal can appear not just at the rotation period itself, but at higher-order harmonics as well. Boisse et al. (2011) tested cases where the photosphere is dominated by one or two spots and found that power appears primarily at one-half and one-third the stellar rotation period (see also Aigrain et al. 2012). Certain configurations resulted in a low-amplitude signal at one-fourth the rotation period as well. Though spot patterns are likely more complex, both Boisse et al. (2011, 2012) and Aigrain et al. (2012) had success modeling observed radial velocity data. With typical observational sampling, power from these stellar signals leak into nearby frequencies (see, e.g., Fig. 15 in Boisse et al. 2011). Thus, stars with rotation periods that are the same as, or two to three times longer than, the habitable zone are not optimal targets for radial velocity searches that aim to discover potentially habitable planets.

The habitable zone from Kopparapu et al. (2013, using values from the erratum) is indicated in Figures 5.1-5.3. We adopt the moist greenhouse limit as the inner edge of the habitable zone and the maximum greenhouse as the outer edge of the habitable zone. We use the Baraffe et al. (2015) solar-metallicity 2 Gyr isochrone to calculate T_{eff} and luminosity (L) at a given stellar mass. We note that the choice of stellar models as well as parameters beyond stellar mass, in particular stellar age and metallicity, affect T_{eff} and L , and therefore also the precise location of the calculated habitable zone.

For $0.35M_{\odot} < M_{*} < 0.5 M_{\odot}$, Figure 5.1 shows that the orbital period of habitable-zone planets is similar to the rotation period of the typical 5 Gyr star. Power can also appear at multiples of the stellar rotation period, so activity signatures can pose problems for habitable-zone planets even with slowly rotating early M dwarfs. This

means that stellar rotation can be a confounding factor for $0.25M_{\odot} < M_* < 0.5 M_{\odot}$. This corresponds to spectral types between M1V and M4V.

We illustrate this idea by considering known M dwarf planet hosts (Fig. 5.2). Our planet-host sample is drawn from the *exoplanet.eu* database (Schneider et al. 2011). We select those stars with $T_{\text{eff}} < 4200$ K, $M_* < 0.7 M_{\odot}$, $R_* < 0.7 R_{\odot}$, and a measured trigonometric parallax. We use the M_K –mass relation from Delfosse et al. (2000) to estimate stellar masses. We use parallaxes from van Leeuwen (2007, from *Hipparcos*), and supplement with additional sources as necessary. We adopt NIR magnitudes from 2MASS (Cutri et al. 2003, , requiring `qual_flag = AAA`). Where 2MASS magnitudes are not available, we use CIT magnitudes from Leggett (1992). We then use the Delfosse et al. (2000) relation to estimate stellar masses and the Boyajian et al. (2012) single-star relation to estimate stellar radii. The Delfosse et al. (2000) relation is based on CIT magnitudes, so we convert 2MASS magnitudes to the CIT system using the relations from Cutri et al. (2006). Stellar rotation periods are compiled from the literature, though many are from Suárez Mascareño et al. (2015). We do not consider estimates from rotational broadening of spectral lines, which are subject to uncertainty in the inclination angle. These data are listed in Table 5.1.

Figure 5.2 shows the rotation periods of these planet hosts. Gl 581, in particular, highlights the challenge early M dwarfs pose for radial velocity surveys seeking to find habitable planets. Though this star has a very long rotation period (130 days), the harmonics dip into the habitable zone. This resulted in the controversy over the potentially habitable planet Gl 581 d ($P_d = 66$ days, at about $P_{\text{rot}}/2$), as well as g ($P_g = 36$ days, between $P_{\text{rot}}/3$ and $P_{\text{rot}}/4$).

Table 5.1. Stellar parameters for M dwarf planet hosts with trigonometric parallaxes

Star	Distance (pc)	Ref. ^a	K_S (2MASS)	Mass (M_\odot)	Radius (R_\odot)	P_{rot} (days)	Ref. ^b
Published rotation period							
Gl 176	9.27	vL07	5.607	0.49	0.47	39.5	R15a
Gl 191	3.91	vL07	5.049	0.27	0.28	143.0	R15b
Gl 433	8.88	vL07	5.623	0.47	0.45	73.2	SM15
Gl 436	10.14	vL07	6.073	0.44	0.42	39.9	SM15
Gl 581	6.21	vL07	5.837	0.30	0.30	132.5	SM15
Gl 667C	6.84	vL07	6.036	0.30	0.30	103.9	SM15
Gl 674	4.54	vL07	4.855	0.35	0.34	32.9	SM15
Gl 832	4.95	vL07	4.461	0.45	0.43	45.7	SM15
Gl 849	9.1	vL07	5.594	0.49	0.46	39.2	SM15
Gl 876	4.69	vL07	5.010	0.33	0.33	96.7	R05
GJ 1132	12.04	J05	8.322	0.18	0.21	125.0	BT15
GJ 1214	14.55	AE13	8.782	0.18	0.21	...	(See note)
HIP 57050	11.1	vL07	6.822	0.34	0.34	73.5	H11
No rotation period available							
Gl 15A	3.59	vL07	4.011	0.40	0.39
Gl 27.1	23.99	vL07	7.394	0.55	0.52
Gl 163	14.99	vL07	7.135	0.40	0.38
Gl 179	12.29	vL07	6.942	0.36	0.35
Gl 180	12.12	vL07	6.598	0.41	0.40
Gl 229	5.75	vL07	4.131	0.58	0.55
Gl 317	15.3	AE12	7.028	0.43	0.41
Gl 328	19.79	vL07	6.352	0.68	0.65
Gl 422	12.67	vL07	7.035	0.35	0.35
Gl 649	10.34	vL07	5.624	0.54	0.51
Gl 682	5.08	vL07	5.606	0.27	0.28
Gl 687	4.53	vL07	4.501	0.41	0.39
GJ 3341	23.2	R10	7.733	0.47	0.44
GJ 3634	19.8	R10	7.470	0.45	0.43

Table 5.1—Continued

Star	Distance (pc)	Ref. ^a	K_S (2MASS)	Mass (M_\odot)	Radius (R_\odot)	P_{rot} (days)	Ref. ^b
HIP 12961	23.01	vL07	6.736	0.67	0.64
HIP 70849	23.57	vL07	6.790	0.67	0.64
HIP 79431	14.4	vL07	6.589	0.49	0.46
Wolf 1061	4.29	vL07	5.075	0.30	0.30

^aReferences for trigonometric distances: J05 = Jao et al. (2005); vL07 = van Leeuwen (2007); R10 = Riedel et al. (2010); AE12 = Anglada-Escudé et al. (2012a); AE13 = Anglada-Escudé et al. (2013a)

^bReferences for stellar rotation periods: R05 = Rivera et al. (2005); H11 = Hartman et al. (2011); R15a = Robertson et al. (2015a); R15b = Robertson et al. (2015b); BT15 = Berta-Thompson et al. (2015); SM15 = Suárez Mascareño et al. (2015)

Note. — GJ 1214 displays photometric modulation, but has not yielded a secure rotation period detection. Berta et al. (2011) tentatively derived a rotation period of 52 days from MEarth photometry and noted that the long-period signal in one season of data indicates that the period may be 80 – 100 days. Our recent re-analysis in Newton et al. (2016) did not yield a firm period detection. Using independent data sets, Narita et al. (2013) and Nascimbeni et al. (2015) found periods of 44 days and approximately 80 days, respectively.

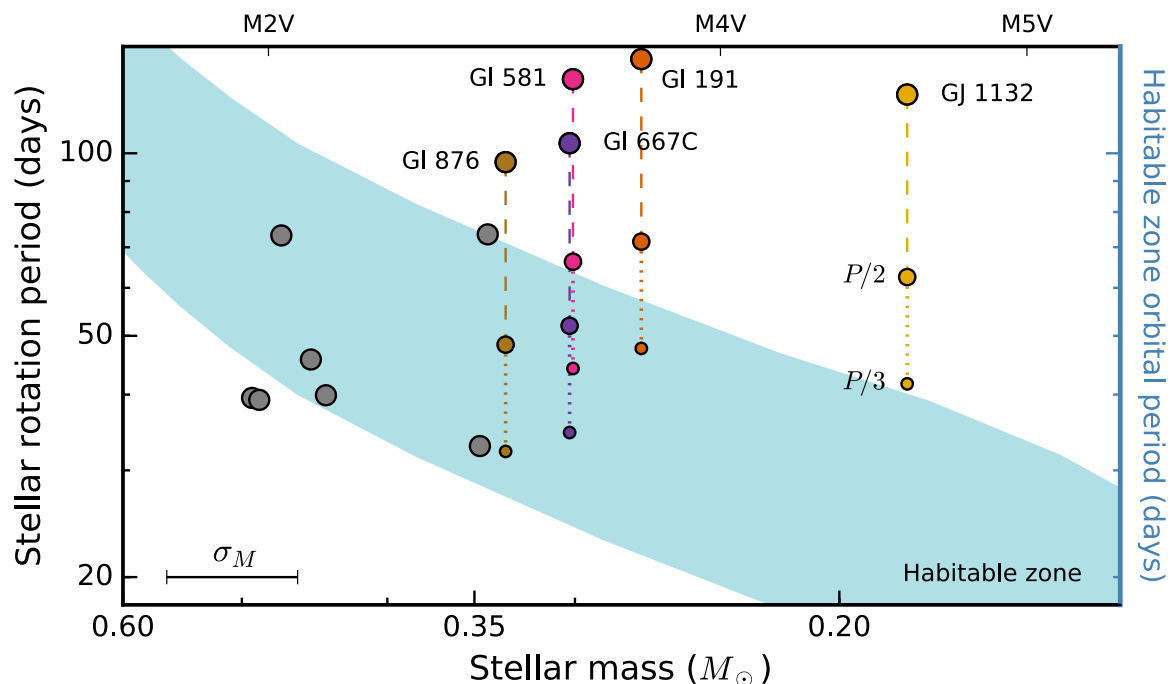


Figure 5.2.— Stellar rotation period vs. stellar mass and its relation to the planetary habitable zone for M dwarfs planet hosts. The error bar in the lower left indicates the 10% scatter in the empirical M_K -mass relation used to infer stellar mass (Delfosse et al. 2000). The blue shaded region shows the habitable zone as a function of stellar mass from Kopparapu et al. (2013). For early M dwarfs, the habitable-zone period overlaps with the rotation periods of typical stars, both of which are about 40 days. GJ 1214 has been excluded from this plot due to the range of published rotation periods (see Table 5.1).

GJ 1132 ($M_* = 0.18 M_\odot$) demonstrates that this is not an issue for many of the lowest-mass M dwarfs. Like many stars of this mass, GJ 1132 has a rotation period ($P_{\text{rot}} = 125$ days Berta-Thompson et al. 2015) comparable to that of Gl 581. We show the periodogram of this data set in Figure 5.3; there is no significant power at periods shorter than around 60 days. In the photometry, we do not see power at the second and third harmonics, which is not surprising given the near-sinusoidal modulation seen in Berta-Thompson et al. (2015). However, power could still appear at these frequencies in the radial velocities. However, its lower-mass results in shorter periods for potentially habitable planets, and the third harmonic of the stellar rotation period still lies outside the outer edge of the habitable zone (although only barely so).

5.4 M dwarfs with photometric monitoring as targets for radial velocity surveys

We have demonstrated that long-period, low-mass rotators provide good targets for radial velocity surveys searching for habitable planets. We have provided a catalog of stars with detected photometric rotation periods in Newton et al. (2016), which will be useful in selecting such targets. We recommend selecting those targets with long photometric rotation periods (grade A or B rotators, $P \gtrsim 100$ days).

Also of interest to the community will be those stars that may be photometrically quiet. Newton et al. (2016) catalog stars for which we did not detect periodic photometric modulation in the MEarth data. For some of these objects, the light curves were noisy or sparse, which could have prohibited period detection. Further

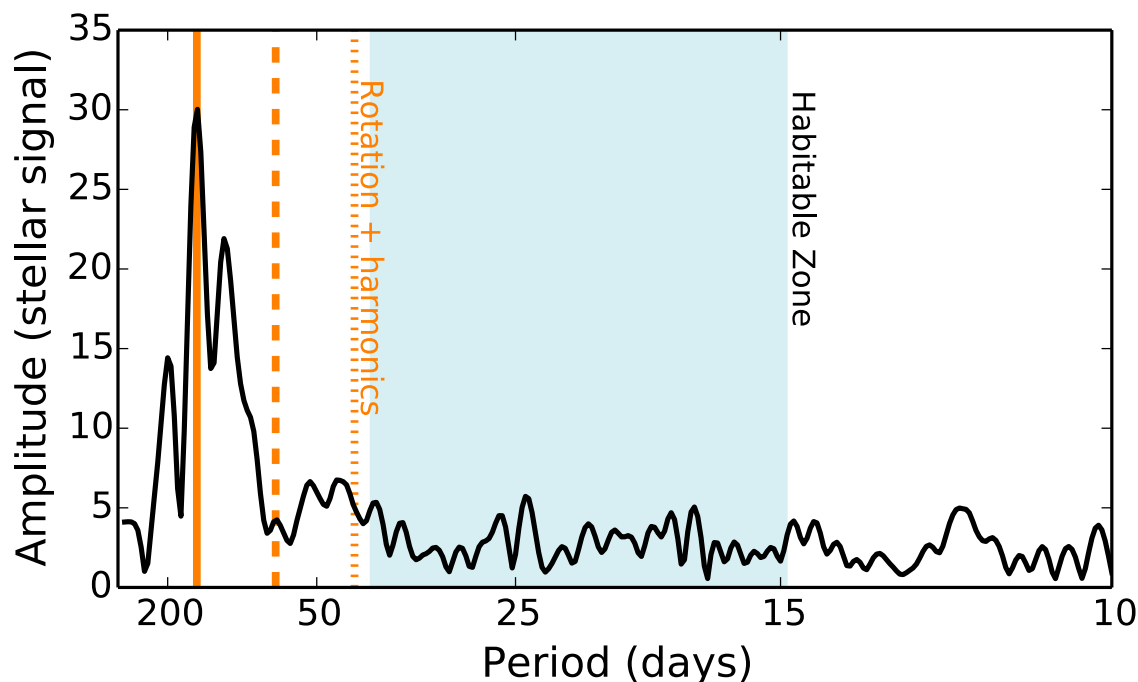


Figure 5.3.— Periodogram of the MEarth light curve for GJ 1132 (Berta-Thompson et al. 2015). The highest peak, indicated by the solid vertical line, is the adopted rotation period. The second and third harmonics are indicated by dashed and dotted lines, respectively; the radial velocity signal from the starspots associated with its photometric variability is expected to have power at these frequencies. The shaded region indicates the planetary habitable zone. The frequency space within which one would find a habitable planet is not expected to be strongly contaminated by stellar activity.

monitoring may indicate whether these stars are good targets for radial velocity surveys. The statistical sample we identified includes the objects more likely to be of immediate interest.

Our statistical sample was the subset of stars for which the number of observations (n_{visits}) and median error (σ) were such that we had good sensitivity to a range of rotation periods ($n_{\text{visits}} > 1200$, $\sigma < 0.005$). Within this sample, we did not detect a periodic signal for 52%. A Kolmogorov-Smirnov test indicates that the distribution of space velocities for the non-detections is statistically indistinguishable from that of the long-period ($P_{\text{rot}} > 70$ days) sample. We infer that, on average, these stars have ages similar to the long-period sample: we generally expect them to be members of the old thin disk and to be slowly rotating. The stars in the statistical sample with no period detections are therefore also promising targets for radial velocity surveys.

5.5 Discussion

We have demonstrated that the habitable zone of early M dwarfs coincides with the stellar rotation period typical for older field stars (approximately 5 Gyr). Because activity signals are also expected at two and three times the frequency of the stellar rotation, the stars for which this is an issue are those with $0.25M_{\odot} < M_{*} < 0.5 M_{\odot}$ (roughly M1V–M4V). This means that stellar activity will be an unavoidable contaminant in radial velocity surveys that are searching for habitable planets around early M dwarfs. Rather than being the exception, we expect that challenges faced in understanding the Gl 581 system are typical for stars with its mass.

The lifetime of stellar activity and of rapid rotation is another important consideration, since precise radial velocity measurements are challenging for stars with strong activity signature and those with rotationally broadened spectral features. West et al. (2008) found that the activity lifetime rises sharply around a spectral type of M4V. Stellar magnetic activity diminishes by 1 Gyr for M0–M3 dwarfs, but may last for 7 – 8 Gyr for M6–M8 dwarfs. It is approximately 4 Gyr for M4–M5 dwarfs. In what is presumably a related phenomenon, lower-mass stars also retain rapid rotation rates for longer than do higher mass stars: few early M dwarfs are found to be rapidly rotating (McQuillan et al. 2013), while nearly all very late M (and L) dwarfs have detectable rotational broadening Mohanty & Basri (2003). In Newton et al. (2016), we found an abundance of slowly rotating mid M dwarfs (M4V–M6V), and estimated that a rapid loss of angular momentum occurs between 2 and 5 Gyr for mid M dwarfs. These considerations disfavor the latest-type M dwarfs, since strong activity signatures and rapid rotation are expected to persist for a substantial part of the stars’ lifetime.

Finally, we consider the prospects for detailed characterization. A key motivation for turning to M dwarfs is that their small stellar size enhances the signals of orbiting planets. However, M dwarfs span nearly a decade in stellar mass and radius. This means that the transit and radial velocity signatures of a planet orbiting a mid-to-late M dwarf are significantly larger than if an analogous planet orbited an early M dwarf. For example, the transit depth of the Earth around the Sun is 0.0084%; for the same size planet orbiting an $R_* = 0.5 R_\odot$ star (M1V), the transit depth is 0.034%, while for an $R_* = 0.15 R_\odot$ star (M5V), it is 0.37%. Similarly, an Earth-mass planet at the inner edge of the habitable zone induces a radial velocity semi-amplitude of 0.25

m/s if it orbits an $M_* = 0.55 M_\odot$ star (M1V), compared to 0.98 m/s if it orbits an $M_* = 0.15 M_\odot$ star (M5V).

A promising avenue to look for biosignatures on habitable exoplanets is the direct detection of the planetary Doppler shift. Snellen et al. (2013) recently explored the prospects for detecting oxygen by looking at exoplanetary telluric features. Rodler & López-Morales (2014) undertook a detailed simulation of the feasibility of this detection if using a high-resolution spectrograph on an Extremely Large Telescope. Their work indicates that the detection of oxygen in the atmosphere of a habitable, Earth-sized planet is a significant time investment that will only be feasible for nearby M dwarfs with $M_* < 0.25 M_\odot$. This is due to the relative size of the star and the planet, and the orbital periods of planets in the habitable zone. Such a measurement would be within reach only for the nearest and brightest mid-to-late M dwarfs.

We have considered three factors critical to understanding the prospects of detecting and characterizing habitable planets around M dwarfs:

1. The coincidence of the habitable-zone orbital periods and stellar rotation periods.
2. The lifetime of activity and rapid rotation.
3. The accessibility of detailed atmospheric characterization.

We have demonstrated that the confluence of these factors make mid M dwarfs ideal targets for radial velocity surveys that have the goal of discovering habitable planets whose atmospheres can be studied with the *James Webb Space Telescope* and

the ELTs. Many of these targets will be discovered in the coming years by radial velocity instruments and transit surveys (the latter of which are likely to receive radial velocity follow-up). Early M dwarfs are tempting targets for such surveys: their relative brightness makes it easier to achieve higher signal-to-noise observations and more precise radial velocity measurements. However, stellar activity signals will be present at the same periods at which the habitable planets are found. Recent debate surrounding the candidate exoplanets orbiting Gl 581, Gl 667C, and Gl 191 have already demonstrated the challenge of disentangling planetary reflex motion from stellar activity signals.

We therefore suggest that radial velocity surveys closely consider the mid M dwarfs, with $0.1 M_{\odot} < M_{*} < 0.25 M_{\odot}$ (M4V–M6V). Recent work by the MEarth team provides a useful starting place from which to build such a sample in the northern hemisphere. Nutzman & Charbonneau (2008) selected M dwarfs from the Lépine & Shara (2005) northern proper motion catalog with estimated stellar radii $R_{*} < 0.33 R_{\odot}$ and trigonometric or photometric distances that placed them within 33 pc. We have since obtained low-resolution near-infrared and optical spectroscopy for a quarter of the sample, and astrometric and photometric analysis of the entire MEarth-North data set. The near-infrared spectroscopic survey conducted by Terrien et al. (2015) also includes substantial overlap with the MEarth-North sample, as do the optical spectroscopic surveys from Lépine et al. (2013), Gaidos et al. (2014), and Alonso-Floriano et al. (2015). Detailed characterization from the MEarth team includes:

- Kinematic radial velocities (Newton et al. 2014).

CHAPTER 5. STELLAR ROTATION AND THE PLANETARY HABITABLE ZONE

- Spectroscopically-estimated stellar parameters (Newton et al. 2015).
- $H\alpha$ measurements (West et al. 2015, and Newton et al. in prep).
- Trigonometric parallaxes (Dittmann et al. 2014).
- Optical colors and estimated metallicities (Dittmann et al. 2016).
- Photometric rotation periods and non-detections (Newton et al. 2016).

Chapter 6

H α Emission in Nearby M dwarfs and its Relation to Stellar Rotation

E R. Newton, J. Irwin, D. Charbonneau, P. Berlind, M.L. Calkins, *and* J. Mink
in preparation

6.1 Introduction

Solar-type stars show a saturated relationship between rotation and chromospheric or coronal activity: with rotation above a certain threshold, activity maintains a saturated value, while at slower spins activity and rotation are correlated. This has been demonstrated using coronal (x-ray) emission (e.g. Pallavicini et al. 1981; Vilhu 1984; Pizzolato et al. 2003; Wright et al. 2011), chromospheric (H α and Ca II) emission (e.g. Wilson 1966; Noyes et al. 1984; Soderblom et al. 1993), and radio

emission from accelerated electrons (Stewart et al. 1988; Slee & Stewart 1989; Berger 2006; McLean et al. 2012, e.g.). Coronal and chromospheric emission is typically assumed to be the result of magnetic heating of the stellar atmosphere, while radio emission is a more direct probe of the magnetic field. The rotation–activity relation is therefore interpreted as being the result of the underlying magnetic dynamo, which for solar-type stars is generally thought to be the $\alpha\Omega$ dynamo. The interface $\alpha\Omega$ dynamo is dependent on rotation and shear at the tachocline, the boundary between the convective and radiative zones. Magnetic field topologies moderate angular momentum losses via magnetized stellar winds, thereby influencing rotational evolution. In turn, faster rotation rates induce increased chromospheric and coronal activity up to the saturation threshold.

Moving across the M spectral class, the convective envelope extends deeper into the stellar interior, with theoretical models indicating that stars become fully convective for masses $< 0.35 M_{\odot}$ (Chabrier & Baraffe 1997). In stars lacking a tachocline, the interface $\alpha\Omega$ cannot be at play and the mechanisms for generating large-scale magnetic fields in fully-convective stars are not well understood. Nevertheless, Zeeman Doppler imaging reveals that some do indeed have large-scale fields (Donati et al. 2008; Morin et al. 2010), and many mid-to-late M-dwarfs have strong signatures of magnetic activity, with emission from the X-ray to the radio (e.g. Berger et al. 2010; Stelzer et al. 2013).

Despite the expected difference in magnetic dynamo, the strong connection between rotation and magnetic activity persists in M dwarfs. Consistent with that seen in more massive stars, the rotation-activity relation in M dwarfs is saturated for rapid rotators, and declines with decreasing rotational velocity (Kiraga & Stepien

2007). This is seen in a wide variety of tracers of magnetic activity, including x-ray flux (Stauffer et al. 1994; James et al. 2000; Wright et al. 2011), Ca H&K, (Browning et al. 2010), H α emission (Delfosse et al. 1998; Mohanty & Basri 2003; Reiners et al. 2012), and global magnetic flux (Reiners et al. 2009). The magnetic activity lifetime of low-mass stars is mass-dependent, with spin-down interpreted as the causative factor (e.g. Stauffer et al. 1994; Hawley et al. 1996; Delfosse et al. 1998).

Until recently, activity studies for low-mass stars have necessarily had to rely on $v \sin i$ measurements of rotation rates, which can only be obtained for the most rapidly rotating M dwarfs. The typical $v \sin i$ survey has a detection threshold of around 3 km/s, which for a $0.2 R_{\odot}$ star corresponds to a rotation period of only 3.3 days. The saturated regime of the rotation–activity relation is seen in stars with detectable rotational broadening, while those without broadening show a range of activity levels. Photometric rotation period measurements, which can probe longer periods, are therefore key to studying the late stages of rotational evolution of low mass stars and the unsaturated rotation–activity relation. The MEarth Project is a transiting planet survey looking for super Earths around 3000 mid-to-late M dwarfs within 33pc (Berta et al. 2012; Irwin et al. 2015). From the MEarth data, we have identified 387 stars with photometric rotation periods (Newton et al. 2016). Our observations often span 6 months or longer, providing excellent sensitivity to long periods (Irwin et al. 2011a; Newton et al. 2016).

West et al. (2015) measured H α emission for 164 M dwarfs with preliminary rotation periods from MEarth. They found that both fraction of stars that are active and the strength of magnetic activity declines with increasing rotation period for early M dwarfs. Late M dwarfs were found to remain magnetically active out to

longer rotation periods, before both the active fraction and activity level diminished abruptly. In this work, we harness the full MEarth rotation period sample, new optical spectra, and a compilation of measurements from the literature to undertake an in-depth study of magnetic activity in nearby M dwarfs.

6.2 Data

6.2.1 Our nearby M dwarf sample

Our sample of M dwarfs is drawn from the MEarth Project, an all-sky survey looking for transiting planets around approximately 3000 nearby, mid-to-late M dwarfs (Berta et al. 2012; Irwin et al. 2015). Nutzman & Charbonneau (2008) selected the northern MEarth targets from the Lépine & Shara (2005) northern proper motion catalog. The sample is composed of all stars with proper motions $> 0''.15 \text{ yr}^{-1}$, and parallaxes or distance estimates (spectroscopic or photometric; Lépine 2005) placing them within 33 pc. The target list for the MEarth transit survey additionally is limited to stars with estimated stellar radii $< 0.33 R_{\odot}$. Trigonometric parallaxes are now available for many of these stars, sometimes resulting in revised distances greater than, or estimated radii larger than, the originally limits (Dittmann et al. 2014).

MEarth-North is located at the Fred Lawrence Whipple Observatory (FLWO), on Mount Hopkins, Arizona, and has been operational since 2008 September. The observatory comprises eight 40 cm telescopes. This work utilizes results from MEarth-North and from our further spectroscopic characterization of the northern sample. Compiled and new rotation period and $H\alpha$ measurements are included in

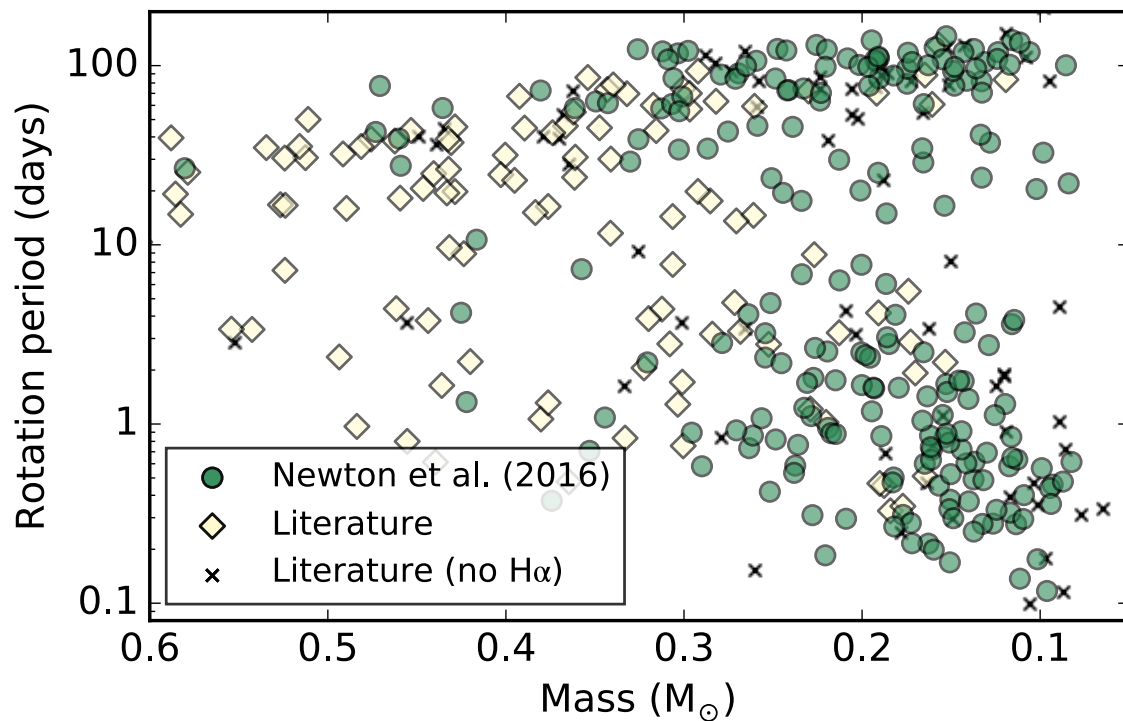


Figure 6.1.— Overview of the sample included in this paper, plotting rotation period versus stellar mass. Masses are estimated from the mass- M_K relation from Delfosse et al. (2000), modified to allow extrapolation as described in Newton et al. (2016). Diamonds and filled circles show stars with both an $H\alpha$ EW and rotation period measurement, while gray crosses show stars lacking an $H\alpha$ measurement. .

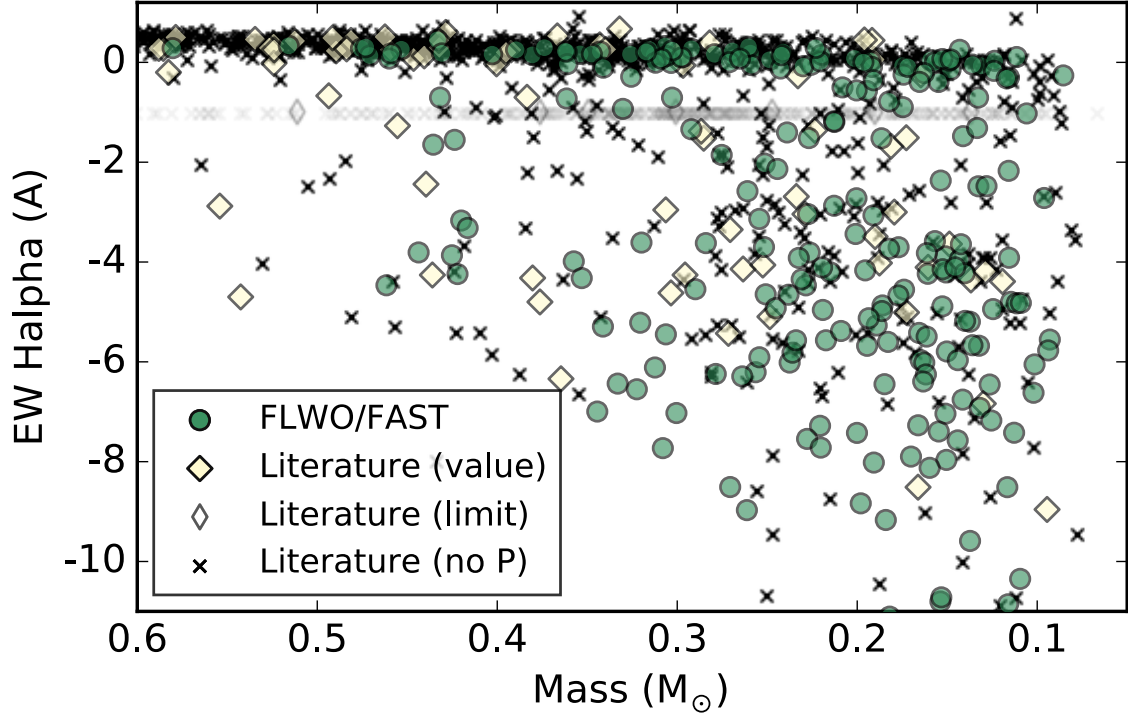


Figure 6.2.— Overview of the sample included in this paper, plotting H α EW (right) versus stellar mass. Masses are estimated from the mass- M_K relation from Delfosse et al. (2000), modified to allow extrapolation as described in Newton et al. (2016). Diamonds and filled circles show stars with both an H α EW and rotation period measurement, while gray crosses show stars lacking a rotation period measurement. Narrow gray diamonds and gray crosses indicate that the H α measurement is an upper limit. .

Table 6.1. Magnetic activity measurements and rotation periods for nearby M dwarfs
(table format)

Column	Format	Units	Description
1	A17	...	2MASS identifier
2	A11	...	LSPM identifier
3	F10.6	deg	RA in decimal degrees (J2000)
4	F11.8	deg	Dec. in decimal degrees (J2000)
5	F8.3	days	Photometric rotation period
6	A19	...	ADS bibliography code reference for rotation period
7	F5.3	M_{\odot}	Stellar mass
8	F5.3	R_{\odot}	Stellar radius
9	F6.2	0.1nm	H α EW from this work
10	F4.2	0.1nm	Error in H α EW from this work
11	A1	...	Flag indicating upper limit on literature H α measurement
12	F6.2	0.1nm	H α EW from literature
13	F4.2	0.1nm	Error in H α EW from literature
14	A19	...	ADS bibliography code reference for H α measurement
15	F4.2	...	χ value $\times 10^{-5}$
16	F4.2	dex	$L_{\text{H}\alpha} / L_{\text{bol}} \times 10^{-4}$

Table 6.1, and are described in the following sections.

6.2.2 Literature compilation

Our team has undertaken a substantial survey of the literature to gather photometric and spectroscopic data on M dwarfs in the solar neighborhood. While MEarth-North observes only the mid-to-late subset, we have retained the full Nutzman & Charbonneau (2008) sample in our database. Though our literature survey focused on the lower-mass stars, our compilation includes stars with estimated masses up to around $0.8 M_{\odot}$. The sample that forms the basis for the present work is drawn from this extended sample. Our sample comprises those stars with photometric rotation period or $H\alpha$ equivalent width (EW) measurements in our compilation, or newly presented in this work. Figures 6.1-6.2 provide an overview of our sample showing rotation period and $H\alpha$ EW as a function of stellar mass.

The literature sources for rotation periods are listed in Table 6.2. 90% of measurements for $M < 0.3 M_{\odot}$ come from Newton et al. (2016), in which we measured photometric rotation periods for 387 M dwarfs using photometry from MEarth-North. These measurements supersede those presented previously in Irwin et al. (2015) and West et al. (2015). The majority of the remaining measurements are from Hartman et al. (2011). In Newton et al. (2016) we showed excellent agreement between the rotation periods from MEarth and those previously reported in the literature with both measurements. However, we found discrepancies in $v \sin i$ measurements, and do not include $v \sin i$ measurements in this analysis.

The sources for $H \alpha$ measurements are listed in Table 6.3. In this work, we

Table 6.2. References for rotation periods

Reference	N_{stars}
1969lls..symp...57K	1
1980AJ.....85..871P	1
1980IBVS.1898....1B	1
1980PASP...92..188P	1
1983ApJ...275..752B	1
1998AJ....116..429B	2
1998ARep...42..649A	1
1998ARep...42..655A	1
1999IBVS.4714....1R	1
2000AJ....120.3265F	1
2007A&A...467..785N	12
2007AcA....57..149K	4
2009AIPC.1135..221E	2
2010ApJ...716.1522S	5
2010MNRAS.408..475H	7
2011A&A...532A..10M	1
2011AJ....141..166H	109
2012AcA....62...67K	11
2013AJ....146..154M	1
2013AcA....63...53K	5
2013MNRAS.432.1203M	6
2016ApJ...821...93N	356

present 247 new measurements of $H\alpha$ emission. In total, we include 1982 stars with $H\alpha$ EW measurements. Of these, 452 have a measured rotation period.

The $H\alpha$ measurements we collect from the literature are derived from spectra from instruments with various resolutions, and sometimes used different definitions of, or different means of calculating, $H\alpha$ EW. We find systematic differences in the EW measurements between the literature sources; additionally, not all sources report values when a star was considered to be inactive. In this paper, we consider $H\alpha$ activity both using a binary "active/inactive" flag, and using the value of the EW measurement.

We include all literature sources when flagging a star as active/inactive. Though West et al. (2015) found that a threshold of -0.75 \AA was appropriate for spectra obtained using the same instrument and settings as we use in this work, the threshold most commonly used in the literature sources we gathered was -1 \AA . We therefore adopt -1 \AA as our active/inactive boundary. There are not many stars with EWs between -0.5 and -1.5 \AA , so choosing a different boundary does not result in significant differences.

When considering the value of the EW measurement, we apply a linear correction to the literature measurement when necessary to ensure consistency with our measurements. We derive this correction using stars with observations both in the literature source and in either our survey or Gaidos et al. (2014). We therefore use only surveys with sufficient overlap to derive a correction. A summary of the restricted subsample is included in Table 6.3.

Table 6.3. References for H α equivalent widths

Reference	Resolution	$N_{\text{full}}^{\text{a}}$	$N_{\text{corr}}^{\text{b}}$	Comment ^b
1995AJ....110.1838R ^c	2000	514	460	No correction necessary
1996A&AS..116..467M	2340	1	0	Insufficient overlap
1996AJ....112.2799H ^c	2000	49	0	Insufficient overlap
1997ApJ...475..604S	44000	2	0	Insufficient overlap
1997PASP..109..849G	2000	8	0	Insufficient overlap
1998MNRAS.301.1031T	19000	1	0	Insufficient overlap
2000AJ....120.1085G	1000	8	0	Insufficient overlap
2002AJ....123.2828C	1400	15	0	Insufficient overlap
2002AJ....123.3356G	19000	371	339	No correction necessary
2002AJ....124..519R	33000	22	0	Insufficient overlap
2003AJ....125.1598L	...	1	0	Insufficient overlap
2003ApJ...583..451M	31000	26	17	No correction necessary
2005AJ....130.1871B	...	6	0	Insufficient overlap
2006A&A...446..515P	1400	5	0	Insufficient overlap
2006A&A...460..695T	50000	1	0	Insufficient overlap
2006AJ....132..866R	1750	36	31	Corrected
2007AJ....133.2825R	1300	30	0	Insufficient overlap
2007ApJ...656.1121R	31000	10	0	Insufficient overlap
2008ApJ...684.1390R	31000	3	0	Insufficient overlap
2009AJ....137.4109L	...	2	0	Insufficient overlap
2009ApJ...699..649S	60000	96	70	Corrected
2010AJ....139..504B	60000	10	6	No correction necessary
2010ApJ...710..924R	31000	11	0	Insufficient overlap
2011AJ....141...97W	1800	12	0	Insufficient overlap
2011AJ....142..104R	800	1	0	Insufficient overlap
2013AJ....145..102L	2000	13	0	Superseded by G14 ^d
2014MNRAS.443.2561G	1000	34	34	No correction necessary
2015A&A...574A..64I	3000	1	0	Insufficient overlap

Table 6.3—Continued

Reference	Resolution	$N_{\text{full}}^{\text{a}}$	$N_{\text{corr}}^{\text{b}}$	Comment ^b
2015A&A...577A.128A	1500	191	163	Corrected
2015ApJ...812....3W	3000	Superseded by this work ^e

^a N_{full} is the number of stars included in full compilation. This sample includes entries where only a limit of $\text{H}\alpha$ EW was reported and was used when considering an "active/inactive" flag. We adopt -1 \AA as the EW limit.

^b N_{corr} is the number of stars included in the corrected subset of data, for which a linear correction to the $\text{H}\alpha$ EW was applied if necessary. An explanation is provided in the comment column. This sample was used when we consider the value of the $\text{H}\alpha$ EW.

^cReid et al. (1995) and Hawley et al. (1996) report $\text{H}\alpha$ indices; we use EWs from I.N. Reid's website <http://www.stsci.edu/~inr/pmsu.html>.

^dMost of the stars presented in Lépine et al. (2013) are also included in Gaidos et al. (2014). After establishing that our $\text{H}\alpha$ EWs are consistent with Gaidos et al. (2014), we opted to have these supersede the previous measurements.

^eWe have re-reduced and re-analyzed the data first presented in West et al. (2015) to ensure consistent results.

6.2.3 New optical spectra from FAST

We obtained new optical spectra for 247 M dwarfs. We targeted M dwarfs with photometric rotation periods from Newton et al. (2016) and the "statistical sample" defined in that work, which includes stars with high-quality, long time-baseline photometry regardless of whether a rotation period was detected. We used the FAST spectrograph on the 1.5 m Tillinghast Reflector at FLWO. We used the 600 lines mm^{-1} grating with a tilt the $2''$ slit, resulting in approximately 2 \AA resolution ($R = 3000$) over 2000 \AA . We used a tilt setting of 752, corresponding to a central wavelength of 6550 \AA , to obtain spectra covering $5550\text{--}7550 \text{ \AA}$.

The data were reduced using standard IRAF long-slit reductions. Using calibration exposures taken at each grating change, the 2D spectra were rectified, bias-subtracted and flat-fielded. The wavelength calibration was determined from a HeNeAr exposure taken immediately after each science observation. A boxcar was used to extract 1D spectra, with linear interpolation to subtract the sky. We did not clean cosmic rays or weight pixels in the cross-dispersion direction, because we found that these processes could suppress the resulting $\text{H}\alpha$ EW by a few percent for strong emission lines. We used spectrophotometric standards to perform a relative flux calibration.

In West et al. (2015), we presented 238 spectra, $\text{H}\alpha$ EWs, and molecular indices from our first FAST program. To ensure consistent analysis, we re-measure the RVs and EWs using the same routines we have developed for this work. These spectra were obtained using the same instrument and settings, but included cleaning and weighting. The difference is a decrease in the EWs of about 3% for the strongest

emission lines.

6.3 Analysis

6.3.1 Radial velocities

We measure radial velocities (RVs) by modeling the wavelength shift and shape change between each spectrum with that of an RV standard. A broad spectral range ($\sim 1500 \text{ \AA}$) is typically used for cross-correlation (e.g. West et al. 2015). To obtain accurate velocities, the standard must be of the same spectral type; this is due to the complex molecular absorption features in M dwarf spectra, which change significantly across the M spectral class (e.g. Bochanski et al. 2007b).

We opt to use only the region between 7000 and 7300 \AA , which comprises the TiO bandhead. We forward model the velocity shift and the difference in shape between the science spectrum and an RV standard, using the non-flux-calibrated spectra. The TiO bandhead is sensitive both to stellar effective temperature and metallicity, and therefore the shape of the bandhead may differ between the science and standard spectrum. We use a 5th-order Legendre polynomial to account for the continuum mismatch (e.g. Anglada-Escudé & Butler 2012). We use linear least squares to determine the coefficients of the Legendre polynomial at a grid of velocity shifts, producing a χ^2 value at each test velocity. We then fit a parabola to velocity shifts with χ^2 values that are within 1% of the lowest χ^2 , and adopt the vertex of the parabola as the best fitting radial velocity.

We use a single RV standard throughout. We tested four different standards, comparing the results to high-resolution RV measurements from Nidever et al. (2002, $R = 20000$), Gizis et al. (2002, $R = 42000$), and Delfosse et al. (1998, $R = 62000$). We additionally compare to the RVs West et al. (2015) measured (we are re-analyzing their spectra), and to RVs we measured in Newton et al. (2014) from $R = 2000$ near infrared spectra. We consider two diagnostics: (1) the absolute offset in RV and (2) mass-dependence in the difference between our RVs and literature measurements. When using either Gl 699 (M4V; Kirkpatrick et al. 1991) or Gl 505B (M0.5V; Alonso-Floriano et al. 2015) as the RV standard, we see an absolute RV shift and mass-dependence in the residuals. The RVs we measure using either Gl 273 (M3.5V Kirkpatrick et al. 1991) or Gl 873 (M3.5V Henry et al. 1994) as our RV standard do not show obvious systematic residuals. As our target list includes stars at a range of spectral types, and without a strong preference between Gl 273 and Gl 873, we have chosen to adopt Gl 873 as our standard.

Table 6.4 lists the mean difference between the RVs we measured—using Gl 873 as the RV standard—and those from the sources mentioned previously. There is not a significant offset compared to Gizis et al. (2002), Nidever et al. (2002), or Newton et al. (2014). There is a 4σ difference in the mean RV compared to Delfosse et al. (1998). We find an absolute (and somewhat mass-dependent) offset of 7.2 km/s compared to West et al. (2015), and larger scatter (RMS=5.2 km/s) than expected given that our measurements are based on the same spectra.

We use the difference between our measurements and from Newton et al. (2014) to estimate our RV error. The standard deviation in the RV difference is 9 km/s. In Newton et al. (2014), the typical error was 4 km/s. This means that the FAST RVs

from this work contribute 8 km/s to the total, which we adopt as the random error on our measurements. We estimate that the systematic error in our absolute RVs is about 2 km/s.

Careful consideration of the RV errors, and in particular of any systematic offsets, is important when using RVs in studies of galactic kinematics. The random errors in RVs derived from low-resolution spectra can dominate the error budget, while systematic offsets will bias a population-level analysis (e.g. calculation of the velocity dispersion of a group of stars). Though we do not undertake such an analysis in this study, we anticipate using the velocities we derive here in future work on the galactic kinematics and ages of nearby M dwarfs (e.g. Newton et al. 2016). For the purposes of measuring H α EWs in our spectra, which have a resolution of about 100 km/s, the differences in RVs discussed above are negligible.

6.3.2 H α EWs

After correcting the radial velocity, we measured EWs and molecular indices from the flux calibrated spectra. We measure H α EWs using the definition of West et al. (2011), which is widely used in recent works (e.g. Gaidos et al. 2014). The continuum F_c is given by the mean flux across two regions to either side of the H α feature, 6500–6550 Å and 6575 – 6625 Å. The EW is:

$$\text{EW} = \int 1 - \frac{F(\lambda)}{F_c} d\lambda \quad (6.1)$$

The limits of the integral are 6558.8–6566.8 Å. We use the trapezoidal rule to integrate the flux above the continuum. EWs for H α in emission are given as negative values.

Table 6.4. Comparison of RV measurements

Reference	N_{stars}	$\overline{\Delta V}$	$\sigma_{\Delta V}$	$\overline{\Delta V}_{<0.15}$	$\overline{\Delta V}_{0.15-0.3}$	$\overline{\Delta V}_{>0.3}$
2002AJ....123.3356G	51	-2.6 ± 1.0	7.4	-4.9 ± 2.9	-3.9 ± 1.5	-0.4 ± 1.5
1998A&A...331..581D	23	-5.5 ± 1.4	6.5	-5.6 ± 3.6	-7.5 ± 2.0	-2.3 ± 1.3
2002ApJS..141..503N	14	-0.9 ± 1.2	4.6	\dots	-2.7 ± 1.2	-0.8 ± 1.5
2014AJ....147...20N	211	-1.0 ± 0.6	9.0	$+3.0 \pm 1.3$	-2.2 ± 0.8	-1.2 ± 1.3
2015ApJ...812....3W ^a	238	$+7.4 \pm 0.3$	5.2	$+5.3 \pm 0.6$	$+7.4 \pm 0.5$	$+9.7 \pm 0.7$

^aThe measurements from West et al. (2015) and this work are based on the same data.

Note. — All RVs are in km/s. ΔV is defined as the mean of $V_{\text{ref}} - V_{\text{FAST}}$. The error on the mean is included. Subscripts indicate the mean for a limited mass range, which is given in solar masses.

There are 60 stars with measurements both from our sample and from Gaidos et al. (2014), including 33 with $H\alpha$ detected in emission in our data. Using a limit of -1 \AA , there are two stars identified as inactive in Gaidos et al. (2014) that have strong $H\alpha$ in our spectra. For 2MASS J17195298+2630026, which is a member of close visual binary, our detection of strong $H\alpha$ emission agrees with previous measurements from Reid et al. (1995, -8.4 \AA), Alonso-Floriano et al. (2015, -8.2 \AA), and Gizis et al. (2002, -5.9 \AA). For 2MASS J03524169+1701056, the only other value is from Reid et al. (1995), who get -1.23 \AA ; this is intermediate to our value (-3.2 \AA) and the non-detection from Gaidos et al. (2014). This case could result from intrinsic stellar variability.

Considering the active stars, the standard deviation in EW measurements is 1.6 \AA with a mean difference of 0.5 \AA . Removing the four outliers (which deviate by $> 3 \text{ \AA}$), the standard deviation amongst the remaining 29 stars is 0.9 \AA with a mean difference of 0.3 \AA . This is similar to the intrinsic variability of around 0.8 \AA seen in time-resolved measurements (Lee et al. 2010; Bell et al. 2012).

6.3.3 $H\alpha$ luminosity and χ

The $H\alpha$ luminosity, $L_{H\alpha}/L_{\text{bol}}$, is commonly used to enable comparison between stars of different intrinsic luminosities. Calculation of intrinsic $H\alpha$ luminosity requires absolutely flux-calibrated spectra. Accurate photometry in the wavelength region covered by our FAST spectra is not widely available for our sample, and absolute flux calibration is beyond the scope of the present work. The χ factor is commonly used in this circumstance (Walkowicz et al. 2004; West & Hawley 2008). The χ

factor is derived from photometric colors, and $L_{\text{H}\alpha}/L_{\text{bol}}$ is then easily calculated: $L_{\text{H}\alpha}/L_{\text{bol}} = \text{EW}_{\text{H}\alpha} \times \chi$. We adopt χ factors from Douglas et al. (2014), who found significant differences compared to previous work. We refer the reader to Douglas et al. (2014) for a thorough discussion.

The Douglas et al. (2014) χ factor is presented as a function of $r' - J$ or $i - J$, where i is an SDSS Sloan magnitude. Neither r' nor i is widely available for our sample, which even if they are within the SDSS footprint are typically saturated. In Dittmann et al. (2016), we calibrated the M_{Earth} photometric system, and presented *M_{Earth}* magnitudes for 1507 M dwarfs. Dittmann (2016) obtained absolute *griz* Sloan photometry for a 150 M_{Earth} M dwarfs using the filters on the FLWO 1.2 m (48 in.). We use these data to derive the conversion between *M_{Earth}* $- J$ and $i_{48} - J$:

$$i_{48} - J = 1.391 \times (M_{\text{Earth}} - J) + 0.139 \quad (6.2)$$

The MAD of this conversion is 0.03 mag and the standard deviation is 0.05. The difference between i_{48} and i_{SDSS} is likely small¹, and we do not make additional corrections.

After removing 2σ outliers in the mass- $(i_{48} - J)$ plane, we calculate χ using the relation presented in the Appendix of Douglas et al. (2014). Figure 6.3 demonstrates excellent agreement between our estimated χ values and the mean values calculated by Douglas et al. (2014) as a function of spectral type. We note that because this analysis requires *M_{Earth}* magnitudes, our $L_{\text{H}\alpha}/L_{\text{bol}}$ estimates are effectively limited

¹We note that this is not the case for r magnitudes, where the filter edge may overlap with a sharp spectroscopic feature, as discussed in Dittmann (2016)

to stars in the MEarth planet search sample.

One potential concern is whether χ depends the level of H α emission itself, or on the rotation period. We see no significance difference between the mean χ values for stars with $P_{\text{rot}} < 10$ and $P_{\text{rot}} > 70$. We do see a statistically significance difference between active and inactive M dwarfs, in that active M dwarfs have slightly lower mean χ values. For M3V–M5V, where we have sufficient numbers of both samples for a meaningful comparison, the difference and standard error, expressed as a percentage of the mean value for inactive stars, is $4 \pm 1\%$, $4 \pm 1\%$, and $10 \pm 4\%$. Redder stars have smaller χ values, so this is equivalent to the more active stars having redder colors. Such an effect has been seen in previous works, e.g. Hawley et al. (1996). If we assume that, at a given spectral type, stars with increasingly larger H α EW are increasingly redder, $L_{\text{H}\alpha}/L_{\text{bol}}$ will scale less than linearly with EW. Whether this is a relevant astrophysical effect or a systematic one requires further investigation, but in either case the intrinsic scatter dominates.

6.4 Results

6.4.1 Activity versus rotation period

Figure 6.4 shows the mass–period–activity diagram. We use the empirically calibrated relationship between mass and absolute K magnitude to infer stellar mass (Delfosse et al. 2000), which we modify as discussed in Newton et al. (2016) to allow extrapolation. We have excluded known binaries from this plot, and so we expect the sample to be primarily composed of single stars. Binaries were excluded using

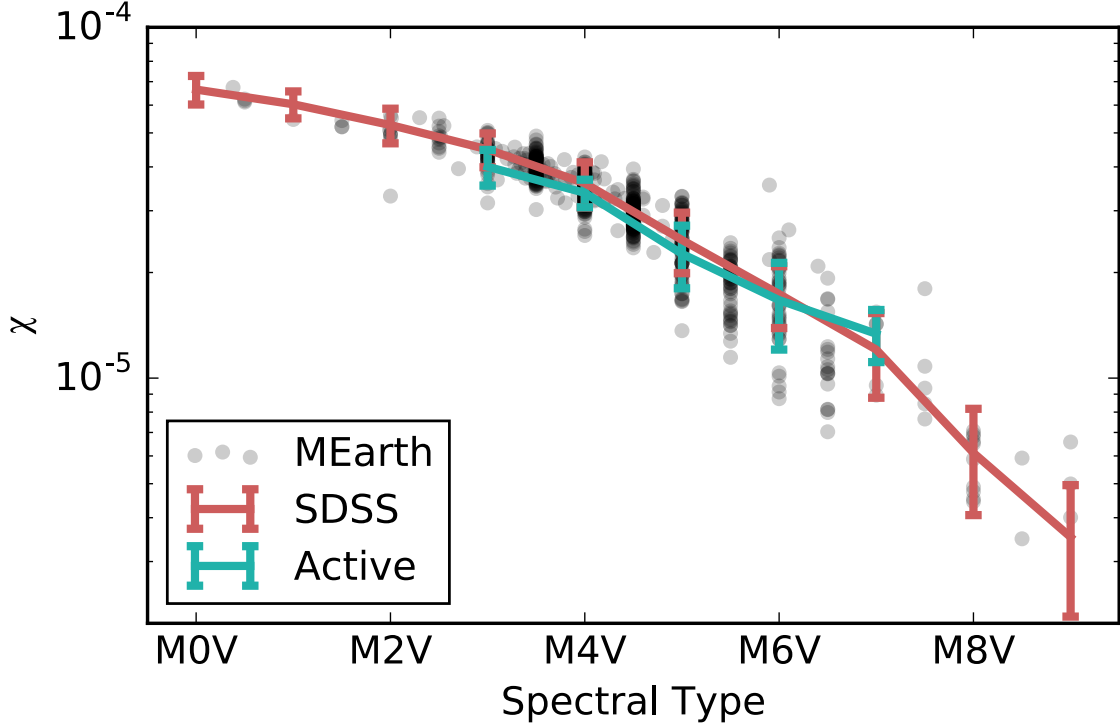


Figure 6.3.— χ values, which are used to infer $L_{H\alpha}/L_{\text{bol}}$ from $H\alpha$ EW versus spectral type. In black are the values we infer for stars in our sample using the new calibration from Douglas et al. (2014), which requires that we estimate $i_{48} - J$ color from $MEarth - J$. Optical spectral types are drawn from the literature. In red are the mean values Douglas et al. (2014) measure for M dwarfs in SDSS, with error bars indicating the standard deviation in each bin. χ for Inactive stars in our sample agree very closely with those from SDSS. In cyan are the mean values of χ for active stars in our sample, again with the error bars indicating the standard deviation. There is a statistically significant difference between the inactive/SDSS sample and the active sample, but it is dominated by the intrinsic scatter.

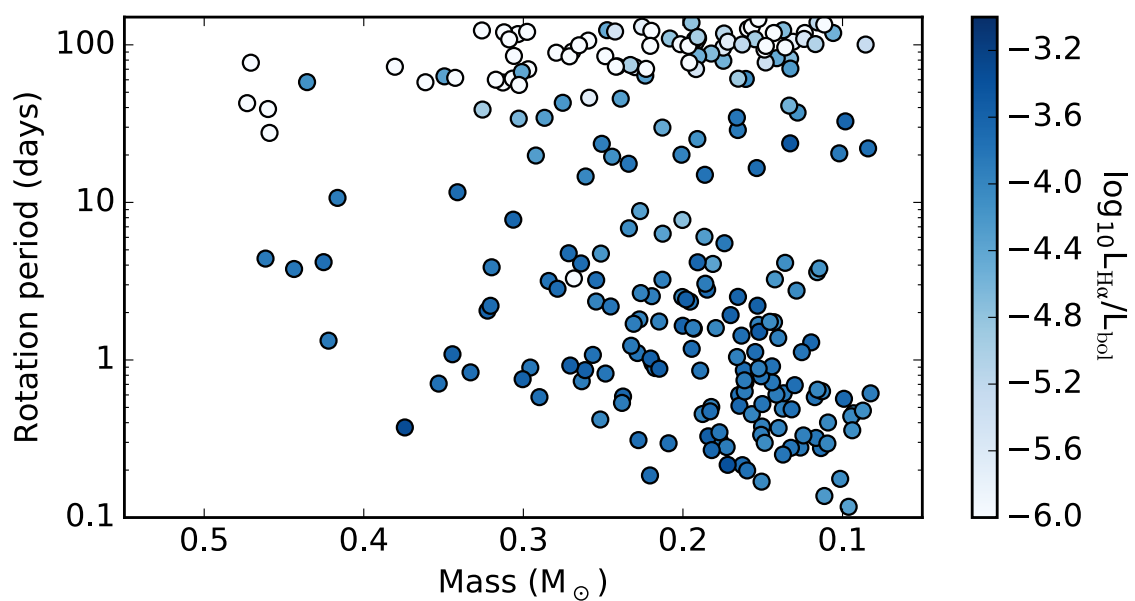


Figure 6.4.— Rotation period versus stellar mass, with points colored by $L_{\text{H}\alpha}/L_{\text{bol}}$. Masses are estimated from a mass- M_K relation, which has a scatter of about 10%. Known or suspected binaries have been removed.

the same criteria as in Newton et al. (2016), which include removing stars with bright, nearby unresolved companions (whether they are background objects or physically associated) and stars that appear over-luminous relative to their colors or spectroscopically-inferred parameters.

We show activity as traced by $L_{\text{H}\alpha}/L_{\text{bol}}$, which represents the relative amount of the star's luminosity that is output as H α emission and enables a more mass-independent comparison between activity levels in M dwarfs. As in West et al. (2015), we see a range of activity levels for stars rotating faster than 10 days, and a sharp decline in activity for longer periods. At the slowest rotation rates, all stars are inactive; we discuss the active/inactive boundary in detail in Section 6.4.2.

The Rossby number (R_o), which compares the rotation period to convective overturn timescale, is often used to compare activity strengths across mass and rotation period ranges. We use the empirical calibration from Wright et al. (2011) to determine convective overturn timescales. Figure 6.5 shows $L_{\text{H}\alpha}/L_{\text{bol}}$ versus Rossby number.

Tracers of magnetism in low-mass stars generally show a saturated relation with R_o . In agreement with previous works, we see a saturated relationship between $L_{\text{H}\alpha}/L_{\text{bol}}$ and R_o , with a break occurring near $R_o = 0.1$. For $R_o < 0.1$ (rapid rotators), $L_{\text{H}\alpha}/L_{\text{bol}}$ takes on a typical value of $1.55 \pm 0.05 \times 10^{-4}$, where the error represents the standard error on the mean. The range of values we find is consistent with that seen in other studies of field stars, for example (Gizis et al. 2002, Fig. 8) and Reiners et al. (2012, Fig. 9), though somewhat higher than the saturation threshold recently reported for the Hyades ($L_{\text{H}\alpha}/L_{\text{bol}} = 1.26 \pm 0.04 \times 10^{-4}$; Douglas et al. 2014).

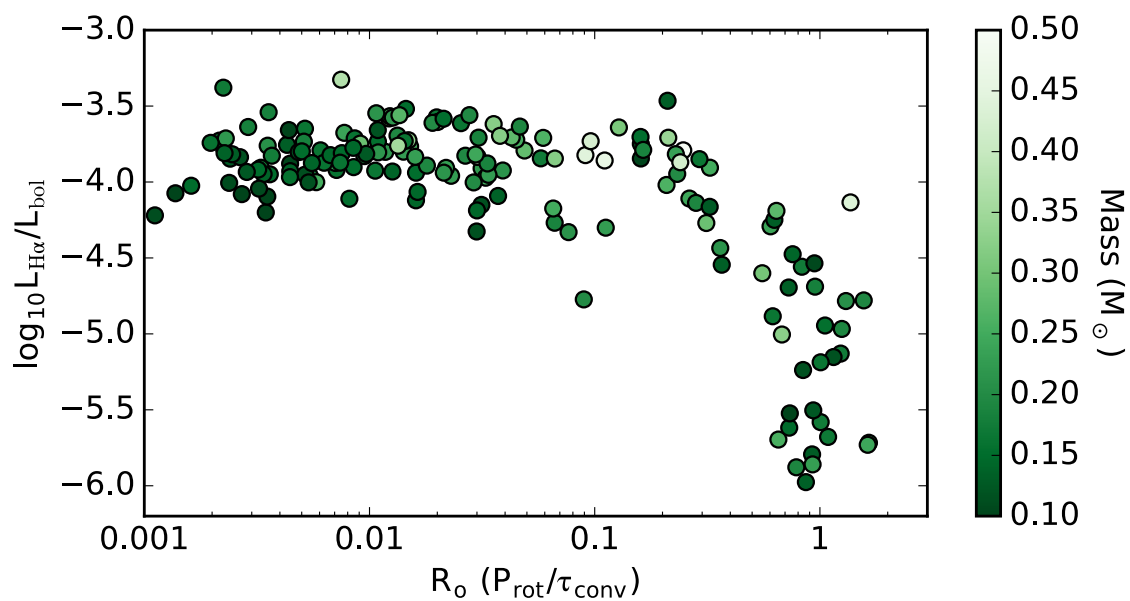


Figure 6.5.— $L_{H\alpha}/L_{bol}$ versus Rossby number (R_o), using the empirical calibration from Wright et al. (2011). Consistent with previous work, we see saturation for rapid rotators (small R_o), and a decline for slower rotators (large R_o). Around $R_o = 1$, we cease to detect H α in emission.

The mean value in the saturated regime is a marginally lower for $M_* < 0.25 M_\odot$ ($1.45 \pm 0.06 \times 10^{-4}$) than it is for $M_* > 0.25 M_\odot$ ($1.8 \pm 0.1 \times 10^{-4}$). West et al. (2004) and Kruse et al. (2010) show a similar decrease in $L_{\text{H}\alpha}/L_{\text{bol}}$ spectral types M6 and later, and similar levels of mean $L_{\text{H}\alpha}/L_{\text{bol}}$.

Our photometric rotation periods allow us to probe to larger R_o than typically accessible for low-mass stars. We see a decline in $L_{\text{H}\alpha}/L_{\text{bol}}$ for $R_o > 0.1$. Around $R_o = 1$, we cease to detect H α emission in stars of all masses.

6.4.2 The active/inactive boundary

West et al. (2015) noted that for M1V–M4V, all stars rotating faster than 26 days are magnetically active. For M5V–M8V, a corresponding limit was seen at 86 days. In Figure 6.6, we consider the active fraction in light of the mass–period relation. We clearly see a mass-dependent threshold in whether a star shows H α in emission. We identify the boundary between the "active class" and the "inactive class" using a support vector machine classifier (Cortes & Vapnik 1995) from the scikit-learn machine learning package (Pedregosa et al. 2011). This classification algorithm finds the boundary separating two classes by maximizing the distance between class members and the boundary. We used a third-order polynomial kernel with $\gamma = 3$, and normalized the data to using the robust scaling algorithm supplied in scikit-learn. The resulting classification scheme is not analytic, but we plot the boundary the classes in Figure 6.6. The threshold is at 30 days for $0.3 M_\odot$ stars and around 70 – 80 days for $0.15 M_\odot$. This threshold corresponds to the lower boundary of the "long period" rotators from Newton et al. (2016), around the point where stars

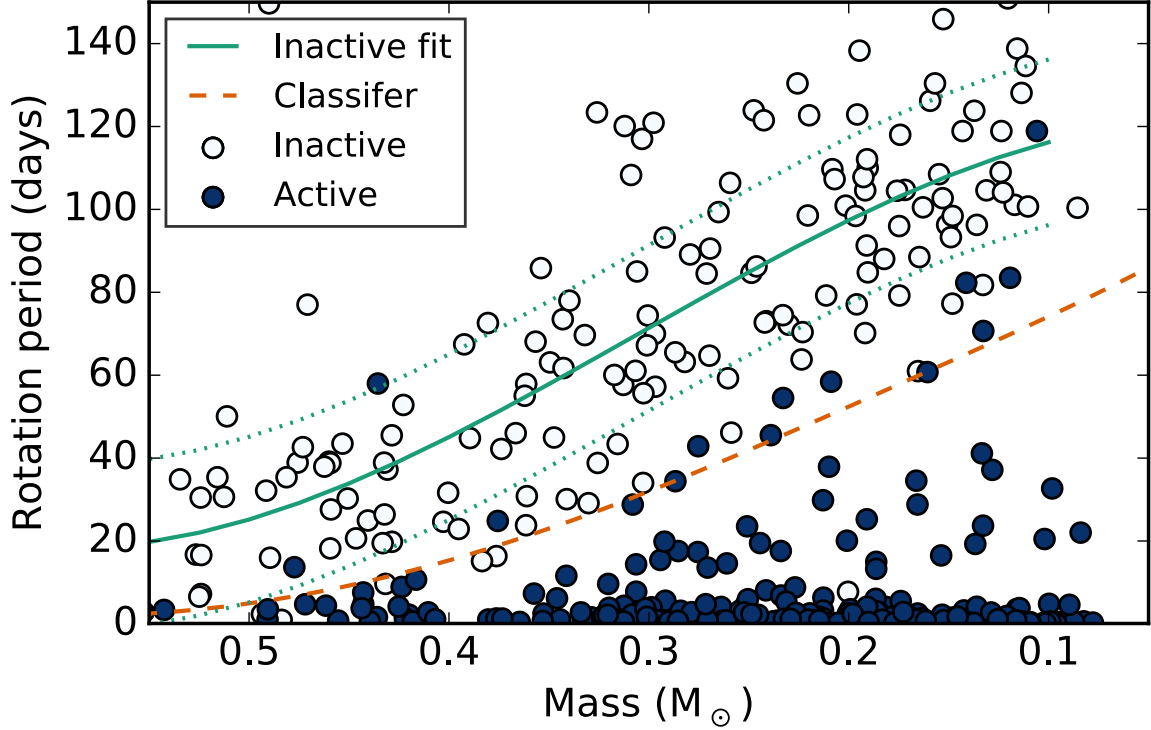


Figure 6.6.— Rotation period versus stellar mass for active (blue circles) and inactive (white circles) stars. There is a well-defined threshold in the mass-period plane which cleanly divides active and inactive stars. We use a machine learning classifier to locate the boundary between the two classes (dashed line). Our best-fitting mass-period relation for inactive M dwarfs is also plotted (solid line), along with lines showing the standard deviation in the residuals (dotted lines).

appear to cease rapid angular momentum evolution.

This implies that the presence of H α emission is a useful diagnostic for whether a star is a long- or short-period rotator. This may be of use to exoplanet surveys, for which slowly rotating stars are often better targets. Furthermore, for an inactive star, its mass can be used to provide guidance as to its rotation period. We fit a polynomial between stellar rotation period and mass for inactive stars in our sample, using 3σ clipping to iteratively improve our fit:

$$\begin{aligned}
 P = & 1134.33 \\
 & - 1038.87 \times M_* \\
 & + 44.124 \times M_*^2 \\
 & + 121.04 \times M_*^3
 \end{aligned} \tag{6.3}$$

The relation is valid between 0.55 and 0.1 M_\odot and has standard deviation of 20 days. The best fit is shown in Figure 6.6. Note that for early M dwarfs, all but the most rapidly rotating stars are inactive. Because the stars included in this fit are selected only by virtue of being inactive, they are likely to have a range of ages and therefore we do not expect this fit to match up with a particular gyrochrone, or with the Sun.

Table 6.5. Stars with unusual activity levels

ID	2MASS ID	EW H α Å	EW H α (Lit.) Å	Reference	RV km/s	RV (Lit.) km/s	Reference	Period days	Reference
Too active									
3106	093014445+2630250	-3.3	2.18	2014MNRAS.443.2561G	+28	+21	2013AJ....146..156D	10.68	arXiv:1511.00957
3857	20245996+0225569	-1.6	-20	57.99	arXiv:1511.00957
Too quiet (mid M)									
1963	08111529+3607285	+0.1	+25	+18	2014AJ....147...20N	3.290	2011AJ....141..166H
4085	23242652+7357437	-0.6	-23	7.738	arXiv:1511.00957
Too quiet (early M)									
1968	08175130+3107455	...	+0.3 \pm 0.1	2014MNRAS.443.2561G	...	+120	2015ApJS...220...16T	0.970	2011AJ....141..166H
2366	20372081+2156525	...	-0.7 \pm 0.2	2014MNRAS.443.2561G	...	-18	1995AJ....110.1838R	2.366	2011AJ....141..166H
3781	19295643+1618398	...	-0.4	2013AJ....145..102L	2.877	2012AcA....62...67K

6.4.3 Stars with unusual activity levels

There are several stars that appear as outliers in the mass–period–activity plane: either they are members of the long-period population and yet are active, or they are members of the short-period population and yet are inactive. We briefly describe this "oddball" sample here, but full investigation is beyond the scope of this work.

There are two long rotator that are active, 2MASS 09301445+2630250 and 2MASS 20245996+0225569, which are listed in Table 6.5. Both are early M dwarfs. Neither are known to binaries, but we cannot rule out a companion with the available data. A third late M dwarf, 2MASS J12250105+2323175 ($P = 119$ days), has an $H\alpha$ EW of -1 and so lies at the border our active/inactive boundary; its emission level is not, however, atypical (see Fig. 6.5) and it is not included in Table 6.5.

There are five rapidly rotating stars that are inactive, which are also listed in Table 6.5. Three are early M dwarfs with masses around $0.5 M_{\odot}$, where we have limited data. Although we do see a general decline in $H\alpha$ EW going towards the early Ms, the R_o for these stars indicate that they should be in the saturated regime. Since we do not have χ values for them, we have not calculated their $L_{H\alpha}/L_{bol}$; however, assuming $\chi = 6.6 \times 10^{-5}$, the average value for SDSS M0V stars from Douglas et al. (2014), two of the three would have $\log_{10} L_{H\alpha}/L_{bol} \sim -4.4$. This would just skirt the lower boundary of the $L_{H\alpha}/L_{bol}$ distribution for the saturated regime.

Though unusual, three previous measurements from West & Basri (2009) indicate the existence of rapidly rotating, inactive M dwarfs. West & Basri (2009) suggested complexity in the rotation–activity relation as the cause. However we have demonstrated a clear connection between rotation and $H\alpha$ activity for M dwarfs of

all masses, which makes these oddball stars even more puzzling.

6.4.4 Activity versus photometric amplitude

Photometric rotational modulation are the result of starspots rotating in and out of view on the stellar surface. Since starspots are the product of the magnetic suppression of flux, we might expect a correlation between the prevalence of starspots and spectral indicators of magnetic activity. The photometric rotation amplitude is indicative of the fraction of the stellar surface that is covered in spots, though it is primarily sensitive to asymmetries in the longitudinal distribution of starspots.

We see a strong positive correlation between $L_{H\alpha}/L_{bol}$ and the amplitude of photometric variability (Figure 6.7). The Spearman rank correlation coefficient ρ is 0.36 ± 0.03 , with a p -value of $< 10^{-5}$. The most active and highly variable stars contribute to the strength of the correlation, but a correlation persists if we exclude stars with $L_{H\alpha}/L_{bol} > 2.5 \times 10^{-4}$ ($\rho = 0.28 \pm 0.03$, $p = 0.0008 \pm 0.0006$).

One potential concern is that we found that active stars are slightly redder than inactive stars, resulting in χ values for the active sample that are 4% lower. However, this has the opposite effect of the observed correlation: if we were to assign χ values on the basis of spectral type rather than color, the active stars of that spectral type would be assigned a larger χ than otherwise, and would therefore have larger $L_{H\alpha}/L_{bol}$. We nevertheless verified that our results are unchanged if we use $H\alpha$ EW in place of $L_{H\alpha}/L_{bol}$ ($\rho = -0.4^{+0.3}_{-0.7}$, $p < 10^{-6}$).

Since photometric amplitudes depend on the bandpass, we only use stars with rotation period measurements from our analysis of MEarth photometry (Newton et al. 2016). One concern with this is that the method we used to determine amplitude tends to suppress amplitude for stars with strong spot evolution or with non-sinusoidal variability; our method for period detection is also most sensitive to stars with stable, sinusoidal spot patterns. Measuring the peak-to-peak amplitude offers an alternative, and was used, e.g. by McQuillan et al. (2014) in their study of rotation in the *Kepler* sample. However, this is a more challenging measurement to make robustly in ground-based data. We therefore proceeded with the amplitude measurements from Newton et al. (2016).

Another complicating factor is the relationship between rotation period and photometric amplitude, since the former is also correlated with $H\alpha$ activity. For stars more massive than $0.25 M_{\odot}$, a negative correlation is seen between variability amplitude and rotation period for periods > 30 days (Hartman et al. 2011; McQuillan et al. 2014; Newton et al. 2016). However, for the mid-to-late M dwarfs that dominate our sample, no correlation is seen (Newton et al. 2016). To address this concern, we performed our analysis on different subsets of data, which are shown in Figure 6.7. In the first, we have restricted the period range to be < 30 days; in the second we have restricted the mass range to be $< 0.25 M_{\odot}$. The results from each restricted sample are consistent, with $\rho = 0.40 \pm 0.04$ for the period-restricted sample and $\rho = 0.34 \pm 0.03$ for the mass-restricted sample, both with $p < 10^{-4}$.

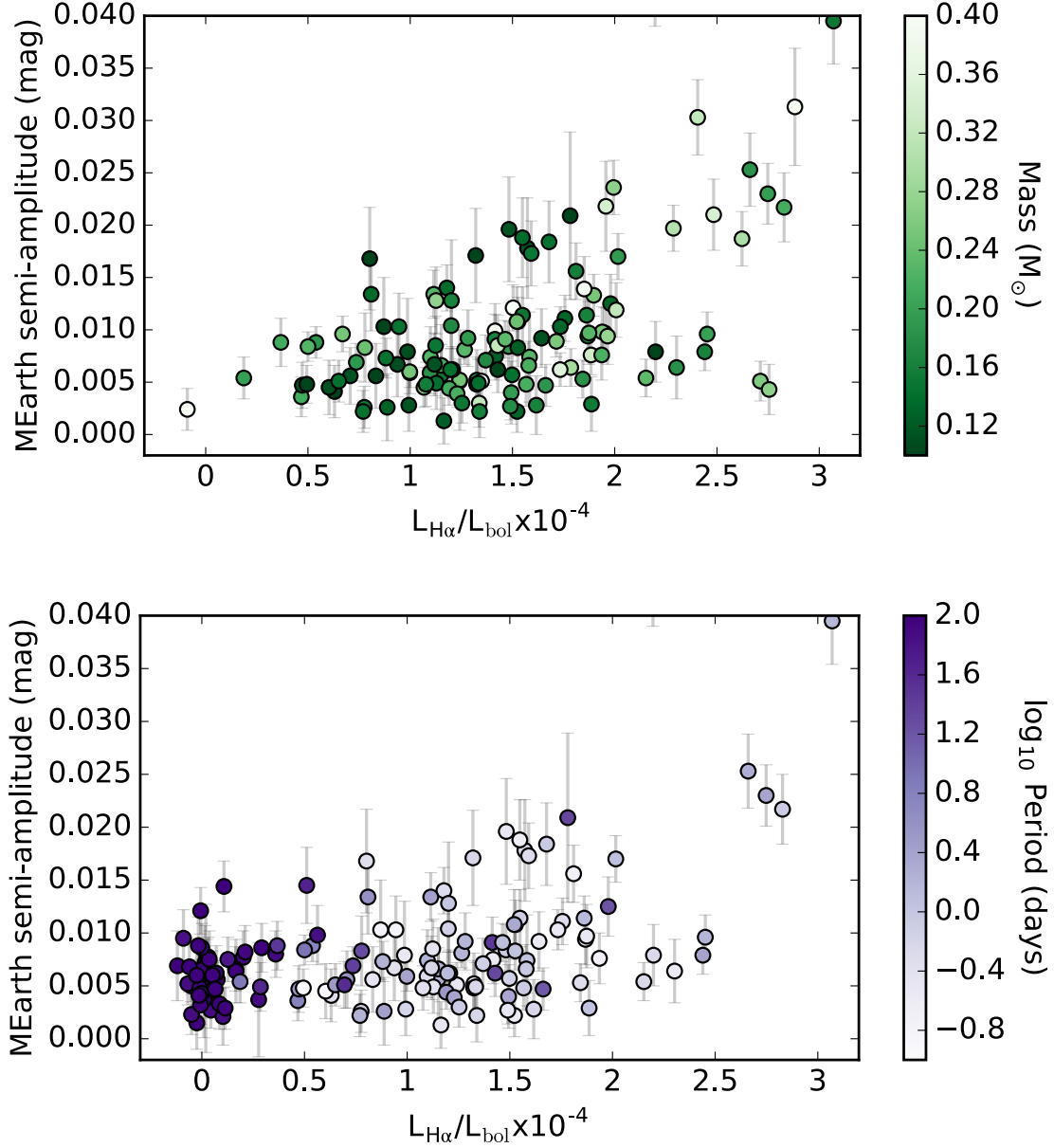


Figure 6.7.— Amplitude of photometric variability versus $L_{H\alpha}/L_{bol}$ for M dwarfs with detected rotation periods from Newton et al. (2016). The mean amplitude in different bins in $L_{H\alpha}/L_{bol}$ is shown, along with the error on the mean. In the top panel, only stars with periods faster than 30 days are shown, and the color of the data point indicates stellar mass. In the bottom panel, only stars with masses less than $0.25 M_{\odot}$ are shown, and the color of the data point indicates rotation period. In both panels, a highly significant correlation between amplitude and magnetic activity is seen.

6.5 Discussion

We have obtained new optical spectra for 247 nearby M dwarfs and measured $H\alpha$ EWs and estimated $L_{H\alpha}/L_{\text{bol}}$. Including measurements compiled from the literature, our sample includes 1982 measurements of or upper limits on $H\alpha$ emission. Of these, 452 have photometric rotation periods.

We found a mass-dependent rotation period threshold for $H\alpha$ emission. In Irwin et al. (2011a) and Newton et al. (2016), we found a lack of mid-to-late M dwarfs with intermediate rotation periods, which we suggests represents a period range over which stars quickly lose angular momentum. The active/inactive threshold coincides with the rotation period at which this rapid evolution appears to cease. This corresponds to a rapid decrease in $L_{H\alpha}/L_{\text{bol}}$ between Rossby numbers of 0.1 and 1. This suggests that when the stellar rotation period becomes comparable to the timescale for convective motions, mid-to-late M dwarfs can no longer sustain a magnetic field strong enough to heat the chromosphere to temperatures high enough for $H\alpha$ to be observed in emission.

For rapidly rotating stars ($R_o < 0.1$), $H\alpha$ emission maintains a saturated value, as seen in many previous works (e.g. Delfosse et al. 1998; Mohanty & Basri 2003; Reiners et al. 2012; Douglas et al. 2014). Our photometric rotation periods allow us to probe the regime where the rotation period becomes comparable to, or longer than, the convective overturn timescale ($R_o \sim 1$) for a range of stellar masses. We see a decline in $L_{H\alpha}/L_{\text{bol}}$ for $R_o > 0.1$. Though their sample of single stars in this regime was limited, Wright et al. (2011) found that x-ray activity continues to decrease at $R_o > 1$. Around $R_o = 1$, $H\alpha$ has diminished to the point where it is not detectable

in our low-resolution spectra. $H\alpha$ can be detected in absorption in high-resolution spectra so high-resolution spectroscopy of the slowly-rotating sample may be able to test whether the rotation-activity relation continues at $R_o > 1$.

Reiners et al. (2014, hereafter R14) suggest that R_o is not the best scaling, and explored a generalized relationship between $L_{H\alpha}/L_{bol}$ and rotation period and stellar radius. They find $L_X \propto P^{-2}R^{-4}$. In Figure 6.8, we show how the R14 scaling and R_o numbers differ in the mass–period plane. The former depends on stellar radius, so we use the mass–radius relation from Boyajian et al. (2012) to estimate stellar radius. The R14 scaling matches the active/inactive boundary, and the shape of the long-period sample, very well. We considered $L_{H\alpha}/L_{bol}$ versus the R14 scaling instead of R_o , and do not see any significant difference.

We have found a highly significant correlation between the strength of $H\alpha$ emission and the amplitude of photometric variability, for stars with detected photometric rotation periods. Both starspots and $H\alpha$ emission are thought to be products of magnetism. We expect that this correlation is the result of differences in the underlying magnetic field strength: stars with stronger magnetic fields have stronger $H\alpha$ emission as well as larger or more abundant spots.

Inferred spot filling factors are on the order of a few percent (Barnes et al. 2015; Andersen & Korhonen 2015) to as high as 40% (e.g. Jackson & Jeffries 2013), though measurements are likely complicated by the unknown spot geometry. For small randomly distributed spots with filling factors $< 20\%$ simulations from Andersen & Korhonen (2015, see Fig. 5) indicate that an increase in the filling factor by a factor of two corresponds to a 50% increase in photometric variability in V . We see a factor

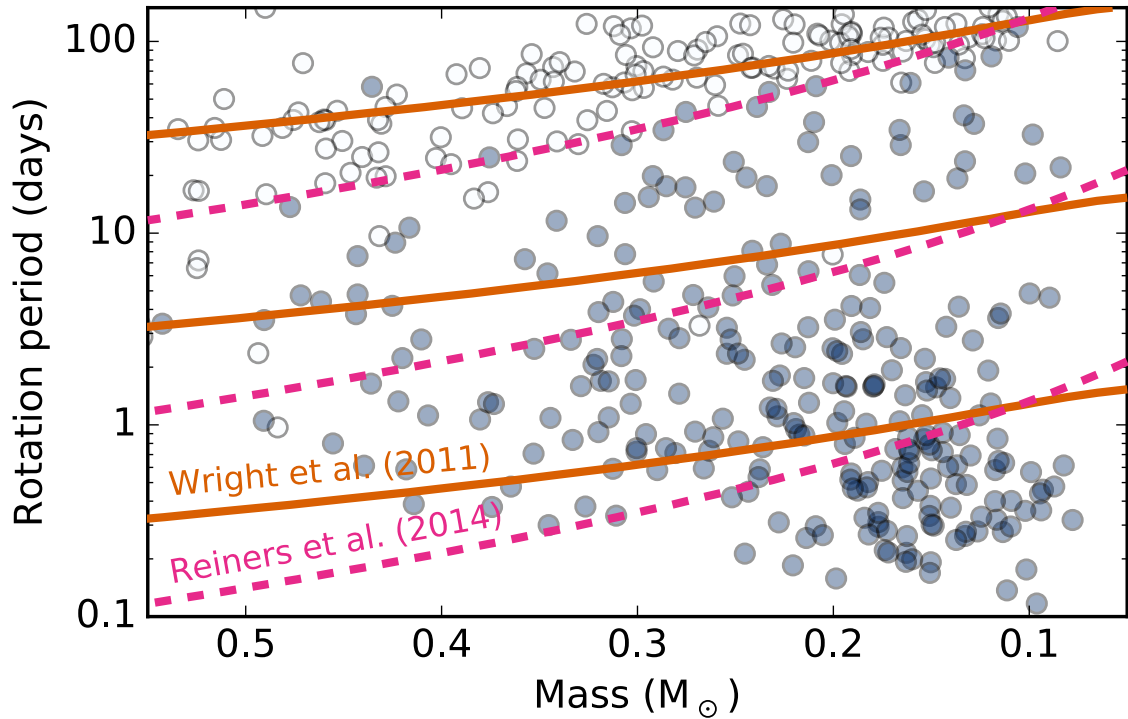


Figure 6.8.— Stellar rotation versus mass, showing active (blue) and inactive (white) stars. Over-plotted are contours of constant R_o (solid lines; using the empirical calibration from Wright et al. 2011), and the "generalized R_o " scaling from Reiners et al. (2014, dashed lines). It is interesting to note that the R14 scaling matches the distribution of masses and rotation periods for M dwarfs.

of two increase in photometric variability between the highly active and the inactive stars, which would require a four-fold increase in the filling factor in this scenario. Alternatively, M dwarfs may be dominated by one or more larger spots. It would also be interesting to examine this correlation for stars in young clusters. For example, Jackson & Jeffries (2012) looked at stars in the open cluster NGC 2516, which had been surveyed photometrically as part of the Monitor survey (Irwin et al. 2007). They found no difference in the chromospheric activity between the stars with and without rotation period measurements, and argued that there were not differences in the spot filling factor between these two groups.

We have shown that with very high confidence, an M dwarf without detectable $H\alpha$ emission is slowly rotating. For inactive M dwarfs, we have presented a relationship between stellar mass and rotation period. These findings may be useful to those building target lists for exoplanet surveys, providing a simple and accessible diagnostic of the stellar rotation period. We also suggest that, in the eventuality that gyrochronology is calibrated for M dwarfs, the lack of $H\alpha$ emission can be used to determine whether it is appropriate to apply the gyrochronology relationship.

We plan to continue investigation of M dwarf activity and angular momentum evolution. We will look at $H\alpha$ activity in M dwarfs in samples of kinematically old stars to explore the decline in activity at older ages, and in stars without detectable rotational modulation to investigate the amplitude–activity relation. We plan to use Zeeman broadening measurements of the global field strength to directly study the magnetic field properties in this sample of stars. The persistence of $H\alpha$ activity indicates that strong magnetic fields may be detectable out to long periods.

E.R.N. is grateful for support from a National Science Foundation Graduate Research Fellowship. The MEarth Project acknowledges funding from the National Science Foundation under grants AST-0807690, AST-1109468, and AST-1004488 (Alan T. Waterman Award) and the David and Lucile Packard Foundation Fellowship for Science and Engineering. This publication was made possible through the support of a grant from the John Templeton Foundation. The opinions expressed here are those of the authors and do not necessarily reflect the views of the John Templeton Foundation. Z.K.B.T was supported by the MIT Torres Fellowship for exoplanet research. This work was based in part on observations at the Infrared Telescope Facility, which is operated by the University of Hawaii under Cooperative Agreement no. NNX-08AE38A with the National Aeronautics and Space Administration, Science Mission Directorate, Planetary Astronomy Program. This research has made use of data products from the Two Micron All Sky Survey, which is a joint project of the University of Massachusetts and the Infrared Processing and Analysis Center / California Institute of Technology, funded by NASA and the NSF; NASA Astrophysics Data System (ADS); and the SIMBAD database and VizieR catalog access tool, at CDS, Strasbourg, France.

This work was conducted in part using on observations obtained from facilities on Mauna Kea. We wish to recognize and acknowledge the very significant cultural role and reverence that the summit of Mauna Kea has always had within the indigenous Hawaiian community. We are fortunate to have had the opportunity to conduct observations from this mountain.

References

- Adams, W. S. 1913, Publications of the Astronomical Society of the Pacific, 25, 258
- Adams, W. S., & Pease, F. G. 1914, Publications of the Astronomical Society of the Pacific, 26, 258
- Agüeros, M. A., Covey, K. R., Lemonias, J. J., et al. 2011, The Astrophysical Journal, 740, 110
- Aigrain, S., Pont, F., & Zucker, S. 2012, Monthly Notices of the Royal Astronomical Society, 419, 3147
- Alekseev, I. Y., & Bondar, N. I. 1998, Astronomy Reports, 42, 655
- Allard, F. 2014, Proceedings of the International Astronomical Union, 8, 271
- Allard, F., Hauschildt, P. H., & Schwenke, D. 2000, The Astrophysical Journal, 540, 1005
- Allard, F., Homeier, D., & Freytag, B. 2011, 16th Cambridge Workshop on Cool Stars, 448
- Almenara, J. M., Astudillo-Defru, N., Bonfils, X., et al. 2015, Astronomy & Astrophysics, 581, L7
- Alonso-Floriano, F. J., Morales, J. C., Caballero, J. A., et al. 2015, Astronomy & Astrophysics, 577, A128
- Ancient Sunspot Records Research Group at Yunnan Observatory. 1977, Chinese Astronomy, 1, 196
- Andersen, J. M., & Korhonen, H. 2015, Monthly Notices of the Royal Astronomical Society, 448, 3053
- Andrews, S. M., Rosenfeld, K. A., Kraus, A. L., & Wilner, D. J. 2013, The Astrophysical Journal, 771, 129

REFERENCES

- Anglada-Escudé, G., Boss, A. P., Weinberger, A. J., et al. 2012a, *The Astrophysical Journal*, 746, 37
- Anglada-Escudé, G., & Butler, R. P. 2012, *The Astrophysical Journal Supplement Series*, 200, 15
- Anglada-Escudé, G., Rojas-Ayala, B., Boss, A. P., Weinberger, A. J., & Lloyd, J. P. 2013a, *Astronomy & Astrophysics*, 551, A48
- Anglada-Escudé, G., Arriagada, P., Vogt, S. S., et al. 2012b, *The Astrophysical Journal*, 751, L16
- Anglada-Escudé, G., Tuomi, M., Gerlach, E., et al. 2013b, *Astronomy & Astrophysics*, 556, A126
- Anglada-Escudé, G., Arriagada, P., Tuomi, M., et al. 2014, *Monthly Notices of the Royal Astronomical Society: Letters*, 443, L89
- Artigau, É., Kouach, D., Donati, J.-F., et al. 2014, in *Proceedings of the SPIE*, ed. S. K. Ramsay, I. S. McLean, & H. Takami, Vol. 9147
- Asplund, M., Grevesse, N., Sauval, A. J., & Scott, P. 2009, *Annual Review of Astronomy and Astrophysics*, 47, 481
- Aumer, M., & Binney, J. J. 2009, *Monthly Notices of the Royal Astronomical Society*, 397, 1286
- Bailer-Jones, C. A. L. 2004, *Astronomy and Astrophysics*, 419, 703
- Bailey, J. I., White, R. J., Blake, C. H., et al. 2012, *The Astrophysical Journal*, 749, 16
- Baliunas, S., Sokoloff, D., & Soon, W. 1996, *The Astrophysical Journal*, 457, L99
- Ballard, S., & Johnson, J. A. 2016, *The Astrophysical Journal*, 816, 66
- Ballard, S., Charbonneau, D., Fressin, F., et al. 2013, *The Astrophysical Journal*, 773, 98
- Baluev, R. V. 2012, *Monthly Notices of the Royal Astronomical Society*, 429, 2052
- Baraffe, I., Homeier, D., Allard, F., & Chabrier, G. 2015, *Astronomy & Astrophysics*, 577, A42
- Barnes, J. R., Jeffers, S. V., Jones, H. R. A., et al. 2015, *The Astrophysical Journal*, 812, 42

REFERENCES

- Barnes, J. R., Jenkins, J. S., Jones, H. R. A., et al. 2012, *Monthly Notices of the Royal Astronomical Society*, 424, 591
- . 2014, *Monthly Notices of the Royal Astronomical Society*, 439, 3094
- Barnes, S. A. 2003, *The Astrophysical Journal*, 586, 464
- . 2007, *The Astrophysical Journal*, 669, 1167
- Basri, G., Mohanty, S., Allard, F., et al. 2000, *The Astrophysical Journal*, 538, 363
- Bayless, A. J., & Orosz, J. A. 2006, *The Astrophysical Journal*, 651, 1155
- Bean, J. L., Benedict, G. F., & Endl, M. 2006a, *The Astrophysical Journal*, 653, L65
- Bean, J. L., Sneden, C., Hauschildt, P. H., Johns-Krull, C. M., & Benedict, G. F. 2006b, *The Astrophysical Journal*, 652, 1604
- Bean, J. L., Désert, J.-M., Kabath, P., et al. 2011, *The Astrophysical Journal*, 743, 92
- Bedell, M., Meléndez, J., Bean, J. L., et al. 2014, *The Astrophysical Journal*, 795, 23
- Bell, C. P. M., Rees, J. M., Naylor, T., et al. 2014, *Monthly Notices of the Royal Astronomical Society*, 445, 3496
- Bell, K. J., Hilton, E. J., Davenport, J. R. A., et al. 2012, *Publications of the Astronomical Society of the Pacific*, 124, 14
- Benedict, G. F., McArthur, B. E., Franz, O. G., Wasserman, L. H., & Henry, T. J. 2000, *The Astronomical Journal*, 120, 1106
- Bensby, T., Feltzing, S., & Lundström, I. 2003, *Astronomy and Astrophysics*, 410, 527
- Bensby, T., Feltzing, S., Lundström, I., & Ilyin, I. 2005, *Astronomy and Astrophysics*, 433, 185
- Berger, D. H., Gies, D. R., McAlister, H. A., et al. 2006, *The Astrophysical Journal*, 644, 475
- Berger, E. 2002, *The Astrophysical Journal*, 572, 503
- . 2006, *The Astrophysical Journal*, 648, 629
- Berger, E., Basri, G., Fleming, T. A., et al. 2010, *The Astrophysical Journal*, 709, 332

REFERENCES

- Berta, Z. K., Charbonneau, D., Bean, J., et al. 2011, *The Astrophysical Journal*, 736, 12
- Berta, Z. K., Irwin, J., & Charbonneau, D. 2013, *The Astrophysical Journal*, 775, 91
- Berta, Z. K., Irwin, J., Charbonneau, D., Burke, C. J., & Falco, E. E. 2012, *The Astronomical Journal*, 144, 145
- Berta-Thompson, Z. K., Irwin, J., Charbonneau, D., et al. 2015, *Nature*, 527, 204
- Bessel, M. S. 1990, *Astronomy and Astrophysics Supplement Series*, 83, 357
- Bessell, M., & Brett, J. M. 1988, *Publications of the Astronomical Society of the Pacific*, 100, 1134
- Beuzit, J.-L., Ségransan, D., Forveille, T., et al. 2004, *Astronomy and Astrophysics*, 425, 997
- Blackwell, D. E., Petford, A. D., & Shallis, M. J. 1980, *Astronomy and Astrophysics*, 82, 249
- Blackwell, D. E., & Shallis, M. J. 1977, *Monthly Notices of the Royal Astronomical Society*, 180, 177
- Blackwell, D. E., Shallis, M. J., & Selby, M. J. 1979, *Monthly Notices of the Royal Astronomical Society*, 188, 847
- Blake, C. H., Charbonneau, D., & White, R. J. 2010, *The Astrophysical Journal*, 723, 684
- Bochanski, J. J., Hawley, S. L., Covey, K. R., et al. 2010, *The Astronomical Journal*, 139, 2679
- Bochanski, J. J., Munn, J. A., Hawley, S. L., et al. 2007a, *The Astronomical Journal*, 134, 2418
- Bochanski, J. J., West, A. A., Hawley, S. L., & Covey, K. R. 2007b, *The Astronomical Journal*, 133, 531
- Boisse, I., Bonfils, X., & Santos, N. C. 2012, *Astronomy & Astrophysics*, 545, A109
- Boisse, I., Bouchy, F., Hébrard, G., et al. 2011, *Astronomy & Astrophysics*, 528, A4
- Bonfils, X., Delfosse, X., Udry, S., et al. 2005a, *Astronomy and Astrophysics*, 442, 635

REFERENCES

- Bonfils, X., Forveille, T., Delfosse, X., et al. 2005b, *Astronomy and Astrophysics*, 443, L15
- Bonfils, X., Delfosse, X., Udry, S., et al. 2013, *Astronomy & Astrophysics*, 549, A109
- Borucki, W. J., Koch, D., Basri, G., et al. 2010, *Science*, 327, 977
- Borucki, W. J., Koch, D. G., Basri, G., et al. 2011, *The Astrophysical Journal*, 736, 19
- Bouvier, J., Forestini, M., & Allain, S. 1997a, *Astronomy and Astrophysics*
- Bouvier, J., Wichmann, R., Grankin, K., et al. 1997b, *Astronomy and Astrophysics*, 318, 495
- Bovy, J., & Hogg, D. W. 2010, *The Astrophysical Journal*, 717, 617
- Bovy, J., Rix, H.-W., & Hogg, D. W. 2012, *The Astrophysical Journal*, 751, 131
- Boyajian, T. S., McAlister, H. A., Baines, E. K., et al. 2008, *The Astrophysical Journal*, 683, 424
- Boyajian, T. S., von Braun, K., van Belle, G., et al. 2012, *The Astrophysical Journal*, 757, 112
- . 2013, *The Astrophysical Journal*, 771, 40
- Brown, T. M., Latham, D. W., Everett, M. E., & Esquerdo, G. A. 2011, *The Astronomical Journal*, 142, 112
- Browning, M. K. 2008, *The Astrophysical Journal*, 676, 1262
- Browning, M. K., Basri, G., Marcy, G. W., West, A. A., & Zhang, J. 2010, *The Astronomical Journal*, 139, 504
- Buchhave, L. A., Latham, D. W., Johansen, A., et al. 2012, *Nature*, 486, 375
- Burgasser, A. J., Looper, D. L., Kirkpatrick, J. D., & Liu, M. C. 2007, *The Astrophysical Journal*, 658, 557
- Cardini, D., & Cassatella, A. 2007, *The Astrophysical Journal*, 666, 393
- Carpenter, J. M. 2001, *The Astronomical Journal*, 121, 2851
- Casagrande, L., Flynn, C., & Bessell, M. 2008, *Monthly Notices of the Royal Astronomical Society*, 389, 585

REFERENCES

- Casagrande, L., Portinari, L., Glass, I. S., et al. 2014, *Monthly Notices of the Royal Astronomical Society*, 439, 2060
- Chabrier, G., & Baraffe, I. 1997, *Astronomy and Astrophysics*
- Chabrier, G., Gallardo, J., & Baraffe, I. 2007, *Astronomy and Astrophysics*, 472, L17
- Chabrier, G., & Küker, M. 2006, *Astronomy and Astrophysics*, 446, 1027
- Charbonneau, D., & Deming, D. 2007, arXiv:0706.1047
- Charbonneau, D., Berta, Z. K., Irwin, J., et al. 2009, *Nature*, 462, 891
- Charbonneau, P. 2005, *Living Reviews in Solar Physics*, 2, 2
- . 2010, *Living Reviews in Solar Physics*, 7, 3
- Chereul, E., Creze, M., & Bienayme, O. 1998, *Astronomy and Astrophysics*, 340, 384
- . 1999, *Astronomy and Astrophysics Supplement Series*, 135, 5
- Choi, J., Dotter, A., Conroy, C., et al. 2016, arXiv:1604.08592
- Christensen, U. R., & Aubert, J. 2006, *Geophysical Journal International*, 166, 97
- Chubak, C., Marcy, G., Fischer, D. A., et al. 2012, arXiv:1207.6212
- Cohen, O., Drake, J. J., Gloer, A., et al. 2014, *The Astrophysical Journal*, 790, 57
- Cohen, O., Ma, Y., Drake, J. J., et al. 2015, *The Astrophysical Journal*, 806, 41
- Collier Cameron, A., Campbell, C. G., & Quaintrell, H. 1995, *Astronomy and Astrophysics*, 298, 133
- Cortes, C., & Vapnik, V. 1995, *Machine Learning*, 20, 273
- Covey, K. R., Lada, C. J., Román-Zúñiga, C., et al. 2010, *The Astrophysical Journal*, 722, 971
- Cox, A. N., Hodson, S. W., & Shaviv, G. 1981, *The Astrophysical Journal*, 245, L37
- Crossfield, I. J. M., Barman, T., & Hansen, B. M. S. 2011, *The Astrophysical Journal*, 736, 132
- Crossfield, I. J. M., Petigura, E., Schlieder, J. E., et al. 2015, *The Astrophysical Journal*, 804, 10

REFERENCES

- Cumming, A., Butler, R. P., Marcy, G. W., et al. 2008, Publications of the Astronomical Society of the Pacific, 120, 531
- Curran, P. A. 2014, arXiv:1411.3816
- Cushing, M., Vacca, W., & Rayner, J. 2004, Publications of the Astronomical Society of the Pacific, 116, 362
- Cushing, M. C., Rayner, J. T., & Vacca, W. D. 2005, The Astrophysical Journal, 623, 1115
- Cutri, R., Skrutskie, M., van Dyk, S., et al. 2006, Explanatory Supplement to the 2MASS All Sky Data Release
- Cutri, R. M., Skrutskie, M. F., van Dyk, S., et al. 2003, VizieR Online Data Catalog, 2246
- Daemgen, S., Siegler, N., Reid, I. N., & Close, L. M. 2007, The Astrophysical Journal, 654, 558
- Dahn, C. C., Harrington, R. S., Riepe, B. Y., et al. 1976, Publications of the U.S. Naval Observatory Second Series, 24, 1
- D'Antona, F., Ventura, P., & Mazzitelli, I. 2000, The Astrophysical Journal, 543, L77
- Davenport, J. R. A., Hebb, L., & Hawley, S. L. 2015, The Astrophysical Journal, 806, 212
- Davison, C. L., White, R. J., Henry, T. J., et al. 2015, The Astronomical Journal, 149, 106
- Dawson, R. I., Chiang, E., & Lee, E. J. 2015, Monthly Notices of the Royal Astronomical Society, 453, 1471
- De Simone, R. S., Wu, X., & Tremaine, S. 2004, Monthly Notices of the Royal Astronomical Society, 350, 627
- Dehnen, W. 1998, The Astronomical Journal, 115, 2384
- Delfosse, X., Forveille, T., Perrier, C., & Mayor, M. 1998, Astronomy and Astrophysics, 331, 581
- Delfosse, X., Forveille, T., Ségransan, D., et al. 2000, Astronomy and Astrophysics, 364, 217

REFERENCES

- Delfosse, X., Bonfils, X., Forveille, T., et al. 2013, *Astronomy & Astrophysics*, 553, A8
- Delorme, P., Cameron, A. C., Hebb, L., et al. 2011, *Monthly Notices of the Royal Astronomical Society*, 413, 2218
- Demory, B.-O., Ségransan, D., Forveille, T., et al. 2009, *Astronomy and Astrophysics*, 505, 205
- Deshpande, R., Martín, E. L., Montgomery, M. M., et al. 2012, *The Astronomical Journal*, 144, 99
- Deshpande, R., Blake, C. H., Bender, C. F., et al. 2013, *The Astronomical Journal*, 146, 156
- Dhital, S., West, A. A., Stassun, K. G., et al. 2012, *The Astronomical Journal*, 143, 67
- Dhital, S., Oswalt, T. D., Muirhead, P. S., et al. 2013, arXiv:1309.1172
- Dittmann, J. 2016, Distances, Masses, Radii, and Metallicities of the Small Stars in the Solar Neighborhood
- Dittmann, J. A., Irwin, J. M., Charbonneau, D., & Berta-Thompson, Z. K. 2014, *The Astrophysical Journal*, 784, 156
- Dittmann, J. A., Irwin, J. M., Charbonneau, D., & Newton, E. R. 2016, *The Astrophysical Journal*, 818, 153
- Dobler, W., Stix, M., & Brandenburg, A. 2006, *The Astrophysical Journal*, 638, 336
- Donati, J.-F., Forveille, T., Cameron, A. C., et al. 2006, *Science*, 311, 633
- Donati, J.-F., Morin, J., Petit, P., et al. 2008, *Monthly Notices of the Royal Astronomical Society*, 390, 545
- Dotter, A., Chaboyer, B., Jevremović, D., et al. 2008, *The Astrophysical Journal Supplement Series*, 178, 89
- Douglas, S. T., Agüeros, M. A., Covey, K. R., et al. 2016, arXiv:1603.00419
- . 2014, *The Astrophysical Journal*, 795, 161
- Dressing, C. D., & Charbonneau, D. 2013, *The Astrophysical Journal*, 767, 95
- . 2015, *The Astrophysical Journal*, 807, 45

REFERENCES

- Ducourant, C., Dauphole, B., Rapaport, M., Colin, J., & Geffert, M. 1998, *Astronomy and Astrophysics*
- Dumusque, X., Lovis, C., Ségransan, D., et al. 2011, *Astronomy & Astrophysics*, 535, A55
- Dumusque, X., Pepe, F., Lovis, C., et al. 2012, *Nature*, 491, 207
- Durney, B. R., De Young, D. S., & Roxburgh, I. W. 1993, *Solar Physics*, 145, 207
- Eggen, O. J. 1958, *Monthly Notices of the Royal Astronomical Society*, 118, 65
- . 1992, *The Astronomical Journal*, 104, 1482
- Faherty, J. K., Burgasser, A. J., Cruz, K. L., et al. 2009, *The Astronomical Journal*, 137, 1
- Famaey, B., Jorissen, A., Luri, X., et al. 2005, *Astronomy and Astrophysics*, 430, 165
- Famaey, B., Pont, F., Luri, X., et al. 2007, *Astronomy and Astrophysics*, 461, 957
- Famaey, B., Siebert, A., & Jorissen, A. 2008, *Astronomy and Astrophysics*, 483, 453
- Feiden, G. A. 2015, in *ASP Conference Series*, ed. S. Rucinski, G. Torres, & M. Zejda, Vol. 496 (San Francisco, CA: ASP), 137
- Feiden, G. A., & Chaboyer, B. 2012, *The Astrophysical Journal*, 757, 42
- . 2013, *The Astrophysical Journal*, 779, 183
- . 2014, *The Astrophysical Journal*, 789, 53
- Feiden, G. A., Chaboyer, B., & Dotter, A. 2011, *The Astrophysical Journal*, 740, L25
- Feroz, F., & Hobson, M. P. 2013, *Monthly Notices of the Royal Astronomical Society*, 437, 3540
- Fischer, D. A., & Valenti, J. 2005, *The Astrophysical Journal*, 622, 1102
- Fleming, S. W., Mahadevan, S., Deshpande, R., et al. 2015, *The Astronomical Journal*, 149, 143
- Forveille, T., Beuzit, J. L., Delfosse, X., et al. 1999, *Astronomy and Astrophysics*, 351, 10
- Forveille, T., Bonfils, X., Delfosse, X., et al. 2011, arXiv:1109.2505

REFERENCES

- Fowler, R. H., & Milne, E. A. 1923, *Monthly Notices of the Royal Astronomical Society*, 83, 403
- Fressin, F., Torres, G., Charbonneau, D., et al. 2013, *The Astrophysical Journal*, 766, 81
- Fuhrmeister, B., & Schmitt, J. H. M. M. 2004, *Astronomy and Astrophysics*, 420, 1079
- Gabriel, M. 1969, *Low-Luminosity Stars*, ed. S. S. Kumar (New York: Gordon and Breach), 271
- Gaidos, E., Mann, A. W., Lepine, S., et al. 2014, *Monthly Notices of the Royal Astronomical Society*, 443, 2561
- Garcia, B. 1989, *Bulletin d'Information du Centre de Donnees Stellaires*, 36
- Garraffo, C., Drake, J. J., & Cohen, O. 2015, *The Astrophysical Journal*, 813, 40
- Gáspár, A., Rieke, G. H., Su, K. Y. L., et al. 2009, *The Astrophysical Journal*, 697, 1578
- Gastine, T., Morin, J., Duarte, L., et al. 2012, *Astronomy & Astrophysics*, 549, L5
- Gatewood, G. 2008, *The Astronomical Journal*, 136, 452
- Gatewood, G., & Coban, L. 2009, *The Astronomical Journal*, 137, 402
- Giampapa, M. S., & Liebert, J. 1986, *The Astrophysical Journal*, 305, 784
- Gizis, J., & Reid, I. 1997, *Publications of the Astronomical Society of the Pacific*, 109, 1233
- Gizis, J. E. 1997, *The Astronomical Journal*, 113, 806
- Gizis, J. E., Monet, D. G., Reid, I. N., et al. 2000, *The Astronomical Journal*, 120, 1085
- Gizis, J. E., Reid, I. N., & Hawley, S. L. 2002, *The Astronomical Journal*, 123, 3356
- Gizis, J. E., & Reid, N. I. 1996, *The Astronomical Journal*, 111, 365
- Gliese, W., & Jahreiß, H. 1991, *On: The Astronomical Data Center CD-ROM: Selected Astronomical Catalogs*
- Gonzalez, G. 1997, *Monthly Notices of the Royal Astronomical Society*, 285, 403

REFERENCES

- Gould, A., & Chaname, J. 2004, *The Astrophysical Journal Supplement Series*, 150, 455
- Goulding, N. T., Barnes, J. R., Pinfield, D. J., et al. 2013, *Monthly Notices of the Royal Astronomical Society*, 427, 3358
- Gray, D. F. 2009, *The Astrophysical Journal*, 697, 1032
- Gregory, P. C. 2011, *Monthly Notices of the Royal Astronomical Society*, 415, 2523
- Gustafsson, B., Edvardsson, B., Eriksson, K., et al. 2008, *Astronomy and Astrophysics*, 486, 951
- Hansen, B. M. S., & Murray, N. 2013, *The Astrophysical Journal*, 775, 53
- Harrington, R. S., Dahn, C. C., Kallarakal, V. V., et al. 1993, *The Astronomical Journal*, 105, 1571
- Hartman, J. D., Bakos, G. Á., Kovács, G., & Noyes, R. W. 2010, *Monthly Notices of the Royal Astronomical Society*, 408, 475
- Hartman, J. D., Bakos, G. Á., Noyes, R. W., et al. 2011, *The Astronomical Journal*, 141, 166
- Hartmann, L., & Stauffer, J. R. 1989, *The Astronomical Journal*, 97, 873
- Hatzes, A. P. 2013, *Astronomische Nachrichten*, 334, 616
- Hauschildt, P. H., Allard, F., & Baron, E. 1999, *The Astrophysical Journal*, 512, 377
- Hawley, S. L., Gizis, J. E., & Reid, I. N. 1996, *The Astronomical Journal*, 112, 2799
- Hawley, S. L., Tourtellot, J. G., & Reid, I. N. 1999, *The Astronomical Journal*, 117, 1341
- Hearnshaw, J. 2010, *Journal of Astronomical History and Heritage*, 13
- Hearnshaw, J. B. 2014, *The Analysis of Starlight: Two Centuries of Astronomical Spectroscopy* (Cambridge University Press), 382
- Henry, G. W., Baliunas, S. L., Donahue, R. A., Soon, W. H., & Saar, S. H. 1997a, *The Astrophysical Journal*, 474, 503
- Henry, T., Jao, W., Subasavage, J., et al. 2006, *The Astronomical Journal*, 132, 2360
- Henry, T. J., Ianna, P. A., Kirkpatrick, J. D., & Jahreiss, H. 1997b, *The Astronomical Journal*, 114, 388

REFERENCES

- Henry, T. J., Kirkpatrick, J. D., & Simons, D. A. 1994, *The Astronomical Journal*, 108, 1437
- Henry, T. J., Jao, W.-C., Winters, J. G., et al. 2015, *American Astronomical Society Meeting Abstracts*, 227
- Herbst, W., & Miller, J. R. 1989, *The Astronomical Journal*, 97, 891
- Herter, T. L., Henderson, C. P., Wilson, J. C., et al. 2008, in *Proceedings of the SPIE*, ed. I. S. McLean & M. M. Casali, Vol. 7014
- Hoaglin, D. C., Mosteller, F., & Tukey, J. W. 1983, in *Wiley Series in Probability and Mathematical Statistics*, ed. D. C. Hoaglin, F. Mosteller, & J. W. Tukey (New York: Wiley)
- Høg, E., Fabricius, C., Makarov, V. V., et al. 2000, *Astronomy and Astrophysics*, 355
- Holmberg, J., Nordström, B., & Andersen, J. 2009, *Astronomy and Astrophysics*, 501, 941
- Houdebine, E. R. 2008, *Monthly Notices of the Royal Astronomical Society*, 390, 1081
- . 2010, *Monthly Notices of the Royal Astronomical Society*, 407, 1657
- . 2012, *Monthly Notices of the Royal Astronomical Society*, 421, 3180
- Houdebine, E. R., & Mullan, D. J. 2015, *The Astrophysical Journal*, 801, 106
- Howard, A. W., Marcy, G. W., Bryson, S. T., et al. 2012, *The Astrophysical Journal Supplement Series*, 201, 15
- Huber, D., Aguirre, V. S., Matthews, J. M., et al. 2014, *The Astrophysical Journal Supplement Series*, 211, 2
- Ida, T., Ando, M., & Toraya, H. 2000, *Journal of Applied Crystallography*, 33, 1311
- Irwin, J., Aigrain, S., Hodgkin, S., et al. 2006, *Monthly Notices of the Royal Astronomical Society*, 370, 954
- Irwin, J., Berta, Z. K., Burke, C. J., et al. 2011a, *The Astrophysical Journal*, 727, 56
- Irwin, J., Hodgkin, S., Aigrain, S., et al. 2007, *Monthly Notices of the Royal Astronomical Society*, 377, 741

REFERENCES

- Irwin, J. M., Berta-Thompson, Z. K., Charbonneau, D., et al. 2015, in 18th Cambridge Workshop on Cool Stars, Stellar Systems, and the Sun, ed. G. van Belle & H. Harris., 767–772
- Irwin, J. M., Quinn, S. N., Berta, Z. K., et al. 2011b, *The Astrophysical Journal*, 742, 123
- Jackson, R. J., & Jeffries, R. D. 2010, *Monthly Notices of the Royal Astronomical Society*, 407, 465
- . 2012, *Monthly Notices of the Royal Astronomical Society*, 423, 2966
- . 2013, *Monthly Notices of the Royal Astronomical Society*, 431, 1883
- James, D. J., Jardine, M. M., Jeffries, R. D., et al. 2000, *Monthly Notices of the Royal Astronomical Society*, 318, 1217
- Jao, W.-C., Henry, T. J., Subasavage, J. P., et al. 2005, *The Astronomical Journal*, 129, 1954
- Jenkins, J. S., Ramsey, L. W., Jones, H. R. A., et al. 2009, *The Astrophysical Journal*, 704, 975
- Johns-Krull, C. M., & Valenti, J. A. 1996, *The Astrophysical Journal*, 459, doi:10.1086/309954
- Johnson, D. R. H., & Soderblom, D. R. 1987, *The Astronomical Journal*, 93, 864
- Johnson, J. A., & Apps, K. 2009, *The Astrophysical Journal*, 699, 933
- Johnson, J. A., Butler, R. P., Marcy, G. W., et al. 2007, *The Astrophysical Journal*, 670, 833
- Johnson, J. A., Gazak, J. Z., Apps, K., et al. 2012, *The Astronomical Journal*, 143, 111
- Jones, H. R. A., Pavlenko, Y., Viti, S., et al. 2005, *Monthly Notices of the Royal Astronomical Society*, 358, 105
- Jurić, M., Ivezić, Ž., Brooks, A., et al. 2008, *The Astrophysical Journal*, 673, 864
- Kafka, S., & Honeycutt, R. K. 2006, *The Astronomical Journal*, 132, 1517
- Karim, A., & Andersson, J. Y. 2013, *IOP Conference Series: Materials Science and Engineering*, 51, 012001

REFERENCES

- Kawaler, S. D. 1988, *The Astrophysical Journal*, 333, 236
- Khrutskaya, E. V., Izmailov, I. S., & Khovrichev, M. Y. 2010, *Astronomy Letters*, 36, 576
- Kiraga, M. 2012, *Acta Astronomica*, 62, 67
- Kiraga, M., & Stepień, K. 2007, *Acta Astronomica*, 57, 149
- Kiraga, M., & Stępień, K. 2013, *Acta Astronomica*, 63, 53
- Kirkpatrick, J. D., Henry, T. J., & McCarthy, D. W. 1991, *The Astrophysical Journal Supplement Series*, 77, 417
- Kirkpatrick, J. D., Henry, T. J., & Simons, D. A. 1995, *The Astronomical Journal*, 109, 797
- Kirkpatrick, J. D., Reid, I. N., Liebert, J., et al. 1999, *The Astrophysical Journal*, 519, 802
- Koch, D. G., Borucki, W. J., Basri, G., et al. 2010, *The Astrophysical Journal*, 713, L79
- Koen, C., Kilkenney, D., van Wyk, F., & Marang, F. 2010, *Monthly Notices of the Royal Astronomical Society*, 403, 1949
- Koenigl, A. 1991, *The Astrophysical Journal*, 370, L39
- Konopacky, Q. M., Ghez, A. M., Fabrycky, D. C., et al. 2012, *The Astrophysical Journal*, 750, 79
- Kopparapu, R. K., Ramirez, R., Kasting, J. F., et al. 2013, *The Astrophysical Journal*, 765, 131
- Kraft, R. P. 1967, *The Astrophysical Journal*, 150, 551
- Kreidberg, L., Bean, J. L., Désert, J.-M., et al. 2014, *Nature*, 505, 69
- Kruse, E. A., Berger, E., Knapp, G. R., et al. 2010, *The Astrophysical Journal*, 722, 1352
- Küker, M., & Rüdiger, G. 1999, *Astronomy and Astrophysics*
- Kurucz, R. L. 1992, in *IAU Symp. 149, The Stellar Populations of Galaxies*, ed. B. Barbuy & A. Renzini (Dordrecht: Kluwer), 225

REFERENCES

- Latham, D. W., Stefanik, R. P., Torres, G., et al. 2002, *The Astronomical Journal*, 124, 1144
- Laughlin, G., Bodenheimer, P., & Adams, F. C. 1997, *The Astrophysical Journal*, 482, 420
- . 2004, *The Astrophysical Journal*, 612, L73
- Law, N. M., Hodgkin, S. T., & Mackay, C. D. 2008, *Monthly Notices of the Royal Astronomical Society*, 384, 150
- Lee, K.-G., Berger, E., & Knapp, G. R. 2010, *The Astrophysical Journal*, 708, 1482
- Leggett, S. K. 1992, *The Astrophysical Journal Supplement Series*, 82, 351
- Leggett, S. K., Allard, F., Dahn, C., et al. 2000, *The Astrophysical Journal*, 535, 965
- Lépine, S. 2005, *The Astronomical Journal*, 130, 1680
- Lépine, S., & Gaidos, E. 2011, *The Astronomical Journal*, 142, 138
- Lépine, S., Hilton, E. J., Mann, A. W., et al. 2013, *The Astronomical Journal*, 145, 102
- Lépine, S., Rich, R. M., & Shara, M. M. 2007, *The Astrophysical Journal*, 669, 1235
- Lépine, S., & Shara, M. M. 2005, *The Astronomical Journal*, 129, 1483
- Lépine, S., Thorstensen, J. R., Shara, M. M., & Rich, R. M. 2009, *The Astronomical Journal*, 137, 4109
- Lissauer, J. J., Ragozzine, D., Fabrycky, D. C., et al. 2011, *The Astrophysical Journal Supplement Series*, 197, 8
- Livingston, W. C. 1969, *Astronomical Society of the Pacific Leaflets*, 10, 265
- Lopez-Morales, M. 2007, *The Astrophysical Journal*, 660, 732
- Lopez-Morales, M., & Ribas, I. 2005, *The Astrophysical Journal*, 631, 1120
- Lord, S. D. 1992
- Luhman, K. L., Briceno, C., Rieke, G. H., & Hartmann, L. 1998, *The Astrophysical Journal*, 493, 909
- Luhman, K. L., & Rieke, G. H. 1999, *The Astrophysical Journal*, 525, 440

REFERENCES

- Lurie, J. C., Henry, T. J., Jao, W.-C., et al. 2014, *The Astronomical Journal*, 148, 91
- MacDonald, J., & Mullan, D. J. 2012, *Monthly Notices of the Royal Astronomical Society*, 421, 3084
- Mahadevan, S., Ramsey, L., Bender, C., et al. 2012, in *Ground-based and Airborne Instrumentation for Astronomy IV*, ed. I. S. McLean, S. K. Ramsay, & H. Takami, Vol. 8446
- Makarov, V. V., & Berghea, C. 2014, *The Astrophysical Journal*, 780, 124
- Malo, L., Artigau, É., Doyon, R., et al. 2014, *The Astrophysical Journal*, 788, 81
- Mamajek, E. E., & Hillenbrand, L. A. 2008, *The Astrophysical Journal*, 687, 1264
- Mamajek, E. E., Bartlett, J. L., Seifahrt, A., et al. 2013, *The Astronomical Journal*, 146, 154
- Mann, A. W., Brewer, J. M., Gaidos, E., Lépine, S., & Hilton, E. J. 2013a, *The Astronomical Journal*, 145, 52
- Mann, A. W., Deacon, N. R., Gaidos, E., et al. 2014, *The Astronomical Journal*, 147, 160
- Mann, A. W., Gaidos, E., & Ansdell, M. 2013b, *The Astrophysical Journal*, 779, 188
- Mann, A. W., Gaidos, E., Lépine, S., & Hilton, E. J. 2012, *The Astrophysical Journal*, 753, 90
- Marcy, G. W., & Chen, G. H. 1992, *The Astrophysical Journal*, 390, 550
- Markwardt, C. B. 2009, *Astronomical Data Analysis Software and Systems XVIII*, 411, 4
- Massarotti, A., Latham, D. W., Stefanik, R. P., & Fogel, J. 2008, *The Astronomical Journal*, 135, 209
- Matt, S., & Pudritz, R. E. 2005, *The Astrophysical Journal*, 632, L135
- Mayor, M., Bonfils, X., Forveille, T., et al. 2009, *Astronomy and Astrophysics*, 507, 487
- McCarthy, C., Zuckerman, B., & Becklin, E. E. 2001, *The Astronomical Journal*, 121, 3259

REFERENCES

- McLean, I. S., McGovern, M. R., Burgasser, A. J., et al. 2003, *The Astrophysical Journal*, 596, 561
- McLean, M., Berger, E., & Reiners, A. 2012, *The Astrophysical Journal*, 746, 23
- McQuillan, A., Aigrain, S., & Mazeh, T. 2013, *Monthly Notices of the Royal Astronomical Society*, 432, 1203
- McQuillan, A., Mazeh, T., & Aigrain, S. 2014, *The Astrophysical Journal Supplement Series*, 211, 24
- Meibom, S., Barnes, S. A., Platais, I., et al. 2015, *Nature*, 517, 589
- Meibom, S., & Mathieu, R. D. 2005, *The Astrophysical Journal*, 620, 970
- Meibom, S., Barnes, S. A., Latham, D. W., et al. 2011, *The Astrophysical Journal*, 733, L9
- Meléndez, J., Asplund, M., Gustafsson, B., & Yong, D. 2009, *The Astrophysical Journal*, 704, L66
- Messina, S., Desidera, S., Lanzafame, A. C., Turatto, M., & Guinan, E. F. 2011, *Astronomy & Astrophysics*, 532, A10
- Meunier, N., Desort, M., & Lagrange, A.-M. 2010, *Astronomy and Astrophysics*, 512, A39
- Minchev, I., Martig, M., Streich, D., et al. 2015, *The Astrophysical Journal*, 804, L9
- Mitchell, W. M. 1915, *Popular Astronomy*, 24
- Mohanty, S., & Basri, G. 2003, *The Astrophysical Journal*, 583, 451
- Mohanty, S., Basri, G., Shu, F., Allard, F., & Chabrier, G. 2002, *The Astrophysical Journal*, 571, 469
- Monet, D. G., Dahn, C. C., Vrba, F. J., et al. 1992, *The Astronomical Journal*, 103, 638
- Montagnier, G., Ségransan, D., Beuzit, J.-L., et al. 2006, *Astronomy and Astrophysics*, 460, L19
- Montet, B. T., Crepp, J. R., Johnson, J. A., Howard, A. W., & Marcy, G. W. 2014, *The Astrophysical Journal*, 781, 28
- Morales, J. C., Gallardo, J., Ribas, I., et al. 2010, *The Astrophysical Journal*, 718, 502

REFERENCES

- Morales, J. C., Ribas, I., & Jordi, C. 2008, *Astronomy and Astrophysics*, 478, 507
- Morgan, D. P., West, A. A., Garcés, A., et al. 2012, *The Astronomical Journal*, 144, 93
- Morin, J., Donati, J.-F., Petit, P., et al. 2010, *Monthly Notices of the Royal Astronomical Society*, 407, 2269
- . 2008a, *Monthly Notices of the Royal Astronomical Society*, 390, 567
- Morin, J., Donati, J.-F., Forveille, T., et al. 2008b, *Monthly Notices of the Royal Astronomical Society*, 384, 77
- Muirhead, P. S., Hamren, K., Schlawin, E., et al. 2012a, *The Astrophysical Journal*, 750, L37
- Muirhead, P. S., Johnson, J. A., Apps, K., et al. 2012b, *The Astrophysical Journal*, 747, 144
- Muirhead, P. S., Vanderburg, A., Shporer, A., et al. 2013, *The Astrophysical Journal*, 767, 111
- Muirhead, P. S., Becker, J., Feiden, G. A., et al. 2014, *The Astrophysical Journal Supplement Series*, 213, 5
- Muirhead, P. S., Mann, A. W., Vanderburg, A., et al. 2015, *The Astrophysical Journal*, 801, 18
- Mulders, G. D., Pascucci, I., & Apai, D. 2015, *The Astrophysical Journal*, 798, 112
- Mullan, D. J., & MacDonald, J. 2001, *The Astrophysical Journal*, 559, 353
- Narita, N., Fukui, A., Ikoma, M., et al. 2013, *The Astrophysical Journal*, 773, 144
- Nascimbeni, V., Mallonn, M., Scandariato, G., et al. 2015, *Astronomy & Astrophysics*, 579, A113
- Neves, V., Bonfils, X., Santos, N. C., et al. 2013, *Astronomy & Astrophysics*, 551, A36
- . 2012, *Astronomy & Astrophysics*, 538, A25
- Newton, E. R. 2015a, doi:10.5281/zenodo.35686
- . 2015b, doi:10.5281/zenodo.35687

REFERENCES

- Newton, E. R., Charbonneau, D., Irwin, J., et al. 2014, *The Astronomical Journal*, 147, 20
- Newton, E. R., Charbonneau, D., Irwin, J., & Mann, A. W. 2015, *The Astrophysical Journal*, 800, 85
- Newton, E. R., Irwin, J., Charbonneau, D., et al. 2016, *The Astrophysical Journal*, 821, 93
- Nidever, D. L., Marcy, G. W., Butler, R. P., Fischer, D. A., & Vogt, S. S. 2002, *The Astrophysical Journal Supplement Series*, 141, 503
- Nordstrom, B., Mayor, M., Andersen, J., et al. 2004, *Astronomy and Astrophysics*, 418, 989
- Norton, A. J., Wheatley, P. J., West, R. G., et al. 2007, *Astronomy and Astrophysics*, 467, 785
- Noyes, R. W., Hartmann, L. W., Baliunas, S. L., Duncan, D. K., & Vaughan, A. H. 1984, *The Astrophysical Journal*, 279, 763
- Núñez, A., Agüeros, M. A., Covey, K. R., et al. 2015, *The Astrophysical Journal*, 809, 161
- Nutzman, P., & Charbonneau, D. 2008, *Publications of the Astronomical Society of the Pacific*, 120, 317
- Ofek, E. O. 2009, *Publications of the Astronomical Society of the Pacific*, 121, 814
- Önehag, A., Heiter, U., Gustafsson, B., et al. 2012, *Astronomy & Astrophysics*, 542, A33
- Pallavicini, R., Golub, L., Rosner, R., et al. 1981, *The Astrophysical Journal*, 248, 279
- Payne, C. H. 1925, *Proceedings of the National Academy of Sciences*, 11, 192
- Pecaut, M. J., & Mamajek, E. E. 2013, *The Astrophysical Journal Supplement Series*, 208, 9
- Pedregosa, F., Varoquaux, G., Gramfort, A., et al. 2011, *Journal of Machine Learning Research*, 12, 2825
- Perryman, M. A. C., Lindegren, L., Kovalevsky, J., et al. 1997, *Astronomy and Astrophysics* 323, L49-L52

REFERENCES

- Perryman, M. A. C., Brown, A. G. A., Lebreton, Y., et al. 1998, *Astronomy and Astrophysics*, 331, 40
- Petigura, E. A. 2014, *Prevalence of Earth-size Planets Orbiting Sun-like Stars*
- Pickles, A. 1998, *Publications of the Astronomical Society of the Pacific*, 110, 863
- Pizzolato, N., Maggio, A., Micela, G., Sciortino, S., & Ventura, P. 2003, *Astronomy and Astrophysics*, 397, 147
- Popper, D. M. 1997, *The Astronomical Journal*, 114, 1195
- Poveda, A., Allen, C., Costero, R., Echevarría, J., & Hernández-Alcántara, A. 2009, *The Astrophysical Journal*, 706, 343
- Pravdo, S. H., Shaklan, S. B., & Lloyd, J. 2005, *The Astrophysical Journal*, 630, 528
- Queloz, D., Bouchy, F., Moutou, C., et al. 2009, *Astronomy and Astrophysics*, 506, 303
- Quillen, A. C., & Minchev, I. 2005, *The Astronomical Journal*, 130, 576
- Quintana, E. V., Barclay, T., Raymond, S. N., et al. 2014, *Science*, 344, 277
- Quirrenbach, A., Amado, P. J., Caballero, J. A., et al. 2014, in *Proceedings of the SPIE*, ed. S. K. Ramsay, I. S. McLean, & H. Takami, Vol. 9147
- Rajpaul, V., Aigrain, S., Osborne, M. A., Reece, S., & Roberts, S. 2015, *Monthly Notices of the Royal Astronomical Society*, 452, 2269
- Rajpurohit, A. S., Reylé, C., Allard, F., et al. 2013, *Astronomy & Astrophysics*, 556, A15
- Rappaport, S., Swift, J., Levine, A., et al. 2014, *The Astrophysical Journal*, 788, 114
- Rayner, J., Toomey, D., Onaka, P., et al. 2003, *Publications of the Astronomical Society of the Pacific*, 115, 362
- Rayner, J. T., Cushing, M. C., & Vacca, W. D. 2009, *The Astrophysical Journal Supplement Series*, 185, 289
- Rebassa-Mansergas, A., Schreiber, M. R., & Gansicke, B. T. 2013, *Monthly Notices of the Royal Astronomical Society*, 429, 3570
- Reid, I. N., & Hawley, S. L. 2005, *New Light on Dark Stars* (Springer Berlin Heidelberg)

REFERENCES

- Reid, I. N., Hawley, S. L., & Gizis, J. E. 1995, *The Astronomical Journal*, 110, 1838
- . 1997, *VizieR On-line Data Catalog: III/198*. Originally published in: 1995AJ....110.1838R; 1996AJ....112.2799H
- Reid, I. N., Kirkpatrick, J. D., Liebert, J., et al. 2002, *The Astronomical Journal*, 124, 519
- Reiners, A. 2012, *Living Reviews in Solar Physics*, 9
- Reiners, A., & Basri, G. 2007, *The Astrophysical Journal*, 656, 1121
- . 2008, *The Astrophysical Journal*, 684, 1390
- . 2009a, *The Astrophysical Journal*, 705, 1416
- . 2009b, *Astronomy and Astrophysics*, 496, 787
- . 2010, *The Astrophysical Journal*, 710, 924
- Reiners, A., Basri, G., & Browning, M. 2009, *The Astrophysical Journal*, 692, 538
- Reiners, A., Joshi, N., & Goldman, B. 2012, *The Astronomical Journal*, 143, 93
- Reiners, A., & Mohanty, S. 2012, *The Astrophysical Journal*, 746, 43
- Reiners, A., Schüssler, M., & Passetger, V. M. 2014, *The Astrophysical Journal*, 794, 144
- Rempel, M., & Schlichenmaier, R. 2011, *Living Reviews in Solar Physics*, 8
- Reuyl, D. 1938, *The Astronomical Journal*, 47, 144
- Ribas, I. 2006, *Astrophysics and Space Science*, 304, 89
- Riedel, A. R., Subasavage, J. P., Finch, C. T., et al. 2010, *The Astronomical Journal*, 140, 897
- Rivera, E. J., Lissauer, J. J., Butler, R. P., et al. 2005, *The Astrophysical Journal*, 634, 625
- Robb, R. M., Balam, D. D., & Greimel, R. 1999, *Information Bulletin on Variable Stars*, 4714
- Robertson, P., Endl, M., Henry, G. W., et al. 2015a, *The Astrophysical Journal*, 801, 79

REFERENCES

- Robertson, P., & Mahadevan, S. 2014, *The Astrophysical Journal*, 793, L24
- Robertson, P., Mahadevan, S., Endl, M., & Roy, A. 2014, *Science*, 345, 440
- Robertson, P., Roy, A., & Mahadevan, S. 2015b, *The Astrophysical Journal*, 805, L22
- Robin, A. C., Reyl  , C., Derri  re, S., & Picaud, S. 2003, *Astronomy and Astrophysics*, 409, 523
- Rodler, F., & L  pez-Morales, M. 2014, *The Astrophysical Journal*, 781, 54
- Rogalski, A. 2012, *Opto-Electronics Review*, 20
- Rogers, L. A. 2015, *The Astrophysical Journal*, 801, 41
- Rojas-Ayala, B., Covey, K. R., Muirhead, P. S., & Lloyd, J. P. 2010, *The Astrophysical Journal*, 720, L113
- . 2012, *The Astrophysical Journal*, 748, 93
- Ruiz, M. T., Wischnjewsky, M., Rojo, P. M., & Gonzalez, L. E. 2001, *The Astrophysical Journal Supplement Series*, 133, 119
- Saar, S. H., Butler, R. P., & Marcy, G. W. 1998, *The Astrophysical Journal*, 498, L153
- Saar, S. H., & Donahue, R. A. 1997, *The Astrophysical Journal*, 485, 319
- Saha, M. N. 1921, *Proceedings of the Royal Society A: Mathematical, Physical and Engineering Sciences*, 99, 135
- Salim, S., & Gould, A. 2003, *The Astrophysical Journal*, 582, 1011
- Santos, N. C., Israelian, G., & Mayor, M. 2004, *Astronomy and Astrophysics*, 415, 1153
- Santos, N. C., Israelian, G., Mayor, M., et al. 2005, *Astronomy and Astrophysics*, 437, 1127
- Santos, N. C., Mayor, M., Bonfils, X., et al. 2011, *Astronomy & Astrophysics*, 526, A112
- Saumon, D., Bergeron, P., Lunine, J. I., Hubbard, W. B., & Burrows, A. 1994, *The Astrophysical Journal*, 424, 333
- Schiavon, R. P., Barbuy, B., & Singh, P. D. 1997, *The Astrophysical Journal*, 484, 499
- Schlaufman, K. C., & Laughlin, G. 2010, *Astronomy and Astrophysics*, 519, A105

REFERENCES

- . 2011, *The Astrophysical Journal*, 738, 177
- Schmidt, S. J., Cruz, K. L., Bongiorno, B. J., Liebert, J., & Reid, I. N. 2007, *The Astronomical Journal*, 133, 2258
- Schneider, J., Dedieu, C., Le Sidaner, P., Savalle, R., & Zolotukhin, I. 2011, *Astronomy & Astrophysics*, 532, A79
- Scholz, A., & Eisloffel, J. 2007, *Monthly Notices of the Royal Astronomical Society*, 381, 1638
- Scholz, A., Irwin, J., Bouvier, J., et al. 2011, *Monthly Notices of the Royal Astronomical Society*, 413, 2595
- Scholz, F. W., & Stephens, M. A. 1987, *Journal of the American Statistical Association*, 82, 918
- Schönrich, R., Binney, J., & Dehnen, W. 2010, *Monthly Notices of the Royal Astronomical Society*, 403, 1829
- Schrijver, C. 2002, *Astronomische Nachrichten*, 323, 157
- Schrijver, C. J., & Zwaan, C. 2000, *Solar and Stellar Magnetic Activity* (Cambridge: Cambridge University Press)
- Schrinner, M., Petitdemange, L., & Dormy, E. 2012, *The Astrophysical Journal*, 752, 121
- Schweitzer, A., Gizis, J. E., Hauschildt, P. H., Allard, F., & Reid, I. N. 2001, *The Astrophysical Journal*, 555, 368
- Seabroke, G. M., & Gilmore, G. 2007, *Monthly Notices of the Royal Astronomical Society*, 380, 1348
- Ségransan, D., Kervella, P., Forveille, T., & Queloz, D. 2003, *Astronomy and Astrophysics*, 397, L5
- Shkolnik, E. L., Anglada-Escudé, G., Liu, M. C., et al. 2012, *The Astrophysical Journal*, 758, 56
- Shkolnik, E. L., Hebb, L., Liu, M. C., Neill Reid, I., & Cameron, A. C. 2010, *The Astrophysical Journal*, 716, 1522
- Skrutskie, M. F., Cutri, R. M., Stiening, R., et al. 2006, *The Astronomical Journal*, 131, 1163

REFERENCES

- Skumanich, A. 1972, *The Astrophysical Journal*, 171, 565
- Slee, O. B., & Stewart, R. T. 1989, *Monthly Notices of the Royal Astronomical Society*, 236, 129
- Smart, R. L., Ioannidis, G., Jones, H. R. A., Bucciarelli, B., & Lattanzi, M. G. 2010, *Astronomy and Astrophysics*, 514, A84
- Smart, R. L., Lattanzi, M. G., Jahreiß, H., Bucciarelli, B., & Massone, G. 2007, *Astronomy and Astrophysics*, 464, 787
- Smith, J. C., Stumpe, M. C., Van Cleve, J. E., et al. 2012, *Publications of the Astronomical Society of the Pacific*, 124, 1000
- Snellen, I. A. G., de Kok, R. J., le Poole, R., Brogi, M., & Birkby, J. 2013, *The Astrophysical Journal*, 764, 182
- Soderblom, D. R. 1983, *The Astrophysical Journal Supplement Series*, 53, 1
- . 2010, *Annual Review of Astronomy and Astrophysics*, 48, 581
- Soderblom, D. R., Duncan, D. K., & Johnson, D. R. H. 1991, *The Astrophysical Journal*, 375, 722
- Soderblom, D. R., Stauffer, J. R., Hudon, J. D., & Jones, B. F. 1993, *The Astrophysical Journal Supplement Series*, 85, 315
- Solanki, S. 2002, *Astronomische Nachrichten*, 323, 165
- Soubiran, C., Bienaymé, O., Mishenina, T. V., & Kovtyukh, V. V. 2008, *Astronomy and Astrophysics*, 480, 91
- Sousa, S. G., Santos, N. C., Israelian, G., Mayor, M., & Monteiro, M. J. P. F. G. 2006, *Astronomy and Astrophysics*, 458, 873
- Sousa, S. G., Santos, N. C., Israelian, G., Mayor, M., & Udry, S. 2011, *Astronomy & Astrophysics*, 533, A141
- Sousa, S. G., Santos, N. C., Mayor, M., et al. 2008, *Astronomy and Astrophysics*, 487, 373
- Sozzetti, A., Torres, G., Latham, D. W., et al. 2009, *The Astrophysical Journal*, 697, 544
- Spada, F., Demarque, P., Kim, Y. C., & Sills, A. 2013, *The Astrophysical Journal*, 776, 87

REFERENCES

- Stauffer, J. R., Balachandran, S. C., Krishnamurthi, A., et al. 1997a, *The Astrophysical Journal*, 475, 604
- Stauffer, J. R., Caillault, J.-P., Gagne, M., Prosser, C. F., & Hartmann, L. W. 1994, *The Astrophysical Journal Supplement Series*, 91, 625
- Stauffer, J. R., & Hartmann, L. W. 1986, *The Astrophysical Journal Supplement Series*, 61, 531
- Stauffer, J. R., Hartmann, L. W., & Latham, D. W. 1987, *The Astrophysical Journal*, 320, L51
- Stauffer, J. R., Hartmann, L. W., Prosser, C. F., et al. 1997b, *The Astrophysical Journal*, 479, 776
- Stelzer, B., Marino, A., Micela, G., Lopez-Santiago, J., & Liefke, C. 2013, *Monthly Notices of the Royal Astronomical Society*, 431, 2063
- Stewart, R. T., Innis, J. L., Slee, O. B., Nelson, G. J., & Wright, A. E. 1988, *The Astronomical Journal*, 96, 371
- Stumpe, M. C., Smith, J. C., Van Cleve, J. E., et al. 2012, *Publications of the Astronomical Society of the Pacific*, 124, 985
- Stumpff, P. 1980, *Astronomy and Astrophysics Supplement*, 41
- Suárez Mascareño, A., Rebolo, R., González Hernández, J. I., & Esposito, M. 2015, *Monthly Notices of the Royal Astronomical Society*, 452, 2745
- Swift, J. J., Johnson, J. A., Morton, T. D., et al. 2013, *The Astrophysical Journal*, 764, 105
- Tanner, A., White, R., Bailey, J., et al. 2012, *The Astrophysical Journal Supplement Series*, 203, 10
- Tassoul, J.-L., & Tassoul, M. 2014, *A Concise History of Solar and Stellar Physics*, Vol. 28 (Princeton University Press)
- Terrien, R. C., Mahadevan, S., Bender, C. F., et al. 2012, *The Astrophysical Journal*, 747, L38
- Terrien, R. C., Mahadevan, S., Deshpande, R., & Bender, C. F. 2015, *The Astrophysical Journal Supplement Series*, 220, 16
- Testa, P., Saar, S. H., & Drake, J. J. 2015, *Philosophical transactions. Series A, Mathematical, physical, and engineering sciences*, 373

REFERENCES

- Thompson, M. J., Christensen-Dalsgaard, J., Miesch, M. S., & Toomre, J. 2003, *Annual Review of Astronomy and Astrophysics*, 41, 599
- Thompson, P., Cox, D. E., & Hastings, J. B. 1987, *Journal of Applied Crystallography*, 20, 79
- Tinney, C. G., & Reid, I. N. 1998, *Monthly Notices of the Royal Astronomical Society*, 301, 1031
- Tokovinin, A. A. 1992, *Astronomy and Astrophysics*, 256, 121
- Torres, C. A. O., Quast, G. R., da Silva, L., et al. 2006, *Astronomy and Astrophysics*, 460, 695
- Torres, G. 2013, *Astronomische Nachrichten*
- Torres, G., Andersen, J., & Giménez, A. 2009, *The Astronomy and Astrophysics Review*, 18, 67
- Torres, G., & Ribas, I. 2002, *The Astrophysical Journal*, 567, 1140
- Tuomi, M. 2011, *Astronomy & Astrophysics*, 528, L5
- Udry, S., Bonfils, X., Delfosse, X., et al. 2007, *Astronomy and Astrophysics*, 469, L43
- Vacca, W., Cushing, M., & Rayner, J. 2003, *Publications of the Astronomical Society of the Pacific*, 115, 389
- Valenti, J. A., & Fischer, D. A. 2005, *The Astrophysical Journal Supplement Series*, 159, 141
- Valenti, J. A., Piskunov, N., & Johns-Krull, C. M. 1998, *The Astrophysical Journal*, 498, 851
- van Altena, W. F., Lee, J. T., & Hoffleit, E. D. 2001, *VizieR On-line Data Catalog: I/238A*. Originally published in: 1995GCTP..C.....0V
- van Leeuwen, F. 2007, *Astronomy and Astrophysics*, 474, 653
- Vaquero, J. M., & Vázquez, M. 2009, *The Sun Recorded Through History: Scientific Data Extracted from Historical Documents*, 361, doi:10.1007/978-0-387-92789-3
- Vidotto, A. A., Gregory, S. G., Jardine, M., et al. 2014, *Monthly Notices of the Royal Astronomical Society*, 441, 2361

REFERENCES

- Vilhu, O. 1984, *Astronomy and Astrophysics*, 133, 117
- Vogt, S. S., Butler, R. P., Rivera, E. J., et al. 2010, *The Astrophysical Journal*, 723, 954
- Vogt, S. S., Penrod, G. D., & Soderblom, D. R. 1983, *The Astrophysical Journal*, 269, 250
- von Braun, K., Boyajian, T. S., Kane, S. R., et al. 2012, *The Astrophysical Journal*, 753, 171
- von Braun, K., Boyajian, T. S., van Belle, G. T., et al. 2014, *Monthly Notices of the Royal Astronomical Society*, 438, 2413
- Walkowicz, L., Hawley, S., & West, A. 2004, *Publications of the Astronomical Society of the Pacific*, 116, 1105
- Weber, E. J., & Davis, Leverett, J. 1967, *The Astrophysical Journal*, 148, 217
- West, A. A., & Basri, G. 2009, *The Astrophysical Journal*, 693, 1283
- West, A. A., & Hawley, S. L. 2008, *Publications of the Astronomical Society of the Pacific*, 120, 1161
- West, A. A., Hawley, S. L., Bochanski, J. J., et al. 2008, *The Astronomical Journal*, 135, 785
- West, A. A., Weisenburger, K. L., Irwin, J., et al. 2015, *The Astrophysical Journal*, 812, 3
- West, A. A., Hawley, S. L., Walkowicz, L. M., et al. 2004, *The Astronomical Journal*, 128, 426
- West, A. A., Morgan, D. P., Bochanski, J. J., et al. 2011, *The Astronomical Journal*, 141, 97
- Wielen, R. 1977, *Astronomy and Astrophysics*, 60, 263
- Williams, P. K. G., Cook, B. A., & Berger, E. 2014, *The Astrophysical Journal*, 785, 9
- Wilson, O. C. 1963, *The Astrophysical Journal*, 138, 832
- . 1966, *The Astrophysical Journal*, 144, 695
- Wilson, O. C., & Skumanich, A. 1964, *The Astrophysical Journal*, 140, 1401
- Windmiller, G., Orosz, J. A., & Etzel, P. B. 2010, *The Astrophysical Journal*, 712, 1003

REFERENCES

- Winters, J. 2015, Nearby Red Dwarfs and Their Dance Partners: Characterizing More Than 2000 Single and Multiple M Dwarfs Near the Sun
- Wittmann, A. D., & Xu, Z. T. 1987, *Astronomy and Astrophysics Supplement Series*, 70, 83
- Woolf, V., & Wallerstein, G. 2006, *Publications of the Astronomical Society of the Pacific*, 118, 218
- Woolf, V. M., & Wallerstein, G. 2005, *Monthly Notices of the Royal Astronomical Society*, 356, 963
- Woolf, V. M., & West, A. A. 2012, *Monthly Notices of the Royal Astronomical Society*, 422, 1489
- Worley, C. E. 1960, *Publications of the Astronomical Society of the Pacific*, 72, 125
- Wright, N. J., Drake, J. J., Mamajek, E. E., & Henry, G. W. 2011, *The Astrophysical Journal*, 743, 48
- Yadav, R. K., Christensen, U. R., Morin, J., et al. 2015a, *The Astrophysical Journal*, 813, L31
- Yadav, R. K., Gastine, T., Christensen, U. R., & Reiners, A. 2015b, *Astronomy & Astrophysics*, 573, A68
- Yau, K. K. C., & Stephenson, F. R. 1988, *Royal Astronomical Society*, 29, 175
- Zapatero Osorio, M. R., Martin, E. L., Bouy, H., et al. 2006, *The Astrophysical Journal*, 647, 1405
- Zickgraf, F.-J., Krautter, J., Reffert, S., et al. 2005, *Astronomy and Astrophysics*, 433, 151